

**ANISOTROPIC POLYMER BLEND AND GEL NANOCOMPOSITES
USING EXTERNAL ELECTRIC OR MAGNETIC FIELDS**

by

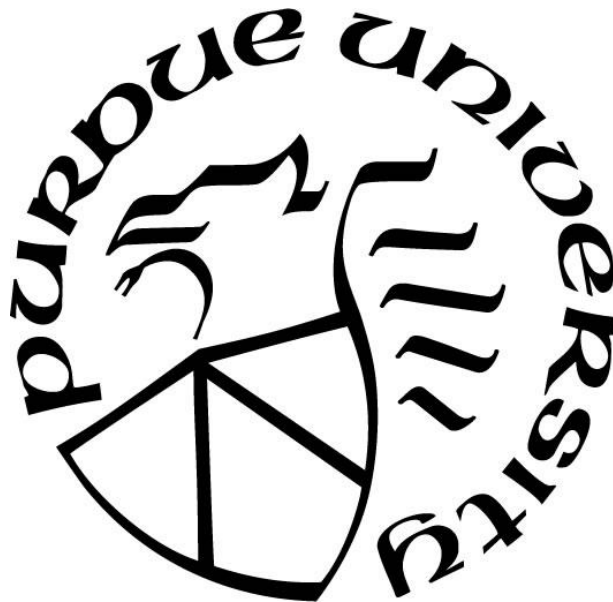
SungHo Yook

A Dissertation

Submitted to the Faculty of Purdue University

In Partial Fulfillment of the Requirements for the degree of

Doctor of Philosophy



School of Materials Engineering

West Lafayette, Indiana

August 2020

**THE PURDUE UNIVERSITY GRADUATE SCHOOL
STATEMENT OF COMMITTEE APPROVAL**

Dr. Mukerrem Cakmak, Chair

School of Materials and Mechanical Engineering

Dr. Jeffrey Youngblood

School of Materials Engineering

Dr. John Howarter

School of Materials Engineering

Dr. Chelsea Davis

School of Materials Engineering

Approved by:

Dr. David Bahr

Head of the Graduate Program

*Dedicated to my parents, DongHack Yook and Myungsook Lee, and my beloved wife Tzu-Yu Lai
for their love, support, and encouragement all along the way*

ACKNOWLEDGMENTS

I sincerely express my deep appreciation and gratitude to Prof. Mukerrem Cakmak for his guidance and support throughout my PhD journey. When I was not matched with any of advisors in first year of PhD, he generously accepted me as a member of his research group. During the time I have worked with him, he has always been patient in guiding me even though I could not produce any meaningful scientific results in the first 3 years of my PhD. Without his financial support for 5 years of my PhD, I certainly could not have achieved a PhD degree.

I wish to thank my committee, Prof. Jeffrey Youngblood, Prof. John Howarter, and Prof. Chelsea Davis. As experts in the fields of polymer science, their valuable guidance and comments substantially improved the contents of my dissertation.

I also appreciate to research scientists, especially Dr. Joonhyung park, Dr. Rosa Diaz Rivas, Dr. Neil Dilley, and Dr. Nicholas Glassmaker, who provided the trainings on the equipment in Birck Nanotechnology Center. Without their help, it would have been hard for me to work with nanotechnology equipment and tools for obtaining the experimental data. I also express my gratitude to Robert Seiler, who taught me how to do ultramicrotome sectioning, and to Tugba Isik in Mechanical Engineering Department, who took beautiful TEM images for one of my publications.

Lastly, I would like to thank my group members: Armen Yildirim, Zeynep Mutlu, Jesse Grant, Mayank Jain, John Bui, Carlos Serratos, Dr. Siamak Shams Es-haghi, Dr. Keke Chen, Dr. Yuanhao Guo, Dr. Enmin Wang, Dr. Fang Peng, and Dr. Megan Forshey. I especially thank to Armen who has been my best friend as well as my English teacher during my five years of PhD. I also appreciate Zeynep and Mayank who helped me a lot when I first joined in MURI projects. I also thank my Korean friends who often enjoyed meals and drinks together with me. Lastly, I thank Jesse who proofread the draft of this dissertation with immense care and skill.

TABLE OF CONTENTS

TABLE OF CONTENTS.....	5
LIST OF TABLES.....	7
LIST OF FIGURES	8
ABSTRACT.....	16
1. INTRODUCTION.....	17
2. BACKGROUND AND LITERATURE REVIEW	23
2.1 Polymer blends and copolymers.....	23
2.1.1 Polymer blends (homopolymer mixture).....	23
2.1.2 Diblock copolymers.....	27
2.2 Polymer nanocomposites	29
2.2.1 Nanoparticles in a homopolymer matrix	30
2.2.2 Nanoparticles in polymer blends	40
2.3 Field-assisted assembly.....	48
2.4 Hydrogel nanocomposites.....	62
3. ANISOTROPIC PHASE-SEPARATED MORPHOLOGY OF POLYMER BLENDS DIRECTED BY ELECTRICALLY PRE-ORIENTED CLAY PLATELETS.....	68
3.1 Introduction.....	68
3.2 Experimental section.....	70
3.2.1 Materials	70
3.2.2 Phase diagram.....	70
3.2.3 Sample preparation	71
3.2.4 Morphological analysis.....	72
3.2.5 Image analysis	73
3.3 Results and discussion	74
3.4 Conclusion	103
4. ANISOTROPIC STRUCTURE IN POLYMER BLENDS BY USING THROUGH-PLANE ORIENTED CLAY PLATELETS.....	104
4.1 Introduction.....	104
4.2 Experimental section.....	106

4.2.1	Materials	106
4.2.2	Sample preparation	107
4.2.3	Sample characterization.....	109
4.3	Results and discussion	110
4.3	Conclusion	128
5.	ANISOTROPIC HYDROGELS FORMED BY MAGNETICALLY ORIENTED NANOCLAY SUSPENSIONS FOR WOUND DRESSINGS.....	129
5.1	Introduction.....	129
5.2	Experimental section.....	131
5.2.1	Materials	131
5.2.2	Sample preparation	131
5.2.3	Sample characterization.....	132
5.3	Results and discussion	134
5.4	Conclusion	154
6.	CONCLUSION.....	155
	REFERENCES	158

LIST OF TABLES

Table 4-1. The surface energies of the pure materials and their dispersive and polar contributions at room temperature ($T = 20\text{ }^{\circ}\text{C}$) and at $T = 150\text{ }^{\circ}\text{C}$	126
Table 4-2. Predictions of clay nanoplatelets based on the wetting coefficient.....	126
Table 5-1. Anisotropic swelling of polymeric gels.....	154

LIST OF FIGURES

Figure 2-1. Three types of polymer blends: miscible, partially miscible, and immiscible state in polymer blends.....	25
Figure 2-2. Theoretical phase diagram of a symmetric binary homopolymer mixture where x , N , and Φ are interaction parameter, degree of polymerization, and volume fraction of the component, respectively (Reprinted from Ref. 56 with permission from the American Association for the Advancement of Science).	25
Figure 2-3. Two different morphological changes (nucleation and growth / spinodal decomposition) over time in a binary homopolymer mixture (Reprinted from Ref. 56 with permission from the American Association for the Advancement of Science).	26
Figure 2-4. Morphological structures of a symmetric diblock copolymer with various xN values ($f = 0.5$) (Reprinted from Ref. 56 with permission from the American Association for the Advancement of Science).	27
Figure 2-5. Phase diagram of diblock copolymers and corresponding mesoporous structures as a function of xN and volume fraction of components (f) (Reprinted from Ref. 57 with permission from MDPI).	28
Figure 2-6. Types of silicate minerals. (Reprinted from Ref. 58 with permission from Elsevier).	30
Figure 2-7. Crystal structure of a 2:1 layered silicate.	31
Figure 2-8. (a) TEM image of a montmorillonite particle and (b) AFM phase image of organically modified montmorillonite particles (Cloisite 30B) on the surface of poly(vinyl chloride) (Reprinted from Ref. 58 and Ref. 60 with permission from Elsevier).....	32
Figure 2-9. Different methods for dispersing layered silicate in a polymer matrix. (a) In-situ intercalative polymerization. (b) Intercalation of polymer from solution (c) Melt intercalation. (Reprinted from Ref. 63 with permission from Royal Society of Chemistry).....	35
Figure 2-10. Schematic illustration of different states of dispersion of organically modified clay platelets in polymers with corresponding X-ray scattering peaks and TEM images (Reprinted from Ref. 64 with permission from Elsevier).	36
Figure 2-11. Schematic illustration of the dispersion of (a) aggregated silica nanoparticles and (b) grafted silica nanoparticles in a polymer matrix (Reprinted from Ref. 67 with permission from American Chemical Society).	38
Figure 2-12. TEM images of the dispersion of (a) 3% graphite and (b) 3% TRG in a PEN matrix (reprinted from Ref. 70 with permission from American Chemical Society).	40
Figure 2-13. TEM images of PC/SAN (70/30) blend morphologies with (a) 0% (b) 1% (c) 3% (d) 5% (e) 10% of Cloisite 20A and (f) 10% of Na ⁺ Cloisite. Dark and bright domains are PC and SAN, respectively (Reprinted from Ref. 83 with permission from American Chemical Society).	42

Figure 2-14. (a) A cross-sectional SEM image of a bijel (dPMMA/SAN/Silica) film. (b) A 3D bijel morphology (water/2,6-lutidine/silica) observed by fluorescence confocal microscopy (scale bar = 100 μm) (Reprinted from Ref. 90 and Ref. 91 with permission from American Chemical Society and from Springer Nature, respectively).....	44
Figure 2-15. (a) TEM image of co-continuous structure in a PS/PVME blend. A percolated network of nanorods was found in the PVME phase. (b) Schematic illustration of the process of the kinetically arrested co-continuous structure through nanorods network formation (Reprinted from Ref. 95 with permission from American Chemical Society).	45
Figure 2-16. Thermodynamic prediction of nanoparticle location in polymer blends. Interfacial energies ($\gamma_{A/B}$, $\gamma_{NP/A}$, $\gamma_{NP/B}$) between materials to determine the location of nanoparticles in blends at thermodynamic equilibrium state.....	47
Figure 2-17. The shape of electric fields when polarizability between a medium and a particle are different (above: $\alpha_m > \alpha_p$ below: $\alpha_p > \alpha_m$) (Reprinted from Ref. 104 with permission from Cambridge University Press).	50
Figure 2-18. Induced dipole–dipole interaction for (a) particles aligned parallel to the applied field and b) particles aligned perpendicular to the applied field.	51
Figure 2-19. The structures of BaTiO ₃ nanoparticles in the AC electric field (100 Hz). Fibrillated structures of BaTiO ₃ were found at high voltage. (a) 300 V/mm, (b) 800 V/mm and (c) 1400 V/mm (Reprinted from Ref. 106 with permission from Royal Society of Chemistry).....	53
Figure 2-20. X-ray micro-CT images of the composite of 3.6 vol% Ni@Ag in PDMS by applying a magnetic field strength of 0.225 T. (Left) 3D view and (right) cross-sectional view (Reprinted from Ref. 114 with permission from American Chemical Society).	54
Figure 2-21. Magnetic-field induced alignment of graphene oxide suspensions. (Left) Schematic illustration of the sample in the magnetic field. (Right) Birefringent graphene oxide suspensions between cross-polarizers after 3 h under a magnetic field strength of 0.25 T (Reprinted from Ref. 121 with permission from John Wiley & Sons, Inc).	56
Figure 2-22. The morphology of a PMMA/PS (50/50) blend from toluene in a 6 kV/cm. The PMMA-rich domains were aligned to the electric field direction. (a) 21 min, (b) 25 min, and (c) 29 min from solution casting process (Reprinted from Ref. 126 with permission from American Chemical Society).	58
Figure 2-23. Phase-separated structures and corresponding 2D Fourier transform for a P2CS/PVEM (30/70) blend containing LiClO ₄ (0.5 wt%) under AC electric field (11.2 kV/cm, 10 Hz) at 118 °C for 20 min, 90 min, 240 min, and 420 min of annealing time (Reprinted from Ref. 125 with permission from American Chemical Society).....	58
Figure 2-24. Cross-sectional SEM image of phase-separated SPEKK/SAN blend, melt casted at 200 °C. The samples were prepared without electric field (left) and with AC electric field (right) (1000 V/mm, 20 Hz) applied along the thickness direction (Reprinted from Ref. 132 with permission from Elsevier).....	59
Figure 2-25. (Left) Electrode and sample layout. (Right) The TEM images of PS-b-PMMA for the area indicated on left image. The sample prepared with (A) 37 kV/cm, (B) 20 kV/cm, and (C) no	

field (Reprinted from Ref. 133 with permission from the American Association for the Advancement of Science).	61
Figure 2-26. (a) Schematic illustration of an LC attached block copolymer and the diamagnetic anisotropy under magnetic field. (b) 2-D SAXS, (c) TEM, and (d) corresponding illustration of an LC attached PS(5.1k)-b-PAA(3.9k) (Reprinted from Ref. 136 with permission from American Chemical Society).	61
Figure 2-27. Tensile stress–strain curves of (a) chemically crosslinked polymer hydrogels with different with different concentration of organic crosslinker (N,N ϵ -methylenebis (acrylamide) (BIS)), C _{BIS} from 0.001 to 3 mol%. Tensile stress–strain curves of (b) Laponite nanocomposite hydrogels with different concentrations of Laponite from 0.05 to 10 mol% (Reprinted from Ref. 34 with permission from Springer Nature).	63
Figure 2-28. Synthesis of anisotropic hydrogel nanocomposites by using shear forces, or magnetic or electric fields (Reprinted from Ref. 160 with permission from John Wiley & Sons, Inc.).	67
Figure 2-29. (b) Optical transparency of titanate nanosheets hydrogel (TiNS: 0.4 wt%) along orthogonal (i) and parallel (ii and iii) directions to the magnetically oriented TiNS plane. (b) 2D SAXS pattern of the titanate nanosheet hydrogel (TiNS: 0.6 wt%), where the illuminating X-ray beam was orthogonal (i) and parallel (ii) to the magnetically oriented titanate nanosheets (Reprinted from Ref. 158 with permission from Springer Nature).	67
Figure 3-1 (a) Viscosity of PS/PVME/toluene sample with and without 5 vol% clay fillers.(b) Viscosity at 10 s ⁻¹ shear rate.	72
Figure 3-2 Schematic illustration of the sample preparation process (a) without electric fields and (b) with electric fields. (c) Direction of top and cross-sectional view of the films for investigating blend morphologies along with AC field direction.	74
Figure 3-3 Phase diagram of a PS/PVME blend. The blend shows a LCST behavior with a critical temperature of 124 °C at 50/50 composition.	75
Figure 3-4 (a) POM images (top view) with a first order lambda (λ) plate of a PS/PVME (50/50) blend containing 5 vol% oriented clay nanofillers. Clay nanofillers were oriented to the AC field direction in a single-phase PS/PVME blend after drying with AC field (1000 V/mm, 100 Hz) at room temperature. POM images were acquired by rotating the sample every 45° counterclockwise. (b) Refractive index of clay nanoplatelets and corresponding interference color chart (scale bar: 100 μ m).	76
Figure 3-5. AFM phase image of the sample (5 vol% of clay particles) prepared with a 500 V/mm of AC field. (a) 25 μ m \times 25 μ m, (b) 5 μ m \times 5 μ m, and (c) 2 μ m \times 2 μ m images. The region of black dotted square in (a) is corresponding to (b) image.	78
Figure 3-6 (a) 25 μ m \times 25 μ m AFM phase image of the sample (5 vol% of clay particles) prepared with 1500 V/mm. (b) Magnified 5 μ m \times 5 μ m AFM phase image of the region of a white dotted square in (a). The surface was slightly etched by methanol.	79
Figure 3-7 Phase-separated morphology of a neat PS/PVME (50/50) blend. Top-view OM images (a, c, e) and cross-sectional SEM images (b, d, f) annealed for (a, b) 5 min, (c, d) 7.5 min, and (e,	

f) 10 min at 128 °C. (Scale bar: 10 μm) (Inset: Critical temperature (124 °C) and annealing temperature (128 °C) are indicated in the phase diagram of the PS/PVME blend.).....	81
Figure 3-8 Cross-sectional SEM images of a PS/PVME (50/50) blend morphology with 5 vol% clay platelets annealed at 128 °C in the absence of AC field. Phase-separated morphology annealed for (a, b) 5 min, (c) 7.5 min, (d) 10 min, (e) 12.5 min, and (f) 15 min. (Scale bar: 10 μm).....	82
Figure 3-9 Cross-sectional SEM images of a PS/PVME (50/50) blend morphology with pre-oriented 5 vol% clay platelets annealed at 128 °C. The arrow indicates the AC field (500 V/mm, 100 Hz) direction. Phase-separated morphology annealed for (a, b) 5 min, (c) 7.5 min, (d) 10 min, (e) 12.5 min, and (f) 15 min. (Scale bar: 10 μm).....	84
Figure 3-10 Optical microscope images (top view) of the PS/PVME (50/50) blend morphology with an AC electric (500 V/mm, 100 Hz) at 128 °C. The sample were annealed for (a) 10 min, (b) 15 min, (c) 17.5 min, and (c) 20 min. (Scale bar: 100 μm)	85
Figure 3-11 Optical microscope images (top view) of the PS/PVME (50/50) blend morphology with pre-oriented clay platelets at different clay concentrations. (a) 1 vol% annealed for 10 min, (b) 2 vol% annealed for 30 min, and (c) 5 vol% annealed for 30 min at 128°C. AC electric field (500 V/mm, 100 Hz) was applied for all the samples.....	85
Figure 3-12 Characteristic domain size (ξ) over annealing time for PS/PVME (50/50) blends annealed at 128 °C. (Red: neat PS/PVME, blue: PS/PVME/non-oriented 5 vol% clay platelets, green: PS/PVME/pre-oriented 5 vol% clay platelets)	86
Figure 3-13 Phase-separated morphology of a PS/PVME (50/50) blend containing 5 vol% clay platelets annealed at 128 °C for 30 min with and without the AC electric field. The arrow indicates the AC field (500 V/mm, 100 Hz) direction. (a) OM images (top view) and (c) corresponding SEM images (cross-sectional view) of the sample prepared with AC fields. (b) OM images (top view) and (d) corresponding SEM images (cross-sectional view) of the samples prepared without AC fields. (Scale bar: 50 μm).....	88
Figure 3-14 (a) 2D-FFT pattern of the optical image (the sample containing 5 vol% clay nanofillers with a 500 V/mm electric field strength at 128 °C for 60 min). (b) The corresponding plot of the integrated intensity of the 2D-FFT pattern against the azimuthal angle (ϕ) (c) 2D-FFT pattern of the optical image (the sample containing 5 vol% clay nanofillers without AC field at 128 °C for 15 min). (d) The corresponding plot of the integrated intensity of the 2D-FFT pattern against the azimuthal angle (ϕ).	89
Figure 3-15 OM images (top view) of the PS/PVME (50/50) blend morphology containing 5 vol% clay nanofillers annealed at 128 °C with and without an AC electric field. (a) 60 min and (b) 120 min annealing time with 500 V/mm AC fields. (c) 60 min without AC fields. (Scale bar: 100 μm) (d) domain orientation order parameter of the samples with/without AC fields over annealing time	91
Figure 3-16 OM images (top view) of the PS/PVME (50/50) blend morphology containing 5 vol% clay platelets with various AC electric field strengths for 60 min annealing time at 128 °C. The field strengths are (a) 50 V/mm, (b) 100 V/mm, (c) 200 V/mm, (d) 500 V/mm, (e) 1000 V/mm. (Scale bar: 100 μm) (f) Plots of the orientation order parameter of polymer domains to various	

electric field intensity. The FFT patterns of the corresponding OM images are inserted upper right corner. 92

Figure 3-17. SEM top view and cross-sectional images of a PS/PVME (50/50) blend morphology containing pre-oriented 5 vol% clay nanofillers (500 V/mm, 100 Hz) annealed at 128 °C. Top-view images of (a) 15 min, (c) 60 min, and (e) 120 min annealed samples. Cross-sectional images of (b) 15 min, (d) 60 min, and (f) 120 min annealed sample. (Scale bar: 50 μm)..... 94

Figure 3-18. (a) AFM height image (100 × 100 μm) of the top surface of a PS/PVME (50/50) blend containing 5 vol% pre-oriented clay nanofillers (500 V/mm, 100 Hz) annealed at 128 °C for 15 min ($\Delta z = 3360$ nm). (b) 2D topological feature of corresponding white dotted line. 95

Figure 3-19 (a) 2D WAXS scattering pattern of a PS/PVME (50/50) blend containing 5 vol% clay platelets. The sample prepared with (a-1) 0 V/mm and 0 min annealing, (a-2) 0 V/mm and 120 min annealing, (a-3) 1000 V/mm and 0 min annealing, and (a-4) 1000 V/mm and 120 min annealing. (b) The corresponding plot of the integrated intensity of the 2D WAXS pattern against the azimuthal angle. 97

Figure 3-20 (a) The orientation order parameter of clay platelets in the samples prepared with the AC electric field (1000 V/mm, 100 Hz) for different annealing times. (b) The orientation order parameter of clay platelets at various electric field strength. (c) The plot of the orientation order parameter of clay to the orientation order parameter of polymer domains..... 98

Figure 3-21 (a, b) TEM image of the cryo-microtomed sample (PS/PVME (50/50) blend containing 5 vol% clay platelets annealed at 128 °C for 15 min with 500 V/mm). (Scale bar: 5 μm) 99

Figure 3-22 AFM topography images (20 × 20 μm) of the (a) height ($\Delta z = 600$ nm) and (b) phase image of the microtomed surface of the sample (PS/PVME (50/50) blend containing 5 vol% clay nanofillers annealed at 128 °C for 12.5 min with 500 V/mm). Lighter regions in (a) indicate taller features. AFM topography images (10 × 10 μm) of the same region (c) before and (d) after methanol washing ($\Delta z = 600$ nm). The height profiles of the dash line were inserted..... 101

Figure 3-23. Cross-sectional SEM images of the sample indicating the location of clay platelets. The sample was a PS/PVME (50/50) blend morphology with pre-oriented 5 vol% clay platelets (500 V/mm, 100 Hz) annealed at 128 °C for 5 min. The arrows in (a) and in (b) indicate clay platelets and cracks, respectively. (Scale bar: 5 μm 102

Figure 3-24 Cartoons of a PS/PVME top-view phase-separated morphology over annealing time with (a) non-oriented and (b) pre-oriented clay platelets in electric field. 103

Figure 4-1 (a) Scheme of the square cell used for the electric-field assisted alignment of clay platelets during polymer solution drying. Cross-sectional schematic illustration of the sample preparation process (b) with AC field and (c) without AC field. 108

Figure 4-2. (a) A phase diagram of PS/PVME blend along with optical microscope images of a PS/PVME blend (50:50) after annealing at 120 °C for 24 h and after annealing at 130 °C for 24 h. (b) DSC traces of PS, PVEM, and a blend of PS/PVME (50/50)..... 111

Figure 4-3 (a) Real-time monitoring system in JOEY (top view): laser micrometer measures the local film thickness, pyrometer measures the local film surface temperature, and two light sources

(at 0 and 45°) measure birefringence. (b) The real-time change of weight, thickness, and surface temperature of the sample (5 vol% clay/PS/PVME/Toluene) for 6 h of drying process. (c) The instant change of in-plane birefringence (Δn_{12}), out-of-plane birefringence (Δn_{12}), and thickness upon applying AC field (750 V/mm, 100 Hz) and (d) without AC field..... 112

Figure 4-4 (a) Direction of sample preparation for characterizing orientation clay platelets along with AC field direction (750 V/mm, 100 Hz). (b) The direction of the sample rotation between cross polarizers along with a red wave plate. (c) POM images of samples (c1) No AC field, (c2, c3) dried sample (750 V/mm, 100 Hz), (c4) annealed sample (750 V/mm, 100 Hz). (d) Michel-Levy interference colors based on the clay orientation under cross-polarizers with a red wave plate. 114

Figure 4-5 2D WAXS patterns of the dried sample (750 V/mm, 100 Hz) when X-ray beam direction was the orthogonal and parallel to the applied AC field. (b) 2D WAXS patterns (X-ray \perp AC field) of the dried samples dried with different AC fields. (c) Q vs intensity peak of a pure clay powder and a clay composite. 116

Figure 4-6 (a) 2D WAXS patterns (X-ray \perp AC field) of the dried sample (750 V/mm, 100 Hz) and the annealed sample (750 V/mm, 100 Hz). (b) Orientation order parameter before and after the annealing. 117

Figure 4-7 (a) TEM image of a PS/PVME blend with clay platelets after annealing. (b) Magnified TEM image of a clay tactoids. 118

Figure 4-8. (a) Atomic structure of montmorillonite basic crystal unit. (b) Shapes of clay mineral particles and aggregates. AFM images of the annealed sample. 119

Figure 4-9. (a) 1 $\mu\text{m} \times 1\mu\text{m}$ height ($\Delta z = 34 \text{ nm}$) and (b) phase AFM images and (c) 5 $\mu\text{m} \times 5\mu\text{m}$ phase AFM images of the annealed sample (750 V/mm, 100 Hz). Figure (a) and (b) are a corresponding region of a black square in Figure (c). 120

Figure 4-10 Cross-sectional AFM phase image (25 $\mu\text{m} \times 25\mu\text{m}$) of the dried sample (750 V/mm, 100 Hz)..... 122

Figure 4-11. Cross-sectional AFM phase image (25 $\mu\text{m} \times 25\mu\text{m}$) of the annealed sample (750 V/mm, 100 Hz). 122

Figure 4-12. (a) Cryo-fractured cross-sectional morphology of the annealed sample (a) without AC field and (b) with AC fields (750 V/mm, 100 Hz) by SEM imaging. (Scale bar: 10 μm) 124

Figure 4-13. Cross-sectional phase-separated morphology of polymer blends with (a) randomly dispersed clay platelets and (b) with oriented clay platelets..... 127

Figure 5-1 (a) TEM images of nontronite nanoclays. (b) Average length and (c) average width of nanoclays with polydispersity..... 135

Figure 5-2 (a) The atomic structure of nontronite clay (NAu-2). (b) X-ray diffraction patterns of nontronite nanoclays. (c) Schematic illustration of preparation process of an anisotropic clay hydrogel sample. 136

Figure 5-3 The viscosity of hydrogel precursors with different concentration of initiator and catalysis as a function of time..... 137

Figure 5-4 (a) Anisotropic hydrogels with different concentrations of nanoclay (0.05 wt%, 0.1 wt%, 0.2 wt%, and 0.4 wt%) prepared under 9 T magnetic field. (b) The direction of the sample rotation between cross polarizers. (c) The optical microscope image of 0.2 wt% anisotropic hydrogels prepared at (c-1) 1 T, (c-2) 3 T, and (c-3) 9 T of magnetic field strength under cross polarizers. (c-4) Identical POM image of (c-3) with a first-order lambda plate (red wave plate) (scale bar: 300 μm). (d) Nanoclay orientation under crossed polarizers with a red wave plate and a corresponding interference color chart.	140
Figure 5-5 The optical microscope image of a pure hydrogel prepared in 9 T under crossed polarizers at every 45° degree rotation. (Scale bar: 300 nm).....	141
Figure 5-6 Anisotropic hydrogel samples (0.05 wt%, 0.1 wt%, 0.2 wt%, 0.4 wt% of nontronite clays) prepared with various magnetic field strength (0, 1, 3, 5, 7, 9 tesla) (a) without crossed polarizers and (b) with crossed polarizers.	142
Figure 5-7 The retardation value of nanoclays hydrogel samples with different clay concentration and magnetic field strength. (a) Schematic illustration of retardation measurement of isotropic and anisotropic hydrogel samples. In-plane retardation values of nanoclays hydrogels prepared at various magnetic field strengths with (b) 0.05 wt%, (c) 0.1 wt%, (d) 0.2 wt%, and (e) 0.4 wt% nanoclay concentrations.....	143
Figure 5-8 Magnetic-field induced birefringence of anisotropic nanoclay hydrogels.....	145
Figure 5-9 (a) Schematic layout of a 2D SAXS experimental setup. (b) 2D SAXS patterns of hydrogels (0.1 wt%) in different magnetic field strength. (c) 2D SAXS patterns of various concentrations of nanoclays prepared at 9 T.....	147
Figure 5-10 (a) Azimuthal angle plots for hydrogels (0.1 wt%) in different magnetic fields. (b) Azimuthal angle plots for anisotropic hydrogels in different concentrations prepared in 9 T magnetic fields.....	148
Figure 5-11 (a) The orientation order parameter of 0.1 wt% nanoclay hydrogels as a function of the magnetic field strength. (b) The orientation order parameter of nanoclay hydrogels as a function of nanoclay concentration. (c) The correlation between birefringence and orientation order parameter (0.1 wt% nanoclay hydrogels).	149
Figure 5-12 (a) 2D WAXS patterns of nanoclay powder, pure hydrogel, and nanoclay hydrogels (0.05% and 0.4%). (b) X-ray diffraction patterns of nanoclay powder, pure hydrogel, and nanoclay hydrogels.....	150
Figure 5-13 Mechanical properties of hydrogels prepared in 0 T and 9 T magnetic field strength with different clay concentrations in uniaxial compression test. (a) Stress–strain curves of completely random (0 T) and highly oriented (9 T) hydrogels with different clay concentrations. (Compression direction is parallel to nanoclay orientation direction for 9 T samples.) (b) Tangent elastic modulus at 50% strain of hydrogels.	151
Figure 5-14 (a) The nanoclay hydrogels with different concentrations prepared at 0 T and 9 T. (b) Schematic illustration of nanoclay orientation with respect to magnetic fields and incident light. (c) Optical light transmission of nanoclay hydrogels with different concentrations prepared at 0 T and 9 T.	152

Figure 5-15 Swelling behavior of a 0.4 wt% clay hydrogels prepared in 0 T and 9 T magnetic field. (a) Schematic illustration of a hydrogel before and after swelling and directions of measurement. Time dependence of the swelling to the radius (X) and thickness (Y) direction along with the weight-percent increase of (b) the oriented sample and (c) the non-oriented sample. (d) Anisotropic swelling ratio ($Y\% / X\%$) of the oriented and non-oriented samples over the swelling time. ... 153

ABSTRACT

Morphology control in polymeric materials is essential to optimize the properties of polymeric materials for the desired application. Often, the desired enhancement of properties is highly directional, such as those in energy conversion and storage devices. For example, in a proton-exchange membrane in fuel-cell applications, the main property to enhance is ion conductivity in the direction normal to the film plane, which is not easily achieved by conventional material-composition design or processing methods.

In this dissertation, new ways for controlling the internal structures of a system of polymer composites, polymer blends, and hydrogel composites by means of external electric or magnetic fields are presented. The first part of this study addresses the development of an anisotropic phase-separated morphology in polymer blends by using electrically pre-oriented clay particles. It was observed that electrically pre-oriented montmorillonite clay particles in a homogenous single-phase blend lead to anisotropic phase-separated morphology of the blends, undergoing demixing upon temperature shift to a two-phase regime. The initial co-continuous microstructure developed into a coarsened and directionally organized phase-separated morphology parallel to the direction of oriented clay particles (applied AC electric field direction) over the annealing time. It was also found that the degree of clay orientation under AC electric field was linearly proportional to the degree of polymer-phase orientation. The temporal morphological evolution was thoroughly analyzed by electron microscopy and X-ray diffraction studies. The second part of the study covers anisotropic hydrogel nanocomposites developed by orienting magnetically sensitive nontronite clay minerals under the strong magnetic fields. Anisotropic hydrogel nanocomposites were formed by magnetic-field assisted orientation of nontronite clays suspended in a hydrogel precursor solution followed by a gelation process. The degree of orientation of nontronite minerals was quantitatively characterized by birefringence and small-angle X-ray scattering. The resultant hydrogels exhibited anisotropic optical, mechanical, and swelling properties along the direction of oriented clay minerals. Anisotropic water swelling behaviors can be particularly applied in medical dressing materials, where vertical wicking of fluid into the wound dressing is sought after for minimizing periwound maceration damage.

1. INTRODUCTION

In the fields of polymer science and engineering, polymeric materials reinforced with inorganic filler have been topics of interest in the polymer community over the past few decades.¹ The properties of classic polymeric materials can be improved by adding inorganic fillers while maintaining their advantageous characteristics. Their applications are varied, such as light-emitting diodes (LEDs), aerospace, electromagnetic interference (EMI) shielding, electrocatalysts, and biomedical imaging.²⁻⁷ The field of research on polymer-based composites may cover various areas, such as selecting of fillers, processing of composites, characterizing of internal structure, and measuring of properties. By incorporating different types of inorganic nanoparticles, including carbon-based, glass-based, metallic, semiconducting, or ferroelectric nanoparticles, the polymer nanocomposite can exhibit the sought-after property. Methods of incorporating inorganic fillers into polymeric materials are also critical to achieve desired structures in the polymer composites. Hence, material selection and processing methods are both essential to create a composite with the desired properties.

The progress in nanotechnology has impacted almost every field of scientific study, as it has been recognized as a key technology of the 21st century. Nanotechnology in the polymer community has also opened a new pathway for developing polymer nanocomposites—defined as a mixture of a polymer with reinforced particles with a size range of 1–100 nm. Polymer nanocomposites can exhibit properties dramatically different from the properties of the individual components, resulting in significant synergistic properties. High-resolution electron microscopy, as well as other characterization techniques, have provided a detailed view of local morphology and explained the structure–property relationship of polymer nanocomposites. A detailed understanding of the nanoscale structures of polymer nanocomposites via innovative nanotechnology has enabled us to improve the manufacturing and processing approaches.

One of the oldest classes of polymer composite materials is filler-reinforced vulcanized rubber. As automobiles first became popular, the need to improve the mechanical properties of tire rubber became obvious. Even though zinc oxide had already been used as a reinforcing filler for tire rubber in early applications, further improvements were needed due to their short lifetime. In 1904, S.C. Mote, a chief chemist at India Rubber, first reported extraordinary reinforcing effects of very fine carbon black on vulcanized rubber.⁸ As carbon black became the prevalent in tire

industry, zinc oxide was mostly replaced by carbon black as the reinforcing filler material between 1910 and 1915.⁹ Other well-known additives for tire rubbers in the early 20th century were fumed silica and precipitated calcium carbonate.

Although polymer-based composites were studied in the early 20th century for tire-tread applications, the development of the clay/polymer nanocomposite system by Toyota can be considered a key milestone in the modern polymer nanocomposites era. In 1993, researchers at Toyota Central Research & Development Labs reported that less than 8 wt% of exfoliated montmorillonite in polyamide 6 increased the tensile modulus by a factor of 3, while increasing the heat distortion temperature from ~70 °C to ~150 °C.¹⁰ Since this pioneering work on polymer nanocomposites, there has been an exponential growth in the research on clay/polymer nanocomposites. Intensive studies on clay/polymer nanocomposites have shown that exfoliation of organically modified clay particles in a polymer matrix lead to an extraordinarily large amount of interfacial contacts between clay platelets and the polymer matrix on a nanometer scale. For example, a glass fiber with a diameter of 13 μm and with a length of 300 μm is about 5×10^9 times the size of a typical silicate clay mineral with a thickness of 1 nm and a width of 100 nm. If identical volumes of glass fibers and silicate clay minerals were equally dispersed in a polymer matrix, a roughly 110 times higher surface area of silicate layers would be interacting with polymer chains.¹¹ Thus, nanoscale dispersion of clay platelets in a polymer matrix enhances the mechanical properties in clay/polymer nanocomposites at a much lower volume fraction of nanoparticles as compared with the conventional nanocomposites. The nanocomposites with low concentrations of clay nanofillers also can exhibit lightweight, transparent, and low-cost properties while keeping high mechanical strength.¹²⁻¹⁴ Furthermore, significant improvements in other properties such as thermal stability, low gas permeability, and flame retardancy of clay/polymer nanocomposite at very low particle concentrations have been reported.¹⁵⁻¹⁷ Various clay/polymer systems, such as polyethylene terephthalate (PET), poly(ethylene 2,6-naphthalene dicarboxylate) (PEN), polyethylene (PE), and polypropylene (PP), paired with montmorillonite (MMT), have been studied.¹⁸⁻²¹ These composite materials have shown enhancement in mechanical strength,²¹⁻²³ thermal stability,²⁴⁻²⁶ and gas-barrier properties.²⁷⁻²⁹

Montmorillonite, which can be easily found in many soils and sediments, is one of the most common clay minerals used for compounding with various polymers.³⁰ As a member of the group of dioctahedral smectites, this mineral consists of a central octahedral (Al) sheet sandwiched by

two tetrahedral (Si) sheets.³¹ Although a single layer of montmorillonite mineral has a thickness of roughly 1 nm, montmorillonite minerals are generally found in thick stacks of layers due to the electrostatic attraction force between layers.³² The interlayer, which is a gap between the two layers, contains alkali-metal and alkaline-earth-metal cations.³³ The metal cations in the interlayers counteractively generate negative charges on the surface of the montmorillonite layers.

Due to the polar nature of clay minerals including montmorillonite, they are compatible with hydrophilic mediums. For example, natural-clay aqueous suspensions are extensively used in various industrial applications such as drilling fluids, and the food and cosmetic industries. They are also particularly advantageous for forming hydrogel nanocomposites. When clay minerals are dispersed in hydrogel precursor beyond a certain concentration, they can form stable hydrogels through the strong physical interaction between the polymer chains and clay minerals. It has also been demonstrated that mechanical strength, transparency, and swelling ratios of clay/hydrogel nanocomposites outperform those of other chemically crosslinked hydrogels.³⁴

While natural clay minerals are compatible with hydrogel-type or hydrophilic polymers, satisfactory compatibility with hydrophobic polymers is largely not guaranteed. Hydrophilic clay minerals are often aggregated in a hydrophobic polymer matrix and often lead to inhomogeneous particle dispersions. To enhance compatibility between clay minerals and polymers, organic modifications of the clay surfaces are generally carried out by exchanging the metal cations in the interlayers with organic alkylammonium ions.³⁵ By adjusting the length and type of alkylammonium, the hydrophilic/hydrophobic characteristics of clay minerals can be adjusted.³⁶⁻³⁸ The field of clay synthesis is another area of research in the clay-research community.

Organically modified clay nanoparticles are not just effective in homopolymer matrices, but also effective in immiscible polymer-blend systems. Organically modified clay minerals can stabilize the phase-separated morphology in polymer blend systems by suppressing macroscopic phase separation like other compatibilizers, such as block copolymers and polymer-grafted nanoparticles.³⁹ A binary mixture undergoing phase separation generally coarsens into larger domains and eventually turns into a macroscopic phase-separated morphology in the absence of compatibilizers due to the large unfavorable enthalpy. Compatibilizers in the binary mixture can effectively inhibit coalescence between domains by reducing interfacial tension. For example, block copolymers, graft copolymers, and fumed silica nanoparticles are well-known traditional compatibilizers for immiscible binary mixtures. Clay nanoparticles also can be used as

compatibilizers in polymer blends by having a large amount of interfacial contacts with polymer chains through intercalated or exfoliated structures.

The final physical and chemical properties of the clay/polymer nanocomposites are determined not only by dispersion states of clay nanoparticles in polymer matrices, but also by the array of dispersed nanofillers. The structure of dispersed clay platelets in polymer matrices can be tuned by applying external forces. For example, the major axis of disk-like clay particles can be easily oriented along the flow direction in polymer melts when clay platelets are exposed to high shear stress during melt processing.^{40–42} Rheological studies as well as X-ray scattering analysis have proved the flow-induced orientation of clay platelets during melt processing. The response of the intercalated or exfoliated clay nanoparticles to external shear flow is vital to determine their processing conditions to produce nanocomposites with the desired physical or chemical properties.

In addition to shear field, clay minerals are sensitive to external electric fields because they possess negative charges on the surface, along with metal cations in the interlayers. In external electric fields, either DC or AC, induced dipoles can be generated on the surface of clay particles. Hence, the external electric field can be used to tune the morphology of clay/polymer nanocomposites. For example, it was reported that the exfoliation of organically modified montmorillonite could be facilitated with an AC field in a polymer melt.^{43–45} The electrostatic repulsive forces between charged surfaces of clay particles promoted the degree of exfoliation or intercalation of clay particles in a polymer medium. Furthermore, the orientation of clay particles under the electric field was observed through dipole–dipole interaction between polarized clay particles.^{46–49} Dipole–dipole interactions between particles generally led to the formation of particle-chain structure.

Some of clay minerals are sensitive to magnetic fields depended on concentration of paramagnetic atoms within the crystal structure. Natural montmorillonite contains roughly 1–4% Fe(II) or Fe(III) in a central octahedral sheet.^{50,51} Furthermore, nontronite clay minerals, which are a family of dioctahedral smectites, have roughly 30% Fe(II) or Fe(III) in octahedral lattice positions.^{52,53} High iron content in some of clay minerals leads to a paramagnetic response under external magnetic fields. Hence, the orientation or alignment of clay suspensions under magnetic fields has been also observed.^{54,55}

The aim of this dissertation is to develop processing methods for controlling the internal morphology of systems of polymer composites, polymer blends, and hydrogel composites by using

external electric or magnetic fields. The morphological change of polymeric materials under external electric or magnetic fields and the structure–property relationship of clay-containing composite materials are described. The dissertation is composed of general introduction (Chapter 1), background and literature reviews (Chapter 2), research articles (Chapters 3–5), and concluding remarks (Chapter 6).

Chapter 2 covers the theoretical background ranging from polymer blends to clay-containing polymeric materials. Polymer nanocomposites, particularly clay/polymer nanocomposites, are reviewed. The effects of organic fillers in polymer blends as compatibilizer are also discussed. Electric and magnetic susceptibility of inorganic fillers and field-assisted alignment of inorganic particles as well as polymer phases are reviewed.

Chapter 3 describes a new way of developing anisotropic phase-separated polymer blends induced by electrically pre-oriented clay particles (montmorillonite) in the in-plane direction of polymer films. An anisotropic phase-separated morphology is found in a partially miscible polymer blend when temperature jumps into a two-phase regime in the presence of pre-oriented clay particles. Temporal morphological evolution of polymer blends, along with orientation of clay nanoparticles, is mainly discussed by using optical microscopy, electron microscopy, and X-ray diffraction techniques.

Chapter 4 discusses the development of anisotropic phase-separated morphology in the through-thickness direction using external AC electric fields. Anisotropic phase-separated polymer phases may be attractive for applications where the properties in the through-thickness direction are critical. For example, a directionally oriented phase-separated structure in the through-plane direction is preferred for a proton-exchange membrane or in organic photovoltaic cells, where an active layer with an interdigitized structure is desired for enhancement of external efficiency. Here, the design and development of this morphology by using electrically pre-oriented clay minerals (montmorillonite) are described.

Chapter 5 discusses the synthesizing of anisotropic clay hydrogels by using external magnetic fields. Nontronite aqueous suspensions in a hydrogel precursor solution are oriented under strong magnetic field (>1 tesla) and the solution containing oriented clay minerals is immobilized by a gelation reaction. The degree of clay-mineral orientation in a gel network is characterized by birefringence and X-ray diffraction. The resultant anisotropic hydrogels exhibit anisotropic optical, mechanical, and swelling properties along the direction of the oriented clay

mineral are useful for wound healing applications where the out-of-plane enhancement of swelling leads to suppression of in-plane tensile stress, which can damage the wound.

Chapter 6 provides overall concluding remarks of the major findings. The main results and the scientific significance are mainly discussed in this chapter.

2. BACKGROUND AND LITERATURE REVIEW

In this chapter, the theoretical background of polymer blends, polymer nanocomposites, and hydrogel nanocomposites will be reviewed. The phase behavior of polymer blends and diblock copolymers will be discussed. Different types of polymeric nanocomposites and the role of nanofillers in polymeric materials will be covered. Moreover, electric or magnetic susceptibility of inorganic particles will be reviewed. The previous studies related to tuning the morphology of polymer nanocomposites and blends by using external electric or magnetic fields will also be described.

2.1 Polymer blends and copolymers

Polymer-hybrid systems are referred to as mixtures composed of more than two different monomers or polymers. Polymer-hybrid systems can be produced either by physical blending (polymer blends) or by chemical blending (copolymers). Physical blending is a result of physically mixing two homopolymers, whereas chemical blending is a result of a polymerization of two or more different monomers. Here, we will discuss the general background of polymer–polymer phase behavior observed in homopolymer blends and copolymers.

2.1.1 Polymer blends (homopolymer mixture)

A mixture of two or more homopolymers for a single product is called a polymer blend. The blending of existing homopolymers into new polymeric materials may require less effort in research and development to produce a new material compared to synthesis of new polymers from monomers. It means that the properties of new materials can be tailored according to their ultimate applications. In general, we can classify the equilibrium behavior of homopolymer mixtures into three types: miscible, immiscible, and partially miscible as shown in Figure 2-1. While miscible blends show homogeneity in a molecular level, the immiscible blends show phase-separated structure in a micro- or nanometer length scale. For example, a pairing of poly(phenylene oxide) (PPO) and poly(styrene) (PS) or a pairing of poly(methyl methacrylate) (PMMA) and poly(vinylidene fluoride) (PVDF) is a miscible polymer blend, whereas a pairing of PS and poly(propylene) is immiscible. Furthermore, some polymer pairings exhibit a partially miscible

state depending on temperature and composition. For example, a pairing of poly(vinyl methyl ether) (PVME) and PS or a pairing of poly(styrene-co-acrylonitrile) and poly(methyl methacrylate) belongs to this category.

Nearly 70 years ago, Flory and Huggins estimated the equilibrium of phase behavior of a linear binary homopolymer mixture. This theory describes the basic concept of the miscibility of two homopolymers at equilibrium. Flory–Huggins solution theory is shown below.

$$\frac{\Delta G}{k_b T} = \frac{\phi_A}{N_A} \ln \phi_A + \frac{(1 - \phi_A)}{N_A} \ln(1 - \phi_A) + \phi_A(1 - \phi_A)x$$

Flory–Huggins solution theory explains the relationship between the free energy change per unit segment (ΔG), combination entropy of mixing (ΔS), and enthalpy of mixing (ΔH). The first two terms on the right side are related to combination entropy of mixing (ΔS). Large molecules (large N) show less-mixed configurations, whereas small molecules (small N) show more-mixed configurations. Thus, small molecules (small N) are favorable for mixing compared to large molecules. The third terms on the right side is related to enthalpy of mixing (ΔH). The interaction parameter (x) is closely related to enthalpy of mixing (ΔH). The effect of entropy of mixing (ΔS) and the effect of enthalpy of mixing (ΔH) mutually influence the change in free energy (ΔG). Figure 2-2 shows the theoretical phase diagram of a partially miscible polymer blend for the symmetric case ($N_A = N_b$). The miscibility of partially miscible polymer blends can vary based on different conditions, such as temperature, composition, and molecular weight of the polymers. Moreover, the phase diagram can show either upper critical solution temperature (UCST) or lower critical solution temperature (LCST) according to the interaction parameter (x). The interaction parameter (x) is simply expressed by $x = \frac{\alpha}{T} + \beta$. For example, the phase diagram may have a LCST result where α is negative and β is positive. However, the phase diagram may exhibit a UCST result when α is positive and β is negative. For example, a poly(vinylidene fluoride) (PVDF)/poly(methyl methacrylate) blend exhibits a UCST behavior, while polystyrene (PS) /

Polymer Blends

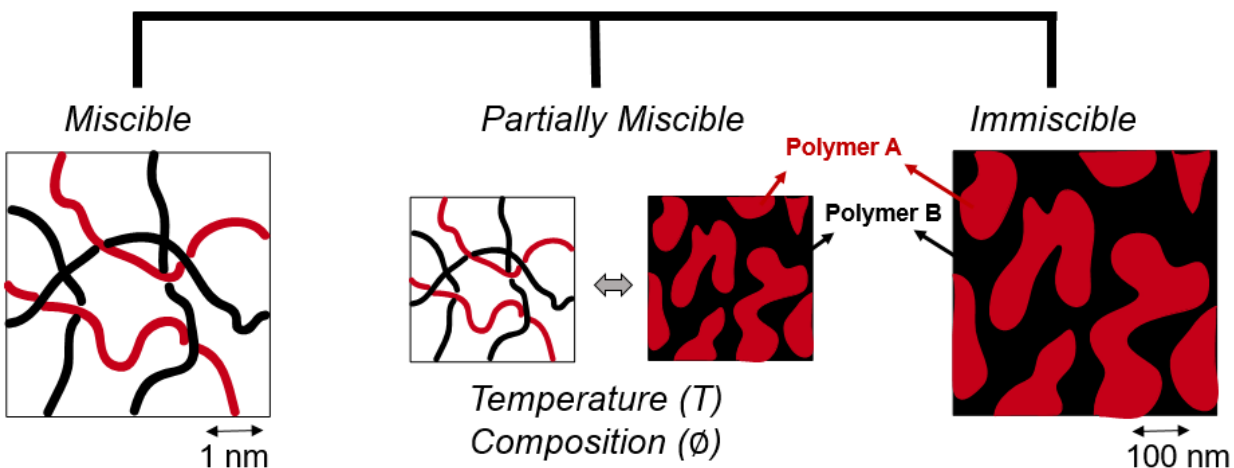


Figure 2-1. Three types of polymer blends: miscible, partially miscible, and immiscible state in polymer blends.

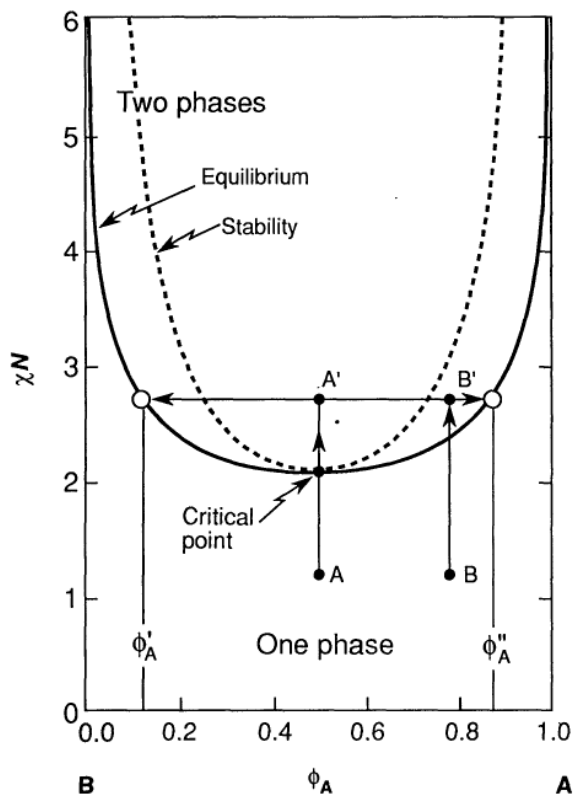


Figure 2-2. Theoretical phase diagram of a symmetric binary homopolymer mixture where χ , N , and Φ are interaction parameter, degree of polymerization, and volume fraction of the component, respectively (Reprinted from Ref. 56 with permission from the American Association for the Advancement of Science).

poly(methyl vinyl ether) (PVME) and PMMA/poly(styrene-r-acrylonitrile) (SAN) are polymer pairings showing a LCST phase separation. When partially miscible polymer blends undergo phase separation, two types of phase separation dynamics (nucleation and growth / spinodal decomposition) can occur based on the phase separation path on the phase diagram. The morphology of nucleation and growth is developed when a homogeneous mixture is brought into a metastable region (path from B to B' in Figure 2-2). In this phase separation process, small droplets of minor phase appear and get enlarged over time by diffusion. However, the phase-separated morphology is quite different when phase separation occurs by passing through a critical composition (path from A to A' on figure 2-2). In this phase separation dynamic, a disordered co-continuous morphology is initially observed. This process is called spinodal decomposition. The co-continuous morphology gets enlarged over time by diffusion processes. The schematic illustration of nucleation and growth and spinodal decomposition phase-separation dynamics over time are depicted in Figure 2-3.

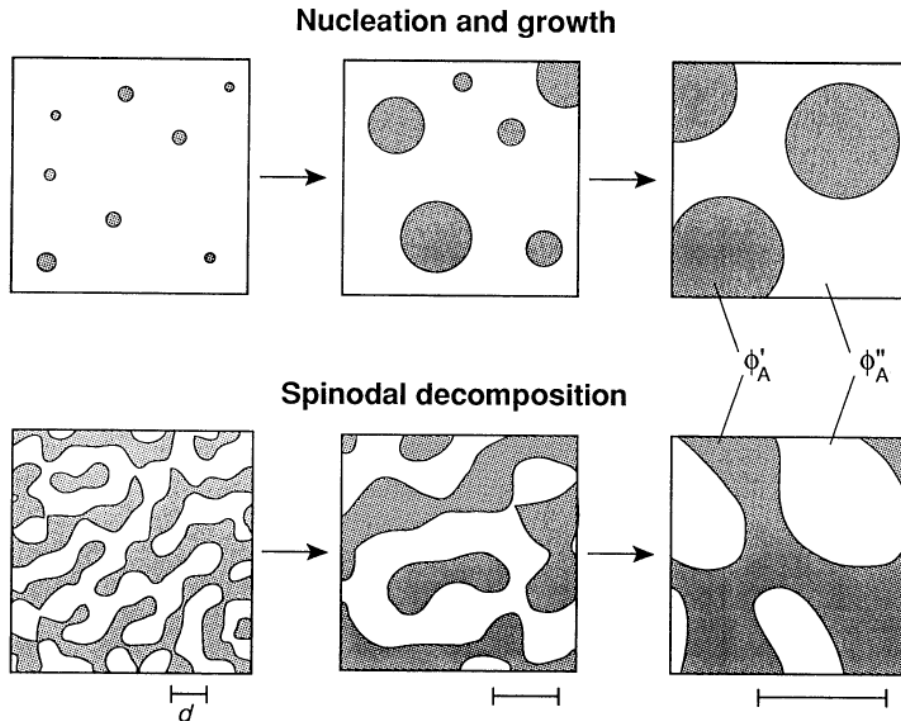


Figure 2-3. Two different morphological changes (nucleation and growth / spinodal decomposition) over time in a binary homopolymer mixture (Reprinted from Ref. 56 with permission from the American Association for the Advancement of Science).

2.1.2 Diblock copolymers

Among the different types of copolymers, such as block, random, and alternating copolymers, diblock copolymers have been widely studied due to their unique phase behavior. A macroscopic phase-separated morphology is not observed in diblock copolymers because the A and B components exist in a single polymer molecule. Thus, the phase-separated morphology for diblock copolymers is observed as a local segregation of A and B phases. The state of phase segregation in diblock copolymers is determined by interaction parameter (χ), molecular size (N), and volume fraction of the component (f). When A and B phases have a low interaction parameter and a molecular weight (χN) $\ll 10$ with a volume fraction (f) of 0.5, phase segregation is not observed. In this condition, the high entropy mixing (S), where $S \sim N^{-1}$, results in a homogeneous state. However, local composition fluctuation is observed as χ or N increases close to $\chi N \leq 10$, as depicted in Figure 2-4. Further increase of χN ($\chi N \geq 10$) sharpens the A and B phase boundaries as the contact between the A segment and B segment decreases. For the state of $\chi N \gg 10$, the morphology of phase segregation with sharp interfaces and flat composition profiles between A and B segments is observed.

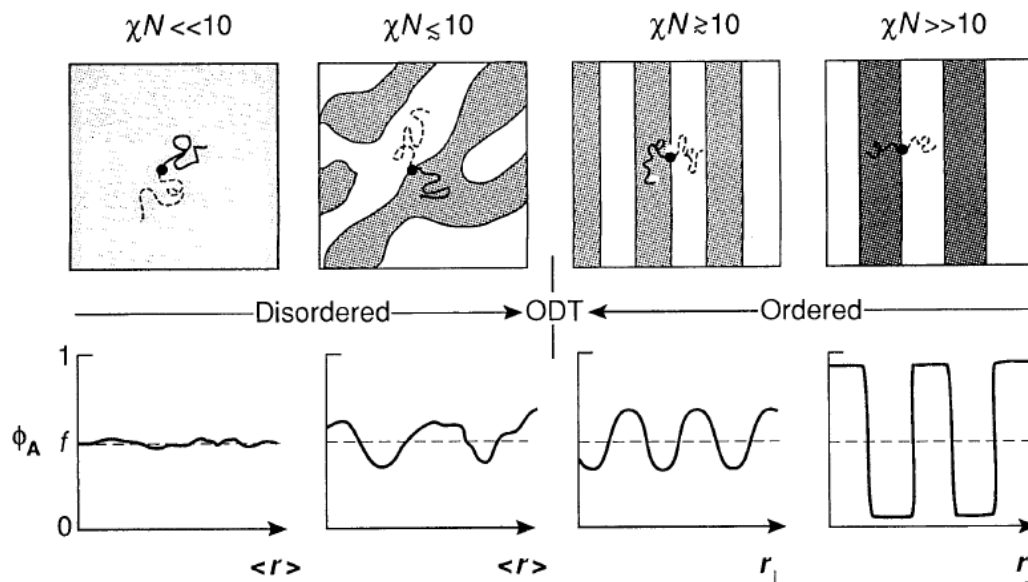


Figure 2-4. Morphological structures of a symmetric diblock copolymer with various χN values ($f = 0.5$) (Reprinted from Ref. 56 with permission from the American Association for the Advancement of Science).

The ordered microstructures of diblock copolymers are more complicated when a factor of volume fraction (f) is also considered. The shape and packing symmetry of microstructure are changed by the variation of f . For $f_A \sim 0.1$, microspheres of A in a matrix of B with a body-centered cubic lattice are observed. As f_A increases to ~ 0.3 , hexagonally packed cylinders of A in a matrix of B is observed. A gyroid microstructure characterized by a co-continuous A and B morphology is found when f_A is between 0.3 and 0.4. The lamellar structure appears where f_A is near 0.5. The lamellar structure appears where f_A is near 0.5. The typical phase diagram of diblock copolymers with varying χN and f is shown in Figure 2-5 along with corresponding microstructures.

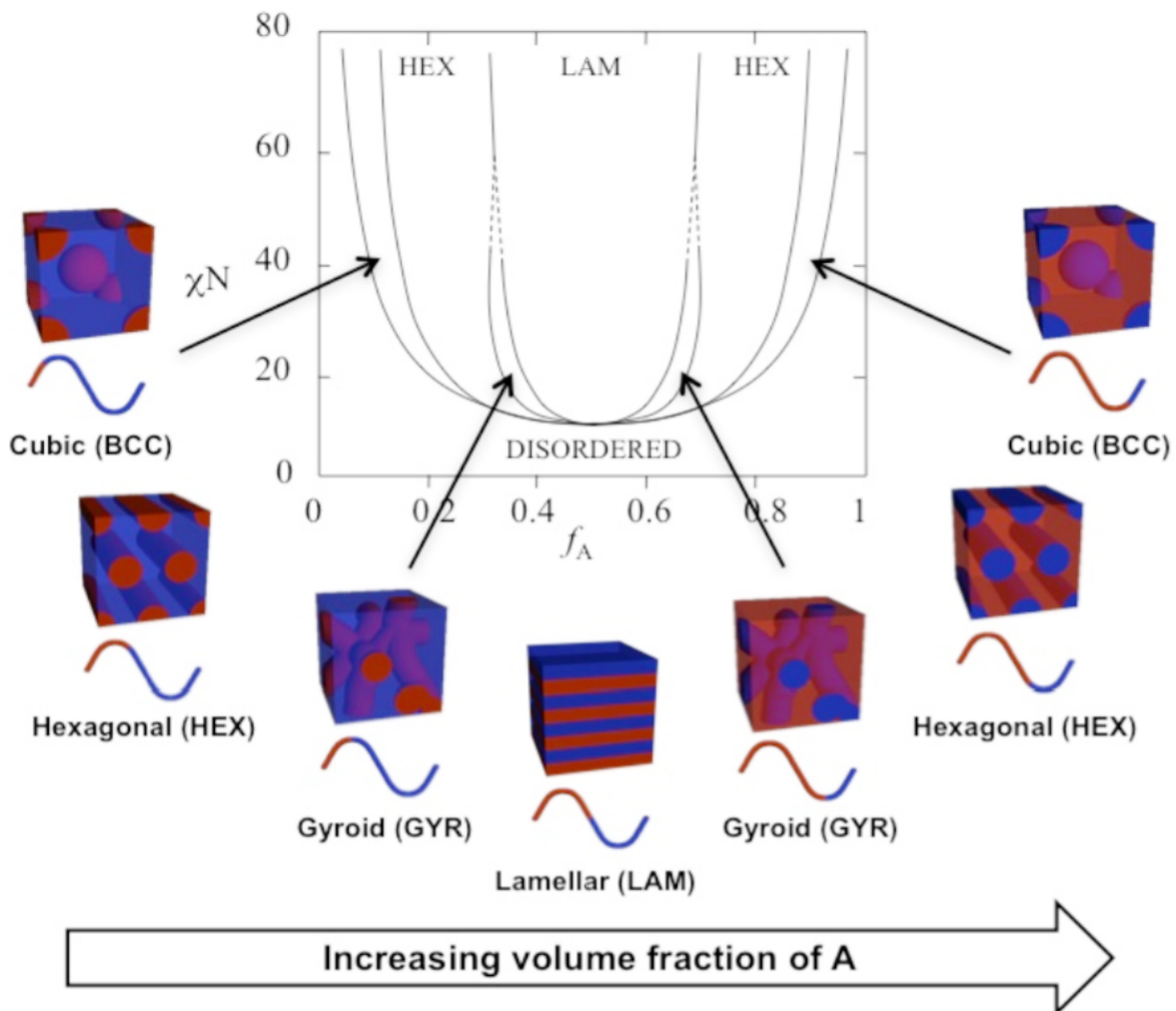


Figure 2-5. Phase diagram of diblock copolymers and corresponding mesoporous structures as a function of χN and volume fraction of components (f) (Reprinted from Ref. 57 with permission from MDPI).

2.2 Polymer nanocomposites

Nanocomposites are materials composed of two or more constituent materials having different physical or chemical properties. When the size of one of constituent falls into the nanometer scale, the composite is called a nanocomposite. Generally, polymer nanocomposites consist of a polymer matrix with dispersed inorganic nanofillers. The properties of nanocomposites depend on various conditions, such as the properties of fillers and matrix, volume fraction of components, and matrix–filler interaction. Thus, the desired mechanical, optical, electric, and magnetic properties can be introduced to the materials by tailoring the aforementioned conditions. However, one of the difficult challenges in processing polymer nanocomposite is to disperse inorganic nanofillers homogeneously in an organic polymer matrix. Because inorganic nanoparticles tend to agglomerate in organic polymers without surface modification, the compatibility between matrix and fillers is an important issue for guaranteeing the composite performance.

Furthermore, nanoparticles can play an important role in the stabilization of phase behavior in polymer blends. Stabilizing the dynamic phase behavior of immiscible polymer blends is a critical factor in determining the performance of the blends because the properties of multiphase polymeric materials are influenced by their morphology. Although block and graft copolymers are conventional methods for reinforcing the interface and stabilizing the phase behavior, very sophisticated and complex synthesis processes are often required. Numerous theoretical and experimental studies have reported that the addition of nanoparticles in phase-separating polymers could act as compatibilizers in polymer blends.

In the first part of this subchapter, different types of polymer nanocomposites (layered silicates, silica nanoparticles, carbon black, carbon nanotubes, and 2D inorganic nanoparticles), along with their properties and applications, will be discussed. The methods for enhancing the compatibility of inorganic nanofillers with organic polymer matrices will be also described. In the second part of this subchapter, the influence of various nanoparticles, such as layered silicates, silica nanoparticles, and ceramic nanoparticles, on dynamic phase behavior and the morphology of binary mixtures will be discussed. Theoretical prediction of nanoparticle localization in a phase-separated morphology will be also described.

2.2.1 Nanoparticles in a homopolymer matrix

Clay/polymer nanocomposites

Clay minerals, especially layered silicates, are one of the most widely used inorganic fillers because they can have large interfacial contacts with polymer chains through exfoliation and intercalation. Since there are various types of silicate minerals, the type of clay minerals needs to be clarified first. It is known that roughly 30% of the minerals in the Earth are silicate minerals, and 90% of the Earth's crust consists of silicate minerals. The basic structure of silicate minerals is SiO_4 tetrahedrons composed of oxygen and silicon, which are two most abundant elements in the Earth's crust. SiO_4 tetrahedrons can have various structures such as single units, double units, sheets, rings, and framework structures. Silicate minerals can be categorized into three main groups (tectosilicates, phyllosilicates, and orthosilicates) based on their crystalline structures, as shown in Figure 2-6. Among different types of silicate minerals, the group of 2:1 phyllosilicates (usually referred to as layered silicates) are widely used for polymer nanocomposites due to their high swelling and cation exchange capacity properties.

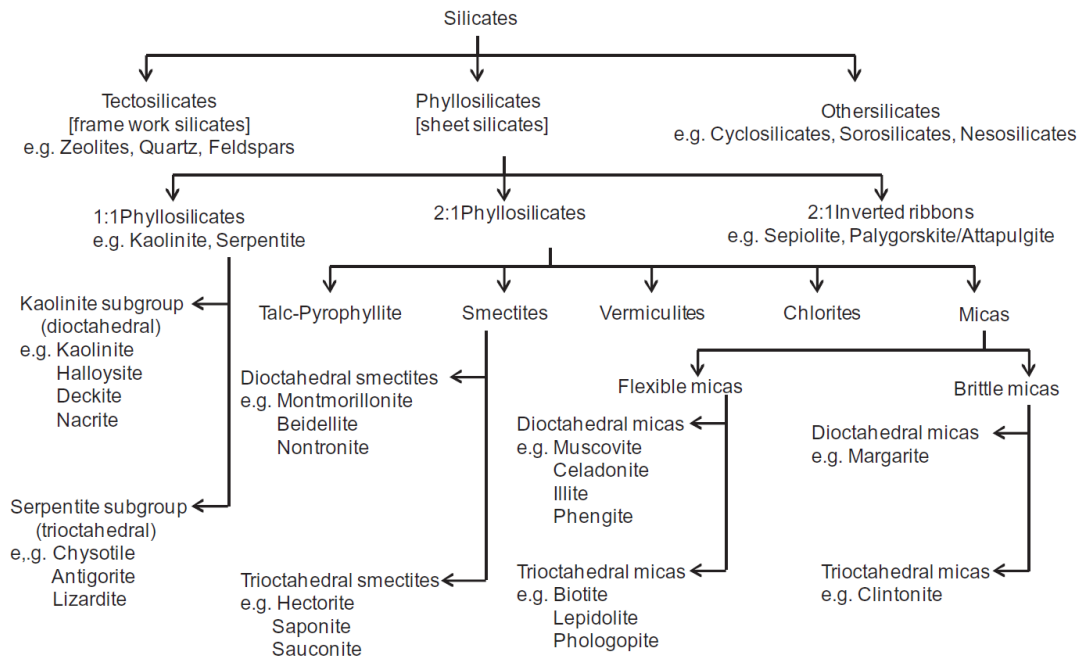


Figure 2-6. Types of silicate minerals. (Reprinted from Ref. 58 with permission from Elsevier).

The group of 2:1 phyllosilicates of clay minerals is in a form of a single-layer crystal structure that is composed of a central octahedral sheet sandwiched by two tetrahedral sheets with a thickness of roughly 1 nm (Figure 2-7). Generally, a silicon atom is surrounded by four oxygen atoms in tetrahedral sheets, whereas an aluminum atom is surrounded by eight oxygen atoms in an octahedral sheet. The width of a single layer is varied from 30 nm to several microns depending on the type of minerals. These layered silicates naturally exist in stacks of hundreds or thousands layers held together by van der Waals forces and/or electrostatic forces. The stacked layers have a regular gap between the layers, called the interlayer or gallery. Isomorphous substitution within the layers (e.g., Al^{3+} replaced by Mg^{2+} or by Fe^{2+} , or Mg^{2+} replaced by Li^+) provides negative charges on the surface of layers. The degree of isomorphous substitution varies. Negative charges between 0.5 and 1.3 in each unit cell are generally counterbalanced by alkaline-earth-metal or hydrated-alkali-metal cations in the interlayers.

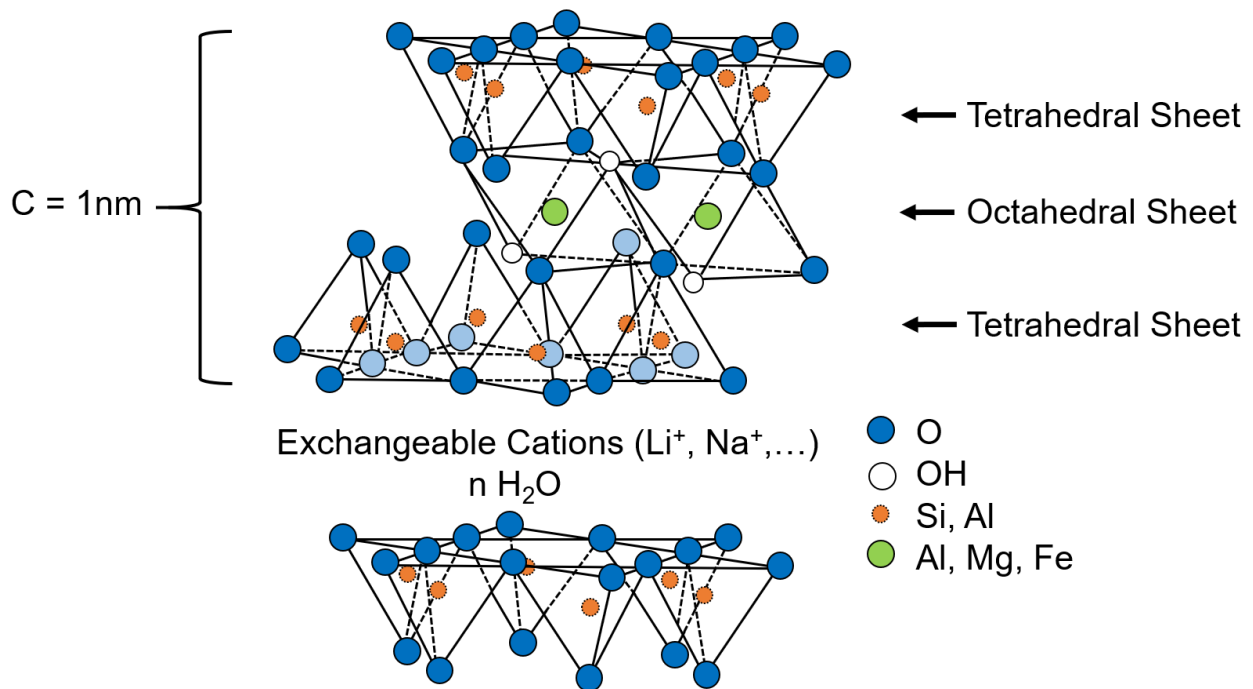


Figure 2-7. Crystal structure of a 2:1 layered silicate.

Montmorillonites are most widely used as clay fillers because they are the most abundant and inexpensive minerals among the group of 2:1 smectites. The width of two-dimensional crystallites of montmorillonite can vary from 2 μm to 0.1 μm . The shape of montmorillonites can be in the form of fibers, laths, hexagonal platelets, and thin flakes, but experimental findings reveal that most of the montmorillonites have an irregular shape. Due to their irregular edges, the shape of montmorillonites is often described as “cornflakes”.⁵⁹ Figure 2-8 shows the typical morphological shape of a single montmorillonite particle by TEM and AFM. A single particle of montmorillonite with a size of $\sim 1 \mu\text{m}$ is observed under TEM. The edges of the particle were frayed, and the contour lines were irregular. In the AFM phase image, the irregular edges of montmorillonite particles with sizes ranging from 100 nm to 500 nm on a polymer surface were more clearly observed. Organically modified montmorillonite particles (Cloisite 30B) were dispersed in poly(vinyl chloride) by melt mixing.

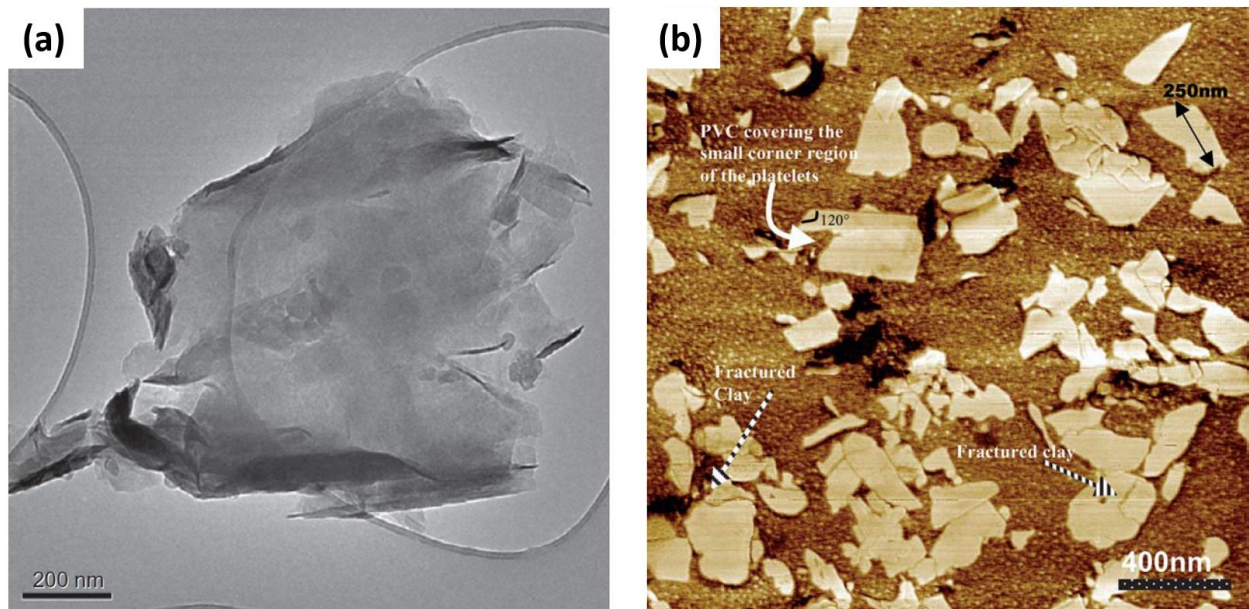


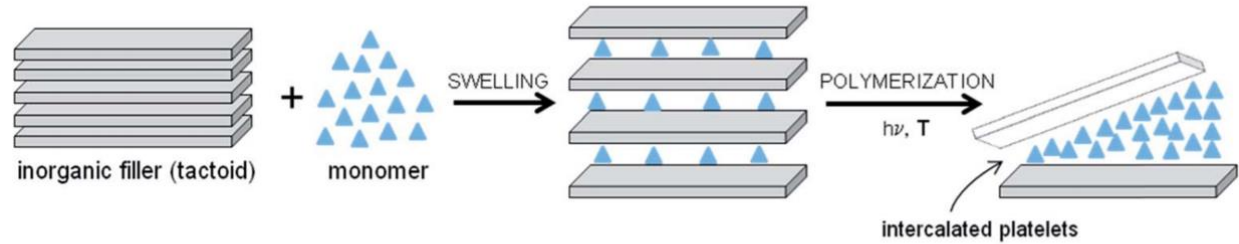
Figure 2-8. (a) TEM image of a montmorillonite particle and (b) AFM phase image of organically modified montmorillonite particles (Cloisite 30B) on the surface of poly(vinyl chloride) (Reprinted from Ref. 58 and Ref. 60 with permission from Elsevier).

Natural layered silicates have polar and high-energy hydrophilic surfaces with hydrated Na^+ or K^+ ions in the interlayers. In the natural states, layered silicates are only compatible with hydrophilic polymers such as poly(acrylic acid) (PAA), poly(vinyl alcohol) (PVA), or poly(ethylene oxide) (PEO). The hydrophilic surfaces of layered silicates should be organically modified to reduce high surface energy and to enhance compatibility with many hydrophobic polymers. Generally, organic modification of natural layered silicates can be carried out by ion-exchange reactions. For example, montmorillonite platelets containing Na^+ or K^+ ions can swell uniformly in water. If alkylammonium or alkylphosphonium salts are added to the dispersed montmorillonite aqueous mixture, the alkylammonium or alkylphosphonium cations are exchanged with the sodium ions in the interlayers. This ion-exchange reaction provides the organophilic property to the surfaces of the natural layered silicates. Furthermore, surface modification leads to an increase in the spacing between layers, which is also an advantage for intercalation of polymer chains. By modifying the length and type of alkylammonium salts, the extent of hydrophobicity of layered silicates can be adjusted to obtain good compatibility with the target polymers. However, the cation exchange does not work well with some clay minerals exhibiting high charge density. Layered silicates like mica do not swell in water due to very strong electrostatic forces between layers. Thus, their surface cannot be easily organically modified by ion-exchange reactions in water.

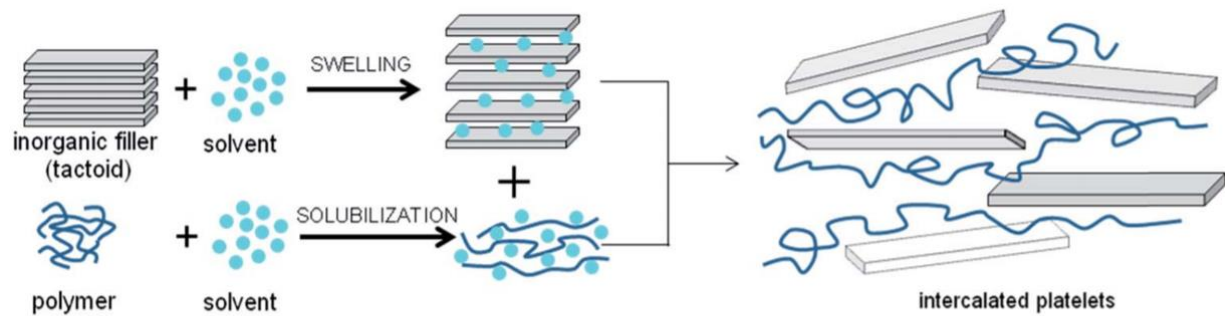
Clay/polymer nanocomposites can be obtained in various ways, such as template synthesis, in situ intercalative polymerization, exfoliation–adsorption, and melt intercalation, depending on polymers and clay minerals.^{17,61,62} The template-synthesis method is different from other preparation methods in that clay minerals are not directly used. In this method, clay minerals are synthesized from clay precursors in the presence of a polymer matrix. During the nucleation and growth process of clay precursors, polymer chains get trapped within layered silicates. This method is an attractive one-step process, as there is no need for onium-ion treatments of silicate layers. However, the method is limited to specific heat-resistant polymers because the synthesis of clay minerals often requires high temperature, which may thermally degrade polymer materials during the process. Also, aggregation of clay particles is still observed, although clay minerals are synthesized in situ. For the in-situ intercalative polymerization method, the layered silicates are first dispersed in a liquid of monomers or a monomer solution. The monomers migrate into the interlayer of the layered silicate, and then polymerization takes place in the interlayers. The

formation of polymer chains in the interlayers leads to an exfoliated or intercalated morphology. This technique was first proposed by Toyota researchers to synthesize a clay/polyamide 6 nanocomposite. In this method, reaction parameters, such as temperature, reaction time, and precursor concentration, are critical to achieve well-exfoliated layered silicate nanocomposites. An exfoliation–adsorption method is similar to the in-situ intercalative polymerization method, except for in-situ polymerization. Layered silicates are dispersed in a solvent in which the polymer can be soluble. After the layered silicates are swollen in the solvent, the polymer chains are dissolved in the solution. The dissolved polymer chains intercalate the galleries of layered silicates. Upon the removal of the solvent, the polymer chains with intercalated clay particles form a clay/polymer nanocomposite. This method can be used for water-soluble systems such as poly(ethylene oxide) (PEO), poly(acrylic acid) (PAA), and poly(vinyl alcohol) (PVA), as well as organophilic systems. The melt intercalation method is the most commercially relevant way for producing clay/polymer nanocomposites, as this technique does not require complex reactions or solvent. This method involves simply compounding the layered silicate with the molten polymer. A polymer melted in a twin-screw extruder at high temperature and shear is mixed with the organically modified layered silicate. The compounding temperature should be delicately controlled to provide efficient mixing of molten polymer and layered silicates at optimal viscosity and to prevent degradation of polymers in high temperature. This method is also attractive in that polymer chains can intercalate in the galleries of layered silicate even though they are thermodynamically not compatible. The stacks of layered silicate can be broken under high shear and high temperature, and the morphology is kinetically trapped in the nanocomposites after cooling. For this reason, many clay/polymer nanocomposites have been produced by melt intercalation method. Figure 2-9 illustrates different methods for clay/polymer nanocomposite preparation.

(a) In situ Intercalative Polymerization



(b) Intercalation of Polymer from Solution



(c) Melt Intercalation

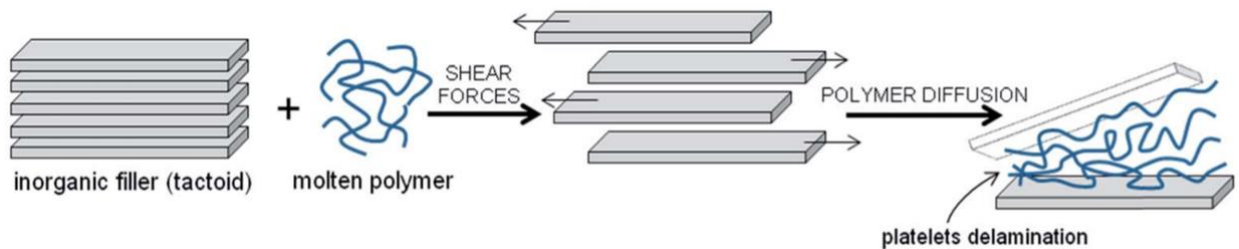


Figure 2-9. Different methods for dispersing layered silicate in a polymer matrix. (a) In-situ intercalative polymerization. (b) Intercalation of polymer from solution (c) Melt intercalation. (Reprinted from Ref. 63 with permission from Royal Society of Chemistry).

Regardless of processing method, the desired morphological state of the clay nanocomposite is the high exfoliation of the clay platelets in a homopolymer matrix. Generally, there are three types of dispersion states of layered silicate in polymers (immiscible, intercalated, and exfoliated).⁶⁴ Figure 2-10 shows TEM images of immiscible, intercalated, and exfoliated layered silicates in an epoxy medium, along with X-ray diffraction patterns. For the immiscible state, thick stacks of silicate layers were observed in the TEM image. The X-ray scattering peak of clay nanocomposites is almost identical to that of pure clay particles because (001) crystal lattices of layered silicates are well preserved in this immiscible state with no intercalation or

exfoliation in the polymer medium. For the intercalated state, thin stacks of silicate layers were observed in the TEM image. A decrease in the (001) X-ray scattering peak values indicates the d spacing of clay layers is slightly expanded by polymer chains. When clay platelets are almost fully exfoliated in a polymer matrix, layered silicates do not form (001) crystal lattices anymore. Nearly single silicate layers were observed in a polymer matrix in the TEM image. Also, the X-ray scattering (001) peak disappears in this case as layered silicates are almost fully exfoliated in polymer mediums.

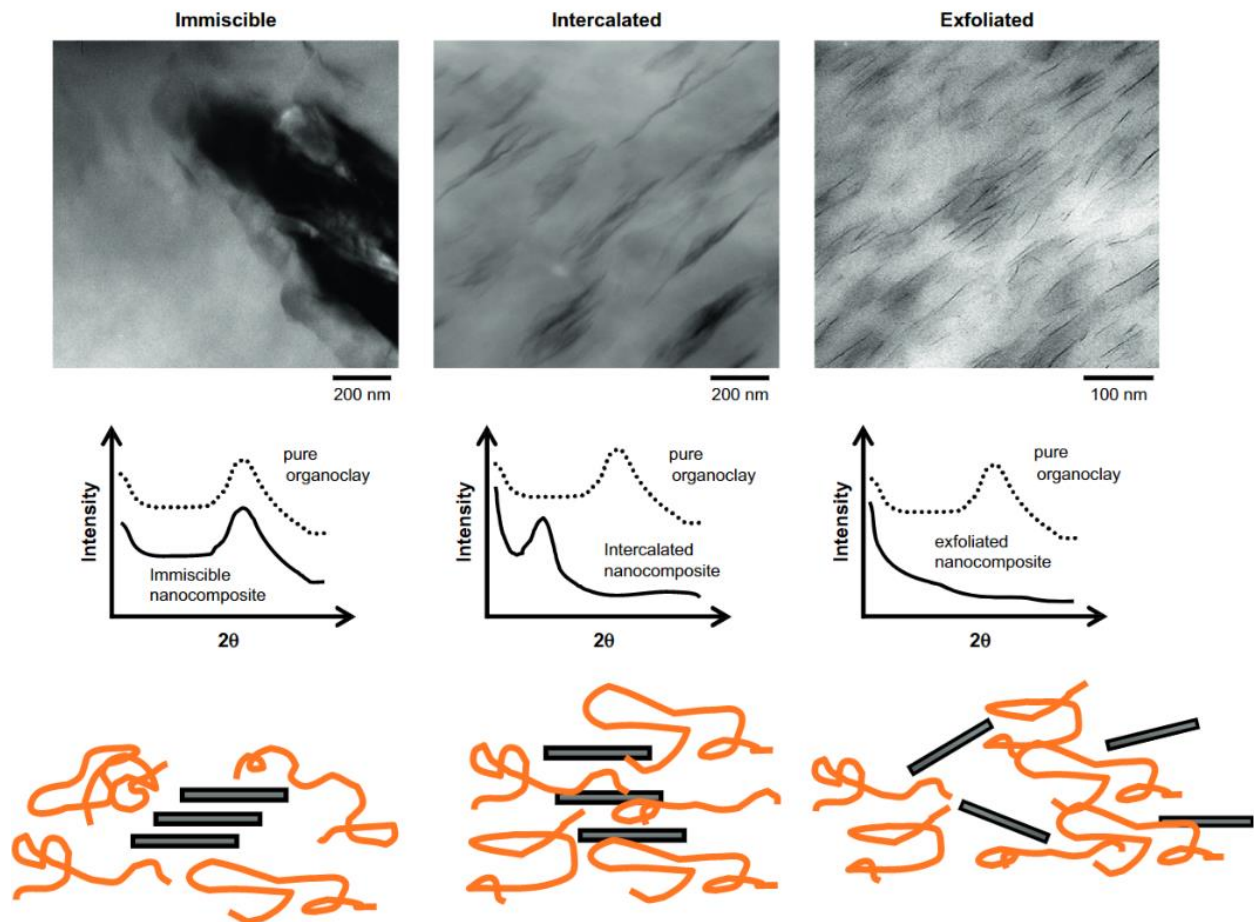


Figure 2-10. Schematic illustration of different states of dispersion of organically modified clay platelets in polymers with corresponding X-ray scattering peaks and TEM images (Reprinted from Ref. 64 with permission from Elsevier).

Clay/polymer nanocomposites can be applied as packing materials because the materials exhibit low gas permeability in the presence of clays. The inclusion of nanoclays in a polymer matrix can elongate the diffusion path of penetrant gas molecules. It was reported that the oxygen permeability of clay/PET nanocomposites reduced nearly by half with 1 wt% clay compared to pure PET.⁶⁵ The clay/PET nanocomposites prepared directly by using a clay-supported catalyst showed oxygen permeability reduction up to 10 times with 5 wt% of nanoclays.⁶⁶

Other polymer nanocomposites

In addition to layered silicates, silica nanoparticles are another popular candidate for filler material in polymer nanocomposites. The simple blending of silica nanoparticles in a polymer does not give a homogeneous composite material because nanoparticles have a strong tendency to agglomerate. To overcome this difficulty, surface modification of silica nanoparticles could be carried out by treating with surface agents or by grafting polymers on silica surface. It was reported that grafting polymers on silica surface is very important for enhancing dispersion of silica nanoparticles in polymer matrix by providing (i) improved miscibility between filler and the matrix and (ii) molecular entanglement between grafted polymers and matrix.⁶⁷ Figure 2-11 shows a schematic illustration of the dispersion of silica nanoparticles in a polymer matrix with and without grafting polymers.

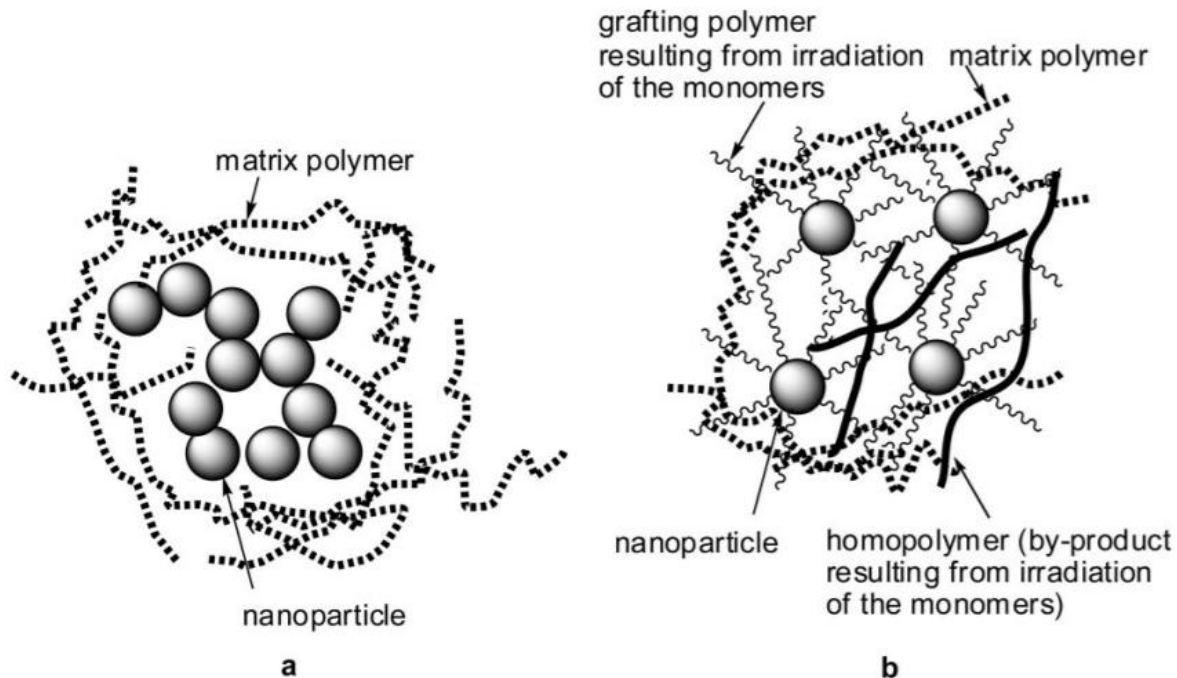


Figure 2-11. Schematic illustration of the dispersion of (a) aggregated silica nanoparticles and (b) grafted silica nanoparticles in a polymer matrix (Reprinted from Ref. 67 with permission from American Chemical Society).

The mechanical properties of the silica nanocomposite are also highly influenced by the dispersion of nanoparticles in a polymer. It was reported that the mechanical properties of silica/poly(ethylene 2,6-naphthalate) (PEN) composites could be worse than those of pristine PEN matrix because of the bad dispersion of silica particles in a PEN matrix.⁶⁷ Silica nanoparticles grafted with various polymers (PS, poly(n-butylacrylate) (PBA), poly(vinyl alcohol) (PVA), PMMA) enhanced the tensile strength, even though the miscibility between a graft polymer and a polymer matrix are varied. The results indicated that the reinforcement effect is dependent not on the miscibility between a grafted polymer and a polymer matrix, but on the entanglement of the grafting polymers with a polymer matrix.

Carbon-based fillers are also widely incorporated with polymer materials due to their extraordinary thermal, electrical, and mechanical properties. For example, the theoretical elastic modulus and strengths of carbon nanotubes (CNTs) are 10–100 times higher than the strongest steel.⁶⁸ The electric conductivity of CNTs is also much higher than that of copper wires.⁶⁹ A single layer of graphene exhibiting a ultimate strength of 130 GPa and a Young's modulus of 1 TPa is known as the strongest material.⁷⁰ This material also has a thermal conductivity of 5000 W/(m·K)

and an electrical conductivity of 6000 S/cm.⁷⁰ Because of their exceptional properties, many studies related to the properties of CNT/polymer or graphene/polymer nanocomposites have been reported.

Like silica nanoparticles, non-functionalized carbon nanomaterials tend to aggregate in a polymer matrix. The aggregation of carbon nanomaterials results in the reduction of their physiochemical properties. To achieve stable dispersion of the nanomaterials, the surface modification of carbon nanomaterials has been applied. Li et al. demonstrated the functionalization of single-walled CNTs with polystyrene by the Cu(I)-catalyzed Huisgen cycloaddition.⁷¹ The polystyrene-functionalized CNTs maintained a stable colloid dispersion in tetrahydrofuran (THF) solvent for 3 weeks. Ezzeddine et al. showed the enhanced dispersion of CNTs in a PMMA matrix after being functionalized with imidazole groups.⁷² Kim et al. reported that thermally reduced graphene oxide (TRG) showed a better dispersion compared to non-functionalized graphite in a poly(ethylene-2,6-naphthalate) (PEN) matrix.⁷³ TRG, produced by oxidizing graphite and applying a thermal treatment up to 1050 °C, exhibited the increased surface area of graphite as a result of thermal expansion. Figure 2-12 shows TEM images of the graphite and TRG in PEN. The enhanced exfoliation of the particles was observed when thermally reduced graphene oxide was used.

The mechanical properties of polymers can be improved by adding carbon nanomaterials. This mechanical enhancement effect is more drastic for soft elastic polymers than for rigid polymers. Rafiee et al. showed that 0.1 wt% of graphene platelets in an epoxy increases Young's modulus by 31%.⁷⁴ Ramanathan et al. demonstrated that the elastic modulus of PMMA increased by 33% only with the addition of 0.01 wt% of functionalized graphene sheets.⁷⁵ It was also reported that polymer insulators became electrically conductive when electrically conductive carbon nanomaterials were incorporated. Stankovich et al. reported 0.1 vol% of graphene in PS exhibits an electrical percolation threshold.⁷⁶ Grossiord et al. showed stabilized conductivity of 10^{-3} S/m when 1.75 wt% of CNT was added in PS.⁷⁷ However, thermal conductivity of polymers is not improved dramatically compared with the electrical-conductivity enhancement of polymers. This is probably due to the difference in thermal conductivity for polymers (0.1–1 W/m·K) and carbon materials (5000 W/m·K) not being as high as that in electrical conductivity (polymer: 10^{-18} – 10^{-13} S/cm, carbon nanomaterials: 6000 S/cm). Furthermore, anharmonic lattice vibrations at the interface between polymer and nanoparticles may significantly increase thermal resistance. It was

reported that 5 wt% graphene oxide in an epoxy resin resulted in just a four times increase in thermal conductivity.⁷⁸ For a 30 times increase in thermal conductivity of an epoxy, very high loading (33 vol% of graphite particles) was required.⁷⁹

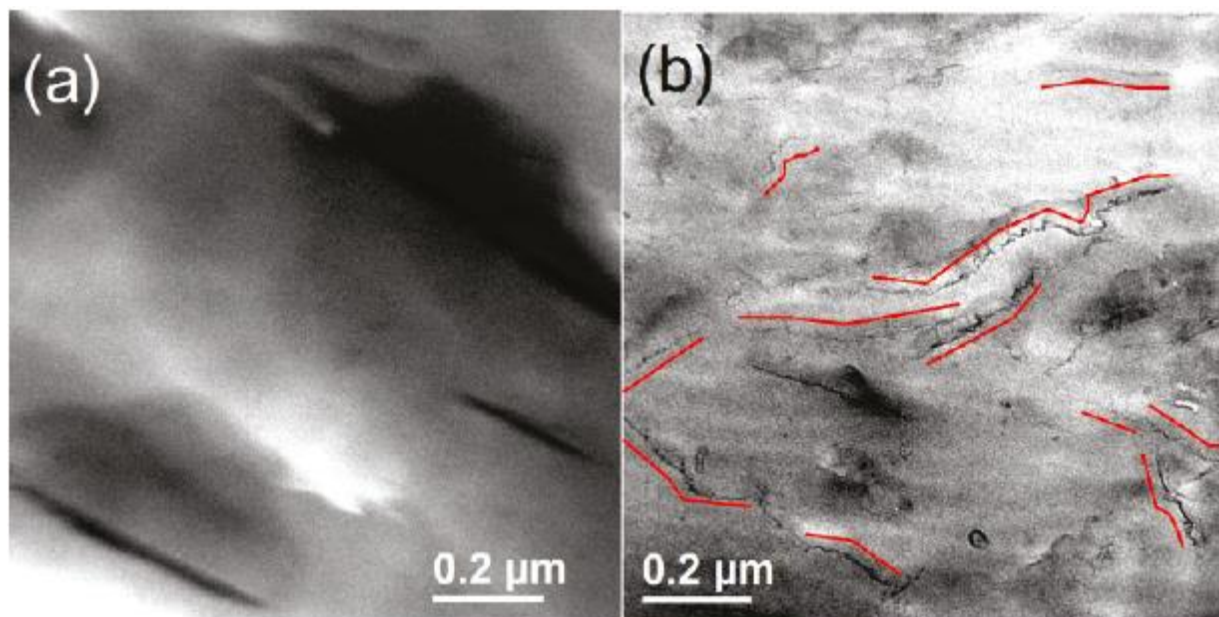


Figure 2-12. TEM images of the dispersion of (a) 3% graphite and (b) 3% TRG in a PEN matrix (reprinted from Ref. 70 with permission from American Chemical Society).

2.2.2 Nanoparticles in polymer blends

Clay nanoparticles in blends

The presence of particles can influence the coarsening dynamics and structural evolution in immiscible polymer blends. Tanaka first observed that the coarsening process of a binary liquid mixture in the presence of glassy particles was retarded by the pinning effect of glassy particles.⁸⁰ Later, Balazs et al. demonstrated this mechanism by computational simulation.⁸¹ They reported that hard solid particles, which were preferentially wetted by one of the two domains, significantly hindered the growth of domains and changed the final morphology of polymer blends undergoing phase separation. Since their pioneering work, the effect of micro- or nanoparticles on the dynamic

phase behavior in binary mixtures has been widely investigated. Organically modified layered silicates have been a popular candidate for solid additives because they can create large interfacial contacts with polymer chains by intercalation or exfoliation. Li et al. reported a decrease in the size of domains in a poly(phenylene oxide) (PPO)/polyamide 6 (PA6) blend in the presence of organically modified clays.⁸² They observed the clay particles were preferentially located in the PA6 phase due to a high affinity after melt mixing. They concluded that the increase in viscosity of PA6 resulted in hindering the domain growth of PA6 and PPO by changing the viscosity ratio between the two phases. Si et al. found that organically modified clays can act as a compatibilizer in polymer blends by decreasing interfacial tension between two polymers via interfacial segregation.⁸³ They observed interfacial localization of clay particles in three different polymer blends (PS/PMMA, PC/SAN, and PS/PVC). Figure 2-13 shows that interfacially located organically modified clays increased the compatibility between PC and SAN polymers, whereas unmodified clay particles were not very effective. The result was striking, in that the addition of organically modified clays in polymer mixtures can be an alternative for conventional surfactants to enhance the compatibility in immiscible polymers. Later, the role of organically modified clays in immiscible polymer mixtures was more widely reported. For example, Trifkovic et al. showed that organically modified clays can stabilize a polyethylene (PE)/poly(ethylene oxide) (PEO) blend by jamming at the interface.⁸⁴ They found that clay nanoparticles at the interface significantly suppressed the coarsening of the two phases during thermal annealing. Filippone et al. have intensively studied the effects of organically modified clays on the formation of co-continuous morphology in various polymer blends.⁸⁵⁻⁸⁸ They observed that interfacial localization of organically modified clays in HDPE/PA6 and PS/PMMA blends promoted a co-continuous phase-separated morphology in blends.

Other nanoparticles in blends

As discussed earlier, the presence of nanoparticles can stabilize the phase behavior of polymer blends. However, this could be more dramatic if nanoparticles can freeze the process of phase separation. It is reported the phase-separated morphology could be maintained in the form of the initial co-continuous structure without further enlargement of phases when nanoparticles are interfacially aggregated. This formation is generally observed when the phase separation of a

mixture occurs via spinodal decomposition in the presence of nanoparticles. To address this formation, the morphological evolution of a partially miscible blend by spinodal decomposition should be discussed in advance. When thermally induced phase separation takes place by passing the critical temperature in the phase diagram, a co-continuous morphology can be formed at initial phase-separation stage. This early state of the co-continuous morphology is generally coarsened into two large phase-separated domains over annealing time. However, interfacially segregated nanoparticles in the mixture often halt the phase-separation process at this early stage and provide the stable co-continuous morphology.

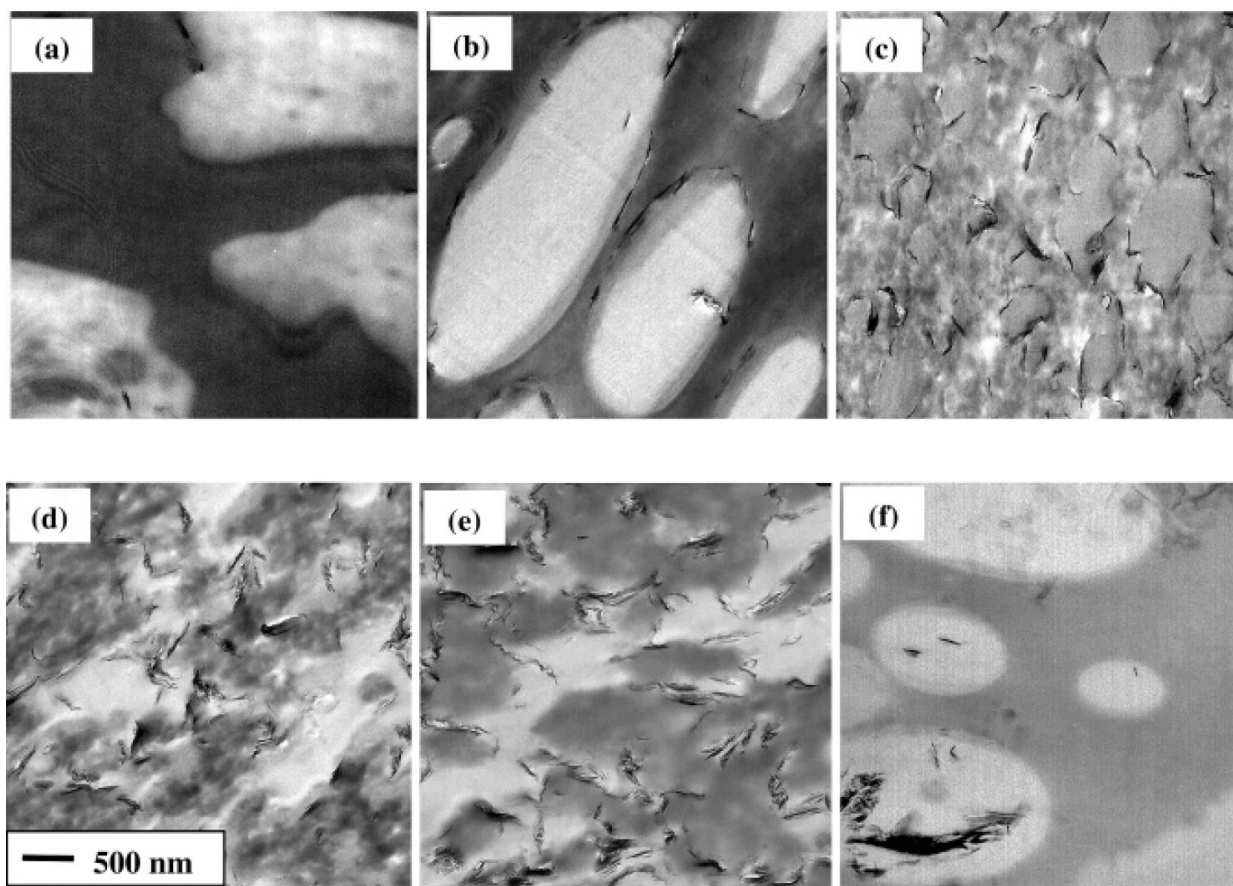


Figure 2-13. TEM images of PC/SAN (70/30) blend morphologies with (a) 0% (b) 1% (c) 3% (d) 5% (e) 10% of Cloisite 20A and (f) 10% of Na⁺ Cloisite. Dark and bright domains are PC and SAN, respectively (Reprinted from Ref. 83 with permission from American Chemical Society).

In 2005, two different research groups simultaneously reported that nanoparticles jammed at the interface can stabilize an initial co-continuous morphology formed by a spinodal phase separation. Stratford et al. performed a numerical study of the demixing process in binary low-viscosity fluids with neutrally wetting particles.⁸⁹ They found that the particles located at the interface slowed down the coarsening process of binary mixture remarkably and eventually arrested the initial co-continuous morphology. They called the new material a co-continuous interfacially jammed emulsion gel (bijel). Chung et al. experimentally demonstrated a bijel with a binary polymer blend and neutrally wetting particles.⁹⁰ They showed that a deuterated poly(methyl methacrylate) (dPMMA) and poly(styrene-ran-acrylonitrile) (SAN) blend at above LCST of ~160 °C could be stabilized in the form of the initial co-continuous structure for several days with interfacially segregated PMMA (Mw~1,800 g/mol) grafted silica nanoparticles.⁹⁰ They also stated that particles jammed at the interface could suppress the coarsening more effectively compared to particles jammed in one phase of binary blends. Since then, this new material, a so called “bijel”, has widely been investigated. In addition to polymer blends, the formation of a bijel in an immiscible fluid mixture was also reported. Herzig et al. found that silica partitioned at the interface can stabilize the co-continuous water and 2,6-lutidine mixture for several months.⁹¹ The different binary liquid pairs, such as ethylene glycol (EG)/nitromethane (NM) and ethylene carbonate (EC)/p-xylene, were also used to form a bijel.^{92,93} Silica surface with hexamethyldisilazane (HMDS) became partially hydrophobic and the particles were found at the interface for both EG/NM and EC/p-xylene systems. Bai et al. showed styrene-butene oligomers could produce a bijel formation with hydrophobic nanoparticles.⁹⁴ The co-continuous morphology was stable for several hundred seconds when hydrophobic particles were located at interface. However, the initial co-continuous morphology was broken in a few seconds with nanoparticles located in the PS phase. Figure 2-14 shows two different bijel formations produced by a polymer blend (dPMMA/SAN) and a fluid mixture (water/2,6-lutidine) with interfacially located silica nanoparticles.

Co-continuous structure in blends could be formed by aggregating particles in one phase of a binary mixture. Li et al. found that the co-continuous structure of a PS/PVME blend was arrested by cadmium selenide (CdSe) nanorods and nanospheres grafted with the native ligands trioctylphosphine oxide (CdSe-TOPO).⁹⁵ They demonstrated that both CdSe-TOPO nanorods and nanospheres, which were selectively partitioned into PVME-rich domains, formed a percolated

network structure beyond certain concentrations. They observed that the co-continuous morphology with sizes on the order of several microns was not coarsened into the large discrete domains for a long period of annealing time due to a network formation of nanoparticles. The local morphology of a PS/PVME blend filled with CdSe–TOPO nanorods was identified by transmission electron microscopy (TEM) as depicted in Figure 2-15a. The schematic illustration of the PS/PVME phase-separation process with CdSe–TOPO nanorods over time is shown in Figure 2-15b. The randomly dispersed CdSe–TOPO nanorods became located in the PVME phase as phase separation occurred, and they halted the co-continuous phase-separated PS/PVME morphology at the initial stage. Yeganeh et al. reported the effect of hydrophobic fumed silica on a PS/PVME blend.⁹⁶ Hydrophobic fumed silica slowed down the process of phase separation through partitioning within the PS phase, analogous to CdSe–TOPO nanoparticles, although the blend did not exhibit the co-continuous morphology.

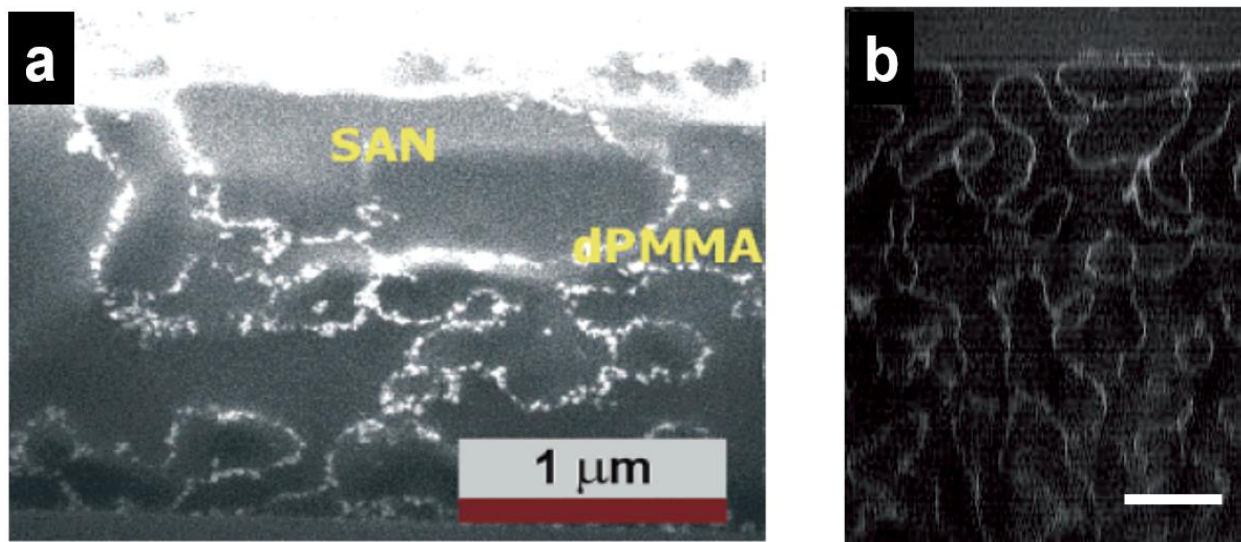


Figure 2-14. (a) A cross-sectional SEM image of a bijel (dPMMA/SAN/Silica) film. (b) A 3D bijel morphology (water/2,6-lutidine/silica) observed by fluorescence confocal microscopy (scale bar = 100 μm) (Reprinted from Ref. 90 and Ref. 91 with permission from American Chemical Society and from Springer Nature, respectively).

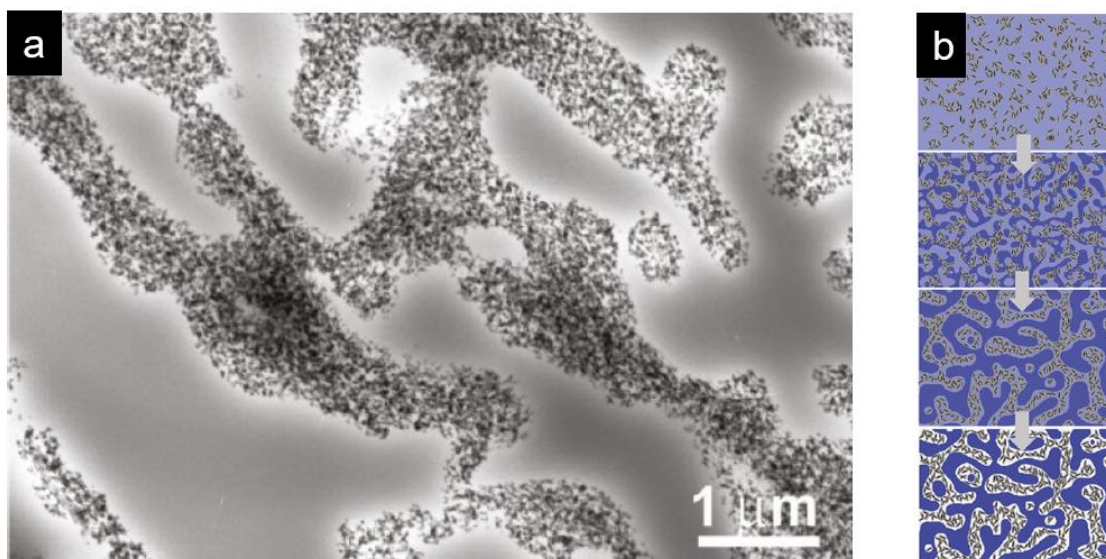


Figure 2-15. (a) TEM image of co-continuous structure in a PS/PVME blend. A percolated network of nanorods was found in the PVME phase. (b) Schematic illustration of the process of the kinetically arrested co-continuous structure through nanorods network formation (Reprinted from Ref. 95 with permission from American Chemical Society).

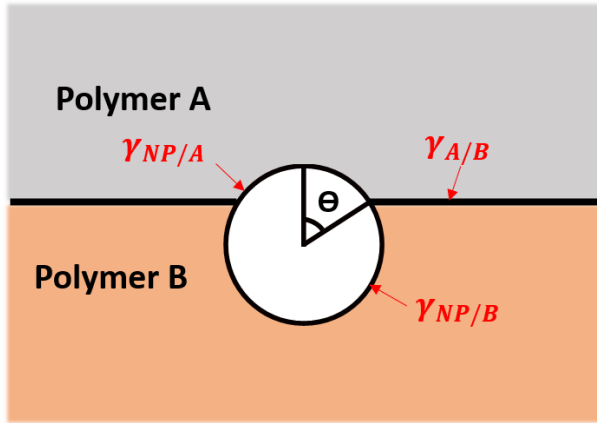
In addition to partially miscible blend systems, the co-continuous morphology was formed in immiscible polymer blends by melt mixing. Huang et al. reported the co-continuous morphology of PE/PEO blends with interfacially jammed fumed hydrophobic silica nanoparticles after melt mixing.⁹⁷ They found that a single layer of silica nanoparticles was located at the PE/PEO interface by SEM after extracting PEO phases. The coarsening process of PE/PEO domains during thermal annealing was significantly suppressed with interfacially jammed silica nanoparticles. Liu et al. reported that the hydrophobic fumed silica nanoparticles segregated into one of the phases in a blend could slow down the coarsening process of a polyamide (PA)/acrylonitrile-butadiene-styrene (ABS) blend.⁹⁸ They observed that silica nanoparticle in ABS phases formed a network structure and suppressed the coarsening dynamics. The final morphology exhibited a co-continuous PA/ABS morphology with silica nanoparticles partitioned in ABS phases. Gubbels et al. showed that a polyethylene(PE)/polystyrene(PS) blend was stabilized by carbon black.^{99,100} They showed that 4 wt% of carbon black localized in the PE phase formed a co-continuous phase-separated morphology in PE/PS blends.

Thermodynamic prediction of nanoparticle localization

The location of nanoparticles in phase-separated polymer blends can be estimated by a thermodynamic prediction. The equation with interfacial-energy terms is as below.^{94,96,101,102}

$$\omega = \frac{\gamma_{\text{Particles/PolymerA}} - \gamma_{\text{Particles/PolymerB}}}{\gamma_{\text{PolymerA/PolymerB}}}$$

γ is interfacial energy between two materials, where A and B stand for each phase in binary mixture. Since the location of colloidal particles is determined by the interfacial energy between materials, the surface chemistry of particles is an important factor for forming a bijel. For example, a mixture of oil and water with a $\gamma_{A/B}$ value ranging from 10 to 50 mJ/m² can form a bijel relatively easily because of the high interfacial energy ($\gamma_{A/B}$) between water and oil.¹⁰² However, the sophisticated surface modification of nanoparticles is necessary for a polymer blend because the interfacial energy ($\gamma_{A/B}$) value of polymer blends is usually much smaller (~ 1 mJ/m²) than that of oil-and-water mixtures. If we assume that the mixture is at thermodynamic equilibrium, we can estimate the location of particles. If $-1 < \omega < 1$, the particles will be localized at the interface of two polymers. If $\omega < -1$ or $\omega > 1$, the particles will preferentially be located either in polymer A phase or polymer B phase, respectively. Figure 2-16 shows the thermodynamic prediction for locations of nanoparticles in binary mixtures based on interfacial energies.



Young's Equation

$$\omega = \cos \theta = \frac{\gamma_{NP/A} - \gamma_{NP/B}}{\gamma_{A/B}}$$

	Particle location
$-1 < \omega$	A phase
$-1 < \omega < 1$	Interface
$\omega < 1$	B phase

Figure 2-16. Thermodynamic prediction of nanoparticle location in polymer blends. Interfacial energies ($\gamma_{A/B}$, $\gamma_{NP/A}$, $\gamma_{NP/B}$) between materials to determine the location of nanoparticles in blends at thermodynamic equilibrium state.

Generally, the polymer–polymer or polymer–particles interfacial energies are difficult to obtain directly. The Owens and Wendt equation is the one of the ways to estimate the interfacial energies between component A and component B. The Owens and Wendt equation can be expressed as follows:

$$\gamma_{A/B} = \gamma_A + \gamma_B - 2\sqrt{\gamma_A^d \gamma_B^d} - 2\sqrt{\gamma_A^p \gamma_B^p}$$

where the exponents d and p stand for the dispersive and polar components of the surface tension, respectively. If we know the value of the surface energies and their dispersive and polar distributions, the interfacial energies can be estimated by the above equation. Elias et al. estimated the location of hydrophilic and hydrophobic silica particles in a polypropylene (PP)/polystyrene (PS) blend by using Owens and Wendt equation.¹⁰³ They predicted that hydrophilic nanoparticles would be in the PS phase ($\omega = 4.78$) and hydrophobic ones would be in the PP phase ($\omega = -1.13$) at thermodynamic equilibrium. They also pointed out that the molten polymers in a twin-screw extruder might not be at thermodynamic equilibrium because they were dominated by kinetic effects due to their high viscosity. It was shown that hydrophilic particles were found only in the

PS phase and hydrophobic particles were found in the PP phase and at the PP–PS interface. The results matched the prediction calculated by the wetting coefficient.

Even though the prediction from Owens and Wendt equation is very useful, sometimes, even surface energies of materials are hard to measure. In this case, surface energies of materials are estimated by indirect methods. A common way is to measure the water contact angle and estimate the surface energy based on their affinity to water (hydrophilic or hydrophobic). For example, Chung et al. indirectly determined the location of the nanoparticles from the relatively affinity of polymer phases to water.¹⁰² In this study, they investigated nanoparticles grafted with different molecular weights of PMMA branches (2 kg/mol, 21 kg/mol, 160 kg/mol). The contact angle results showed that nanoparticles were getting more hydrophilic as the length of PMMA branches increased. They stated that the nanoparticles tended to locate in the PMMA phase as the surface of nanoparticles became more hydrophilic. The experimental data also showed that nanoparticles with short PMMA branches (2 kg/mol) jammed at the interface between PMMA and SAN, whereas nanoparticles with long PMMA branches were preferentially located in the PMMA phase.

2.3 Field-assisted assembly

The internal structure of polymeric materials (polymer blend, block copolymers, polymer nanocomposites, and hydrogel composites) can be tailored by applying external electric or magnetic fields. If two materials show a strong contrast in electric or magnetic properties (dielectric constants, electric conductivity, or magnetic susceptibility), the morphology of the mixture can be influenced by external electric or magnetic fields. Generally, where the electric or magnetic properties of inorganic nano/micro particles are very different compared to those of organic polymer mediums, electric or magnetic fields have been widely applied to modify the morphologies of polymer nanocomposites. In addition to inorganic/organic hybrid systems, two-polymer phase systems such as polymer blends or block copolymers can be directionally organized under external fields despite their low contrasts in electric or magnetic properties. In this subchapter, we will discuss the mechanism of electric and magnetic field assisted alignment of inorganic fillers or organic polymer materials. Previously reported field-alignment studies on

polymer nanocomposites, binary polymer blends, and polymer block-copolymers will be comprehensively reviewed.

Electric-field assisted particle alignment

The mechanism of electric-field assisted alignment of inorganic polarizable particles in a mobile medium can be explained by Clausius–Mossotti relation. When a particle is exposed to a uniform AC electric field, the particle exhibits instantaneous dipoles. The ability to create instantaneous dipoles in the electric fields is called polarizability (α). Polarizability is closely related to the dielectric constant expressed by Clausius–Mossotti relation.

$$\frac{\epsilon_r - 1}{\epsilon_r + 2} = \frac{N\alpha}{3\epsilon_0}$$

where ϵ_r , ϵ_0 , N , and α are dielectric constant of the material, dielectric constant of vacuum, number density of the molecules, and molecular polarizability, respectively. Thus, the materials with high dielectric constant tend to generate high polarizability in electric field. When a medium with dispersed particles is exposed to a uniform AC electric field, there are two possible scenarios: (1) $\alpha_p > \alpha_m$ and (2) $\alpha_m > \alpha_p$ (α_p : polarizability of particle, α_m : polarizability of medium). If the polarizability of the solid particles is higher than that of medium, the electric field vectors get distorted into the particle and pass through it. If the polarizability of solid particles is lower than that of medium, the electric field vectors get distorted away from the particle and bypass it. These two mechanisms are illustrated in Figure 2-17.

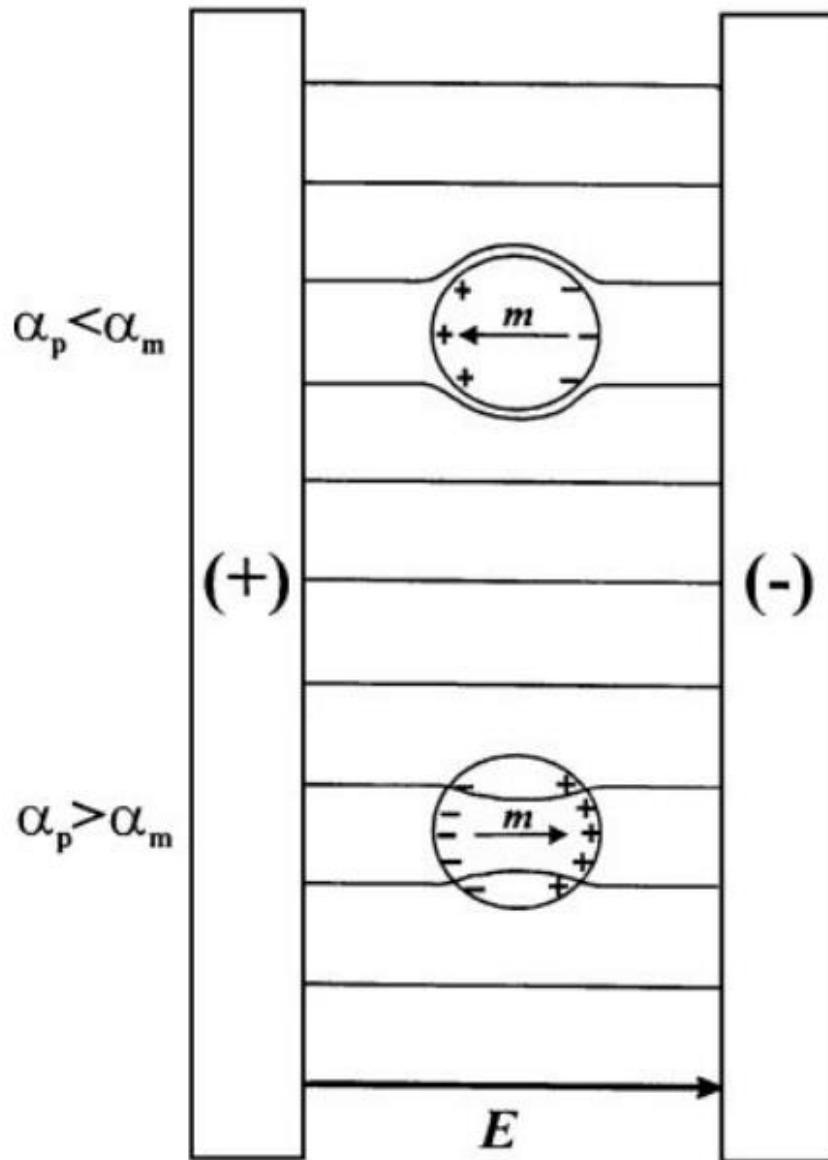


Figure 2-17. The shape of electric fields when polarizability between a medium and a particle are different (above: $\alpha_m > \alpha_p$ below: $\alpha_p > \alpha_m$) (Reprinted from Ref. 104 with permission from Cambridge University Press).

Because inorganic solid particles generally exhibit a higher polarizability than the organic mobile medium, the electric field vectors tend to get distorted toward the particles. Upon the polarization of dispersed particles in the uniform AC field, attractive and repulsive forces between particles are induced. When particles are located parallel to electric field direction, as shown in Figure 2-18(a), the induced dipole–dipole interaction is attractive. However, the induced dipole–dipole interaction is repulsive when particles are located perpendicular to electric field direction, as depicted in Figure 2-18(b). The two types of forces between particles result in the formation of particle-chain structure parallel to the AC field.

Although the exact mechanism of polarization of the clay particles under the electric field is still unclear due to complex surface properties, it is considered that clay platelets have a strong anisotropy of electric susceptibility due to their shape having a high aspect ratio.¹⁰⁵ In the presence of an external electric field, clay platelets tend to be polarized along the in-plane direction (i.e., direction of stacking layers is perpendicular to the direction of polarization) and oriented either parallel or perpendicular to applied field direction. Koerner et al.⁴⁶ found that intercalated clay tactoids,

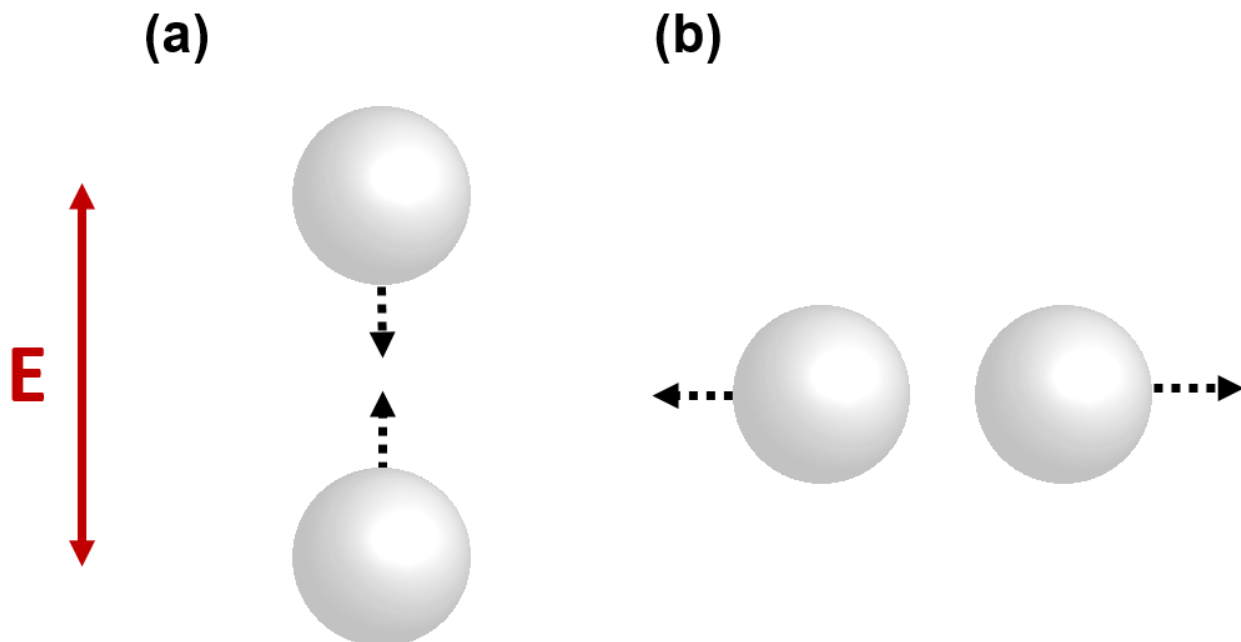


Figure 2-18. Induced dipole–dipole interaction for (a) particles aligned parallel to the applied field and b) particles aligned perpendicular to the applied field.

initially orientated parallel to the in-plane direction of the film, were reoriented in the out-of-plane direction when the AC electric field was applied parallel to the out-of-plane direction. In-situ X-ray scattering showed a change in orientation and lattice spacing of clay platelets upon the application of AC field. Batra et al. tracked the electric-field assisted orientation of clays in epoxy precursors by measuring real-time birefringence.⁴⁷ They observed the occurrence of real-time out-of-plane birefringence of clay/epoxy nanocomposites when external electric field was applied. They stated that enhancement of optical anisotropy in nanocomposite film was solid evidence for the orientation of birefringent clay particles. The application of electric field also influences the interlayer spacing of clay platelets. Kim et al. observed that interlayer galleries of clay platelets were expanded under the application of AC field.⁴⁴ They stated that a change in surface charge distribution on the surface of clay particles due to an externally applied AC field modified electrostatic forces between layers. This led to an increase the interlayer spacing between layers.

The field-assisted alignment of ceramic particles in polymers was also widely demonstrated. Because some ceramic particles such as barium titanate (BaTiO_3), zinc oxide (ZnO), and lead zirconate titanate (PZT) exhibit significant dielectric constants, the dispersed particles form a chain-like structure in electric fields.¹⁰⁶⁻¹⁰⁸ Batra et al. demonstrated orientated BaTiO_3 nanoparticles under electric field in a polydimethylsiloxane (PDMS) matrix. Dispersed BaTiO_3 nanoparticles in a PDMS precursor solution formed fibrillated structures along the applied AC field direction and the morphology was frozen in place by a thermal cross-linking reaction. Figure 2-19 shows SEM images of elongated chains of BaTiO_3 nanoparticles in PDMS. Yildirim et al. also demonstrated the alignment of PZT particles along with graphene nanoplatelets (GNPs) in a PDMS matrix. The nanocomposite, with aligned PZT particles, exhibited ultrasensitive piezoelectric properties in the aligned direction.¹⁰⁹ Electric-field assisted carbon-based particle alignment in an organic medium has also been reported. Prasse et al. demonstrated randomly dispersed CNF in epoxy precursors that were aligned under the electric field.¹¹⁰ The cured film after the particle alignment showed enhanced dielectric properties in the aligned direction. Guo et al. showed graphite particles could be aligned under electric field in a PDMS matrix.¹¹¹ They demonstrated enhanced electrical and thermal conductivities along the direction of oriented graphite particles in a cured film.

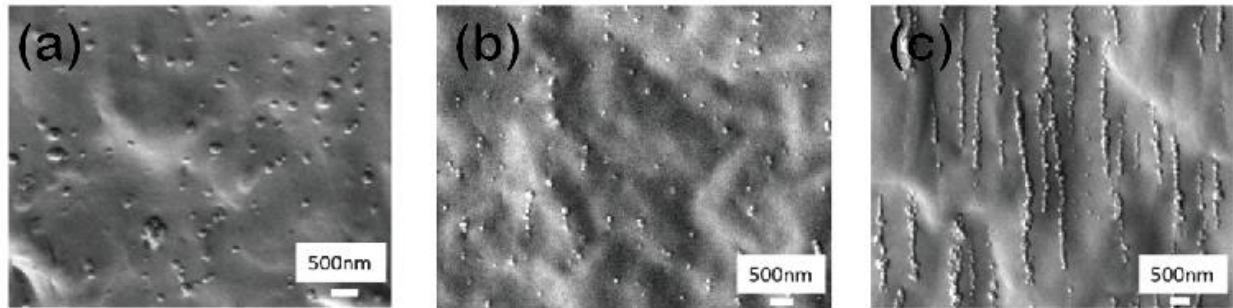


Figure 2-19. The structures of BaTiO₃ nanoparticles in the AC electric field (100 Hz). Fibrillated structures of BaTiO₃ were found at high voltage. (a) 300 V/mm, (b) 800 V/mm and (c) 1400 V/mm (Reprinted from Ref. 106 with permission from Royal Society of Chemistry).

Magnetic-field assisted particle alignment

To orient solid particles in a mobile medium by applying an external magnetic field, the energy reduction from particle orientation in the magnetic field should be higher than thermal motion energy of the particles. Since ferromagnetic materials such as iron, nickel, and cobalt are very sensitive to low magnetic field strength by having high magnetic susceptibilities ($\chi \sim 10^3$), the particles can easily form a columnar structure along the magnetic field direction. For this reason, the alignment of ferromagnetic particles under magnetic fields has been widely demonstrated. Gaska et al. aligned iron oxide particles (Fe₃O₄) with an average size of 62 μm in epoxy by applying moderate magnetic field strength of 0.4 tesla (T).¹¹² Directionally organized iron oxide nanoparticles in epoxy exhibited anisotropic thermal conductivity with an improvement of 120% compared to epoxy with randomly dispersed iron oxide particles. Chen et al. demonstrated field-oriented nickel (Ni) particles with a size of 3–6 μm in PDMS by applying 0.2 T of magnetic field strength in a continuous roll-to-roll process.¹¹³ The aligned Ni composites showed a 13 times increase in the thermal conductivity compared to non-aligned Ni composites. Peng et al. showed magnetic-field assisted alignment of nickel (core)–silver (shell) particles (containing 15 wt% Ag) in PDMS at 0.58 T of magnetic field strength.¹¹⁴ The PDMS with aligned particles decreased the percolation threshold of electrical conductivity from 28 vol% to 1 vol%. The micro-CT image of oriented Ni–Ag core–shell nanoparticles in PDMS matrix at 0.225 T of magnetic field strength is shown in Figure 2-20.

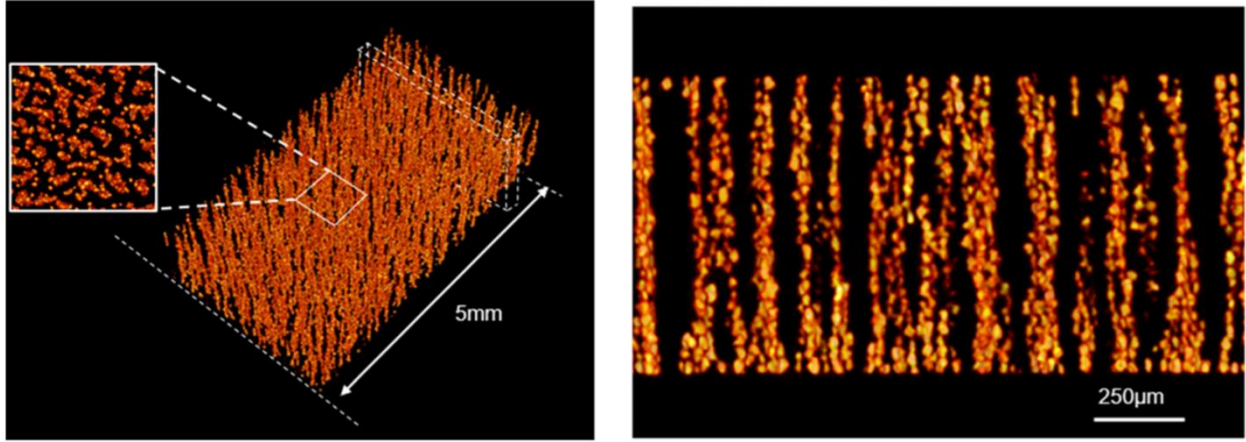


Figure 2-20. X-ray micro-CT images of the composite of 3.6 vol% Ni@Ag in PDMS by applying a magnetic field strength of 0.225 T. (Left) 3D view and (right) cross-sectional view (Reprinted from Ref. 114 with permission from American Chemical Society).

Unlike ferromagnetic materials, other particles such as carbon-based materials, clay minerals, and organic nanocrystals, show relatively small anisotropic magnetic susceptibilities. The diamagnetic orientation of materials is simply given as,

$$\Delta E = -\frac{N}{2\mu_0} \Delta\chi B^2$$

where ΔE , N , μ_0 , $\Delta\chi$, and B are magnetic orientation energy, number of molecules, vacuum permeability, diamagnetic anisotropy, and magnetic field, respectively. To orient nanoparticles, magnetic orientation energy in the magnetic fields should overcome the thermal fluctuation (kT) of nanoparticles in the medium. To obtain high magnetic orientation energy (ΔE), diamagnetic materials of low magnetic susceptibility ($\Delta\chi \sim 10^{-9}$) require very high magnetic field strength (B), which is beyond experimental capabilities. Nevertheless, carbon-based nanomaterials composed of large number of aromatic rings such as CNTs, graphene, and graphene oxide tend to orient their ring planes parallel to the magnetic field because the aromatic molecules have a relatively large magnetic susceptibility in the direction perpendicular to the benzene ring plane compared to that in the parallel direction ($\Delta\chi \sim 10^{-5}$). This is due to aromatic ring current effect of conjugated pi (π)

systems.^{115,116} Choi et al. reported magnetically aligned CNTs in an uncured epoxy resin by applying 25 T of magnetic field strength. The epoxy with oriented CNTs exhibited an increase in thermal conductivity by just 10% compared to the sample with random CNTs.¹¹⁷ Abdalla et al. also demonstrated CNT orientation in epoxy precursors in 9 T of magnetic field strength. The epoxy with oriented CNTs exhibited a 25% increase in the modulus along the alignment direction compared to the modulus along the direction perpendicular to alignment. For clay minerals, the magnetic susceptibilities are determined by the concentration of paramagnetic or ferromagnetic ions within the crystal structure. For example, montmorillonites (MMT) containing 1–4% iron in the crystal structure show a paramagnetic response with magnetic susceptibility ($\Delta\chi \sim 10^{-5}$) at 300 K.⁵⁴ To orient MMT with a diameter of 100 nm, the threshold of external magnetic field strength is around 1–3 T. Koerner et al. demonstrated that montmorillonite nanoparticles were oriented in an epoxy precursor at 1.2 T by using small-angle X-ray scattering technique.⁵⁴ They showed that the basal axis of clay platelets can be oriented either parallel to or perpendicular to the direction of the magnetic field depending on the type of clay minerals. Kitajima et al. demonstrated magnetically oriented MMT layers in a poly(ethylene oxide) (PEO) film, along with LiClO₄, to enhance Li⁺ conductivity.¹¹⁸ They found that a PEO film with MMT oriented along the thickness direction showed a better Li⁺ conductivity at 30 °C compared to the sample with non-oriented MMT. The orientation of organic nanocrystals in a polymer medium was also reported. Kaneko et al. oriented trans-4-[4-(dimethylamino)] stilbazolium toluenesulfonate (DAST) nanocrystals in a UV-curable monomer medium at various magnetic field strengths, from 2 T to 15 T, and then immobilized the solution by UV curing.¹¹⁹ The visible light absorbance (554 nm) of materials was significantly changed depending on the orientation of DAST nanocrystals. They also mentioned that the possible reason for the nanoparticle orientation in the magnetic field is the relatively high anisotropic magnetic susceptibility of aromatic rings in the particle's chemical structure.¹²⁰

Beside nanomaterials in a polymer matrix, the field-assisted alignment of nanoparticles was also observed in aqueous suspensions. If colloidal nanoparticles are intrinsically birefringent, the orientation of nanoparticles can be detected by measuring the birefringence of the aqueous medium. As optically anisotropic nanoparticles undergo field-induced alignment, the medium becomes birefringent ($\Delta n \neq 0$). Hydrophilic clay minerals, which can form colloidal suspensions in water, are optically anisotropic nanoparticles. Dozov et al. studied the electric-field induced birefringence of beidellite-clay aqueous suspensions.¹⁰⁵ They observed that optically isotropic

aqueous medium containing clay colloids became optically anisotropic as the strength of electric field and the concentration of particles were increased. Graphene oxide (GO) suspensions are alternative optically anisotropic nanomaterials.^{121,122} Shen et al. observed the alignment of graphene oxide aqueous suspensions by applying electric fields in the high frequency region (10 kHz).¹²³ They demonstrated an electro-optic graphene-oxide liquid-crystal device using wire electrodes for display applications. The magnetic-field assisted alignment of aqueous suspensions has also been widely reported. Compared to electric fields, the magnetic fields may be a better option because electric fields can cause chemical reduction or electrolysis in aqueous systems. Michot et al. found that nontronite clay aqueous suspensions in aqueous mediums were sensitive to magnetic fields due to the presence of ferric iron in their structure.¹²⁴ 2D SAXS pattern indicated that isotropic nontronite clay suspensions were highly oriented in a magnetic field of 1 T. It was also reported that graphene oxide (GO) suspensions were fairly responsive to magnetic fields.^{115,121} Figure 2-21 shows the orientation of GO suspensions under magnetic field (0.25 T) observed by polarized optical microscope.

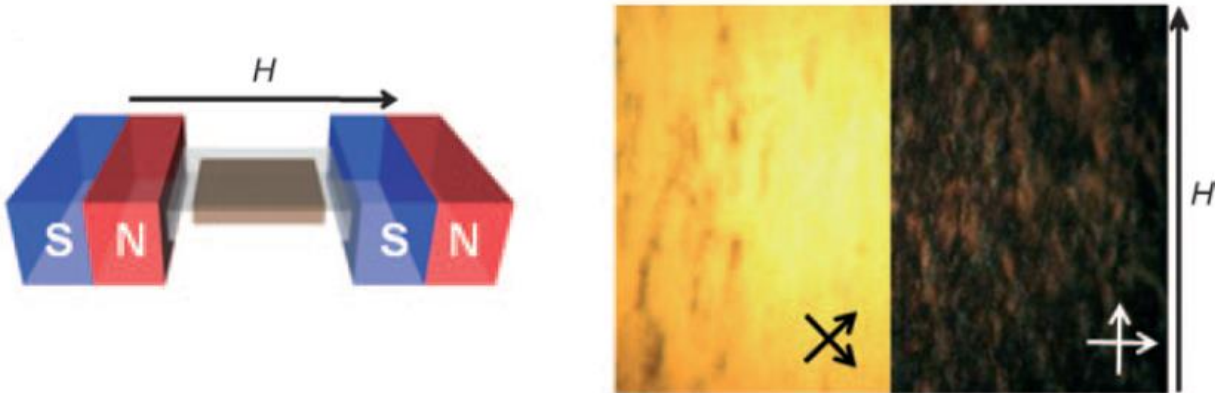


Figure 2-21. Magnetic-field induced alignment of graphene oxide suspensions. (Left) Schematic illustration of the sample in the magnetic field. (Right) Birefringent graphene oxide suspensions between cross-polarizers after 3 h under a magnetic field strength of 0.25 T (Reprinted from Ref. 121 with permission from John Wiley & Sons, Inc).

Alignment of polymer phases in electric/magnetic fields

Theoretically, dipoles of a pendant group on the polymer backbone can be oriented in an electric field. If the electric field strength of 10 kV/cm is applied to the dipole ($\mu = 2 \text{ D}$) of a pendant group at 300 K, the average orientation angle ($\cos \theta$) between the dipole vector and the electric field vector is 5.4×10^{-4} . This means that the degree of orientation of the pendant group is negligible for a realistic electric field strength, where the maximum field strength is a few kV/cm.¹²⁵ For this reason, the orientation of polymers by using external fields has mainly been reported in two-phase polymer systems.¹²⁵⁻¹²⁹ When two immiscible binary liquids (polymer solution or polymer melt) are exposed to external electric fields, the electric stress forms normal to the interface between the two liquids.^{130,131} The induced electric stress at the interface can deform the interface between the two phases if it overwhelms the interfacial tension. Venugopal et al. studied the in-plane electric field effect on the morphology of a PMMA/PS/toluene mixture.¹²⁶ PMMA-rich droplets in a PS-rich matrix became coarsened and ellipsoidal with a major axis parallel to the applied electric field direction (6 kV/cm). As the phase separation process continued, the ellipsoidal PMMA-rich domains coarsened and turned into fibrillated structures. The electric-field assisted orientation of PMMA-rich liquid domains over time is shown in Figure 2-22. Even though one phase was strongly oriented in the electric field direction in this ternary mixture, the relative compositions were changing during solvent evaporation. As a result, the electrical properties (dielectric constant and electrical conductivity) of the two phases also changed over time. To overcome this limitation, Hori et al. investigated the morphological change of a partially miscible polymer blend in the electric field when a mixture underwent thermally induced phase separation.¹²⁵ A poly(2-chlorostyrene) (P2CS)/poly(vinyl methyl ether) (PVME) blend with 0.5 wt% of lithium perchlorate (LiClO_4) showed the oriented morphology parallel to electric field direction in the presence of AC electric field (11.2 kV/cm and 10 Hz). They pointed out that the addition of LiClO_4 was effective at forming an anisotropic morphology by enhancing the difference in conductivities of the two polymers. The electrically oriented phase-separated morphology of a P2CS and PVME blend over time is shown in Figure 2-23.

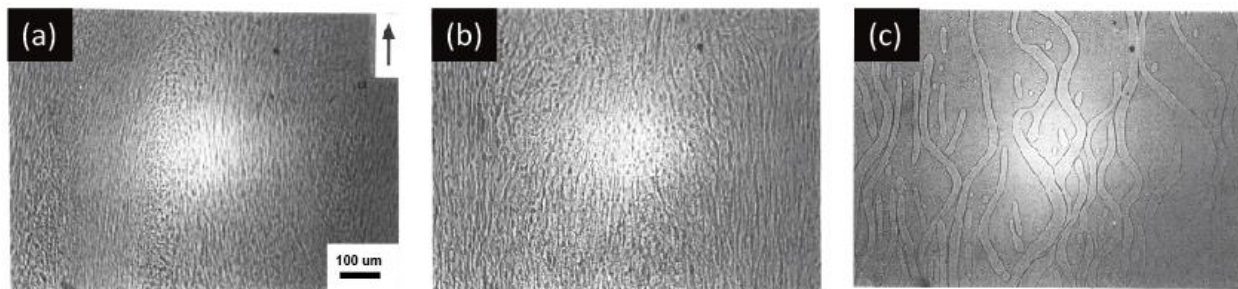


Figure 2-22. The morphology of a PMMA/PS (50/50) blend from toluene in a 6 kV/cm. The PMMA-rich domains were aligned to the electric field direction. (a) 21 min, (b) 25 min, and (c) 29 min from solution casting process (Reprinted from Ref. 126 with permission from American Chemical Society).

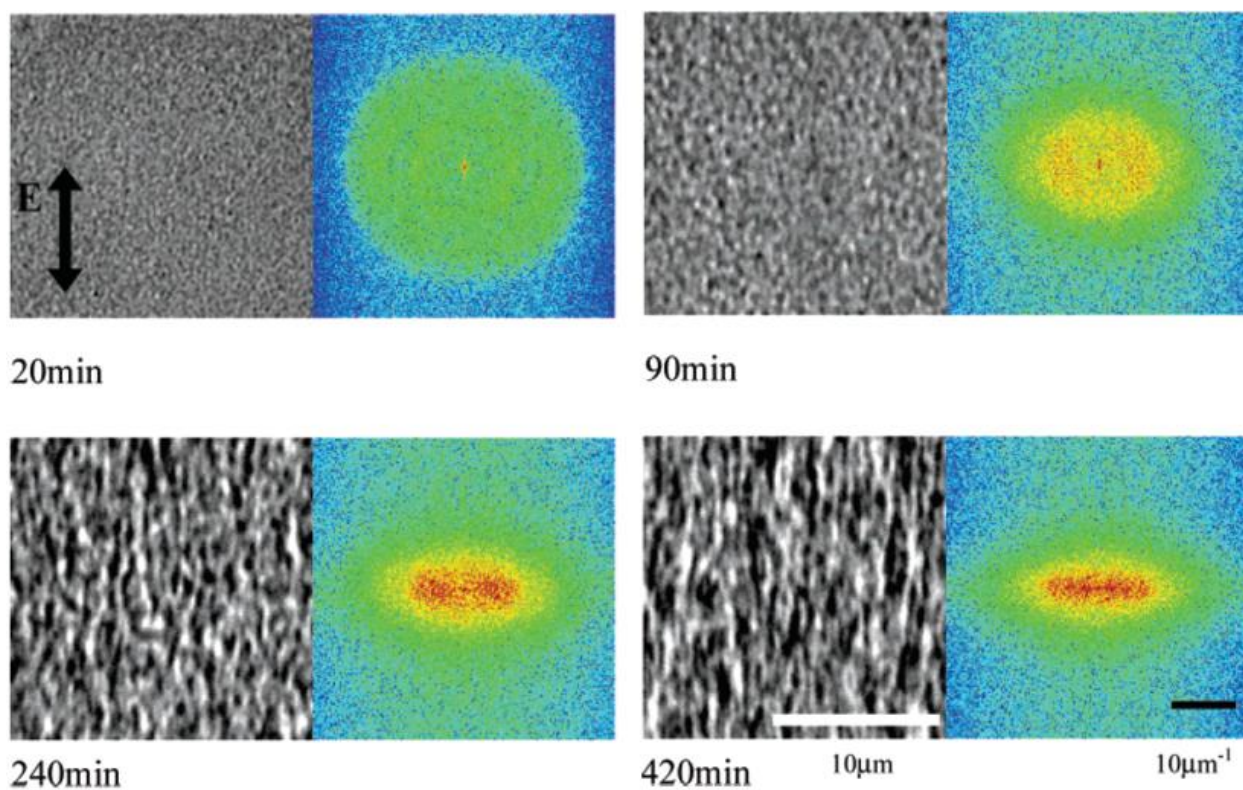


Figure 2-23. Phase-separated structures and corresponding 2D Fourier transform for a P2CS/PVEM (30/70) blend containing LiClO₄ (0.5 wt%) under AC electric field (11.2 kV/cm, 10 Hz) at 118 °C for 20 min, 90 min, 240 min, and 420 min of annealing time (Reprinted from Ref. 125 with permission from American Chemical Society).

Gasa et al. demonstrated that an anisotropic phase-separated morphology of the polymer blends could be used to enhance the performance of proton-exchange membrane fuel cell systems.¹³² Two immiscible polymer blends, a conductive sulphonated poly(ether ketone ketone) (SPEKK) phase dispersed in an insulating poly(ether imide) (PEI) matrix phase, were used for proton-exchange membrane materials. They showed that a blend of sulfonated SPEKK/PEI (30/70) in the melt state was directionally aligned along the thickness direction in the presence of AC electric field (1000 V/mm, 20 Hz). They stated that the residual NMP solvent (10–15 wt%) in the blends facilitated the orientation process of SPEKK and PEI phases at 200 °C under AC field by increasing the mobility of the polymer phases. The aligned structure of the SPEKK/PEI blend in the thickness direction enhanced the ionic conductivity by about three orders of magnitude compared to the ionic conductivity of isotropic blends. They also demonstrated that the SPEKK phases dispersed in an insulating styrene–acrylonitrile copolymer (SAN) matrix phase were oriented along the AC field direction (1000 V/mm, 20 Hz). Figure 2-24 shows isotropic and anisotropic phase-separated morphology of SPEKK/SAN blends in the thickness direction of the polymer films.

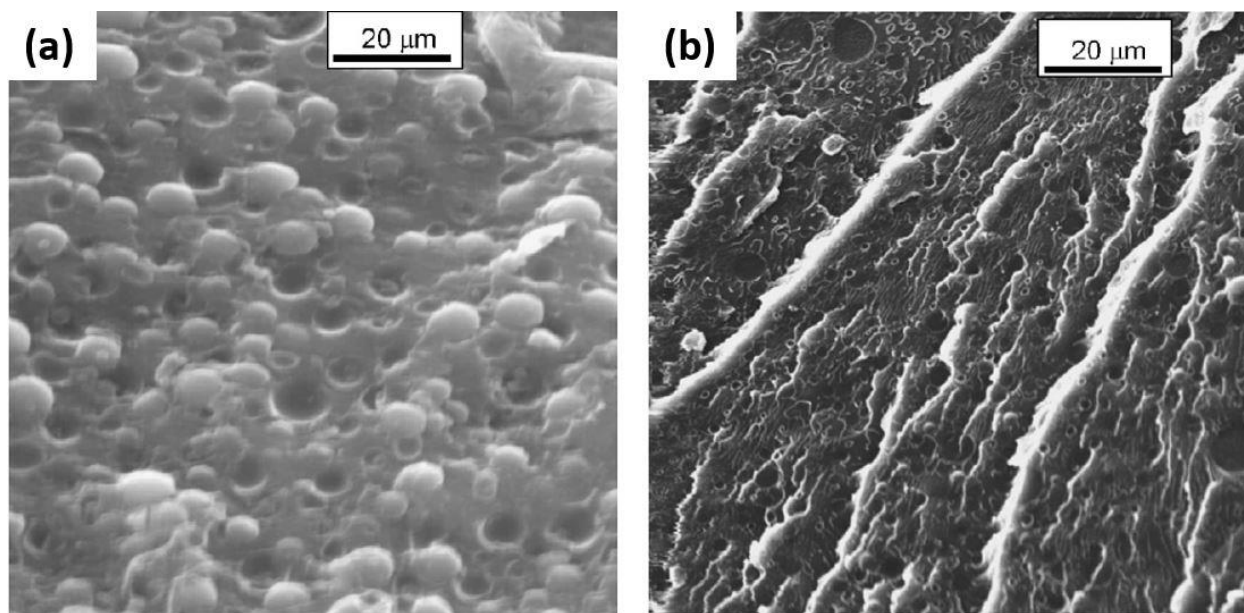


Figure 2-24. Cross-sectional SEM image of phase-separated SPEKK/SAN blend, melt casted at 200 °C. The samples were prepared without electric field (left) and with AC electric field (1000 V/mm, 20 Hz) applied along the thickness direction (Reprinted from Ref. 132 with permission from Elsevier).

The electric-field assisted polymer-domain orientation has been extensively reported in block copolymer systems.^{127–129,133} Morkved et al. first reported the oriented microstructures of a PS-*b*-PMMA diblock copolymer in electric field.¹³³ When the PS-*b*-PMMA film was annealed at 250 °C without electric field, the orientation of the cylindrical PMMA domains was completely random. However, the cylinder PMMA phases were oriented parallel to the applied electric field direction when the film was annealed at 250 °C in the presence of a strong in-plane electric field (37 kV/cm). The morphology of diblock copolymers observed by TEM is shown in Figure 2-25. Boker et al. demonstrated the oriented lamellar structure of a polystyrene-*b*-poly(2-hydroxyethyl methacrylate)-*b*-poly(methyl methacrylate) (PS-*b*-PHEMA-*b*-PMMA) triblock copolymer parallel to the electric field direction from the polymer solution.¹²⁷ They stated that the solution-casting method used in this study could overcome the high annealing temperature where block copolymers could be easily degraded without inert gases. They also mentioned that the lamellar microdomains were oriented with a relatively low electric field strength (1.8 kV/cm). The orientation of the microdomains in block copolymers under electric field is attributed to the lower free energy when domains are aligned to the electric field direction. Because the free energy of the microstructure is proportional to $(\Delta\epsilon V)^2$, the dielectric contrast between two blocks and applied electric field strength are critical factors to orient microdomains. This indicates that the morphology of oriented PS and PMMA block copolymers ($\epsilon_{ps} = 2.4$, $\epsilon_{pmma} = 3.6$) has a lower free energy when the electric field strength of 37 kV/cm was applied.¹³⁴ In addition to the electric field, the oriented cylinders or lamellar microstructure in block copolymers in a magnetic field was also demonstrated. Osuji et al. reported an oriented morphology of a liquid-crystal (LC) attached diblock copolymers such as poly(styrene)-*b*-poly(isoprene-LC) and poly(styrene)-*b*-poly(acrylic acid-LC) by applying a few tesla of magnetic field strength.^{135,136} The anisotropy of magnetic susceptibility in a typical diblock copolymer is relatively small ($\Delta\chi \sim 10^{-9}$) for orienting the microdomains morphology in a few Tesla of magnetic field strength. However, an LC mesogen attached to one of the blocks exhibits high anisotropy of magnetic susceptibility ($\Delta\chi \sim 10^{-5}$) by having rigid aromatic groups. As a result, the block copolymer containing LC system can be oriented parallel to the magnetic field direction by means of LC orientation at the strength of a few tesla. Figure 2-26 shows the magnetic-field assisted orientation of LC attached diblock copolymers demonstrated by his group.

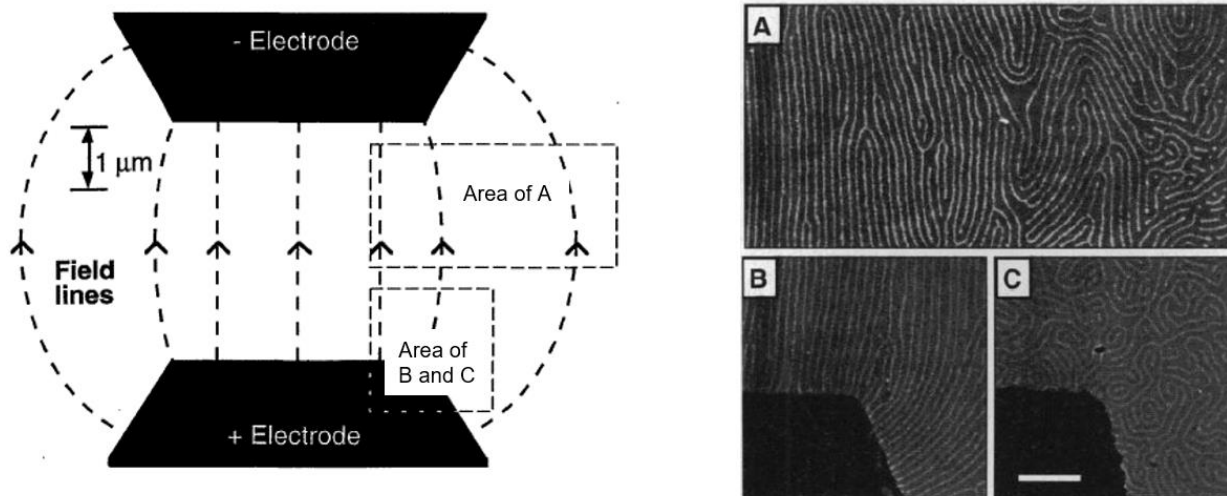


Figure 2-25. (Left) Electrode and sample layout. (Right) The TEM images of PS-b-PMMA for the area indicated on left image. The sample prepared with (A) 37 kV/cm, (B) 20 kV/cm, and (C) no field (Reprinted from Ref. 133 with permission from the American Association for the Advancement of Science).

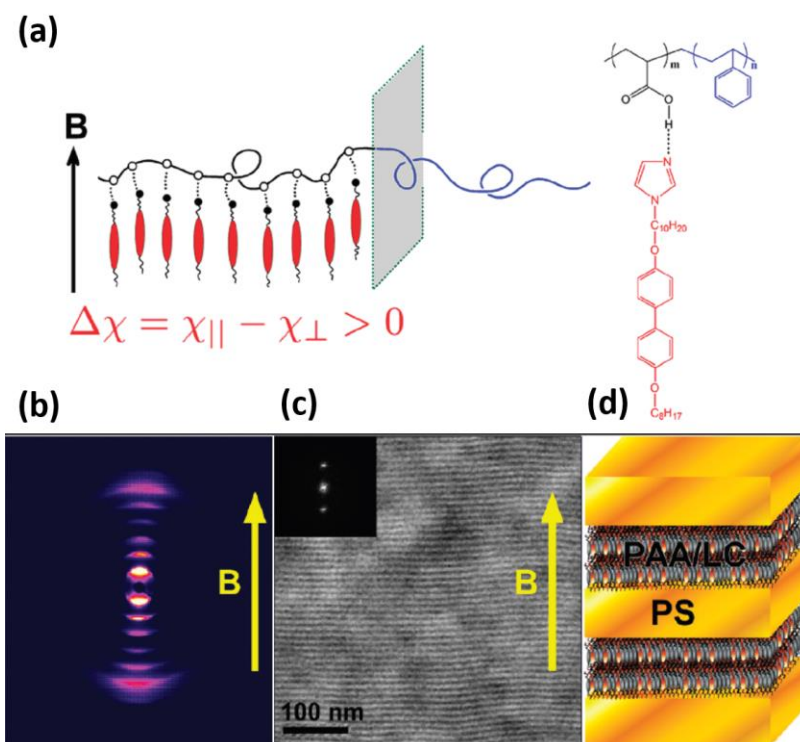


Figure 2-26. (a) Schematic illustration of an LC attached block copolymer and the diamagnetic anisotropy under magnetic field. (b) 2-D SAXS, (c) TEM, and (d) corresponding illustration of an LC attached PS(5.1k)-b-PAA(3.9k) (Reprinted from Ref. 136 with permission from American Chemical Society).

2.4 Hydrogel nanocomposites

Nanocomposite hydrogels are generally defined as crosslinked water-based gels with dispersed inorganic nanoparticles. These materials are quite different from traditional polymer nanocomposites in that the matrix of gels can accommodate a large amount of water. These water-rich soft materials are expected to be used for biomaterials and tissue engineering applications. Moreover, the addition of nanomaterials into a gel matrix may provide better chemical, physical, and biological characteristics to the materials. In this subchapter, the various types of nanocomposite hydrogels and their properties will be discussed. Anisotropic hydrogels synthesized by applying external electric or magnetic fields will be also described.

Silicate-based hydrogel nanocomposites

Layered silicates (clay) can be easily incorporated into a hydrogel because hydrophilic natural silicate nanomaterials can form stable suspensions in water. Due to this characteristic, clay hydrogels are simply formed by the gelation of a solution containing clay suspensions. One very interesting fact is that clay nanoparticles (Laponite) dispersed in water can form a hydrogel without cross-linker agents. These physically crosslinked clay hydrogels are different from conventional chemically crosslinked polymer hydrogels, where an organic crosslinker is used for forming three-dimensional (3D) polymer networks through covalent bonding. Although molecular-level details on the interaction between clay nanoparticles and polymers are still not clear, many researchers consider that polymerization from the surface of the clay probably results in network formation throughout the material. Haraguchi et al. reported outstanding physical properties of Laponite poly(N-isopropyl acrylamide) hydrogels, such as optical transparency, mechanical strength, and degree of water swelling.¹³⁷ In conventional hydrogels, the crosslinking points are structurally inhomogeneous at high concentration of the crosslinker because crosslinking reaction by an organic crosslinker does not occur at regularly spaced positions. Inhomogeneous crosslinking points in conventional hydrogels results in a significant decrease in mechanical stress by localizing the stress during a tensile test. Furthermore, nonuniform crosslinking structures also decrease optical transparency of the materials at a high concentration of an organic crosslinker. However, Laponite hydrogels formed by well-dispersed clay colloids showed enhanced mechanical properties at high concentrations of Laponite without heterogeneous aggregation of crosslinking

points.³⁴ Differences in tensile strength between conventional hydrogels and clay-hydrogels are shown in Figure 2-27.

The internal structures and viscoelastic properties of clay hydrogels are influenced by various parameters such as composition, temperature, and pH. For example, Laponite/PEO hydrogels can be in different states such as solution, flowing gels, and permanent gels based on Laponite concentration, temperature, and PEO molecular weight.^{138–140} Furthermore, clay hydrogels exhibit different physical and chemical properties based on type of clay minerals. For example, a fast swelling rate was observed in montmorillonite hydrogels and a good reversibility in swelling/deswelling cycles were found in mica hydrogels.¹⁴¹

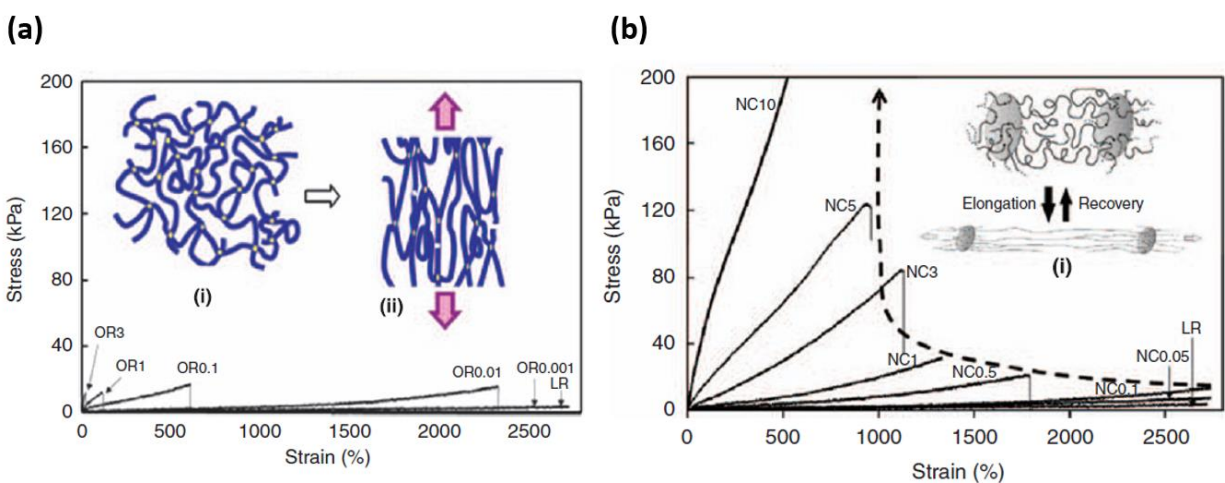


Figure 2-27. Tensile stress–strain curves of (a) chemically crosslinked polymer hydrogels with different with different concentration of organic crosslinker (*N,N*¢-methylenebis (acrylamide) (BIS)), C_{BIS} from 0.001 to 3 mol%. Tensile stress–strain curves of (b) Laponite nanocomposite hydrogels with different concentrations of Laponite from 0.05 to 10 mol% (Reprinted from Ref. 34 with permission from Springer Nature).

Metal/hydrogel nanocomposites

By incorporating metal nanoparticles in a crosslinked gel, stimuli-sensitive properties can be introduced for various applications.¹⁴² Unlike clay minerals, metal nanocomposite gels are hard to produce from a colloid state because metal nanoparticles cannot form a stable suspension in water. One of the ways to synthesize metal nanocomposite hydrogels is by the reduction of metal ions in a gel state. This method proceeds by polymerization of aqueous medium containing metal ions and monomers, followed by the reduction of metal ions with an addition of reductants, such as sodium hydroxide (NaOH). The reduced metal nanoparticles appear within the hydrogel network. It was demonstrated the electrical conductivity in Au-nanoparticle hydrogels is changed according to temperature or pH.¹⁴³ The change of electrical conductivity by temperature or pH is attributed to the changes in the gold interparticle distance within a hydrogel network due to hydrogel shrinkage from external stimuli. Thermosensitive drug release mechanism of Au-nanoparticles hydrogels was also demonstrated by Skirtach et al.¹⁴⁴ They showed that the localized heating of Au-nanoparticles hydrogels, by illuminating a laser at plasmonic peak of Au, induced the remote release of encapsulated polymers by structural transition of temperature-responsive the gel matrix. In addition to Au nanoparticles, magnetic nanoparticles also have been incorporated into a hydrogel matrix for drug release applications. Gels containing ferromagnetic nanoparticles, such as iron, nickel, and cobalt, can be heated up by applying alternating magnetic field with high frequency. A local rise in temperature around the magnetic nanoparticles induces a thermosensitive response in the surrounding hydrogel matrix, which could be used for remote drug-delivery systems. Beside drug delivery applications, the local heating of hydrogel nanocomposites is also of particular interest for biosensors, soft robotics, and nanomotors.¹⁴⁵

Other hydrogel nanocomposites

Other nanomaterials such as graphene oxide (GO) and metal oxide also can be incorporated into hydrogels. GO with hydroxyl functional group on its aromatic backbone can form a stable aqueous suspension.⁷⁰ It was reported that a hydrogel containing GO exhibited a 4.5 times increase in tensile strength and 30 times enhancement in elongation compared to pure hydrogels.¹⁴⁶ Furthermore, electrical conductivity can be provided to the materials by converting electrically insulating GO to conductive reduced GO within a hydrogel matrix, followed by freeze drying.^{147–}

¹⁴⁹ The resultant nanocomposites with porous 3D structure as well as electrical conductivity could be used for energy storage, catalysis, and sensor applications.¹⁵⁰ Recently, hydrogels containing titanate nanosheets were developed by exposure to UV light.¹⁵¹ Here, titania was used as a photocatalytic crosslinker for forming hydrogels. When titanate aqueous suspensions are exposed to UV light, photoexcited titanate materials generate an electron–hole pair. Hydroxyl radicals induced by the electron–hole pair causes a radical polymerization of the monomer (N-isopropylacrylamide). The resultant titania nanosheets hydrogels showed a change in optical transmission based on temperature. Optical transmission of the gels changed from 86% to 0% as temperature increased from 32 °C to 34 °C. This result was attributed to dehydration and aggregation of polymer chains at 34 °C. Carbon nitride (CN) or boron nitride (BN) based hydrogels were also reported recently.^{152,153} After functionalization of CN or BN nanomaterials, they can form a stable dispersion. Similarly, the gelation of the colloidal suspension results in CN or BN hydrogel nanocomposites. The dispersed CN or BN nanoparticles provided mechanical toughness to the nanocomposites.

Anisotropic hydrogel nanocomposites

In addition to isotropic hydrogel nanocomposites, anisotropic hydrogel nanocomposites have attracted attention for actuator and biomedical applications.^{154,155} The simplest approach for producing anisotropic hydrogel nanocomposites is the gelation of a pre-oriented nanoparticle suspension in an aqueous medium. For orientation of nanoparticles before gelation, external stimuli such as shear, electric, or magnetic fields can be applied as shown in Figure 2-28. Oriented nanoparticles trapped within a hydrogel matrix can provide anisotropic mechanical, electrical, optical, and swelling properties to the hydrogels. Miyamoto et al. demonstrated oriented clay hydrogels within a glass capillary tube.¹⁵⁶ Shear force applied to gel precursor while it was loaded into the glass capillary resulted in hydrogels with oriented clay nanoparticles. The resultant gels exhibited anisotropic thermosensitive volume change and ionic conductivity parallel to the clay orientation direction. Inadomi et al. synthesized anisotropic clay hydrogels by orienting fluorohectorite clay nanoparticles in poly(N-isopropylacrylamide) (PNIPA) aqueous solution by applying an external electric field.¹⁵⁷ The hydrogel nanocomposites showed temporal expansion parallel to the direction of nanoparticle alignment when the gel was exposed to the visible light.

Aida's group showed magnetically oriented GO within a hydrogel.¹¹⁵ 2D SAXS patterns of the hydrogel revealed that the aromatic ring planes of GO were oriented parallel to magnetic field direction. They also mentioned that GO dispersion with an average size of 50 μm showed higher orientation than that of GO with an average size of 0.3 μm . Aida's group also reported magnetically oriented titanate and niobate nanosheets in hydrogels.^{158,159} Interestingly, the 2D plane of titanate nanosheets cofacially oriented perpendicular to an applied magnetic field while niobate nanosheets oriented parallel to the magnetic field. Hydrogels with cofacially oriented titanate fillers showed significant anisotropy in mechanical strength and optical transparency. The optical transparencies of anisotropic titanate hydrogel nanocomposites according to different direction and corresponding X-ray diffraction results are shown in Figure 2-29.

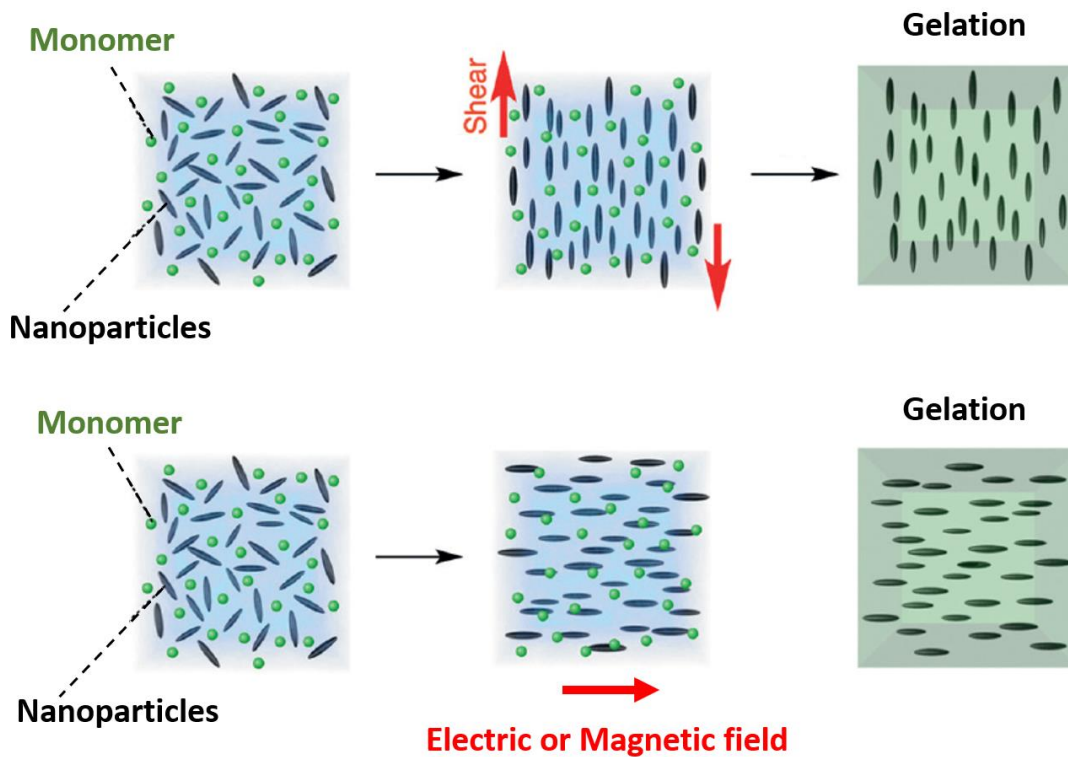


Figure 2-28. Synthesis of anisotropic hydrogel nanocomposites by using shear forces, or magnetic or electric fields (Reprinted from Ref. 160 with permission from John Wiley & Sons, Inc.).

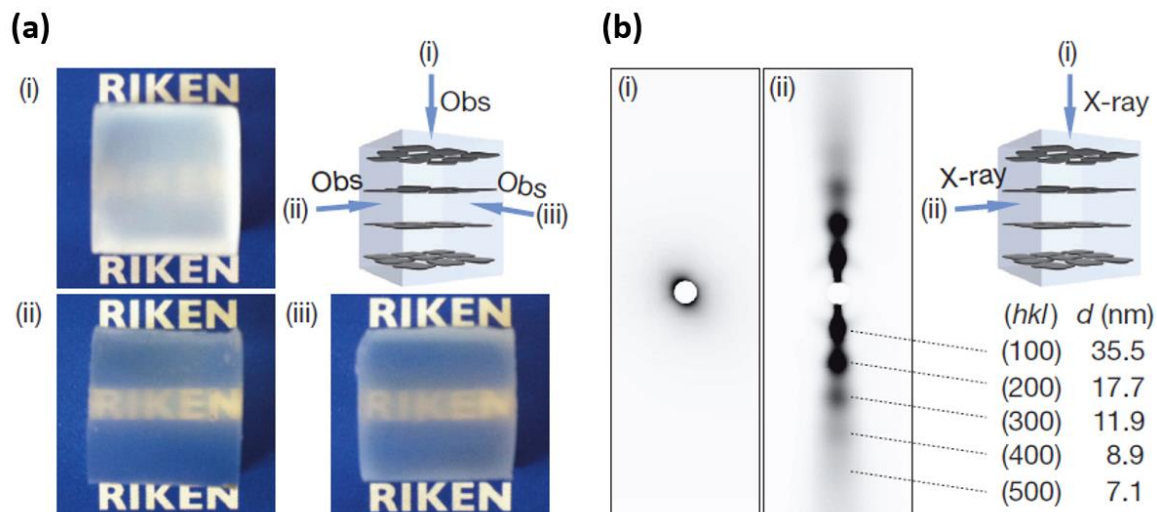


Figure 2-29. (b) Optical transparency of titanate nanosheets hydrogel (TiNS: 0.4 wt%) along orthogonal (i) and parallel (ii and iii) directions to the magnetically oriented TiNS plane. (b) 2D SAXS pattern of the titanate nanosheet hydrogel (TiNS: 0.6 wt%), where the illuminating X-ray beam was orthogonal (i) and parallel (ii) to the magnetically oriented titanate nanosheets (Reprinted from Ref. 158 with permission from Springer Nature).

3. ANISOTROPIC PHASE-SEPARATED MORPHOLOGY OF POLYMER BLENDS DIRECTED BY ELECTRICALLY PRE-ORIENTED CLAY PLATELETS

In this chapter, temporal evolution of phase-separated morphology of PS/PVME blends was studied in the presence of electrically pre-oriented clay platelets. Many of the previous studies demonstrated the effect of external fields or nanoparticles on blend morphology. Here, we studied the morphological evolution of polymer blends in the presence of electrically pre-organized nanoparticles while phase separation took place. The morphological change from a co-continuous to directionally oriented structure in a polymer blend was observed over time, along with the direction of pre-oriented clay platelets. An anisotropic phase-separated morphology of the blend by means of oriented nanoparticles suggests new approach to developing anisotropic morphology, which could be designed for the internal structure of proton-exchange membranes or photovoltaic cells. This chapter contains contents reproduced from Ref. 161 with permission from The Royal Society of Chemistry.

3.1 Introduction

Control of morphology in a polymer blend is essential, as the properties of the polymer blends are highly dependent on their morphology.^{56,162} The development of the desired nano-/micro-structures in block copolymers, partially miscible polymer blends, and immiscible homopolymers has been widely demonstrated. Among the different types of morphologies, the globally well-oriented morphologies are an ideal structural motif, particularly for enhancing desired functional properties such as proton conductivity in a proton-exchange membrane¹³² or efficiency in an organic photovoltaic cell¹⁶³ in the desired direction. However, the directionally oriented morphology in immiscible polymer blends is difficult to achieve because the phase separation generally occurs isotropically in the absence of external forces.

To produce oriented morphology in polymer blends, shear,^{164,165} electric,^{125,126,166,167} or magnetic¹³⁶ forces can be applied. The use of shear field during phase separation usually leads to the formation of a string-like phase-separated morphology, with the primary axes oriented along the flow direction. This deformation of polymer fluids is due to the softening of interfacial tension between two fluids at high shear rate. Beside shear fields, external electric field can be used to

produce anisotropic structures. When an electric field is applied to binary fluids, electric stresses are produced at fluid–fluid boundaries due to the difference in electrical properties of two fluids.^{168,169} The shape of binary morphology in the electric field is determined by the balance between electric stress and interfacial tensions of two polymeric fluids. Krause et al. showed the anisotropically phase-separated morphology of two immiscible polymers under electric field during phase separation induced by solvent removal.^{126,166,167} They found the columnar structures of PMMA domains in a PS domain while a common solvent of two polymers (toluene) was evaporated. Despite an anisotropic phase-separated morphology, the final morphology in this study was not only influenced by the electric field, but also by solution drying kinetics. During polymer-solution drying, the rapid solvent evaporation from the top surface of the film generates inhomogeneity in solvent concentration in the film. Furthermore, the solvent generally prefers one of the components in the blends. These two effects can lead to a nonuniform component distribution along the film thickness direction during drying.^{170,171} Thermally induced phase separation of partially miscible polymer blends is a better alternative method to avoid the problems caused by solvent drying.

Urakawa et al. examined the morphology of a partially miscible polymer blend near critical temperature under electric field.¹²⁵ They observed anisotropic phase-separated poly(2-chlorostyrene) (P2CS) and poly(vinyl methyl ether) (PVME) morphologies when lithium perchlorate (LiClO₄) was dissolved in the blend. The role of LiClO₄ in the blends was to enhance the difference in electrical properties of the two polymer phases. They reported that P2CS and PVME domains were oriented parallel to the electric field direction in the process of phase separation.

Adding compatibilizers in polymer blends is another way to control the morphology in polymer blends. Surface-tailored nanoparticles,^{90,95,172–174} block copolymers,^{175–177} and organically modified clay platelets^{83,84,87,178–180} in a binary blend have been considered effective compatibilizers. It has been reported that the compatibilizers stabilize the morphologies of immiscible blends by reducing interfacial tension via interfacial localization or increasing viscosity of the blends.⁸⁴ Moreover, some colloidal particles even freeze in the nonequilibrium co-continuous structure of blend morphology by aggregating at the interface, and ultimately lead to a stable co-continuous morphology called a “bijel”.^{90,91,93–95,174} Although the morphology of the

blends can be stabilized by adding compatibilizers, the anisotropic morphology is still hard to achieve due to the intrinsically isotropic demixing of polymer blends.

From this viewpoint, the presence of well-oriented particles in polymer blends may influence the phase separation mechanism by directionally affecting the diffusion process by their presence. If they are organized to create large barriers, the effect of particles on the phase-separated morphology would be further amplified. Organically modified clay platelets are good candidates for forming particle barriers, as they exhibit 2D platelet shapes. They are also easily aligned in an AC electric field due to high polarizability^{44,46,47} on the surface of particles. Therefore, we hypothesize that the clay platelets, having large 2D surface area and high polarization under electric fields, can be applied to develop anisotropic morphology in blends.

In the current study, we report a novel approach to produce anisotropic phase-separated morphology in a bulk polystyrene (PS)/poly(vinyl methyl ether) (PVME) blend near the critical temperature as directed by pre-oriented clay platelets in AC field. The evolution of morphology at near-critical composition from co-continuous structure to coarsened anisotropic structure was investigated with microscopes and X-ray scattering techniques at different annealing times and electric field strengths.

3.2 Experimental section

3.2.1 Materials

PS (Mw: 35kg/mol) was purchased by Sigma Aldrich and used as received. PVME (Mw: 30 kg/mol) was purchased from Polysciences Inc. as a 50 % aqueous solution. The residual water in the PVME material was removed by drying the solution overnight at 120 °C in vacuum oven before usage. The organically modified montmorillonite clay (Cloisite 15A) was provided by BYK Additives & Instruments.

3.2.2 Phase diagram

PS and PVME at a series of blend ratios were dissolved in toluene and casted on a cover glass at room temperature. The samples were dried overnight at 110 °C in a vacuum oven to remove residual toluene solvent. Cloud points of the blends were determined by optical

microscope (OM) observation on the heating stage. The temperature of the heating stage was stepwise increased 1 °C every 5 min until phase separation was observed under OM.

3.2.3 Sample preparation

PS and PVME (50/50) homopolymers were dissolved in toluene by a planetary centrifugal mixer (Thinky Mixer) for 1 h. After achieving a homogeneous polymer solution, the 5 vol% of clay platelets (with respect to the polymer) were dispersed in the polymer solution by Thinky Mixer for 3 h. The sample was cast on a glass side between two copper electrodes (100 μm thickness and 50 mm length) with a 4 mm gap to create films with 40 μm –60 μm final thickness. The AC electric field was applied to the sample with an initial viscosity of 0.98 Pa·s (Figure 3-1). The AC field, ranging of from 0 V/mm to 1000 V/mm at 100 Hz, was generated by a high-voltage amplifier (Matsusada, AMT-20B10-LC) and a function generator (HP, 33120A). During the application of the AC fields to the samples, toluene was gradually evaporated at room temperature. The electrically oriented clay fillers in the blends were immobilized as the sample were solidified. To remove residual toluene completely, the samples were dried in a vacuum oven at room temperature for a week. The PS–PVME phase-separation was induced for the samples on a 128 °C hot plate (4 °C above critical temperature) with N₂ gas purging in the presence of AC fields. The samples were annealed for different time from 5 min to 120 min. The identical AC field strength was applied for both the drying and annealing process. The control samples without AC field were prepared under the same conditions. Overall sample preparation steps are shown in Figure 3-2. We mainly investigated a PS/PVME (50/50) blend with 5 vol% clay platelets throughout the study.

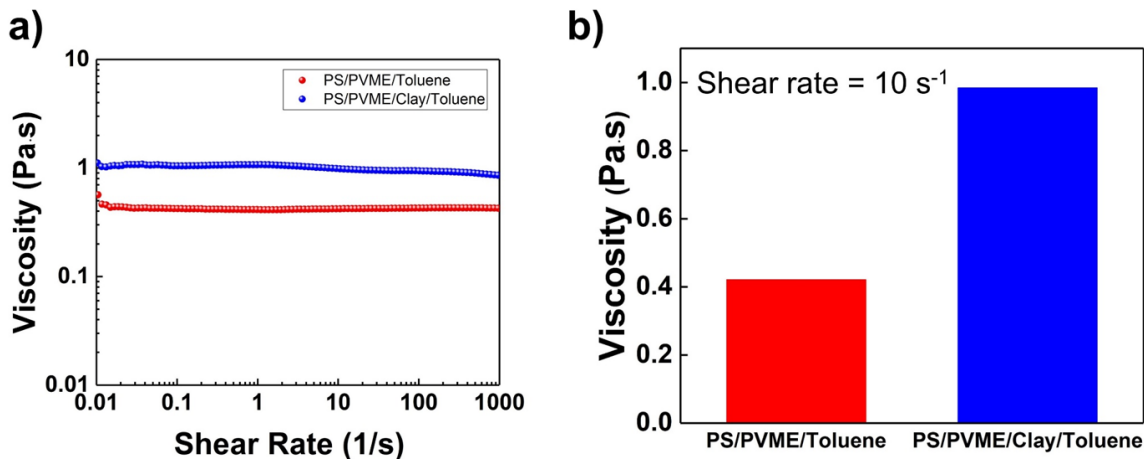


Figure 3-1 (a) Viscosity of PS/PVME/toluene sample with and without 5 vol% clay fillers.(b) Viscosity at 10 s⁻¹ shear rate.

3.2.4 Morphological analysis

The orientation of clay platelets in a PS/PVME blend (single phase) was examined by a polarized optical microscope (POM) (Leitz Laborlux 12 Pol S) equipped with a CCD camera. The sample was placed between two crossed polarizers with a first order red wave plate (λ) at 45° to the crossed polarizers. The optical anisotropy from the sample was characterized by observing interference colors in the Michel-Levy color chart at every 45° rotation. The phase-separated morphology of PS/PVME blends was examined by OM (Leitz Laborlux 12 Pol S) (top view) and by scanning electron microscope (Hitachi S-4800 Field Emission SEM) (cross-sectional view). The direction of imaging morphology and the corresponding direction of the application of the AC electric field were shown in Figure 3-2c. To observe cross-sectional morphology, the sample with ~50 thickness was fractured in liquid nitrogen. The PVME phase on the cross-sectional plane was selectively extracted by immersing the sample in the methanol overnight. The remaining PS morphology was visualized by SEM after the samples were sputter-coated with 9 nm of Au/Pd. An accelerating voltage of 3 kV with an 8 mm working distance was used for SEM characterization. For WAXS experiments (Anton Paar SAXSpoint 2.0), an X-ray beam with monochromatized to Cu K α radiation was used. An X-ray beam orthogonal to the applied AC electric field (Figure 3-2c, top view direction) was applied to the samples. The sample to detector distance was 363 mm and X-ray exposure time was 5 minutes for each sample. The azimuthal plots of X-ray scattering pattern were constructed by integrating the scattering intensity from $q = 0.7 \text{ nm}^{-1}$ to $q = 2 \text{ nm}^{-1}$ for

every 1° by using SAXS analysis software offered by Anton Paar. For the sample of TEM experiment, the cross-sectional samples were prepared by using a cryo-microtome (Leica UCT ultramicrotome with EMFCS cryo attachment). Ultrathin sections between 100 nm to 150 nm were cut on a diamond knife at -60 °C at a speed of 1.0 mm/s and collected on 100 mesh formvar/carbon coated double-folding grids. TEM images were obtained using a FEI Talos 200 S/TEM transmission electron microscope operated at an accelerating voltage of 200 kV. For AFM sample preparation, the bulk film was embedded in an epoxy resin for microtubing. The epoxy block containing sample was microtomed with a diamond knife in the cross-sectional direction at room temperature. AFM (Veeco Dimension 3100 atomic force microscope) with tapping mode was used to characterize the surface of the cross-sectioned sample.

3.2.5 Image analysis

The characteristic domains size (ξ) of continuous PS and PVME domains was determined by the image analysis software (ImageJ). The OM images were transformed to black and white binary images by highlighting the interface between two polymers. The interfacial length (L) was calculated by adding the length of interfacial lines. We defined the characteristic domains size (ξ) as total areas (A) over interfacial length (L) ($\xi = A/L$).⁹⁴

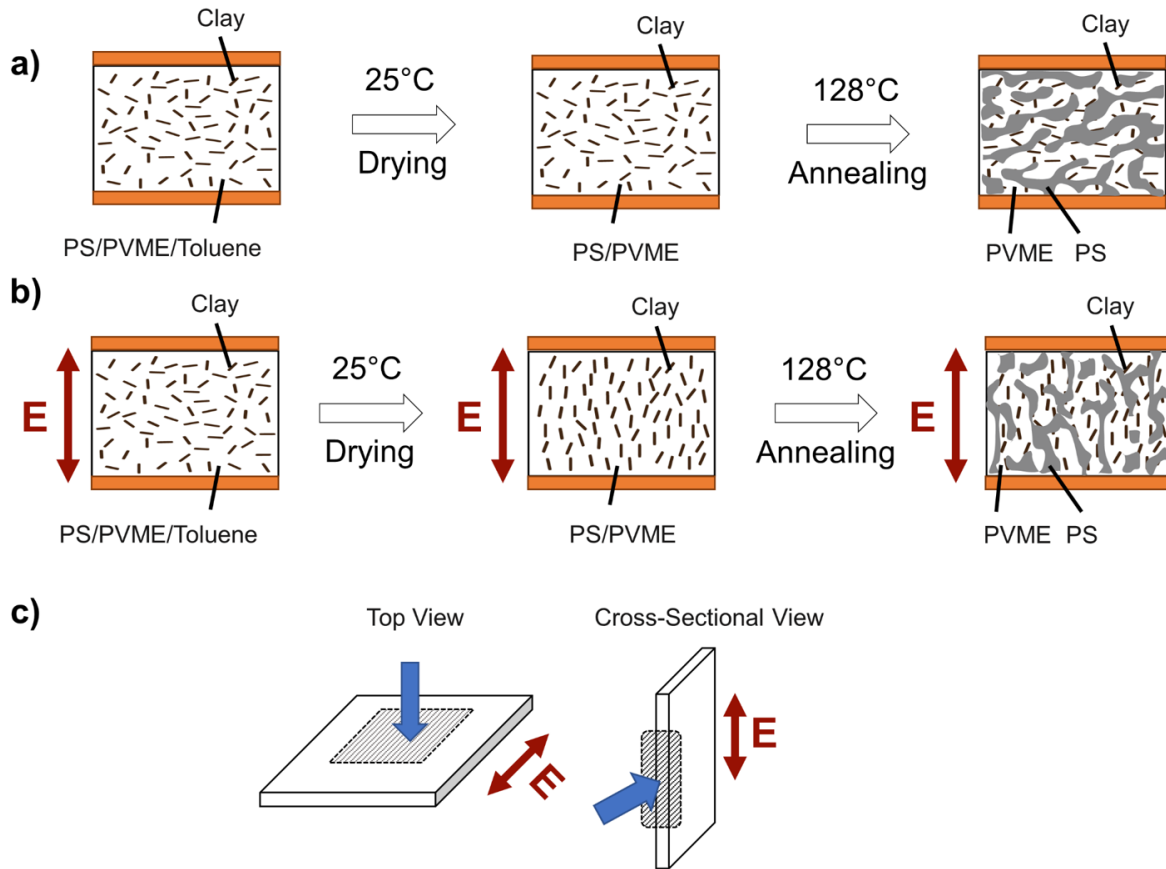


Figure 3-2 Schematic illustration of the sample preparation process (a) without electric fields and (b) with electric fields. (c) Direction of top and cross-sectional view of the films for investigating blend morphologies along with AC field direction.

3.3 Results and discussion

Phase Diagram

The phase diagram of the PS/PVME blend used in this study is shown in Figure 3-3. The blend shows a typical lower critical solution temperature (LCST) system, where the critical temperature of the blend is 124 °C at 50/50 concentration. Since the presence of particles and/or AC electric fields may affect the critical temperature of the blend, we reviewed the relevant previous reports about the effect of nanoparticles and/or electric fields on the phase diagram. It was reported that the addition of 4 vol% layered silicate in the PS/PVME blend does not affect the

phase diagram.¹⁸⁰ However, high electric field may shift the phase separation temperature in a partially miscible polymer blend. Kriisa and Roth showed that the shift in phase separation temperature ($\Delta T_s(E) = T_s(E) - T_s(0)$) is proportional to the square of the applied electric field (E^2).^{181,182} They found that the shift in the critical temperature of a PS/PVME blend is followed by $\Delta T_s/E^2 = (4.8 \pm 0.4) \times 10^{-14} \text{ Km}^2/\text{V}^2$.¹⁸² Based on this equation, the maximum electric field in this study (1 MV/m) shows ΔT_s is about 0.048 K. Therefore, we considered that the presence of 5 vol% platelets or the application of the electric field less than 1 kV/mm would not significantly alter the critical temperature in our experimental system.

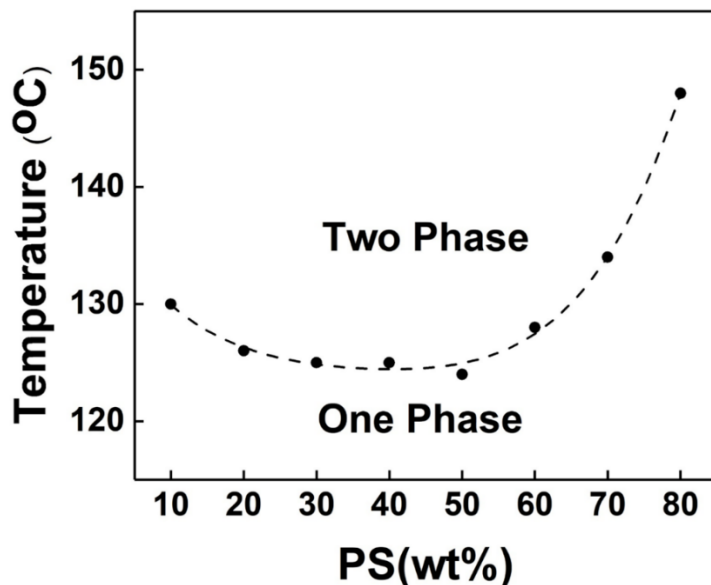


Figure 3-3 Phase diagram of a PS/PVME blend. The blend shows a LCST behavior with a critical temperature of 124 °C at 50/50 composition.

Homogeneous single-phase morphology

Prior to study the phase-separated morphology of the blend, the electrically orientated clay platelets in a homogeneous single-phase PS/PVME blend was examined. The polymer films with electrically oriented clay nanofillers exhibited optical anisotropy due to intrinsic birefringence ($\Delta n^0 = \Delta n^{\circ\perp} - \Delta n^{\circ\parallel} = -0.02$) of clay nanofillers as they have refractive indices of 1.55 and 1.57 along the in-plane and out-of-plane direction, respectively (Figure 3-4b)⁴⁷. POM with a λ plate is

a simple technique to examine birefringent samples by checking interference colors in the Michel-Levy color chart. The role of the λ plate (slow axis), which was inserted in 45° to polarizer and analyzer, is to add a 553 nm optical path difference to all light paths under POM. This path difference produces the violet background POM image corresponding to 553 nm retardation when there is no other retardation by sample, where clay platelets were oriented either parallel or perpendicular to the polarizer. When clay platelets were oriented parallel or perpendicular to slow axis (45° lambda plate direction), however, the phase differences (i.e., retardation) was added or subtracted. A higher polarization color (purple) appeared when the basal plane of clay platelets was oriented parallel to slow axis. In contrast, a lower retardation color (red) appeared when that of clay platelets was oriented to perpendicular direction of the slow axis. The Michael-Levy interference color chart shows gradient colors as birefringence increases (Figure 3-4b). The POM images of the sample with oriented clay nanofillers exhibited color contrast (violet \rightarrow purple \rightarrow violet \rightarrow red) at every 45° rotation (Figure 3-4a).

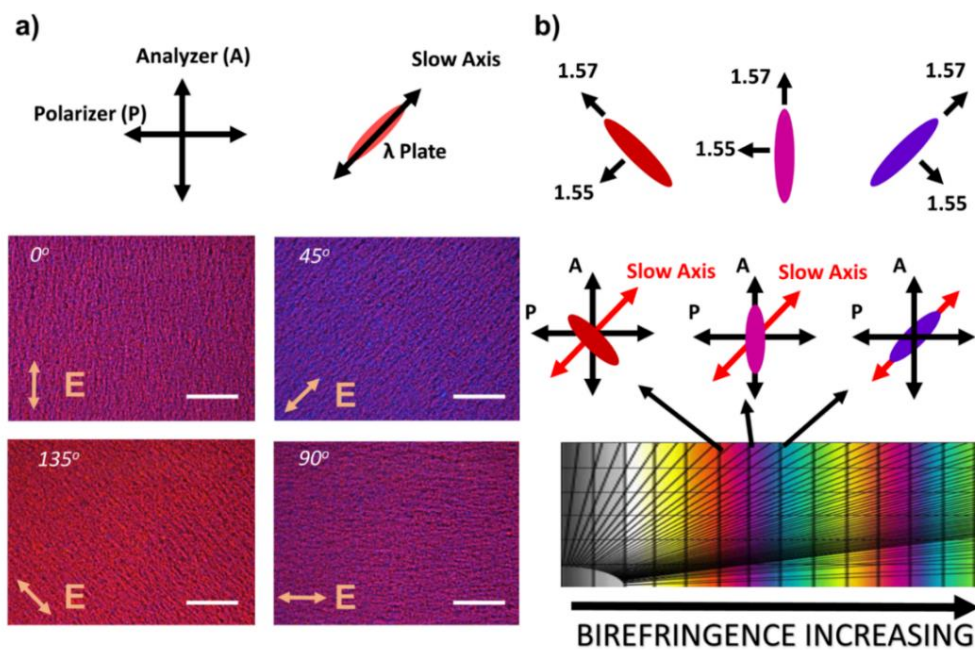


Figure 3-4 (a) POM images (top view) with a first order lambda (λ) plate of a PS/PVME (50/50) blend containing 5 vol% oriented clay nanofillers. Clay nanofillers were oriented to the AC field direction in a single-phase PS/PVME blend after drying with AC field (1000 V/mm, 100 Hz) at room temperature. POM images were acquired by rotating the sample every 45° counterclockwise. (b) Refractive index of clay nanoplatelets and corresponding interference color chart (scale bar: 100 μm).

The surface morphology (top-view) of the sample containing electric field-oriented clay nanoparticles was investigated by AFM prior to the phase separation process. AFM phase-mode imaging can distinguish two materials with different mechanical moduli such as stiff clay nanoplatelets on soft polymer surface. PS and PVME phases were not distinguishable in AFM images. Figure 3-5a shows dispersed clay nanoplatelets (white color) found on polymer surface (yellow color) along with the direction of AC field (500 V/mm, 100 Hz). The formation of columnar structures of clay nanoparticles was found on the polymer film in the $25\ \mu\text{m} \times 25\ \mu\text{m}$ AFM phase image. They formed parallel to AC field direction as marked with red arrows on the AFM image. The magnified AFM phase images indicate that clay particles were each a cluster of tens of individual clay nanoplatelets (Figure 3-5b and 3-5c). Figure 3-5c shows a clay cluster with a size of 1–2 μm composed of around 30 individual clay nanoplatelets with lengths of around 50–300 nm. The individual clay nanoparticles with irregular shapes of edges were aggregated with each other. The results indicate that the clay nanoparticles were not completely exfoliated in the polymer blends and the clay clusters tended to be oriented parallel to AC field direction with a 500 V/mm field strength.

To investigate the internal morphology of clay nanoparticles in the sample, the top surface was slightly etched by methanol and investigated by AFM. Figure 3-6 shows the AFM phase image of the sample prepared with an AC field (1500 V/mm, 100 Hz) after surface etching. The rough surface in AFM image indicates the surface of the sample was not uniformly etched (Figure 3-6a). Analogous to unetched samples, clay clusters were observed in AFM phase images. Clay clusters with a size of 1.5 μm were composed of aggregated clay nanoparticles. The alignment of the clusters parallel to the AC field was not significant compared to that observed in unetched sample (Figure 3-6b). High aggregation and low degree of field-assisted alignment may be due to high viscosity near the bottom of the sample during solution drying. During polymer solution drying, the bottom surface region is relatively more viscous because top surface region contains higher amount of volatile solvent.^{170,171} Furthermore, the precipitation of clay particles by gravity may increase the aggregation of clay particles near the bottom surface of the sample.

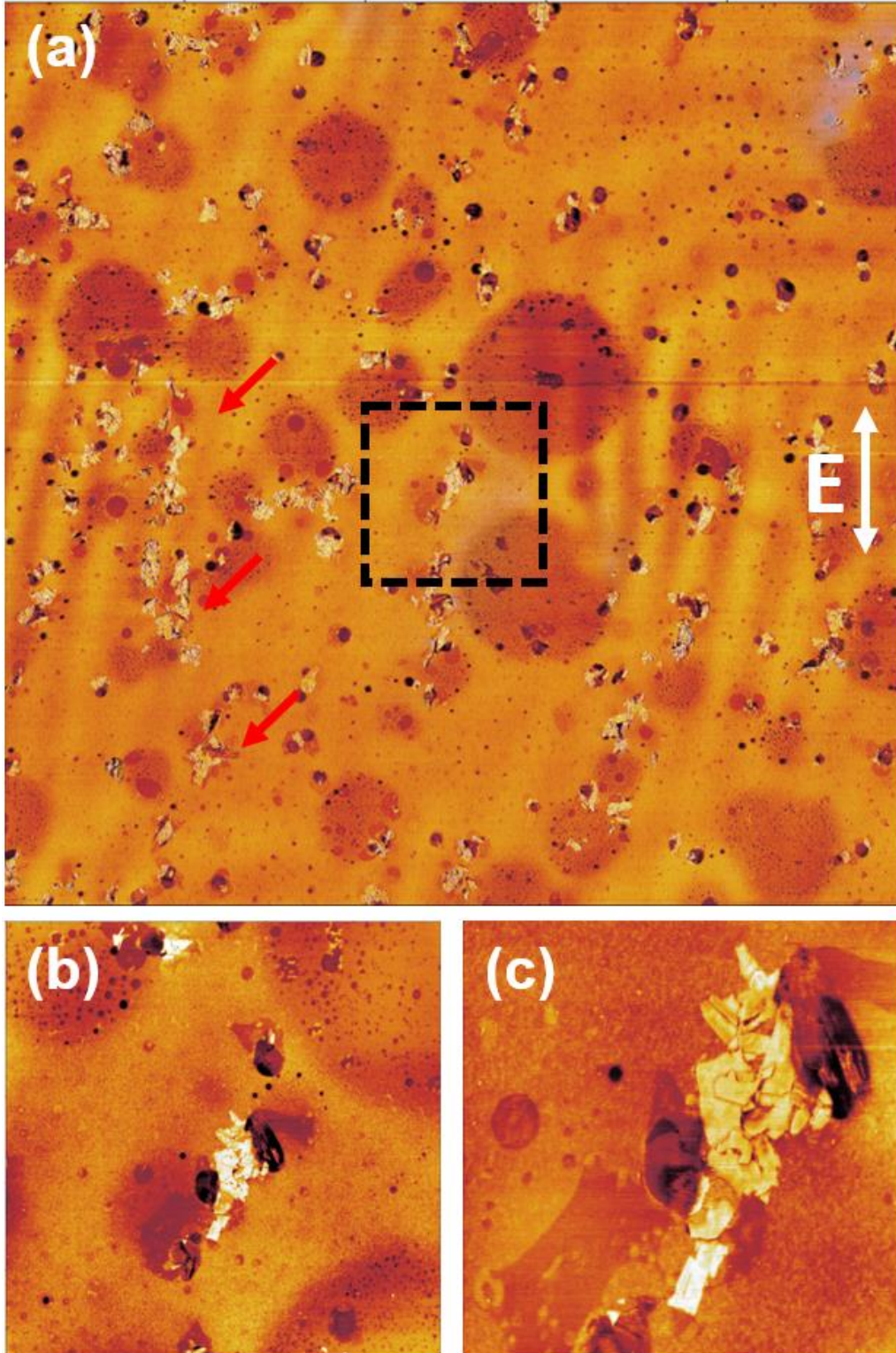


Figure 3-5. AFM phase image of the sample (5 vol% of clay particles) prepared with a 500 V/mm of AC field. (a) $25\ \mu\text{m} \times 25\ \mu\text{m}$, (b) $5\ \mu\text{m} \times 5\ \mu\text{m}$, and (c) $2\ \mu\text{m} \times 2\ \mu\text{m}$ images. The region of black dotted square in (a) is corresponding to (b) image.

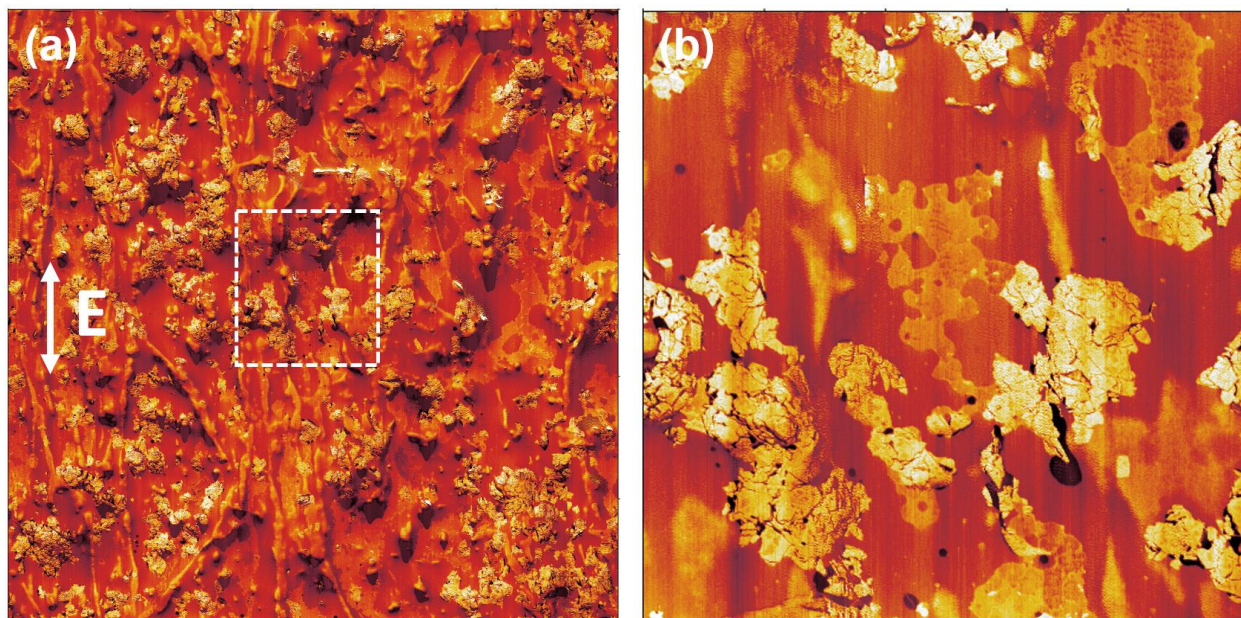


Figure 3-6 (a) $25\ \mu\text{m} \times 25\ \mu\text{m}$ AFM phase image of the sample (5 vol% of clay particles) prepared with 1500 V/mm. (b) Magnified $5\ \mu\text{m} \times 5\ \mu\text{m}$ AFM phase image of the region of a white dotted square in (a). The surface was slightly etched by methanol.

Two-phase PS/PVME morphology

To investigate the temporal morphological evolution of a neat PS/PVME blend in absence of both AC field and nanofillers, the morphology of a PS/PVME (50/50) blend was examined to understand the emerging morphology near critical composition. When a partially miscible polymer blend undergoes spinodal decomposition by crossing phase boundary of the phase diagram at near-critical compositions, isotropic composition fluctuations appear with characteristic length (λ). These isotropic composition fluctuations yield a co-continuous structure at the early phase separation stage and the disordered co-continuous two-phase structure grows exponentially with time.^{56,183} The neat PS/PVME (50/50) blend clearly exhibited co-continuous structure in the early stage as shown in Figure 3-7.

Due to difference in refractive index of each polymer ($n_{\text{PS}}: 1.592$, $n_{\text{PVME}}: 1.467$), top-view images of co-continuous morphology was characterized under OM (Figure 3-7a–Figure 3-7c). The corresponding cross-sectional SEM images of the films also visualized PS domains after selectively etching PVME phase (Figure 3-7d–Figure 3-7f). The isotropic co-continuous structure was coarsened with increasing characteristic domain sizes (ξ) over the annealing time as indicated

by OM and SEM images. The isotropic composition fluctuations during the spinodal decomposition result in an isotropic phase-separated morphology.

To evaluate the effect of clay platelets in blends, we investigated the phase-separated morphology with non-oriented clay platelets over annealing time. The cross-sectional morphologies over time were shown in Figure 3-8. Although clay platelets were hard to distinguish with SEM, PS domains and etched domains (PVME domains) were clearly distinguishable after selectively dissolving the PVME phase. Figure 3-8b and Figure 3-8c show that the isotropic 3D co-continuous structure appeared at the early stage of a phase separation. The disordered co-continuous structure was coarsened isotopically over annealing time with increasing characteristic domain sizes (ξ) even though the rate of phase-separation slowed down in the presence of 5 vol% of clay platelets.

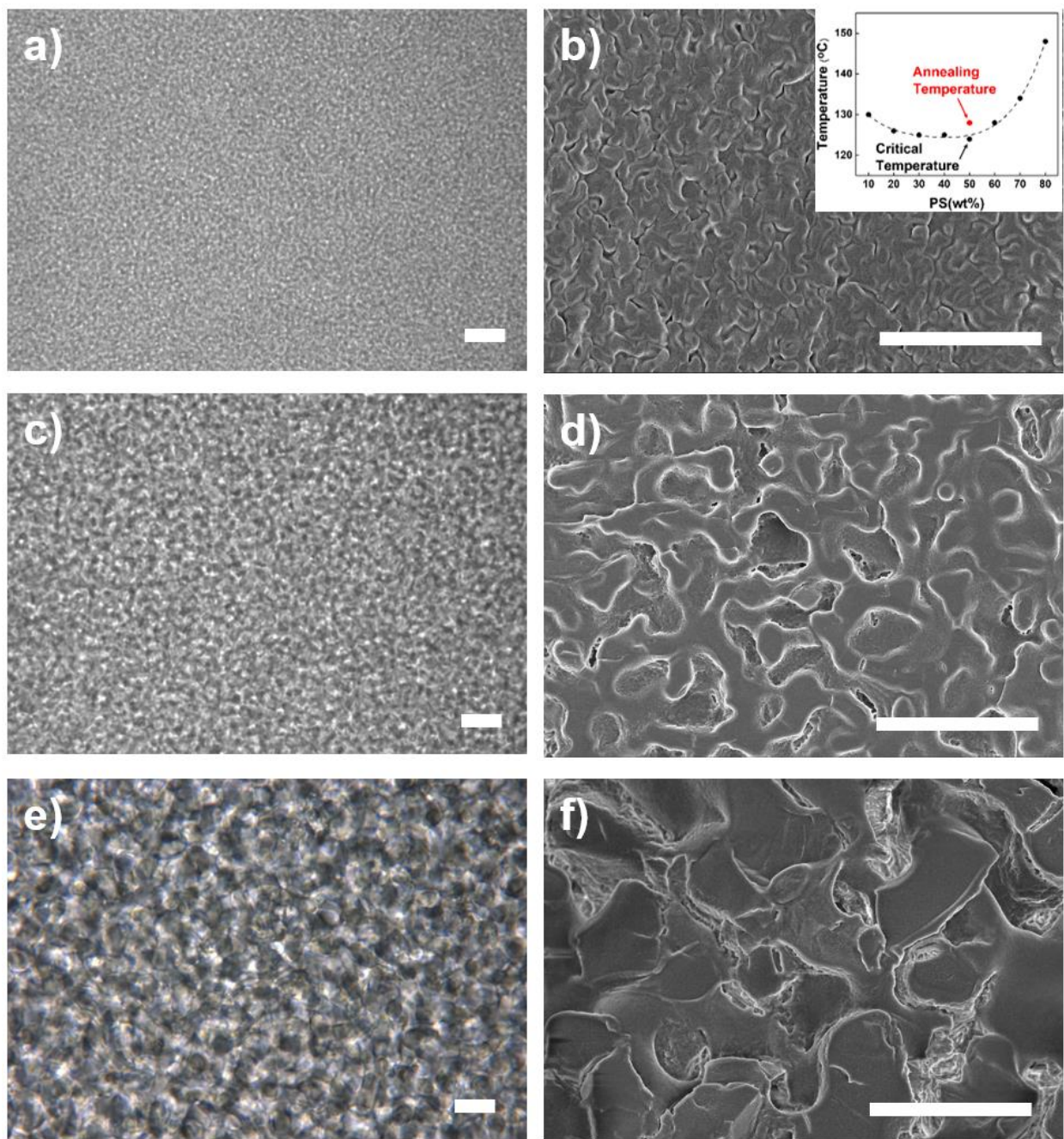


Figure 3-7 Phase-separated morphology of a neat PS/PVME (50/50) blend. Top-view OM images (a, c, e) and cross-sectional SEM images (b, d, f) annealed for (a, b) 5 min, (c, d) 7.5 min, and (e, f) 10 min at 128 °C. (Scale bar: 10 μ m) (Inset: Critical temperature (124 °C) and annealing temperature (128 °C) are indicated in the phase diagram of the PS/PVME blend.)

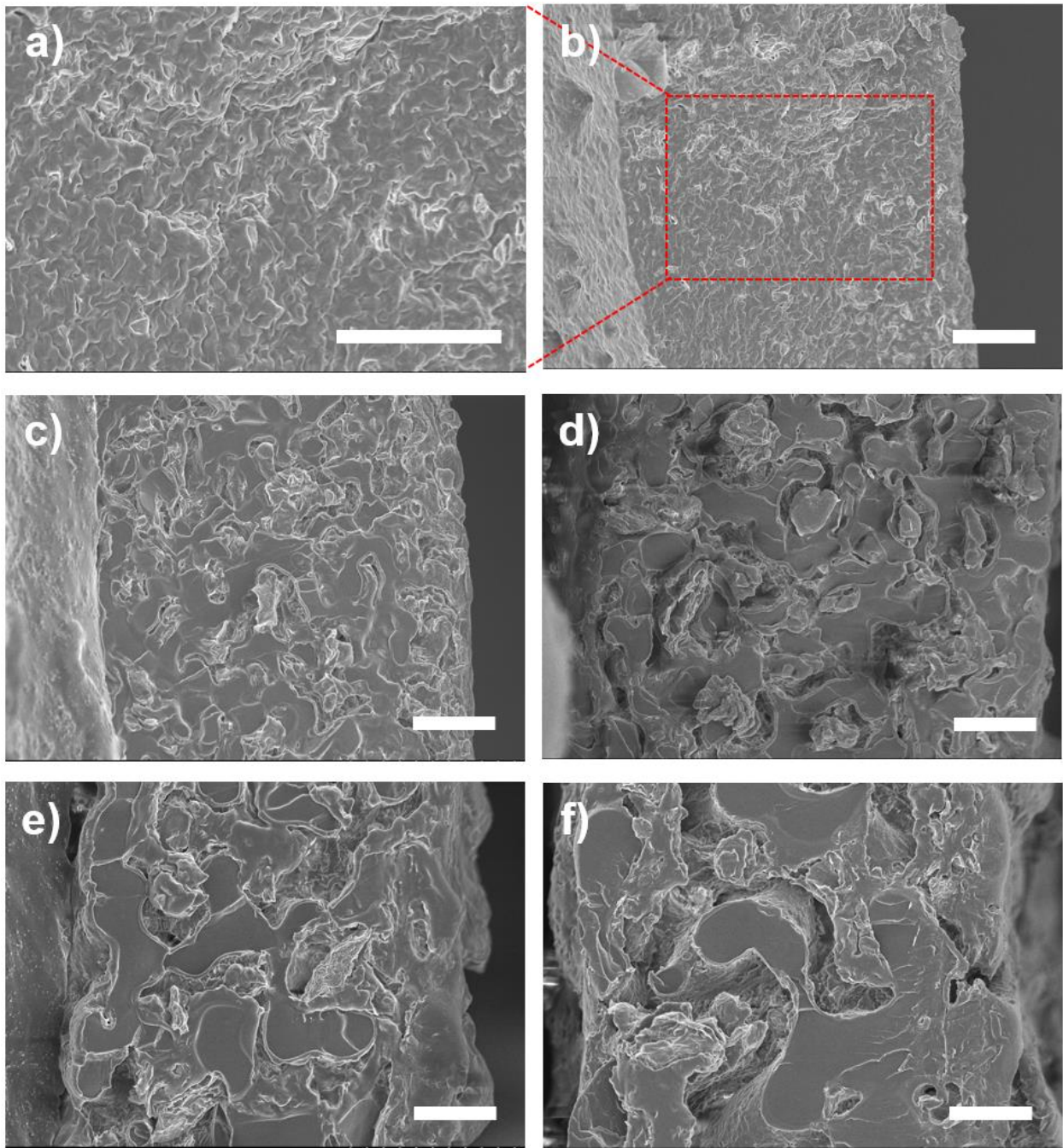


Figure 3-8 Cross-sectional SEM images of a PS/PVME (50/50) blend morphology with 5 vol% clay platelets annealed at 128 °C in the absence of AC field. Phase-separated morphology annealed for (a, b) 5 min, (c) 7.5 min, (d) 10 min, (e) 12.5 min, and (f) 15 min. (Scale bar: 10 μm)

With the electrically pre-oriented clay platelets (500 V/mm, 100 Hz), the evolution of morphology with time was observed to be quite different. The isotropic 3D co-continuous structure also appeared after 5 min annealing, similar to the morphology with non-oriented clay platelets (Figure 3-9a and Figure 3-9b). However, the morphology coarsened and was oriented by growth of PS domains along the AC electric field direction as the phase separation progressed (Figure 3-9c–Figure 3-9f). Figure 3-9f clearly shows that PS domains were elongated parallel to the AC field direction.

In order to verify that the orientation of polymer domains is not due to the difference in electrical properties between two polymers, we also examined the phase-separated morphology under the AC field without clay platelets. The PS/PVME blend was isotropically coarsened in the presence of AC electric field (500 V/mm, 100Hz) as shown in Figure 3-10. This result is attributed primarily to the small difference in electrical properties (i.e., dielectric constant and conductivity) between PS and PVME. The difference in dielectric constant of PS ($\epsilon \sim 2.5$)¹⁸⁴ and PVME ($\epsilon \sim 4.0$)¹⁸⁵ is small. The ionic conductivity of these materials also is negligible (PVME is around 10^{-10} – 10^{-11} S/cm and PS is around 10^{-12} – 10^{-13} S/cm).^{184,186} This small contrast in electrical properties may not create enough electrical and hydrodynamic stresses between two polymers at the AC electric field strength we used in this study (up to 1000 V/mm).

We also found that the degree of anisotropy in the phase-separated morphology was influenced by the concentration of the clay platelets (Figure 3-11). 1 vol% of clay platelets (500 V/mm, 100 Hz) in the blend developed an almost isotropic phase-separation morphology. As the concentration of clays increased to 2 vol%, a slight anisotropic morphology appeared, as evidenced by the 2D-FFT pattern shown in the inset of each optical microscopy image. Strong anisotropy of the phase-separated morphology was found in the blend with 5 vol%. This result indicates that at least about 5 vol% of clay platelet loading was needed to develop a highly anisotropic phase-separated morphology.

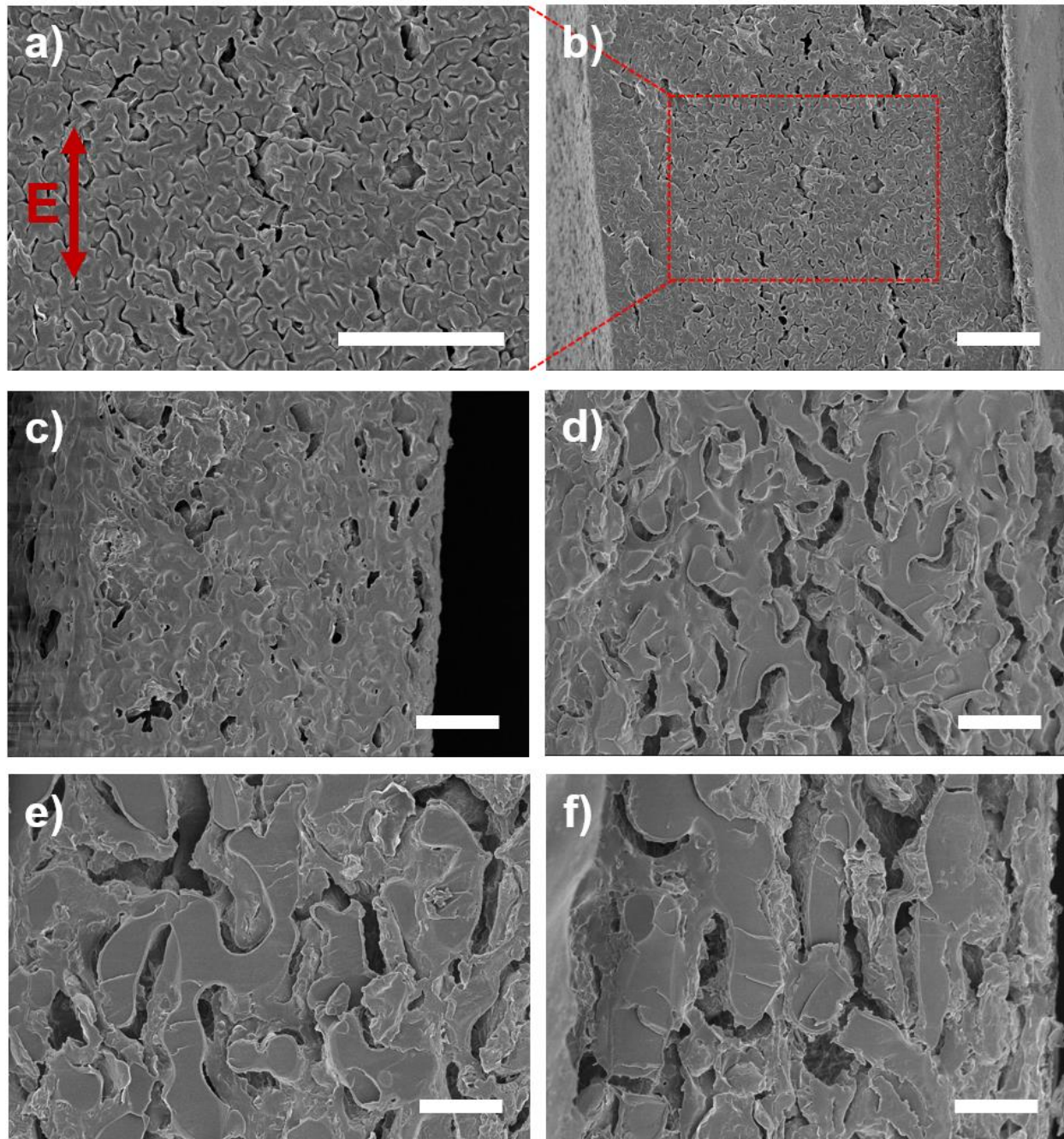


Figure 3-9 Cross-sectional SEM images of a PS/PVME (50/50) blend morphology with pre-oriented 5 vol% clay platelets annealed at 128 °C. The arrow indicates the AC field (500 V/mm, 100 Hz) direction. Phase-separated morphology annealed for (a, b) 5 min, (c) 7.5 min, (d) 10 min, (e) 12.5 min, and (f) 15 min. (Scale bar: 10 μm)

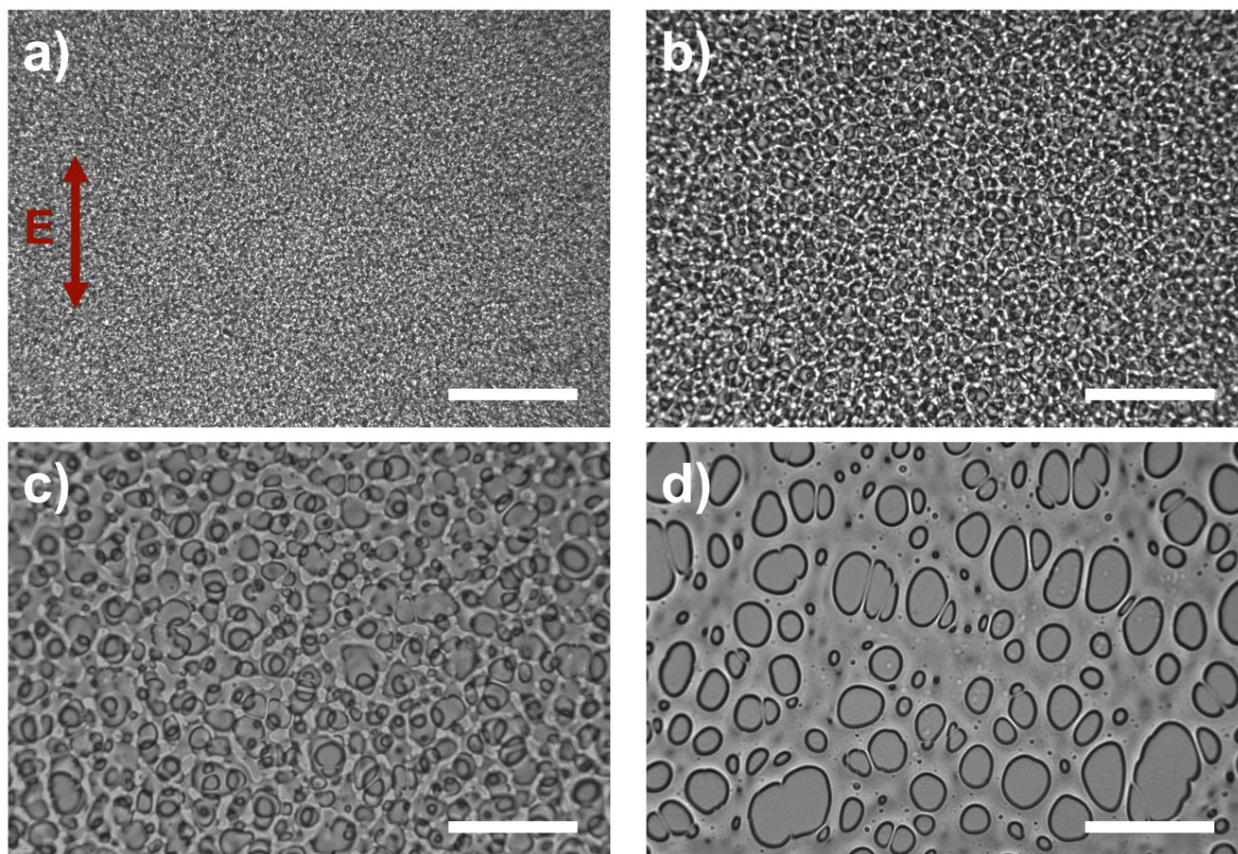


Figure 3-10 Optical microscope images (top view) of the PS/PVME (50/50) blend morphology with an AC electric (500 V/mm, 100 Hz) at 128 °C. The sample were annealed for (a) 10 min, (b) 15 min, (c) 17.5 min, and (c) 20 min. (Scale bar: 100 μ m)

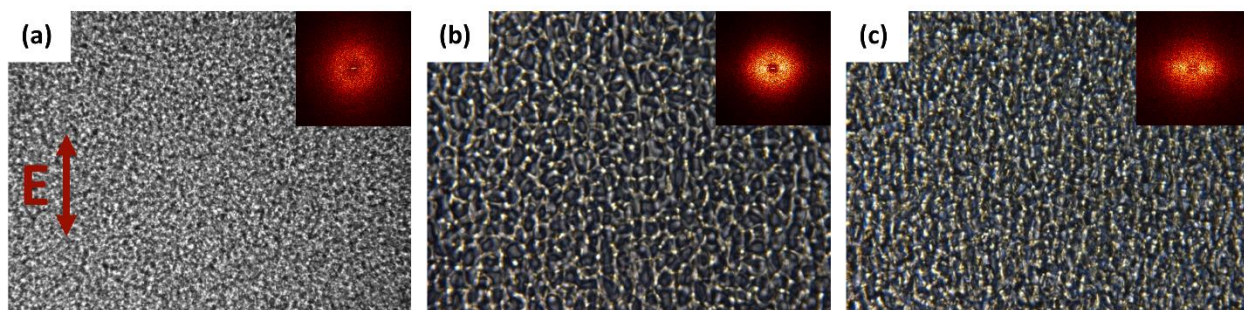


Figure 3-11 Optical microscope images (top view) of the PS/PVME (50/50) blend morphology with pre-oriented clay platelets at different clay concentrations. (a) 1 vol% annealed for 10 min, (b) 2 vol% annealed for 30 min, and (c) 5 vol% annealed for 30 min at 128°C. AC electric field (500 V/mm, 100 Hz) was applied for all the samples.

It is also worth noting that the presence of 5 vol% clay platelets in a blend significantly slowed down the rate of the phase separation process (Figure 3-12). The characteristic domain size (ξ) with annealing time can be characterized by the power law equation, $\xi(t) \propto t^\alpha$, where α is an exponent indicating the rate of phase separation.^{96,125} All data points of the neat blend sample were fit well by a power-law model with the high exponent ($\alpha = 2$). However, the data points of the sample containing 5 vol% clay cannot be fitted by the power-law model as the last two data points showed a plateau. The result indicates that there was a significant suppression of phase coarsening by 5 vol% clay platelets in the last stage of phase separation in either presence or absence of AC field.

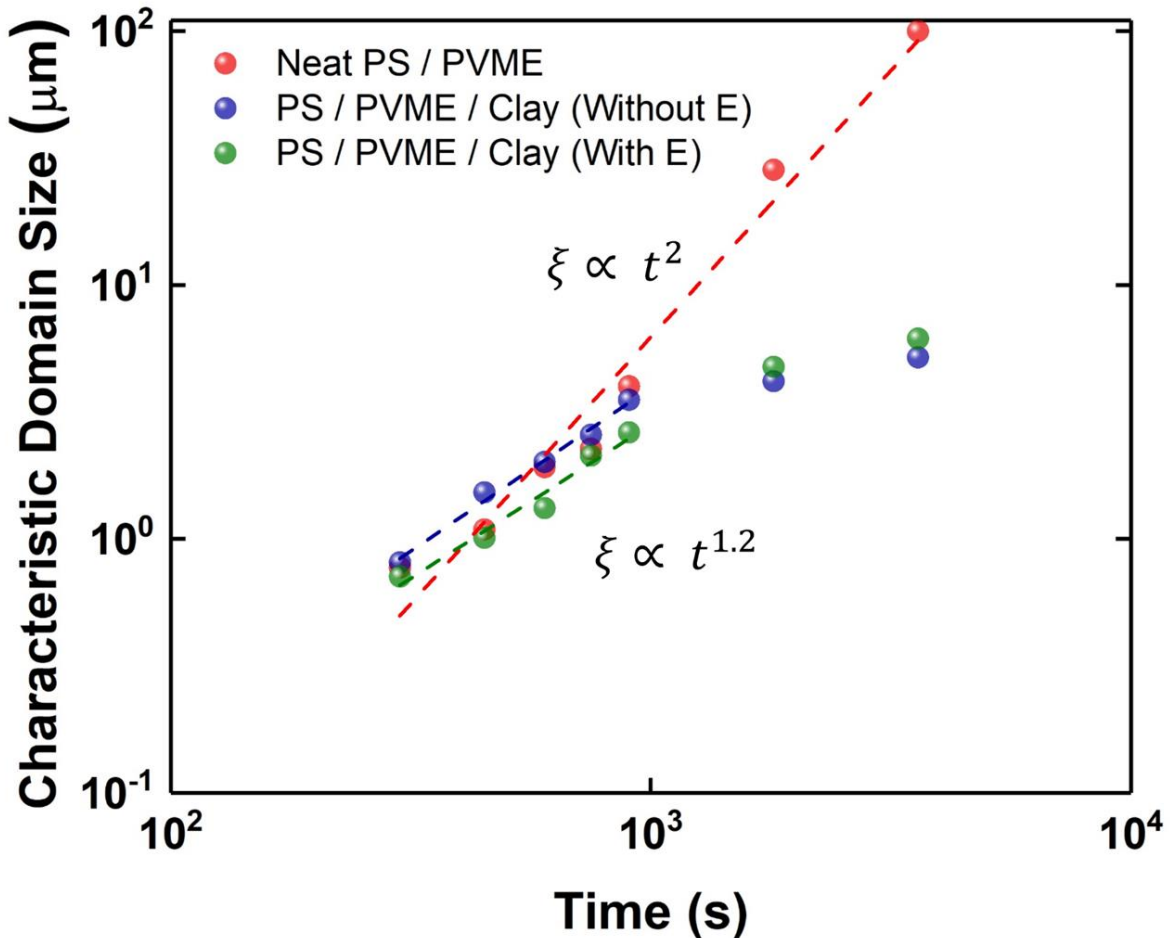


Figure 3-12 Characteristic domain size (ξ) over annealing time for PS/PVME (50/50) blends annealed at 128 °C. (Red: neat PS/PVME, blue: PS/PVME/non-oriented 5 vol% clay platelets, green: PS/PVME/pre-oriented 5 vol% clay platelets)

The anisotropic phase-separated morphology with oriented clay platelets more clearly appeared at the late stage of phase separation. Top-view OM images and cross-sectional SEM images showed the morphology with and without AC field after 30 min of annealing at 128 °C (Figure 3-13). The oriented and coarsened morphology clearly appeared for the sample containing 5 vol% oriented clay platelets (Figure 3-13a and Figure 3-13c). The PS phases (dark regions) in the OM image shows that PS domains tens of microns in size were elongated in the AC electric field direction in a PVEM phase. The corresponding elongated PS phases were also identified in SEM image (dark regions). On the other hand, the sample containing 5 vol% non-oriented clay platelets exhibited an isotropic phase-separated morphology. The PS phases in both OM and SEM images show that they were coarsened isotopically with annealing time to tens of microns in size (Figure 3-13b and Figure 3-13d). Both samples also show that the initial co-continuous PS/PVME morphology developed into large, discrete PS domains in a continuous PVME phase in late stage of phase separation. Fast Fourier transform (2D-FFT) of images shown in the inset of each image indicates the degree of average anisotropy of Figure 3-13a and Figure 3-13c.

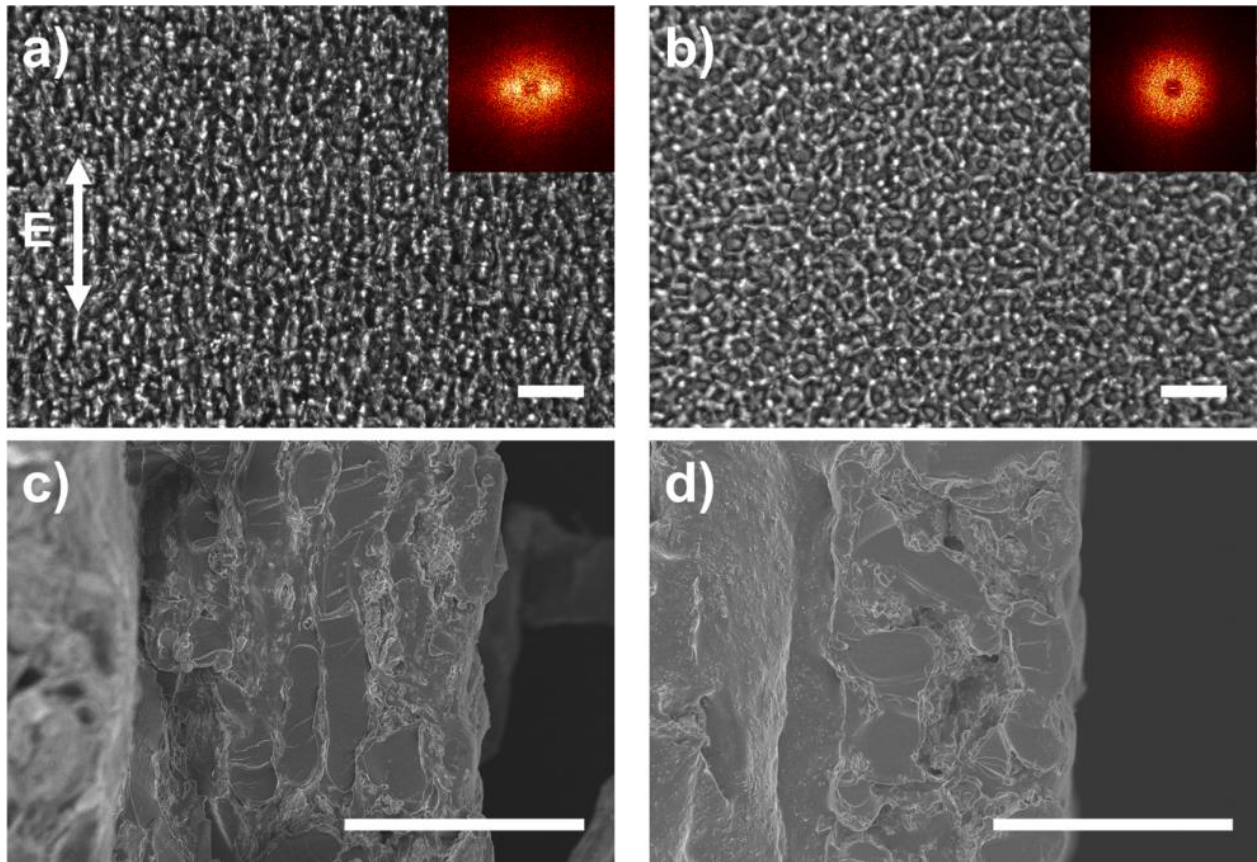


Figure 3-13 Phase-separated morphology of a PS/PVME (50/50) blend containing 5 vol% clay platelets annealed at 128 °C for 30 min with and without the AC electric field. The arrow indicates the AC field (500 V/mm, 100 Hz) direction. (a) OM images (top view) and (c) corresponding SEM images (cross-sectional view) of the sample prepared with AC fields. (b) OM images (top view) and (d) corresponding SEM images (cross-sectional view) of the samples prepared without AC fields. (Scale bar: 50 μm)

To numerically quantify the orientation degree of phase-separated morphology, we calculated the orientation order parameter (S) based on 2D-FFT patterns of each OM image. Accordingly, the integrated intensity of the 2D-FFT pattern was plotted against the azimuthal angle (φ). The integrated intensity of anisotropic 2D-FFT pattern showed a graph with two peaks at $\varphi = 90^\circ$ and 270° , whereas that of isotropic 2D-FFT pattern showed no significant peaks (Figure 3-14). By fitting the plots by a Maier–Saupe distribution function, we can obtain the orientation order parameter, which varies from 0 (totally random) to 1 (perfectly oriented).^{187,188}

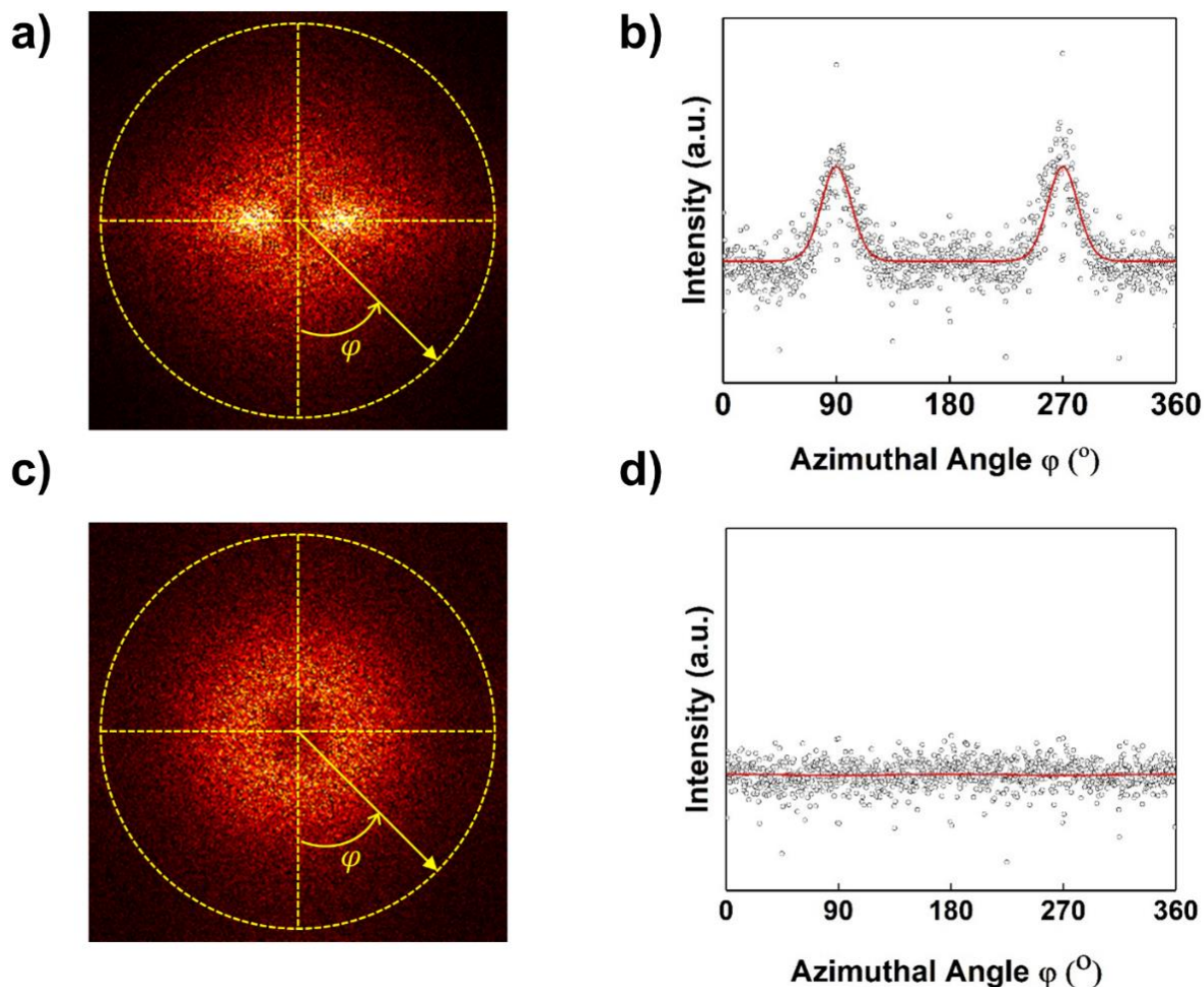


Figure 3-14 (a) 2D-FFT pattern of the optical image (the sample containing 5 vol% clay nanofillers with a 500 V/mm electric field strength at 128 °C for 60 min). (b) The corresponding plot of the integrated intensity of the 2D-FFT pattern against the azimuthal angle (ϕ) (c) 2D-FFT pattern of the optical image (the sample containing 5 vol% clay nanofillers without AC field at 128 °C for 15 min). (d) The corresponding plot of the integrated intensity of the 2D-FFT pattern against the azimuthal angle (ϕ).

Domain growth proceeded in the same fashion for 60 min and 120 min of annealing time in both isotropic and anisotropic samples (Figure 3-15a–c). Orientation order parameters of two different samples over annealing time are shown in Figure 3-15d. The phase separated morphology with pre-oriented clay nanofillers exhibited high orientation parameter ($S \sim 0.8$) with increasing annealing time. The result indicated that the orientation of PS domains was well preserved through the coarsening process. However, the sample with non-oriented clay platelets exhibited no orientation ($S \sim 0$) for different annealing times.

The effect of the AC electric field strength on the orientation of phase-separated domains was also examined. 5 vol% clay platelets were pre-oriented with the various strengths of AC field in PS/PVME blends during drying process and then samples were annealed at 128 °C for 60 min with corresponding electric field strength. Figure 3-16 shows that the orientation of polymer domains highly depends on the strength of the AC electric fields. The isotropic PS domains with the size of tens of microns were observed in a continuous PVME domain at 50 V/mm of AC field strength. As the field strength increased to 100 V/mm, the PS domains were slightly oriented to the AC field. Then, they were highly oriented to AC field direction above 500 V/mm. Figure 3-16f shows the domain orientation order parameters as a function of the electric field strength. The graph shows that the orientation of domains was slightly increased to ~0.1 at 100 V/mm electric field intensity. When the field strength increased to 200 V/mm, the orientation parameter significantly increased to 0.6. A further increase in AC field strength to 500 V/mm caused a more increase of the orientation order parameter (up to ~0.8) and then leveled off with further increase of voltage.

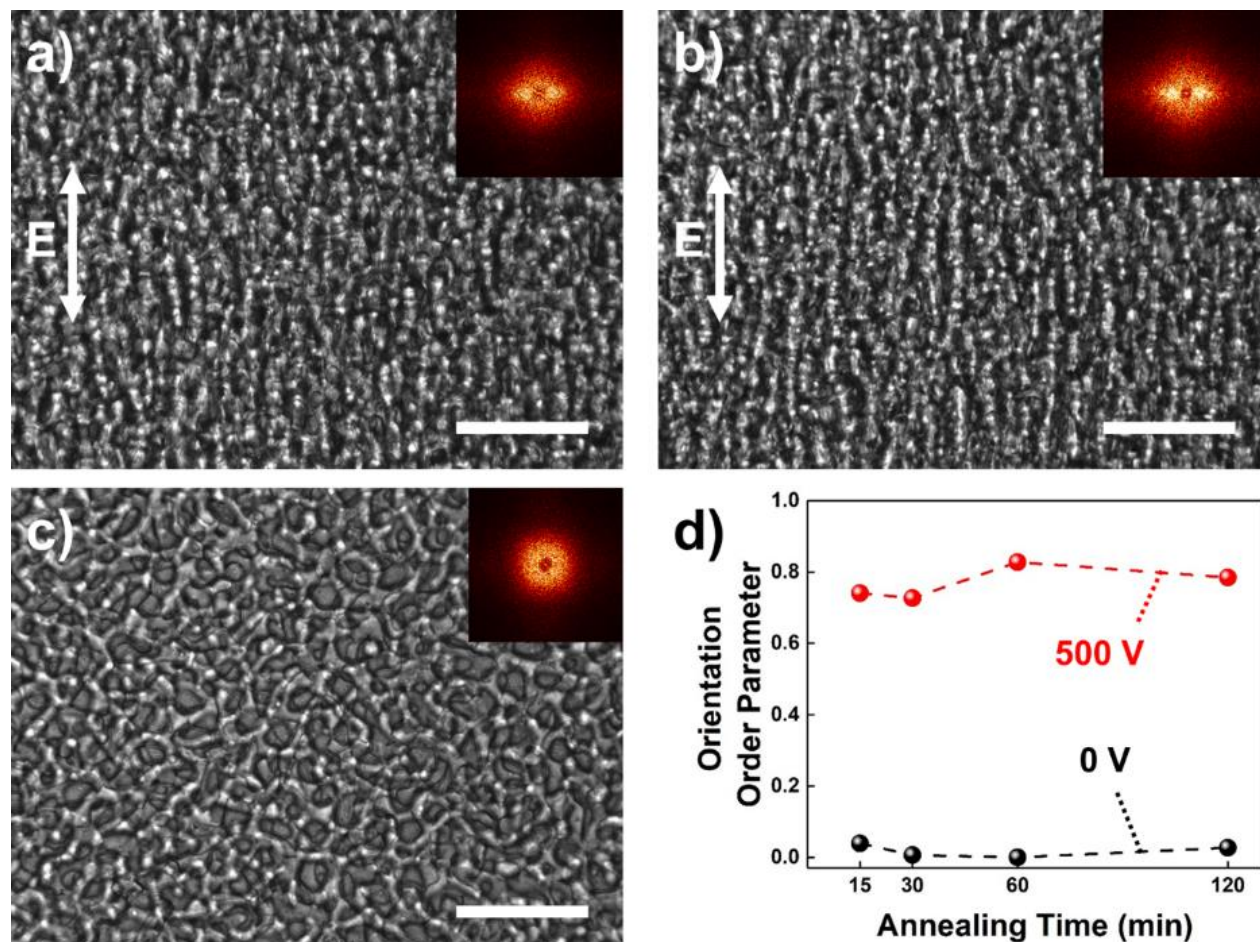


Figure 3-15 OM images (top view) of the PS/PVME (50/50) blend morphology containing 5 vol% clay nanofillers annealed at 128 °C with and without an AC electric field. (a) 60 min and (b) 120 min annealing time with 500 V/mm AC fields. (c) 60 min without AC fields. (Scale bar: 100 μ m) (d) domain orientation order parameter of the samples with/without AC fields over annealing time

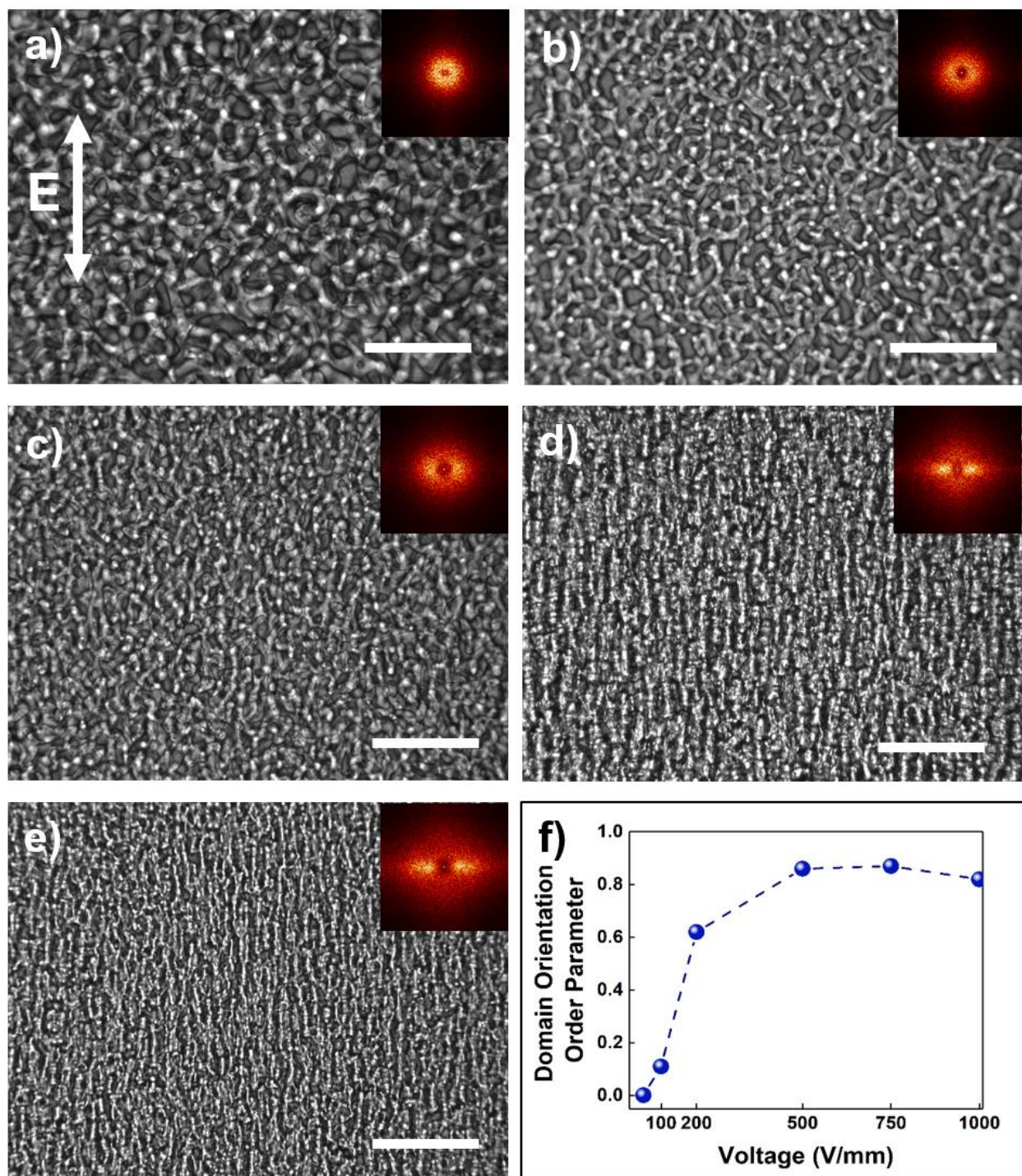


Figure 3-16 OM images (top view) of the PS/PVME (50/50) blend morphology containing 5 vol% clay platelets with various AC electric field strengths for 60 min annealing time at 128 °C. The field strengths are (a) 50 V/mm, (b) 100 V/mm, (c) 200 V/mm, (d) 500 V/mm, (e) 1000 V/mm. (Scale bar: 100 μm) (f) Plots of the orientation order parameter of polymer domains to various electric field intensity. The FFT patterns of the corresponding OM images are inserted upper right corner.

SEM and AFM observations were carried out after etching PVME domains to analyze surface topology. Figure 3-17 depicts the top and cross-sectional morphology of the sample containing 5 vol% oriented clay platelets observed by SEM. SEM images depict PS domains exposed on the top and cross-sectional surfaces after PVME etching. In both top and cross-sectional SEM images, the PS domains were highly oriented parallel to the AC field direction for the sample annealed for 15 min. PS domains with widths of $\sim 5\mu\text{m}$ and lengths of hundreds of microns were observed in the top surface image. The distance between PS domains was $\sim 5\mu\text{m}$. Notably, PS domains that had elongated to hundreds of microns at the early stage of annealing (15 min) broke down discrete PS domains after 60 min of annealing. Droplet morphology of PS domains with widths of $\sim 10\mu\text{m}$ and lengths ranging from $15\mu\text{m}$ to $30\mu\text{m}$ was observed in both top-view and cross-sectional SEM images for the sample annealed for 60 min. The results indicated that further coarsening increased the widths of PS domains from $\sim 5\mu\text{m}$ to $\sim 10\mu\text{m}$ and disconnected PS domains, which were highly elongated to AC field direction. The morphology of the sample annealed for 120 min is similar to that of the sample annealed for 60 min in both top and cross-sectional SEM images.

The exposed PS top-view morphology at the early stage of annealing was also analyzed by AFM to investigate detailed surface topology (Figure 3-18). AFM height image ($100 \times 100\mu\text{m}$) also clearly depicts the oriented PS morphology parallel to AC field direction. AFM height profile of corresponding white dotted line shows that the oriented PS domains has a peak to peak distance range of $\sim 5\mu\text{m}$ (Figure 3-18b). The depth of exposed PS domains on the top surface was $\sim 1.5\mu\text{m}$. The initial stage of phase behavior of a neat PS/PVME blend undergoing spinodal decomposition was widely reported by previous studies.^{189,190} In a single mixture state, PS and PVME phases coexist in the film. When the blend is thermally annealed above their critical temperature, a co-continuous structure of PS and PVME phases appears with the wetting layer of PVME at the air surface and glass substrate. By dissolving top PVME domains on the surface of the film, we observed co-continuous but oriented PS and PVME domains after 15 min of annealing.

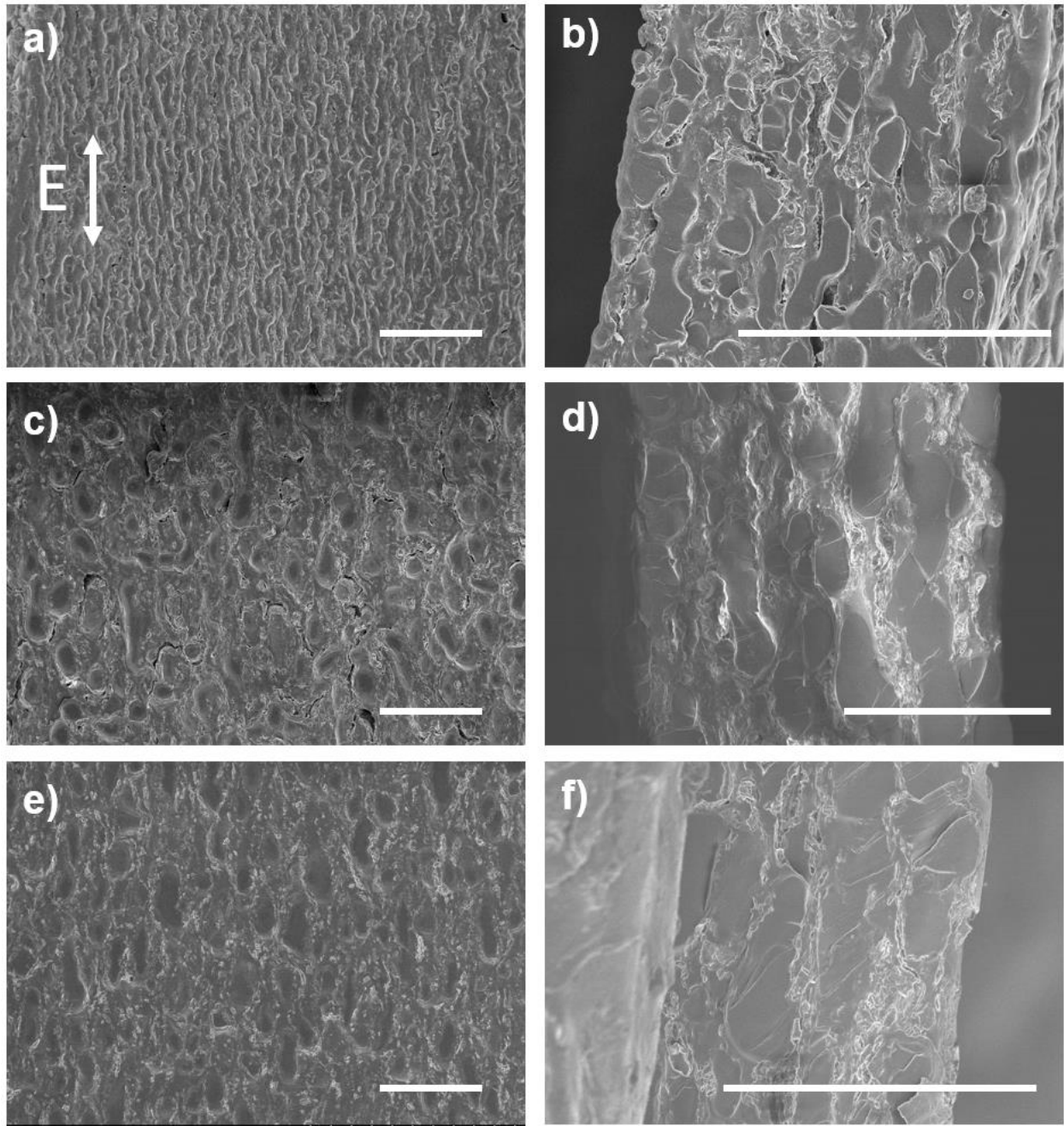


Figure 3-17. SEM top view and cross-sectional images of a PS/PVME (50/50) blend morphology containing pre-oriented 5 vol% clay nanofillers (500 V/mm, 100 Hz) annealed at 128 °C. Top-view images of (a) 15 min, (c) 60 min, and (e) 120 min annealed samples. Cross-sectional images of (b) 15 min, (d) 60 min, and (f) 120 min annealed sample. (Scale bar: 50 μ m)

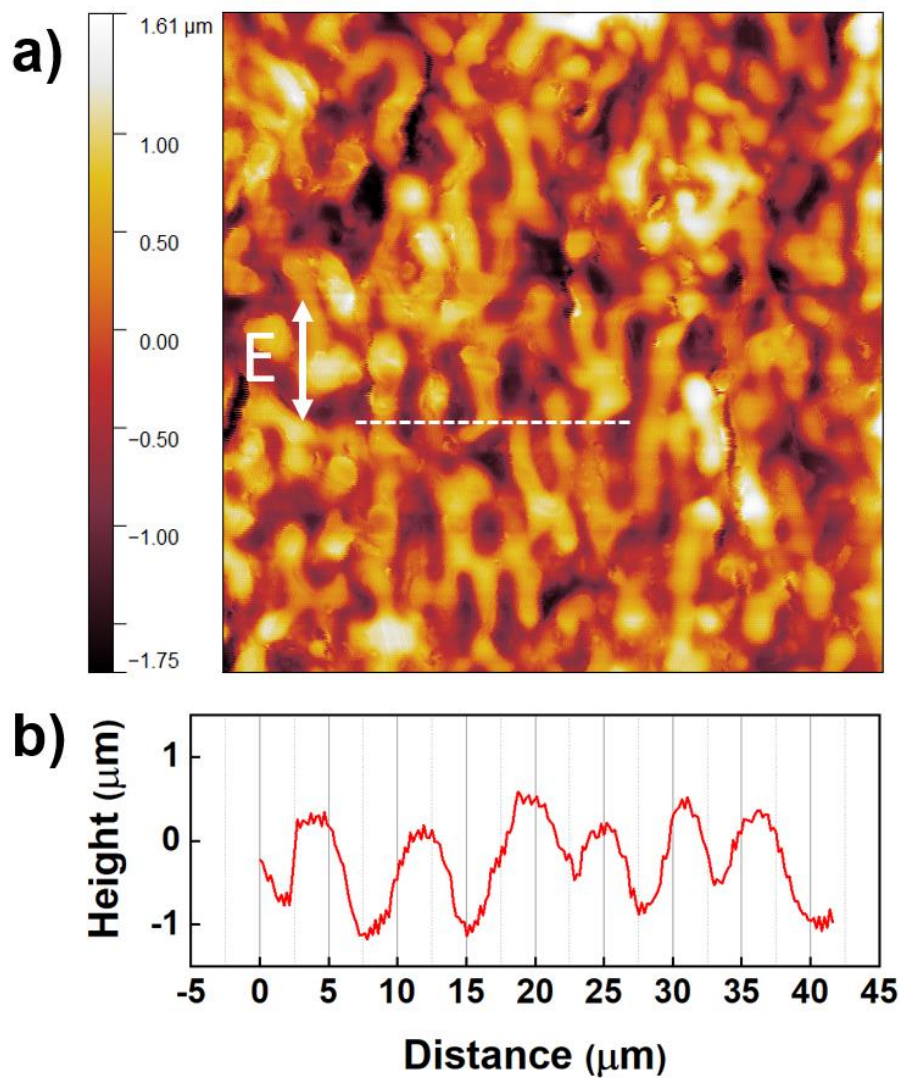


Figure 3-18. (a) AFM height image ($100 \times 100 \mu\text{m}$) of the top surface of a PS/PVME (50/50) blend containing 5 vol% pre-oriented clay nanofillers (500 V/mm, 100 Hz) annealed at 128 $^{\circ}\text{C}$ for 15 min ($\Delta z = 3360 \text{ nm}$). (b) 2D topological feature of corresponding white dotted line.

In the presence of an electric field, the clay platelets undergo polarization. Due to the shape anisotropy of clays, the polarization moment (μ) of clay platelets can be divided into two elements: one parallel to the long axis (μ_{\parallel}) and one perpendicular to the long axis (μ_{\perp}).^{191,192} For clay platelets, the polarizability in the direction of the basal plane is much larger than that in the perpendicular direction. This non-zero net polarization moment on the clays, which is not coordinated with the direction of the electric field, leads to field-induced torque (T) on clay platelets. The torques cause rotational and translational movement of clay platelets in the direction of the electric fields against the viscous drag force of the surrounding polymer medium.⁴⁶ Apart from this field-induced torque, the coulombic attraction is generated between oppositely charged particles.¹⁹² The combined effects lead to the orientation of clay platelets and organization along columns in the electric fields.⁴⁷ In this study, the clay platelets were oriented in the AC electric fields during drying and the orientation was maintained during annealing process. To characterize the clay orientation in blends for each processing steps, 2D WAXS analysis was conducted to detect the (001) Bragg diffraction peak from intact layered clay platelets. For Cloisite 15A, the (001) plane diffraction was observed at 3.6 nm ($q = 1.75 \text{ nm}^{-1}$). In the absence of AC field, the clay platelets were randomly dispersed in blends as indicated by isotropy in diffraction pattern (Figure 3-19 a-1 and a-2). However, two strong 2D arcs were observed the presence of AC field when X-ray beam was directed orthogonal to the applied electric field direction (Figure 3-19 a-3 and a-4). Notably, the X-ray scattering pattern was barely changed even after annealing for 120 min. The plot of X-ray intensity as a function of azimuthal angle (φ) is shown in Figure 3-19b. The similar shape of the plots shows that the array of clay platelets was well maintained while PS and PVME polymers undergo phase separation.

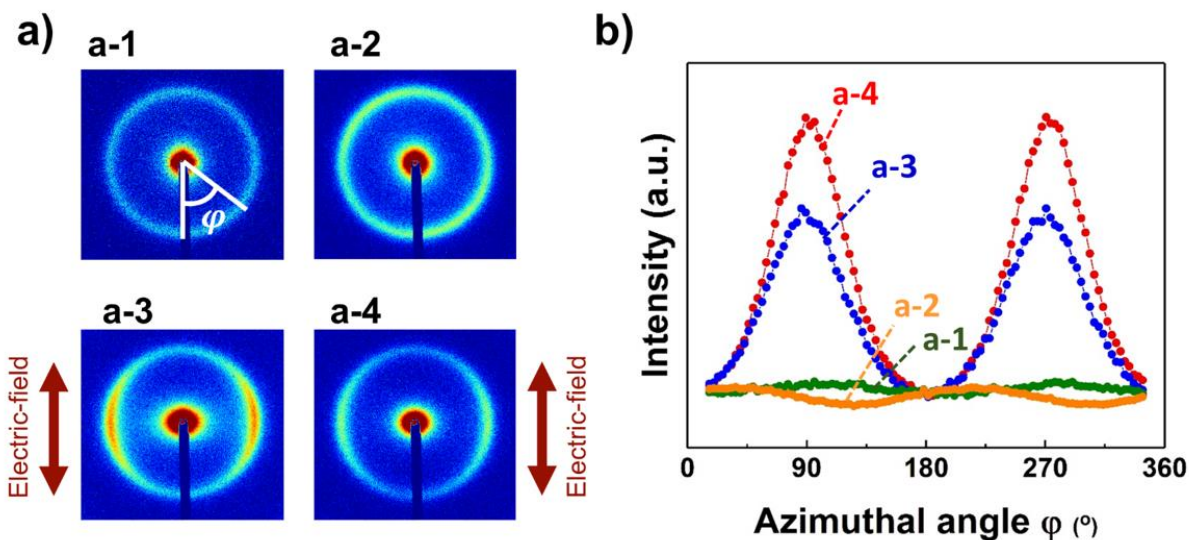


Figure 3-19 (a) 2D WAXS scattering pattern of a PS/PVME (50/50) blend containing 5 vol% clay platelets. The sample prepared with (a-1) 0 V/mm and 0 min annealing, (a-2) 0 V/mm and 120 min annealing, (a-3) 1000 V/mm and 0 min annealing, and (a-4) 1000 V/mm and 120 min annealing. (b) The corresponding plot of the integrated intensity of the 2D WAXS pattern against the azimuthal angle.

The orientation of clay platelets for each annealing step with 1000 V/mm AC electric field is shown in Figure 3-20a. The clay orientation order parameter was calculated by using the aforementioned procedure (Maier–Saupe distribution function). The clay orientation order parameter was 0.42 before annealing process and then it slightly decreased to 0.4 for 30 min annealing. As annealing time increased, it decreased down to 0.39. This indicates that the oriented clay structure was slightly disordered during phase separation process. To study the effect of the electric field strength on clay orientation, we investigated the orientation order parameter of clay platelets at various electric field strengths with 60 min annealing samples (Figure 3-20b). There was no significant orientation of clay platelets at low field strength (below 100 V/mm), indicating that the clay orientation remained randomized at high annealing temperature. However, the orientation of clay platelets appeared at 200 V/mm with 0.3 orientation order parameter. It increased to 0.35 at 500 V/mm and then it was saturated to 0.37 above 750 V/mm. 2D WAXS technique only presents the orientation factors of large particles (i.e., intact layered clay platelets), not the fully exfoliated clay platelets as they do not form full 3D crystal lattice and not show (001) planes. Hence, the effect of fully exfoliated clay platelets on the anisotropic PS/PVME phase-

separated morphology domains cannot be addressed by using 2D WAXS technique. Nevertheless, the phase-separated morphology of PS/PVME blends is related to the orientation of the layered clay platelets. The orientation order parameter of domains (Figure 3-16f) and that of clay platelets (Figure 3-20b) were correlated as shown in Figure 3-20c. The results show the linear correlation between orientation of clay and that of polymer domains, showing the slope of this plot is approximately 2. This correlation implies that the degree of orientation of clay platelets is highly related to the anisotropic morphology of PS/PVME blends.

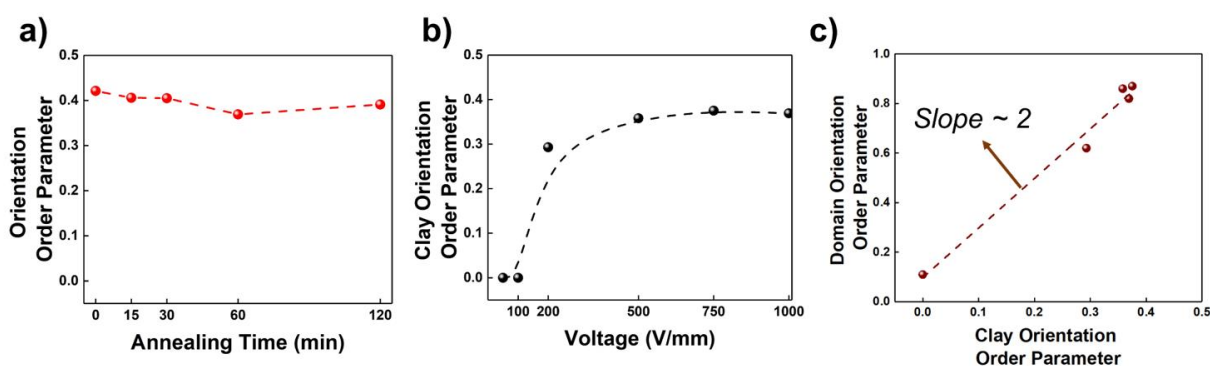


Figure 3-20 (a) The orientation order parameter of clay platelets in the samples prepared with the AC electric field (1000 V/mm, 100 Hz) for different annealing times. (b) The orientation order parameter of clay platelets at various electric field strength. (c) The plot of the orientation order parameter of clay to the orientation order parameter of polymer domains.

To assess the detailed local morphology of a phase-separated sample, the cross-sectional cryo-microtomed sample was observed by TEM. For the sample annealed at 128 °C for 15 min with 500 V/mm, the discrete PS domains in a continuous PVME domain was observed (Figure 3-21). The ellipsoidal PS domains in Figure 3-21a indicated that PS domains were coarsened and elongated parallel to AC electric field direction. The location and orientation of clay platelets are clearly observed in a magnified image shown in Figure 3-21b. Anisotropic clay particles from submicron to several microns in size were observed in a PVME phase surrounding a discrete PS domain. Most of anisotropic clay platelets were oriented with the AC field direction, even though some of the clay platelets formed several micron-sized aggregates. The image of clay particles wrapped around an ellipsoidal PS domain illustrates how the anisotropic phase separation emerged. The clay particles were initially highly oriented with the AC field before phase separation. At the

early stage of the phase separation, the co-continuous PS/PVME morphology appeared. Due to the preferential wetting of clay platelets by a PVME component, pre-oriented clay platelets remained in the PVME phase in ensuing coarsening process. Furthermore, the coarsening PS domains during the phase separation pushed away the clays so that they appeared to wrap around the PS domains. This mechanism causes the loss of the clay orientation as phase separation continues. This is evidenced by the time evolution of orientation of clay particles shown in Figure 3-20a where the clay orientation slightly decreases as the phase separation takes place. The following anisotropic diffusion of PS domains formed highly directionally organized morphology in the late stage of phase separation.

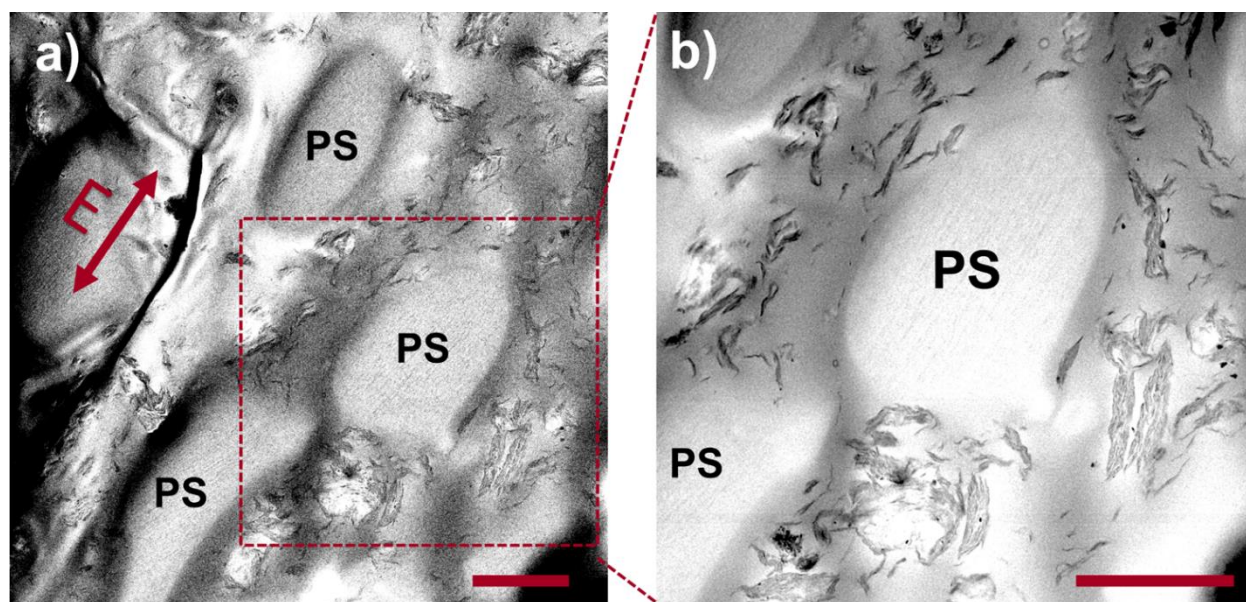


Figure 3-21 (a, b) TEM image of the cryo-microtomed sample (PS/PVME (50/50) blend containing 5 vol% clay platelets annealed at 128 °C for 15 min with 500 V/mm). (Scale bar: 5 μm)

The local morphology of the sample was also characterized by AFM. For AFM analysis of heterogeneous polymer systems, the variation of height between two phases is essential. Higgins et al. reported that the height contrast between two polymer phases originated from a different deformation of the two phases during microtoming.^{183,193} However, the height contrast in this study was mainly obtained during sample collection as PVME phases of thin samples were slightly dissolved in water. The dissolution of PVME in water caused a height contrast between two polymer domains in the thin sectioned sample. Therefore, PS and PVME phases exhibited the

higher (brighter) and lower (darker) features in an AFM image (Figure 3-22a). In order to better clarify the PS and PVME phases, the same area of AFM image was taken before and after methanol etching (Figure 3-22c and d). The height profiles of the white dash line in Figure 3-22c and Figure 3-22d were inserted in the upper right corner. The similar height features of the two profiles clearly show that higher (brighter) regions are PS phases, which were not dissolved in the methanol. The clay nanofillers were observed both in height and phase AFM images, but they are more clearly observable in phase images (Figure 3-22b). The phase contrast generally originates from differences in mechanical properties of two domains and induced topography.¹⁸³ A clear phase contrast between stiff inorganic clay nanofillers and soft polymers was revealed in AFM phase images,⁶⁰ whereas the two polymer domains had a poorer contrast. The preferential location of clay platelets in the PVME phases (dark regions) is in agreement with TEM images as shown above.

The localization of clay platelets was also identified in an SEM image of the sample at the early stage of a co-continuous morphology. Since clay platelets were preferentially located in the PVME phases, they were mostly washed out together with PVME domains when samples were placed in methanol. However, some of residual clay platelets were observed in the sample with co-continuous morphology. Figure 3-23a shows residual clay platelets in a cross-sectional SEM image. Paper-like clay platelets with a length of $\sim 1 \mu\text{m}$ and a thickness of 100 nm stuck between continuous PS domains were observed. All clays particles observed in etched PVME regions indicate that clay particles more likely located in PVME phases. Furthermore, anisotropic cracks with lengths of $2 \mu\text{m}$ to $4 \mu\text{m}$ and thicknesses of 100 nm to 500 nm were observed in a zoomed-out SEM image (Figure 3-23b). These cracks probably correlate to the places where clay platelets were located before methanol washing. The clay platelets that washed out together with PVME domains left anisotropic cracks with similar sizes to the clay particles. It was also found that the anisotropic cracks were oriented AC field direction in the zoomed-out SEM image.

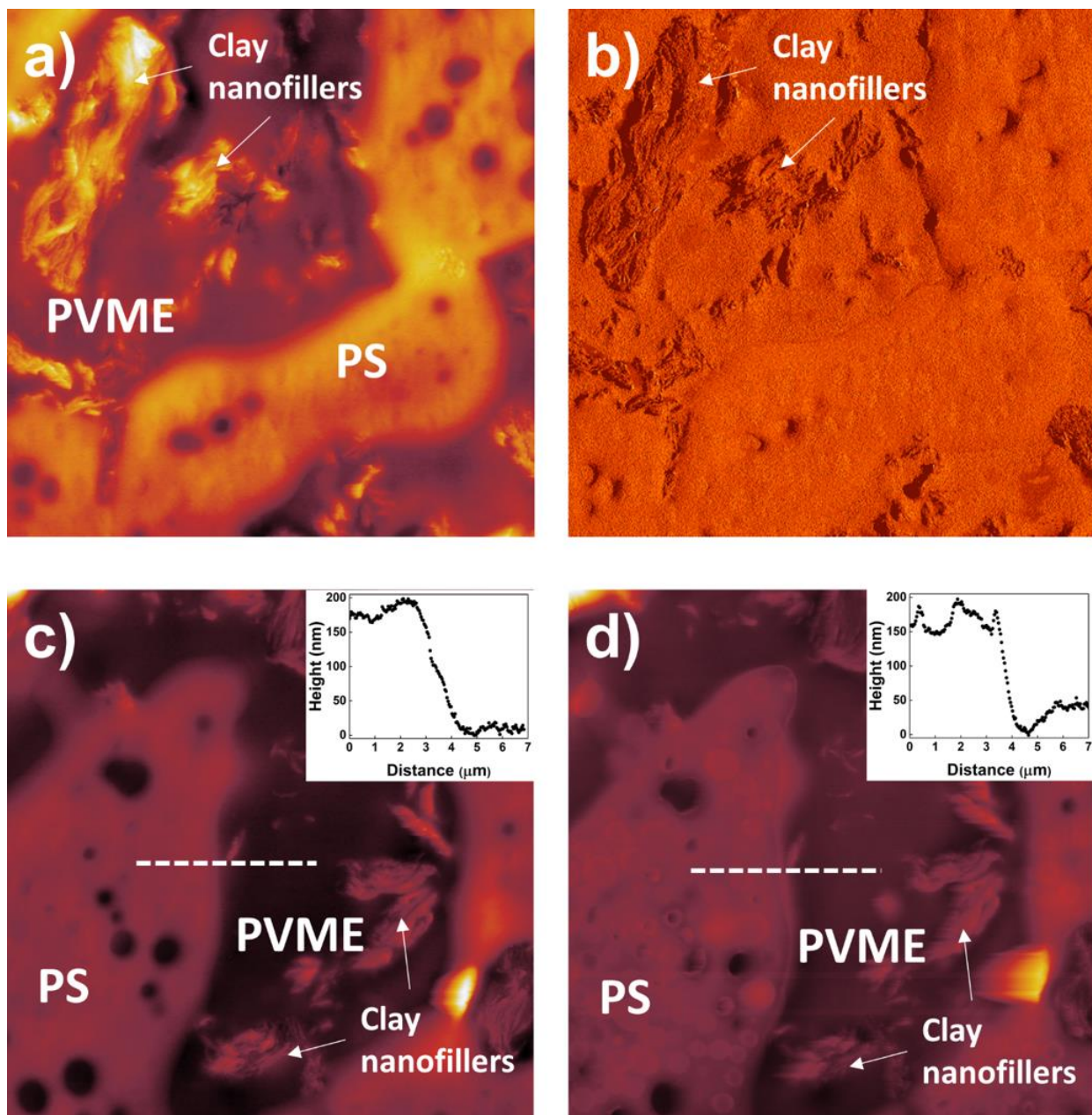


Figure 3-22 AFM topography images ($20 \times 20 \mu\text{m}$) of the (a) height ($\Delta z = 600 \text{ nm}$) and (b) phase image of the microtomed surface of the sample (PS/PVME (50/50) blend containing 5 vol% clay nanofillers annealed at $128 \text{ }^\circ\text{C}$ for 12.5 min with 500 V/mm). Lighter regions in (a) indicate taller features. AFM topography images ($10 \times 10 \mu\text{m}$) of the same region (c) before and (d) after methanol washing ($\Delta z = 600 \text{ nm}$). The height profiles of the dash line were inserted.

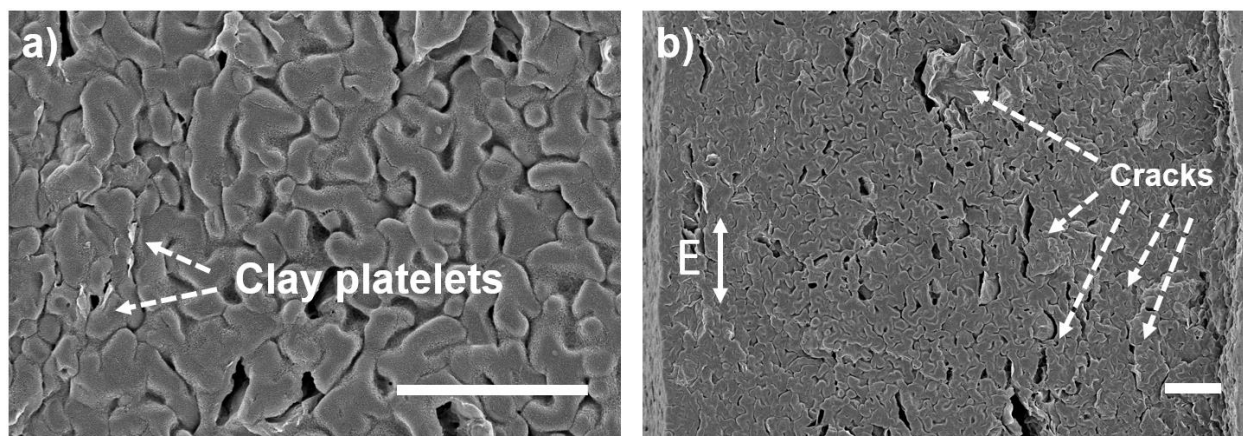


Figure 3-23. Cross-sectional SEM images of the sample indicating the location of clay platelets. The sample was a PS/PVME (50/50) blend morphology with pre-oriented 5 vol% clay platelets (500 V/mm, 100 Hz) annealed at 128 °C for 5 min. The arrows in (a) and in (b) indicate clay platelets and cracks, respectively. (Scale bar: 5 μ m)

Lastly, Figure 3-24 summarizes the two schematic illustrations of phase-separating morphology with non-oriented and electric field pre-oriented clay platelets. The co-continuous structures emerge in both samples in the early stage of phase separation, indicating that the morphology in this stage was not notably affected by clay pre-orientation. As annealing time elapses, the effect of orientation of clay platelets on the morphology in blends becomes noticeable as they act as anisotropic barriers to polymer diffusion to ultimately form phase-separated highly directional structures.

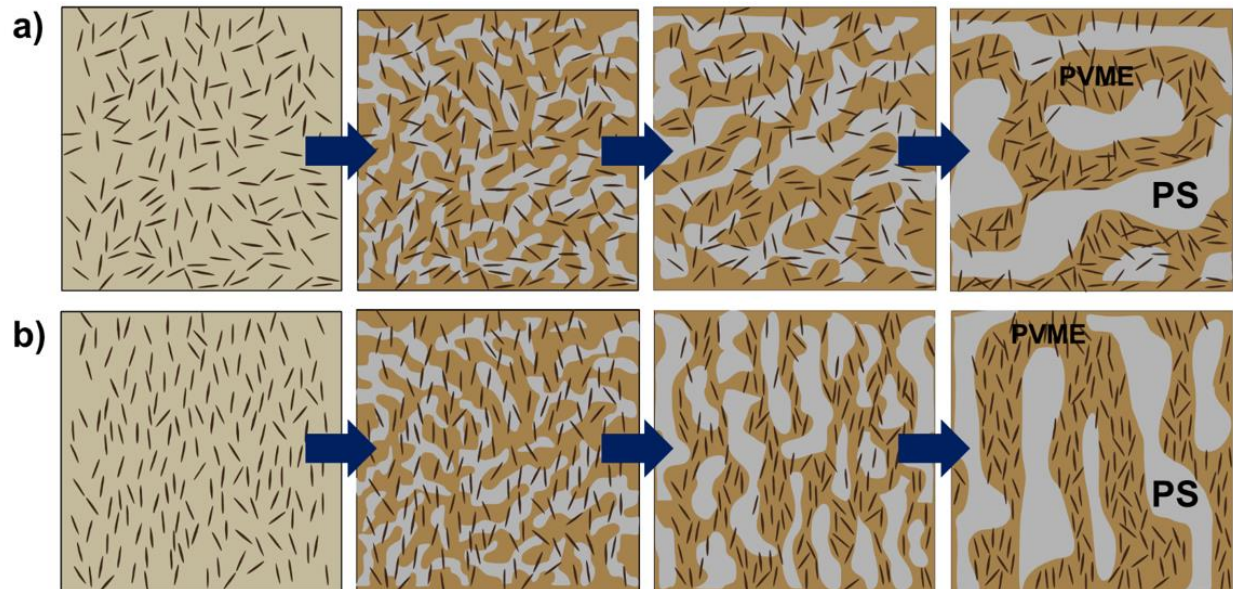


Figure 3-24 Cartoons of a PS/PVME top-view phase-separated morphology over annealing time with (a) non-oriented and (b) pre-oriented clay platelets in electric field.

3.4 Conclusion

We demonstrated that the phase-separated morphology of a PS/PVME polymer blend can be controlled by electrical pre-orientation of organically modified clay platelets in one phase followed by temperature jump to the two-phase regime. The isotropic co-continuous morphology undergoing spinodal decomposition in the early stage was followed by coarsening with primary direction of the clay orientation during phase separation. The formation of the anisotropic phase-separated morphology was attributed to preferential localization of pre-oriented clay platelets in PVME domains that affects the directionality of diffusion process. This method promises to be a general technique to produce anisotropic polymer films with unique anisotropic electrical, ionic, and optical properties.

4. ANISOTROPIC STRUCTURE IN POLYMER BLENDS BY USING THROUGH-PLANE ORIENTED CLAY PLATELETS

In this chapter, directionally organized PS/PVME morphology in the direction of through-plane was demonstrated by aligning clay platelets in a PS/PVME polymer blend. For practical applications, the anisotropic structure may be required along the direction of film thickness to enhance functional properties, such as ionic conductivity needed in such applications as proton exchange membrane or active layers of organic photovoltaics where interdigitated structures are needed to rapidly facilitate electron–hole separation to send to an external circuit for efficiency enhancement. Through-plane oriented clay platelets in a homogeneous single-phase PS/PVME blend by the application of an external electric-field induced anisotropic diffusion between PS and PVME upon temperature increase into a two-phase regime. The kinetics of clay orientation in blends and detailed the cross-sectional morphology of the blend with clay particles was analyzed with various techniques. The results indicated that the anisotropic PS/PVME morphology could be achieved even along the direction of film thickness, which is promising for internal structures of membranes or energy harvesting applications.

4.1 Introduction

Controlling the morphology of multi-phase polymer system is critical to tune the properties of materials.⁵⁶ Among different phase-separated morphologies in a polymer mixture, a directionally organized phase-separated morphology in multicomponent polymer systems is often desired. For example, the ideal morphology of the active layer in an organic photovoltaic cell is an anisotropically ordered morphology of donor and acceptor materials.^{194,195} One computational study suggested that an anisotropic structure in the active layer can enhance the efficiency by 50% compared to a disordered morphology.¹⁹⁶ Structurally ordering morphology by forming a continuous path is also preferred in a proton-exchange membrane. A directionally organized morphology of sulfonated poly(ether ketone ketone) (SPEKK) and poly(ether imide) (PEI) blends in proton-exchange membrane fuel cell showed a three order-of-magnitude increase in proton conductivity.¹³²

One possible route to develop an anisotropic phase-separated structure in blends is the application of external electric field. The behavior of liquid drops in an electric field has been well

exploited within the theoretical framework of electrorheological fluids.¹⁹⁷ When a system of fluid drops dispersed in another immiscible fluid is subjected to external electric field, electric stress at the interface occurs if there is a mismatch in dielectric constants of two phases (commonly droplets with low dielectric constant in a matrix with high dielectric constant). This induced electric surface force can elongate the shape of the droplets parallel to the applied field direction if the electric force overcomes interfacial tension.^{130,131,198} Krause group reported the shape and orientation of dispersed polymer droplets in another polymer matrix in the presence of electric fields for various types of polymer blends.^{126,166,199} One of their studies demonstrated that dispersed PMMA droplets in another immiscible PS medium developed into strings of droplets followed by coarsening into fibrillated structures parallel to the field during evaporation of a common solvent.¹²⁶ When co-continuous phases are exposed to an electric field, however, the morphological evolution may be more complicated. Because electric stresses only act normal to the interface for the phases with different dielectric constants, a net force acting on interpenetrating interfaces may be difficult to interpret. Recently, Hori et al. reported that co-continuous morphology tended to coarsen and orient structures parallel to the electric field.¹²⁵ They demonstrated the development of an anisotropic phase-separated morphology from initial co-continuous phases by adding LiClO₄ in the system. The role of LiClO₄ was to introduce a high contrast in electric conductivities between the two phases. A large difference in electric conductivities between the phases generated a tangential electric force parallel to the interface, which caused deformation of the co-continuous phase, forming oriented structures.

Although electric field is classically used for the development of anisotropic morphology in two immiscible fluids, this method is limited to a two-phase system consisting of a minor phase in a matrix phase or a mixture with a considerable mismatch in electrical properties. Incorporation of nanoparticles in multicomponent polymer systems may be an alternative way to develop a directionally ordered structure. When a blend undergoes phase separation in the presence of nanoparticles, the particles tend to be preferentially located in one of the phases. Due to low interfacial energy between two polymers, it may be an even harder task to locate the nanoparticles at the interface by a delicate surface treatment of the nanoparticles.¹⁰² However, preferential wetting of nanoparticles by one of phase may be favorable for developing anisotropic phase separation in multiphase polymer blends. If nanoparticles are directionally organized in a blend in one phase before demixing, phase separation can occur anisotropically through preferential

attraction of one of the phases to the pre-oriented nanoparticles. It was widely demonstrated that various nanoparticles such as metal,^{200,201} ceramic,^{106,109,202} or carbon-based^{110,111} nanoparticles can be successfully aligned in an insulating mobile medium by the application of an electric field. Among various nanoparticles, organically modified montmorillonite (clay platelets) is a good candidate for two reasons: First, commercially available organically clay platelets are easily exfoliated or intercalated in a polymer matrix.⁸³ Second, highly polarizable clay platelets in an electric field have already been demonstrated to be oriented parallel to the field by forming strings of particles.^{46,47}

In this study, the formation of directionally organized morphology in a polymer blend was demonstrated in the presence of oriented clay particles along the direction of the film thickness. Previously, our group reported anisotropic PS/PVME morphology along the in-plane direction with oriented clay particles.¹⁶¹ However, anisotropic morphology along the in-plane direction is limited for practical applications, such as functional membrane and energy harvesting devices, where the morphology in the direction of through-plane is critical. Here, anisotropic PS/PVME morphology in the through-plane direction was demonstrated by using electrically pre-oriented clay particles. We will demonstrate the utility of electrically oriented clay platelets in a homogeneous single-phase PS/PVME matrix to form induced anisotropic PS/PVME phase separation upon a temperature jump into the two-phase regime. Orientation kinetics of clay nanoparticles under the electric field was tracked using real time birefringence technique, and the detailed shape and size of phase morphology and nanoparticle organization were analyzed by a range of characterization techniques.

4.2 Experimental section

4.2.1 Materials

PS (Mw: 35 kg/mol) and toluene were purchased by Sigma Aldrich and used as received. PVME (Mw: 30 kg/mol) was purchased from Polysciences Inc. as 50% aqueous solution. The PVME aqueous solution was completely dried overnight at 120°C in vacuum oven before usage. Organically modified clay (Cloisite 15A) was provided by BYK Additives & Instruments. A high-voltage amplifier (Matsusada, AMT-20B10-LC) and a function generator (HP, 33120A) were used to generate an alternating current (AC) electric field. Teflon-coated stainless steel mesh (325 Mesh

T304 Green PTFE Stainless .0014" Wire Dia) with a 36 μm of wire diameter and a 43 $\mu\text{m} \times 43 \mu\text{m}$ of opening was purchased from TWP Inc. Indium tin oxide (ITO) coated glass substrate was purchased from SPI Supplies (300 mm \times 300 mm \times 1 mm thick, Resistivity 30–60 Ω).

4.2.2 Sample preparation

Two homopolymers (40 wt%, PS/PVME: 50/50) were dissolved in toluene (60 wt%) by a planetary centrifugal mixer (Thinky Mixer). A homogeneous polymer solution was obtained after 3 h of mixing. Clay platelets (5 vol% clay nanoplatelets with respect to polymers) were dispersed in the homogeneous polymer solution for another 1 h of mixing. The sample was poured into a square cell with a size of 70 mm \times 70 mm composed of a stainless-steel porous mesh (top electrode), ITO coated transparent glass (bottom electrode) and 1 mm slide glasses (spacers) as shown in Figure 4-1a. The top porous and flexible mesh electrode remained in contact with the top surface of the sample while AC electric fields was applied along the film thickness direction during the drying and annealing processes. The detailed experimental design for the application of electric field on polymer solution can be found in our previous studies.^{203,204} In this study, we prepared 4 different samples (dried sample with AC field, annealed sample with AC field, dried sample without field, annealed sample without field) as shown in Figure 4-1b and 4-1c. The sample in the square cell was dried first at 93 $^{\circ}\text{C}$ for 6 h. Additional annealing process at 150 $^{\circ}\text{C}$ for 0.5 h was added if necessary.

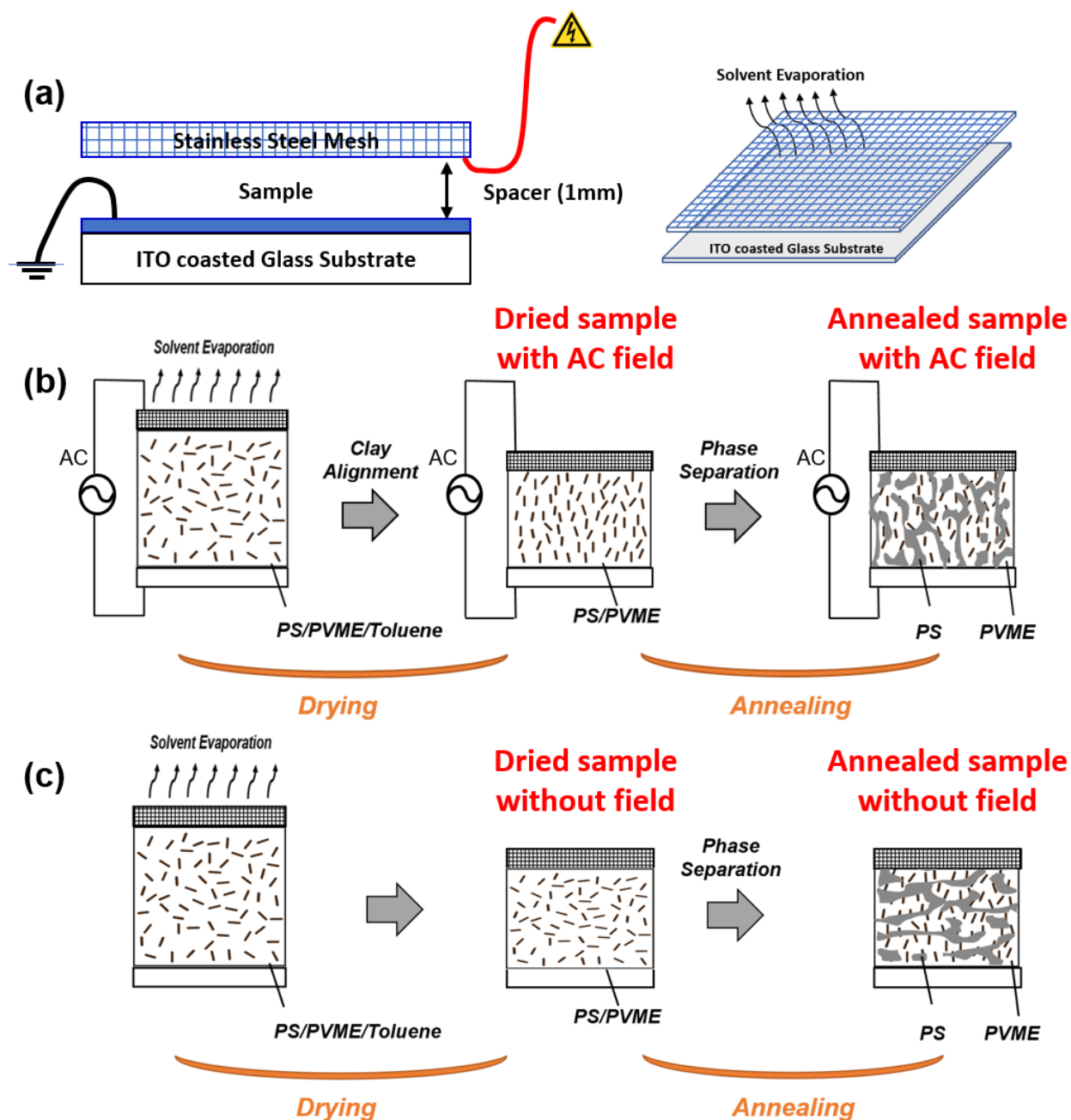


Figure 4-1 (a) Scheme of the square cell used for the electric-field assisted alignment of clay platelets during polymer solution drying. Cross-sectional schematic illustration of the sample preparation process (b) with AC field and (c) without AC field.

4.2.3 Sample characterization

Thermal properties: Thermal transitions of polymers were characterized by differential scanning calorimetry (DSC, Netzsch Instruments) with nitrogen-gas purging. The sample with a weight of 10 mg was measured at the temperature ranging from $-50\text{ }^{\circ}\text{C}$ to $150\text{ }^{\circ}\text{C}$.

Drying characteristic: The orientation of clay nanoplatelets in the presence of AC field was measured by detecting physical properties with a custom-built real-time measurement system. The design and capabilities of this custom-built machine can be found elsewhere.²⁰⁵ In this study, the birefringence change of the sample upon application of AC electric field was measured, as well as real-time weight, temperature, thickness data of the sample. Both dried and annealed samples were prepared in this machine.

Polarized optical microscopy (POM): The electric-field assisted orientation of clay platelets was examined by a POM (Leitz Laborlux 12 Pol S) with and without a first order red wave plate (λ) at 45° to the crossed polarizers. The 1 mm sectioned sample along the thickness direction was placed between two crossed polarizers and rotated at every 45° rotation to characterize optical anisotropy.

Wide-angle X-ray scattering (WAXS): Orientation of clay particles were also characterized by the WAXS technique. The X-ray scattering machine (Anton Paar SAXSpoint 2.0) generated an X-ray beam with monochromatized to Cu K α radiation ($\lambda=0.154\text{ nm}$). Every sample was exposed to X-ray beam for 5 min with 200 mm of sample-to-detector distance.

Atomic force microscopy (AFM): To characterize the morphology of polymer film along the thickness direction, the sample was cross-sectioned with $1\text{ }\mu\text{m}$ thickness at $-30\text{ }^{\circ}\text{C}$ by using a cryostat (Leica CM1850). The cross-sectioned sample with a flat surface was placed on a glass slide for AFM imaging. AFM (Veeco Dimension 3100) with tapping mode was used. The cross-sectioned surface was observed without any special treatment at room temperature. For AFM tips, silicon probes (ACTA-10, APPNano, USA) with a force constant of 13–77 N/m at frequency range of 200–400 kHz were used. Target amplitude of 2 V and amplitude set point of 1.5–1.8 V were used.

Transmission electron microscopy (TEM): Samples were prepared by using a cryo-microtome (Leica UCT ultramicrotome with EMFCS cryo attachment). Ultrathin sections of 100 nm were collected on 100 mesh formvar/carbon coated grids with a diamond knife cutting at

–60 °C. TEM images were captured by a FEI Talos 200 S/TEM transmission electron microscope with an accelerating voltage of 200 kV.

Scanning electron microscopy (SEM): SEM samples were cryo-fractured in liquid nitrogen. The sectioned surface was immersed in methanol before imaging to distinguish PS and PVME phases. Cross-sectional morphology of the sample was imaged by SEM (Hitachi S-4800) with an accelerating voltage of 3 kV and a working distance of 8 mm.

4.3 Results and discussion

PS/PVME polymer blends

The blend of PS/PVME displays an LCST behavior.¹⁸⁹ The critical temperature of a PS (Mw: 35 kg/mol) and PVME (Mw: 30 kg/mol) blend was 124 °C at 50/50 composition.¹⁶¹ Figure 4-2a shows the phase diagram of the PS/PVME blend without clay platelets along with optical microscope images of two different (50/50) blend samples annealed at 120 °C and 130 °C for 24 h, respectively. The sample annealed at 130 °C exhibits a micro-sized phase separation with ~50 µm domains, while no microscopic phase separation is observable for the sample annealed at 120 °C. The glass transition temperature (T_g) of PS, PVME and the blend (50/50) was determined by a differential scanning calorimetry (DSC) curve (Figure 4-2b). T_g of PVME and PS were –27°C and 63 °C, respectively. The blend (50/50) showed T_g at –15°C.

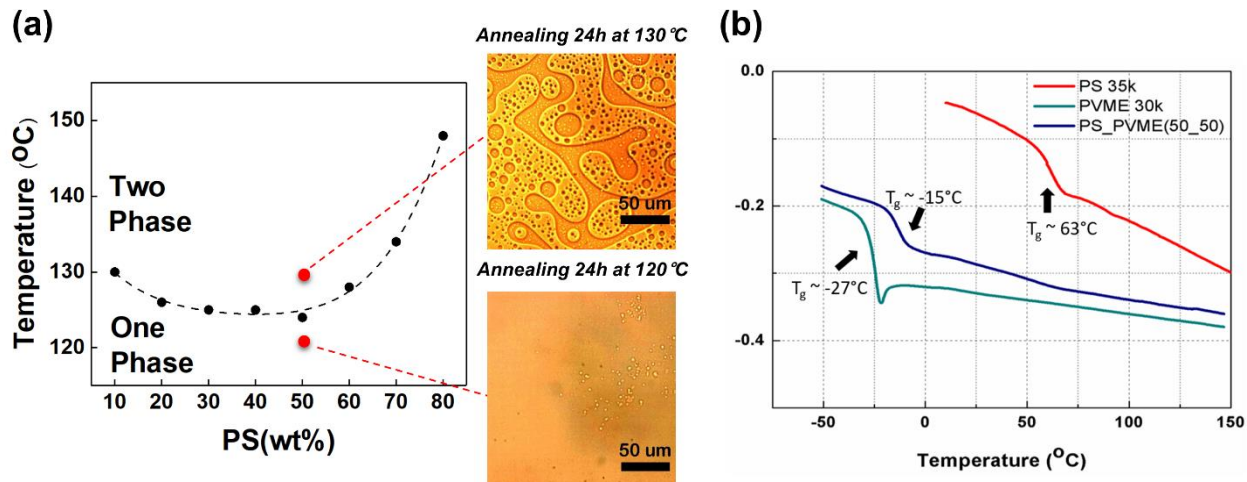


Figure 4-2. (a) A phase diagram of PS/PVME blend along with optical microscope images of a PS/PVME blend (50:50) after annealing at 120 °C for 24 h and after annealing at 130 °C for 24 h. (b) DSC traces of PS, PVEM, and a blend of PS/PVME (50/50).

Kinetics of clay orientation in a polymer solution upon the application of AC field

Figure 4-3a illustrates the top view of the sample in a real-time monitoring system. Birefringence, surface temperature, thickness, and weight changes of the sample in the square cell can be measured in the real-time monitoring system with and without application of AC field during solution drying. Figure 4-3b shows overall changes in weight, thickness, and temperature of the sample under the drying condition for 6 h. The surface temperature of the sample gradually increased and reached 93 °C 30 min after sample was loaded into the preheated chamber. This result indicates a typical drying behavior of polymer solution with a rapid initial drying rate, followed by a significantly slower drying stage. The dried sample with 45% of the initial weight and with a thickness of 0.3 mm was obtained after 6 h of drying. The orientation of clay platelets along the thickness direction of polymer films upon the application of AC field can be detected by a change of birefringence. When clay platelets are randomly dispersed in the polymer solution medium, the medium does not exhibit optical anisotropy due to randomly dispersed clay particles. However, optical anisotropy of the medium may occur when clay platelets collectively are oriented in a certain direction upon the application of AC field. Figure 4-3c shows the occurrence of out-of-plane birefringence throughout the sample by clay orientation at the very early stage of drying process. The appearance of out-of-plane birefringence ($\Delta n_{23} = 3 \times 10^{-6}$) was observed by the application of AC field (750 V/mm, 100 Hz) 100 s after the sample loading, while out-of-plane

birefringence (Δn_{23}) was not changed. This result indicates that orientation of clay platelets along the direction of film thickness induced the increase of refractive index along through-plane direction while in-plane refractive index was not changed. However, both in-plane (Δn_{12}) and out-of-plane birefringence (Δn_{23}) did not change in the absence of AC field (Figure 4-3d). Similar phenomena were reported previously from our group by using dispersed clay nanoplatelets in an epoxy precursor.⁴⁷ The detailed explanation of birefringence calculation can be found in Supporting Information.

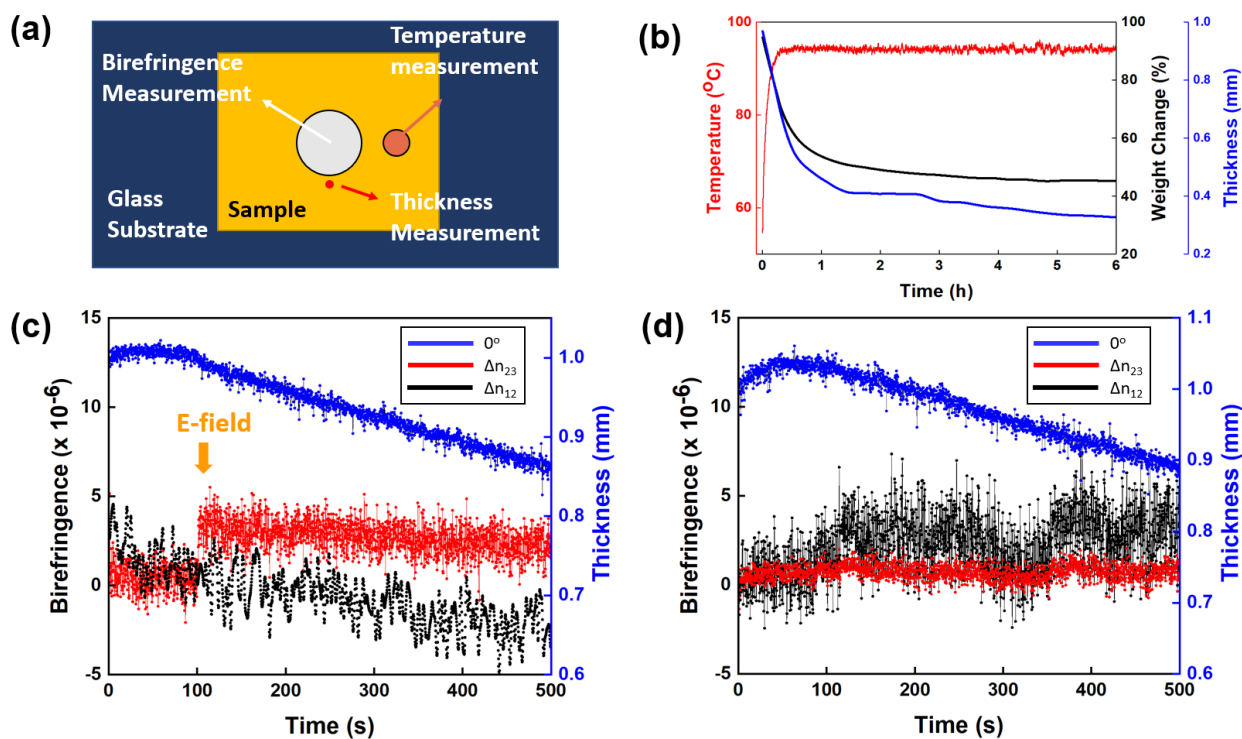


Figure 4-3 (a) Real-time monitoring system in JOEY (top view): laser micrometer measures the local film thickness, pyrometer measures the local film surface temperature, and two light sources (at 0 and 45 $^{\circ}$) measure birefringence. (b) The real-time change of weight, thickness, and surface temperature of the sample (5 vol% clay/PS/PVME/Toluene) for 6 h of drying process. (c) The instant change of in-plane birefringence (Δn_{12}), out-of-plane birefringence (Δn_{12}), and thickness upon applying AC field (750 V/mm, 100 Hz) and (d) without AC field.

Orientation of clay platelets in polymer blends

To characterize the orientation of clay platelets in dried and annealed samples, anisotropic optical properties of the samples were characterized by POM. The sample was sectioned with 1 mm thickness along the direction of film thickness and placed on a glass substrate as shown in Figure 4-4a. The sectioned sample was placed between cross-polarizers to determine optical anisotropy. Optically anisotropic sample exhibits a contrast in brightness between cross polarizers at every 45° rotation shown in Figure 4-4b. The sample prepared without AC field exhibited optical isotropy as indicated by completely black optical images at every 45° rotation (Figure 4-4c1). However, the contrast in brightness was observed every 45° rotation of the dried sample (750 V/mm, 100 Hz) between crossed polarizers (Figure 4-4c2). This result shows that the cross-sectioned sample exhibited optical anisotropy in the presence of AC field. The more detailed light retardation from the sample can be characterized by using POM with a first order red lambda (λ) plate (553 nm, red wave plate) as shown in Figure 4-4b. Clay platelets exhibit intrinsic birefringence ($\Delta n^{\circ} = \Delta n^{\circ\perp} - \Delta n^{\circ\parallel} = -0.02$), as they have refractive indices of 1.55 and 1.57 along the direction of in-plane (basal plane) and out-of-plane, respectively.⁴⁷ The λ plate, inserted at 45° with respect to polarizer and analyzer, is adding a 553 nm (red color in Michel-Levy chart) optical path difference to all optical paths under microscope. Hence, the red background color exhibited when basal planes of clay were not interfered with by the λ plate by aligning themselves parallel to either polarizer or analyzer. However, the optical-path difference is added (blue) or subtracted (orange) by the sample when basal plane is parallel or perpendicular to the direction of the λ plate (Figure 4-4d). In the presence of λ plate, the POM images of the dried sample exhibited a change in colors (red \rightarrow blue \rightarrow red \rightarrow orange) at every 45° rotation (Figure 4-4c3). Interestingly, similar color variation was observed at every 45° rotation with the annealed samples (750 V/mm and 100 Hz) (Figure 4-4c4). The result indicates that the orientation of clays was preserved during the annealing process at 150 °C in the presence of AC fields.

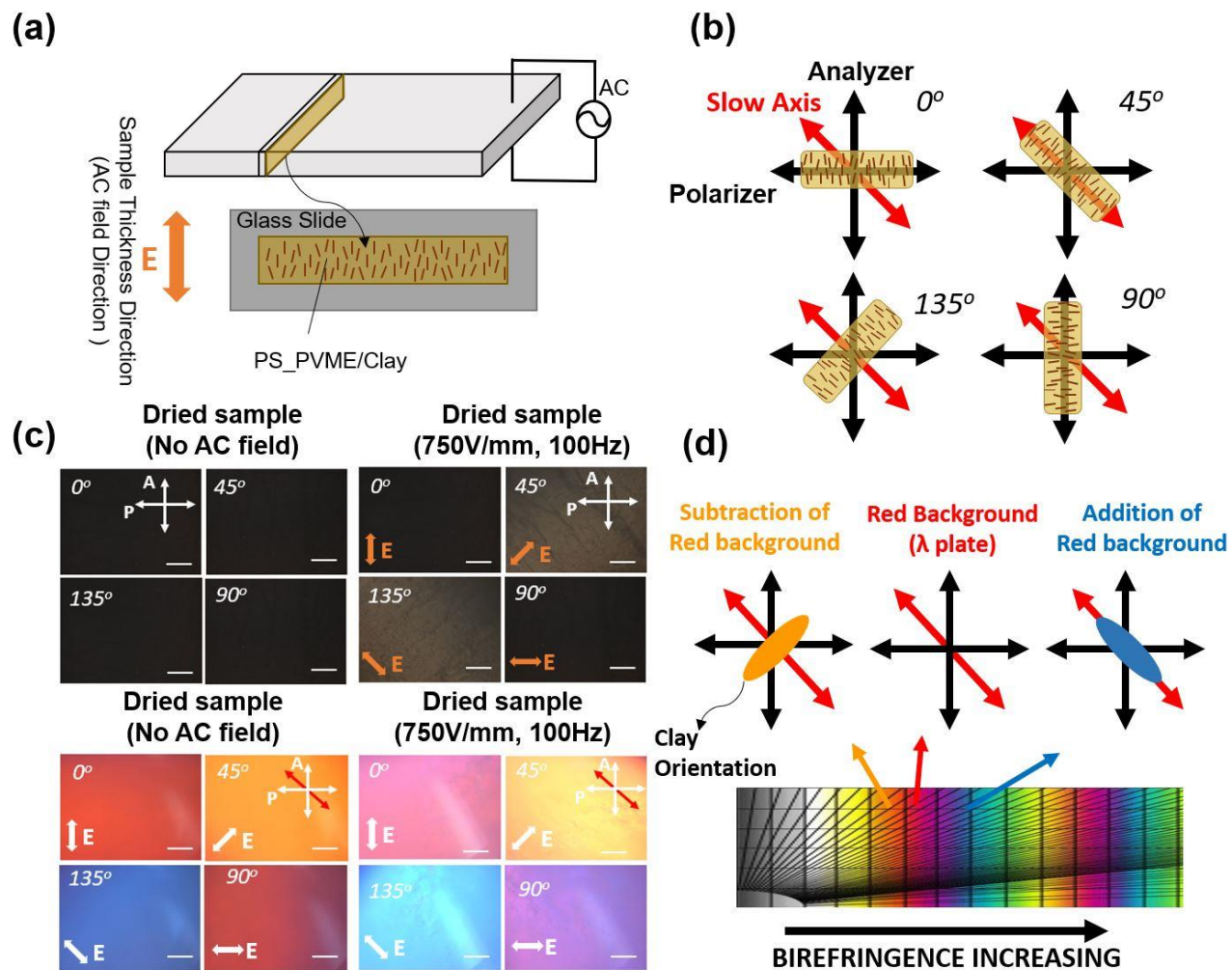


Figure 4-4 (a) Direction of sample preparation for characterizing orientation clay platelets along with AC field direction (750 V/mm, 100 Hz). (b) The direction of the sample rotation between cross polarizers along with a red wave plate. (c) POM images of samples (c1) No AC field, (c2, c3) dried sample (750 V/mm, 100 Hz), (c4) annealed sample (750 V/mm, 100 Hz). (d) Michel-Levy interference colors based on the clay orientation under cross-polarizers with a red wave plate.

2D WAXS technique was also used to determine the orientation of clay tactoids. WAXS can detect the (001) Bragg diffraction peak from non-intercalated silicate layers. Two diffusive arcs were observed along the equator on the X-ray detector for the dried sample (750 V/mm, 100 Hz) when the X-ray beam direction was orthogonal to the AC field direction (film thickness direction), whereas a uniform ring pattern was observed for the identical sample when the X-ray beam direction was parallel to the AC field direction (Figure 4-5a). This result indicates that the basal planes of the clays were oriented parallel to the AC field direction (“Z” direction) without preferential orientation to the in-plane direction. The plot of intensity versus the azimuthal angle shows the anisotropy of each scattering. Strong intensities at 90° and 270° azimuthal angles indicate anisotropic scattering, whereas a flat plateau represents isotropic scattering. The effect of the AC field intensity on the orientation of clay platelets (the dried samples) was also examined with an exposed X-ray beam orthogonal to the AC field direction (Figure 4-5b). In absence of AC field, the basal planes of clay nanoplatelets were likely oriented to in-plane direction of the film after drying as indicated by lower intensities at 90° and 270° of azimuthal angles. However, the intensities at 90° and 270° were slightly increased when AC field with a strength of 500 V/mm was applied. These intensities were more enhanced for the sample prepared with a strength of 750 V/mm (100 Hz), as clays were preferentially oriented to AC field direction. The orientation order parameters were 0, 0.3, and 0.36 when AC field strength was increased from 0 V/mm to 500 V/mm and 750 V/mm, respectively. Figure 4-5c shows the (001) lattice spacing of clay platelets calculated by the q_{\max} peak. Clay powders show q_{\max} at 1.752 nm^{-1} , with a corresponding lattice spacing of 3.57 nm, whereas clays in PS/PVME blends show $q_{\max} = 1.558 \text{ nm}^{-1}$, with a corresponding lattice spacing of 4.03 nm. The result suggests that lattice spacing of clay platelets was expanded in a polymer medium by interactions between polymer chains and clay platelets.

Furthermore, the orientation of clay platelets along the direction of AC field was well preserved after the annealing process (Figure 4-6a). This result is in agreements with the POM images (Figure 4-4e). The result shows that the shape of intensity plot at 90° and 270° from the samples, before and after annealing, was similar despite a slight decrease in the intensity. The orientation order parameters decreased from 0.36 to 0.3 after annealing process (Figure 4-6b).

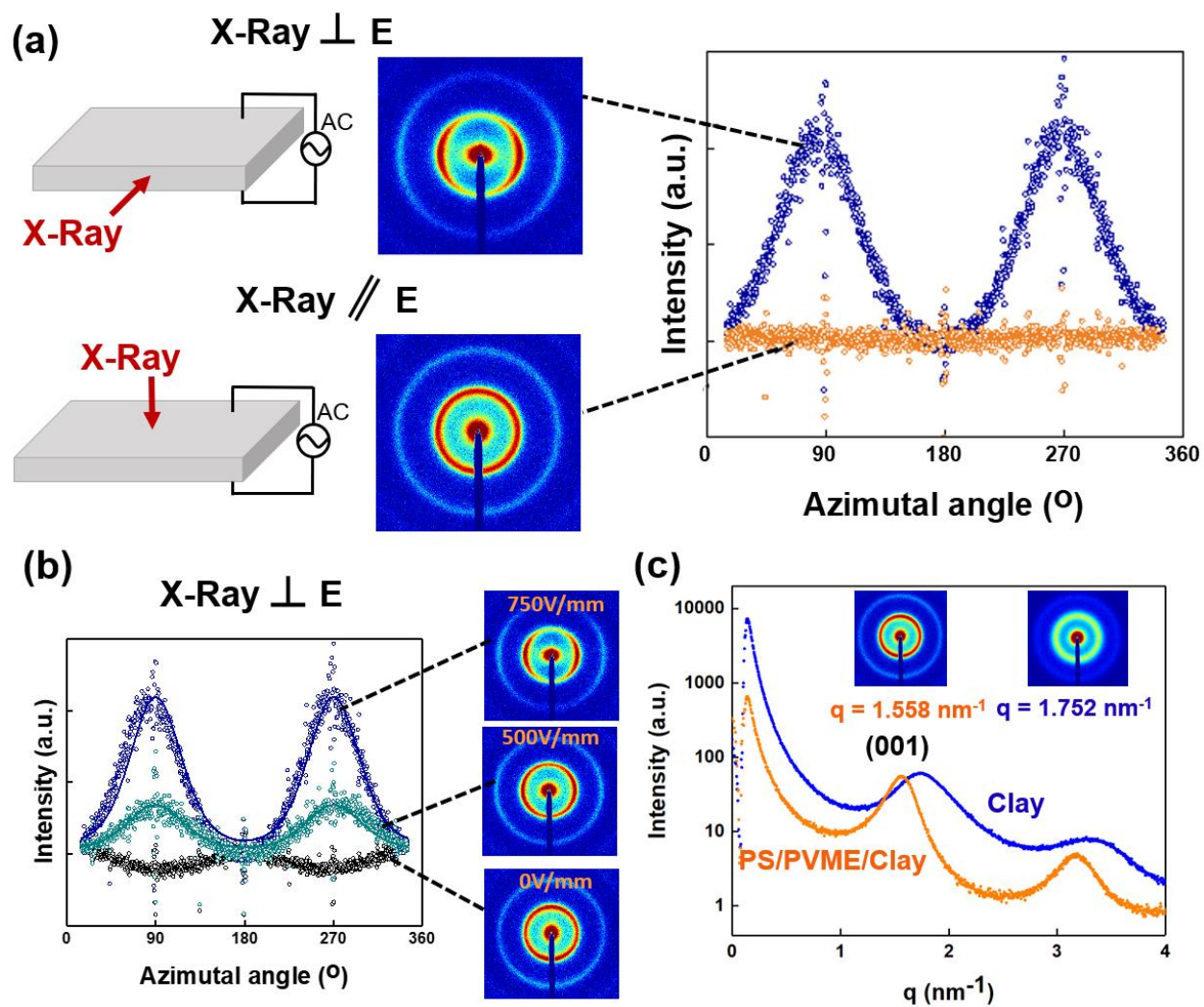


Figure 4-5 2D WAXS patterns of the dried sample (750 V/mm, 100 Hz) when X-ray beam direction was the orthogonal and parallel to the applied AC field. (b) 2D WAXS patterns (X-ray \perp AC field) of the dried samples dried with different AC fields. (c) Q vs intensity peak of a pure clay powder and a clay composite.

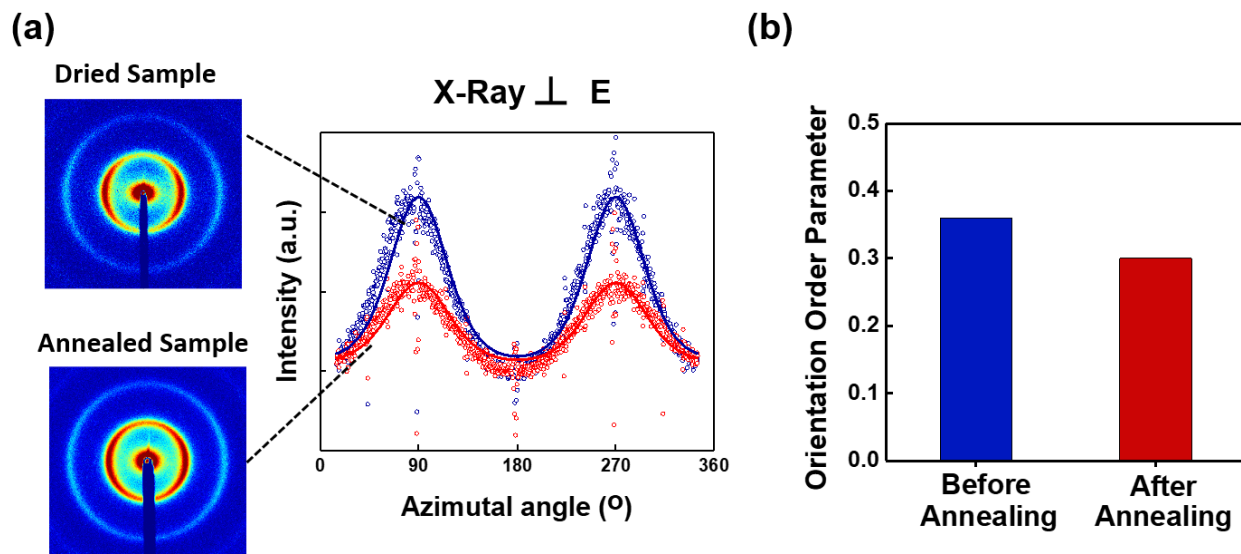


Figure 4-6 (a) 2D WAXS patterns (X-ray \perp AC field) of the dried sample (750 V/mm, 100 Hz) and the annealed sample (750 V/mm, 100 Hz). (b) Orientation order parameter before and after the annealing.

Morphology of phase-separated polymer blends with dispersed clay platelets

The detailed local morphology of the annealed sample (no AC field) was investigated by TEM. TEM image shows the morphology of dispersed PS droplets ($\sim 5 \mu\text{m}$) surrounded by a PVME phase after 30 min of annealing in the absence of AC field (Figure 4-7a). The anisotropic shape of the clay platelets with a length ranging from 100 to 1000 nm were all observed in the PVME matrix as they wrapped around the PS droplet phases. Some aggregated clay nanoplatelets formed a micron-sized clay cluster on the upper right corner of TEM image. The magnified TEM image shows the detailed information of a single clay nanoparticle (Figure 4-7b). The single clay nanoparticle with a length of 173 nm and a width of 28.1 nm was observed in the PVME domain. Nine layers in direction of width of the particle indicated that the layer–layer spacing of Cloisite 15A is about 3.5 nm. The result approximately agrees with a lattice spacing of 3.57 nm of non-intercalated clay platelets determined by X-ray scattering experiments.

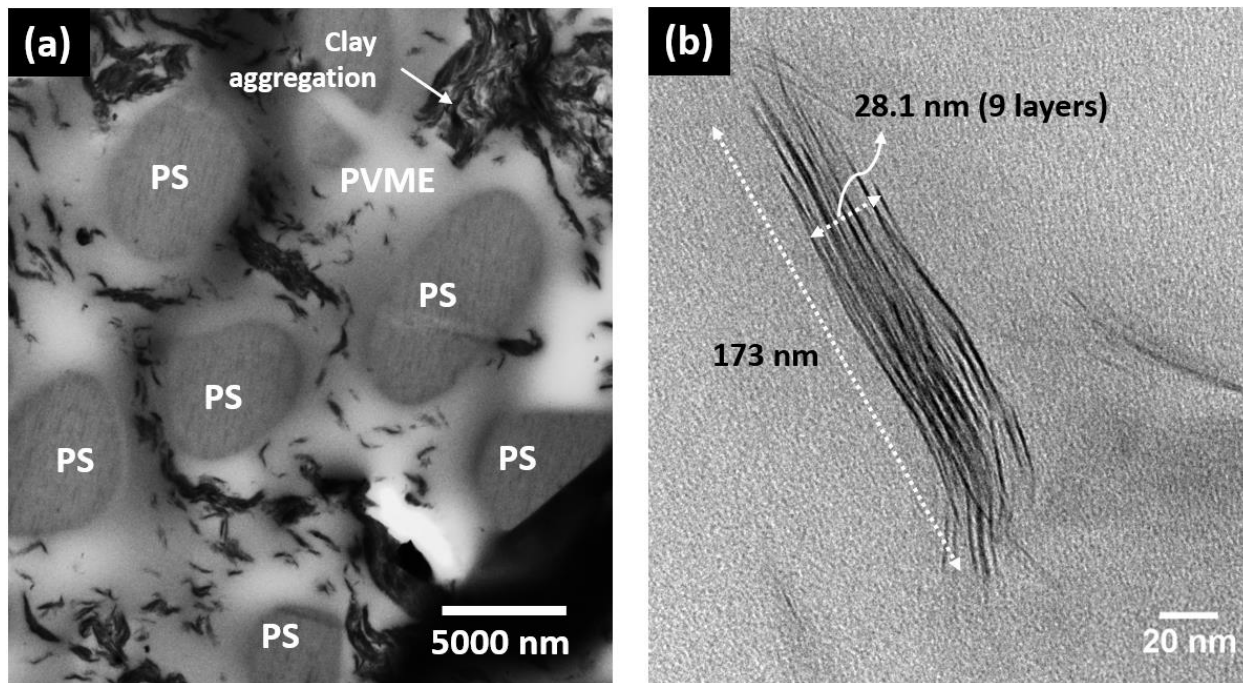


Figure 4-7 (a) TEM image of a PS/PVME blend with clay platelets after annealing. (b) Magnified TEM image of a clay tactoids.

A single layer of montmorillonite clays consists of an octahedral sheet sandwiched by two tetrahedral sheets with a thickness of 1 nm is shown in Figure 4-8a. The length and width of a single sheet of montmorillonite clay mineral can range from a few nanometers to several microns.²⁰⁶ Furthermore, the face-to-face stacked structure of clay minerals exhibits very different shapes of the edges. The common shapes of clay platelets such as rhomb, lamellar, and lath are shown in Figure 4-8b. AFM tapping mode can be used to distinguish phases with different material properties such as modulus, adhesion, and viscoelasticity. Thus, each PS/PVME and clay phase can be distinguished by AFM, as they have different stiffness values. The cross-sectioned surface morphology of the annealed sample was characterized by AFM. The detailed shape and size of the clay platelets in the blend was revealed in small-scale image ($1 \mu\text{m} \times 1 \mu\text{m}$). The surface topology of AFM height images ($1 \mu\text{m} \times 1 \mu\text{m}$), with sub-micron surface roughness, pictured the edges of aggregated clay platelets in blends (Figure 4-9a). The shapes of the clay platelets were more clearly identified in an AFM phase image, as a stiffness difference between rigid inorganic clay platelets and soft polymers provides good contrast to depict the edges of clay particles in AFM phase images (Figure 4-9b). Clay platelets ranging from tens to hundreds of nanometers appeared bright while the soft polymers appeared dark on the cross-sectioned surface. They were also aggregated and

formed a cluster on the cross-sectioned surface. Most of the clay platelets showed subhedral lamellar structures with irregular edges rather than hexagonal lamellar structures with straight edges and 120° angles. It may be due to fracture of clay particles during the mixing which is common to montmorillonite.²⁰⁷ The cornflake-like structures of montmorillonite were found in others' AFM phase images of clay minerals.^{59,60} Figure 4-9c shows $5\ \mu\text{m} \times 5\ \mu\text{m}$ AFM scan image of cross-sectioned surface. The result shows that the aggregation of clay platelets with $\sim 100\ \text{nm}$ size took place up to several microns. In $5\ \mu\text{m} \times 5\ \mu\text{m}$ scan scale, phase separated PS/PVME domains were also identified. As indicated by TEM image, clay platelets were mainly located in the PVME phase (bright phase in AFM image).

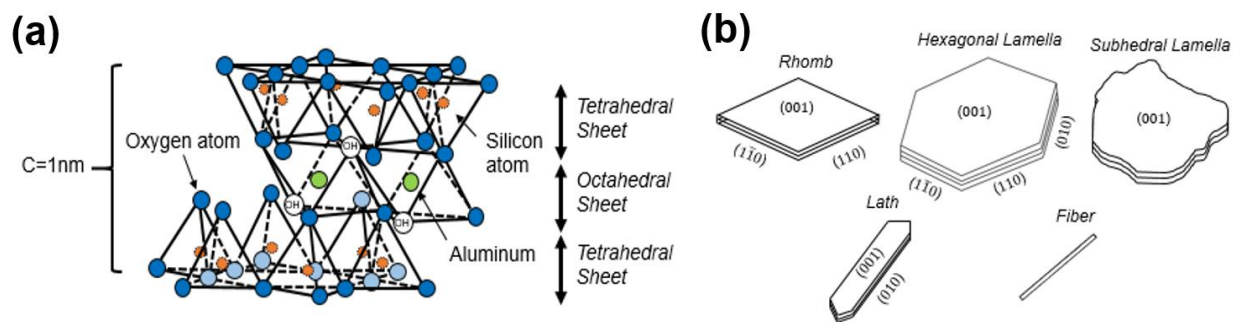


Figure 4-8. (a) Atomic structure of montmorillonite basic crystal unit. (b) Shapes of clay mineral particles and aggregates. AFM images of the annealed sample.

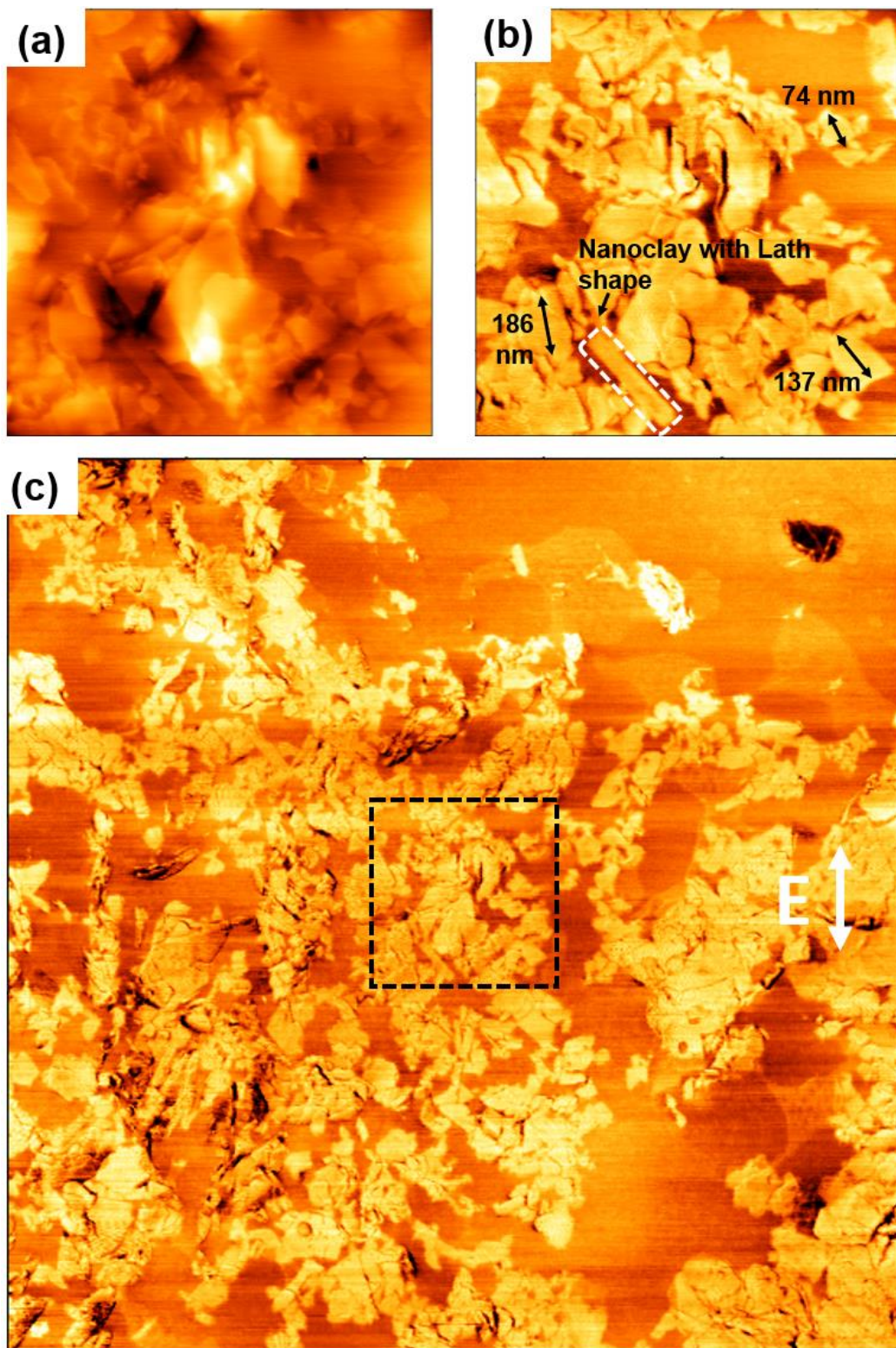


Figure 4-9. (a) $1\ \mu\text{m} \times 1\ \mu\text{m}$ height ($\Delta z = 34\ \text{nm}$) and (b) phase AFM images and (c) $5\ \mu\text{m} \times 5\ \mu\text{m}$ phase AFM images of the annealed sample (750 V/mm, 100 Hz). Figure (a) and (b) are a corresponding region of a black square in Figure (c).

Large-scale AFM images ($25\ \mu\text{m} \times 25\ \mu\text{m}$) show the morphology of aggregated clay nanoplatelets on the prepared cross-sectioned dried and annealed sample. In the dried sample, micron-sized clusters ($\sim 5\ \mu\text{m}$) of clay platelets were found in a homogeneous PS/PVME blend (Figure 4-10). The micron-sized clay clusters were likely oriented along the direction of AC field. The phase-separation between PS and PVME were not observed in the dried sample. Interestingly, the three different phases (clays, PS, and PVME) were clearly distinguished in the annealed sample (Figure 4-11). Micron-sized clusters of clay platelets were also observed, along with phase-separated PS and PVME phases. Most of the aggregated clays were located in PVME phases (bright phase in AFM). The morphology of droplets of PS phases surrounded by a PVME matrix is also in agreement with TEM morphology. The phase-separated morphology, with submicron or several-micron sized PS droplet phases dispersed in a PVME matrix phase, did not show an oriented morphology parallel to AC field direction. It is also worth noting that the degree of clay aggregation increased after the annealing process. One reason is the process of phase separation between PS and PVME probably pushed clusters into and aggregated clusters in the PVME phases.

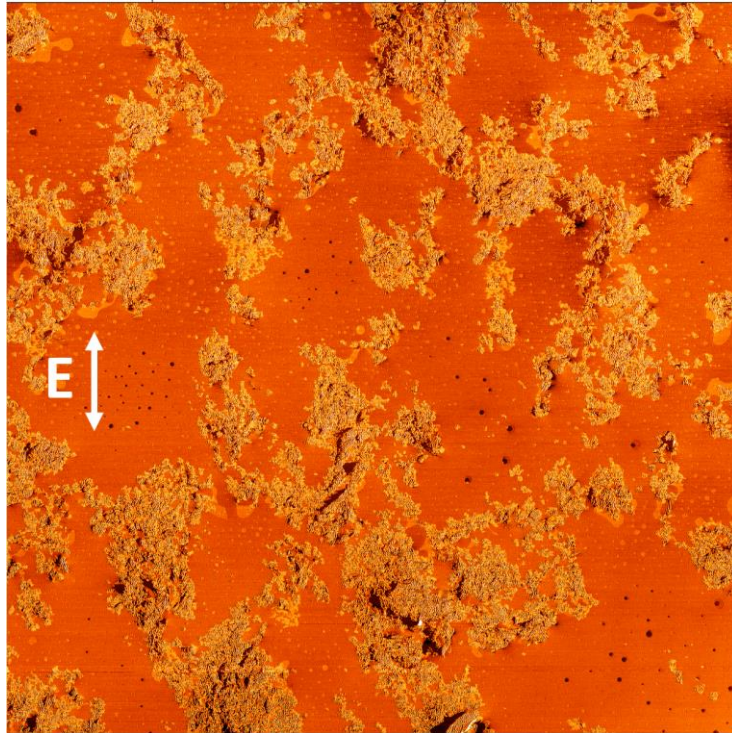


Figure 4-10 Cross-sectional AFM phase image ($25\ \mu\text{m} \times 25\ \mu\text{m}$) of the dried sample (750 V/mm, 100 Hz).

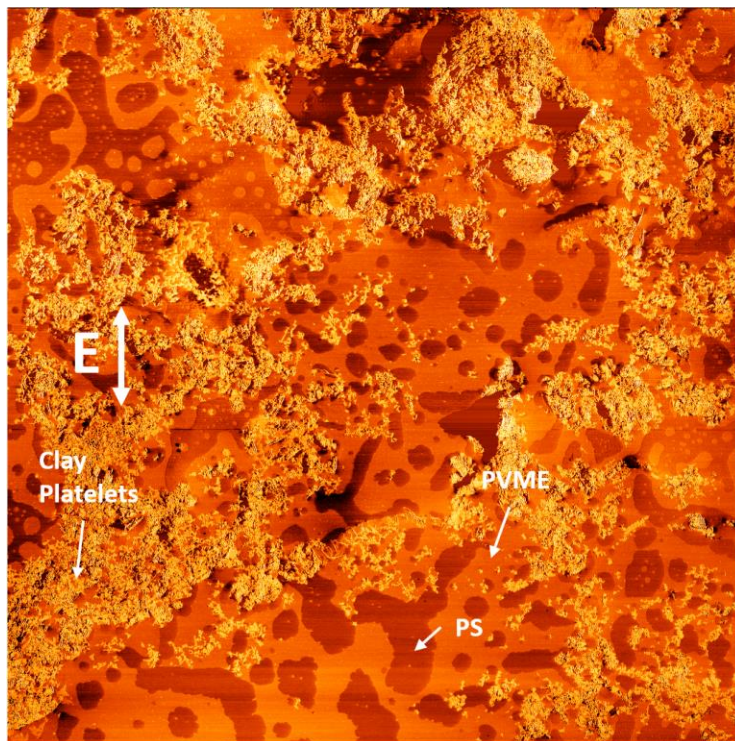


Figure 4-11. Cross-sectional AFM phase image ($25\ \mu\text{m} \times 25\ \mu\text{m}$) of the annealed sample (750 V/mm, 100 Hz).

The larger-scale phase-separated morphology of a PS/PVME blend was characterized by SEM. In the SEM picture, the clean surfaces are denoted by PS domains with less electron scattering of non-dissolved surface, whereas rough surfaces are indicated by slightly dissolved PVME domains with clay platelets and with high electron scattering. Some of the aggregated clay particles ($\sim 5 \mu\text{m}$) in the etched PVME phases were observed for the annealed sample without AC field, although many of clay particles were probably washed out during methanol etching process (Figure 4-12a). The PS/PVME phase-separated morphology was completely isotropic in the absence of AC field. However, PS domains tens of microns in size surrounded by a PVME matrix were likely to be elongated along the direction of the film thickness in the presence of AC field (Figure 4-12b). It was likely that anisotropic phase separation occurred on a large scale ($>10 \mu\text{m}$) rather than on the submicron or micron scale. This is also confirmed that the submicron phase-separated morphology of PS/PVME in the $25\mu\text{m} \times 25\mu\text{m}$ AFM scan images did not show anisotropic phase-separated morphology (Figure 4-11). Anisotropic phase-separation in large scale is probably due to the oriented clay clusters in the blend. The aggregation of clay nanoparticles ($\sim 5 \mu\text{m}$) and their orientation along the applied AC field direction resulted in a directionally organized phase-separated morphology tens of microns in size. As indicated by local morphological information by AFM, submicron phase separation in the early stage of the phase separation occurred independently in the presence of oriented large clay clusters ($\sim 5 \mu\text{m}$). As the phase separation was undergone, the PS droplets increased and oriented along the AC field direction due to the oriented clay clusters ($\sim 5 \mu\text{m}$). Therefore, anisotropic phase separation was only observed in large-scale images as shown in Figure 4-12.

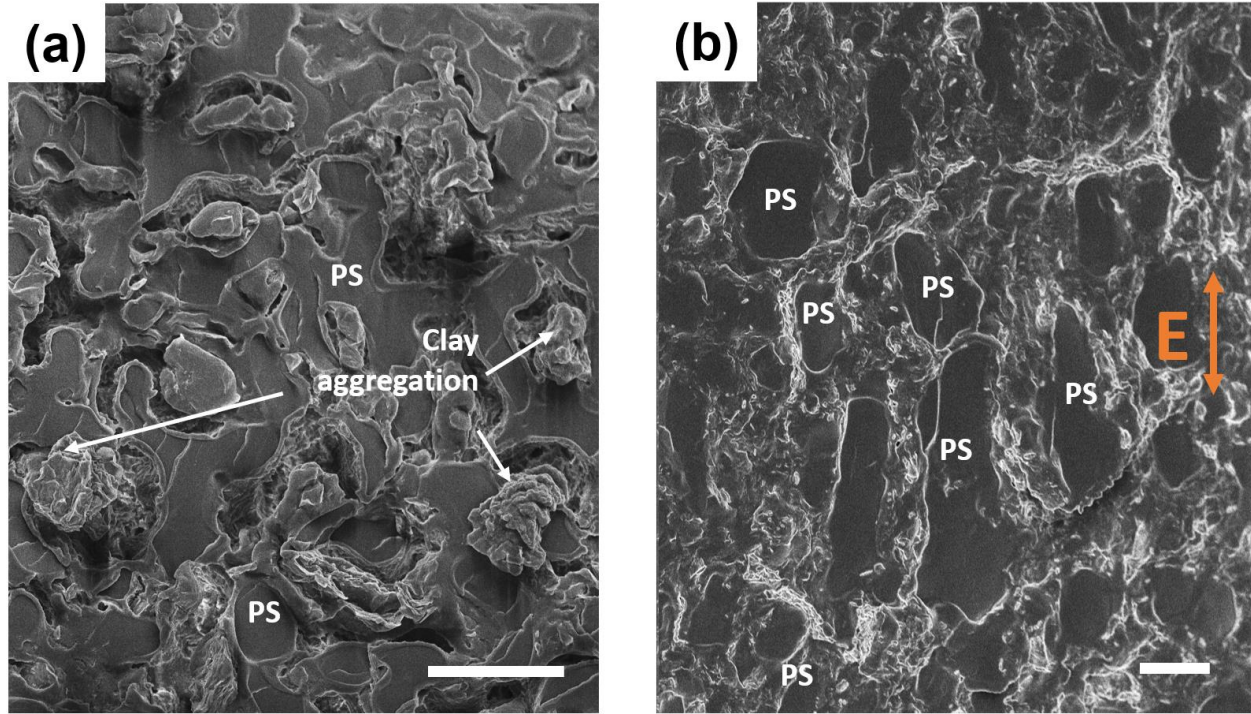


Figure 4-12. (a) Cryo-fractured cross-sectional morphology of the annealed sample (a) without AC field and (b) with AC fields (750 V/mm, 100 Hz) by SEM imaging. (Scale bar: 10 μm)

Thermodynamic prediction of clay location in blends

The location of clay nanoplatelets in a binary blend at equilibrium state can be estimated by considering the wetting coefficient of the system. According to Young's equation, wetting coefficient (ω) is determined by interfacial energies between blend components as shown in equation (1). If $\omega < -1$, the nanoplatelets enrich phase A due to low interface energy between the nanoplatelets and A phase. If $\omega > 1$, the nanoplatelets enrich the phase B. If $-1 < \omega < 1$, the nanoplatelets are localized at the interface between A and B.

$$\omega = \cos \theta = \frac{\gamma_{NP/A} - \gamma_{NP/B}}{\gamma_{A/B}} \quad (1)$$

Because the interfacial energies between the clay nanoplatelets and molten PS or PVME are difficult to evaluate experimentally, they were estimated from known surface energies of the

components. According to Owens–Wendt–Rabel–Kaelble (WORK) approximation, the interfacial energy between two materials can be predicted based on the surface energies of the components and their dispersive and polar contributions, as shown equation (2).^{103,208}

$$\gamma_{A/B} = \gamma_A + \gamma_B - 2 \left(\sqrt{\gamma_A^d \gamma_B^d} + \sqrt{\gamma_A^p \gamma_B^p} \right) \quad (2)$$

The surface energies of the PS and PVME were determined by the contact-angle values of water and methylene iodide on the polymer surface, and the surface energy of clay nanoplatelets was referred from the literature.⁸⁴ The final surface energies of polymers at the annealing temperature were extrapolated from the values in the literature and are shown in Table 4-1. The values of interfacial energies for the polymer–polymer and polymer–clay interfaces were estimated by surface energy of each material. Interfacial energies, wetting coefficient, and predicted location of clay nanoplatelets are summarized in Table 4-2. The value of the wetting coefficient ($\omega = -0.27$) indicates that clay nanoplatelets should be located at the PS–PVME interface at the thermodynamic equilibrium state.

Table 4-1. The surface energies of the pure materials and their dispersive and polar contributions at room temperature ($T = 20\text{ }^{\circ}\text{C}$) and at $T = 150\text{ }^{\circ}\text{C}$.

Material	Surface energy at room temperature [mN/m]			Temperature coefficient $\left(\frac{\partial\gamma_i}{\partial T}\right)$ [mN/m $^{\circ}\text{C}$]	Surface energy at $T = 128\text{ }^{\circ}\text{C}$ [mN/m]		
	Total (γ_i)	Dispersive (γ_i^d)	Polar (γ_i^p)		Total (γ_i)	Dispersive (γ_i^d)	Polar (γ_i^p)
PS ^a	42 mJ/m ²	41.4 mJ/m ²	0.6 mJ/m ²	-0.072	34.2 mJ/m ²	33.7 mJ/m ²	0.5 mJ/m ²
PVME ^b	59.5 mJ/m ²	35.5 mJ/m ²	24 mJ/m ²	-0.07	51.9 mJ/m ²	31.0 mJ/m ²	20.9 mJ/m ²
Cloisite 15A ^c	45.3 mJ/m ²	33.4 mJ/m ²	11.8 mJ/m ²	-0.136	31.0 mJ/m ²	23.6 mJ/m ²	7.4 mJ/m ²

^a From Macromolecules, 2015, 48, 4631–4644.

^b From Surface and Interfacial Properties, in Physical Properties of Polymers Handbook, ed. J. E. Mark, Springer, New York, 2nd edn, 2007.

^c From Soft Matter, 2014, 10, 9270–9280.

Table 4-2. Predictions of clay nanoplatelets based on the wetting coefficient.

Material	Interfacial energy [mN/m]	Wetting coefficient (ω)	Location of clay platelet
PS/PVME/Clay	PS/PVME = 14.99 PS/Clay = 5.65 PVME/Clay = 9.5	-0.27	Interface

This value indicates that the clay platelets are supposed to be at the interface between PS and PVME. However, our experimental results show that clay platelets were found in a PVME domain. In this study, the thermodynamic prediction of clay location is not in agreement with our experimental findings.

Lastly, Figure 4-13 summarizes two scenarios for the evolution of phase-separated morphology with non-oriented and oriented clay platelets. Clay platelets were oriented randomly dispersed in the through-plane direction during the drying process of the polymer solution. Then, PS/PVME isotropic phase separation occurred in the presence of randomly dispersed clay platelets (Figure 4-13a). However, anisotropic phase separation appeared in the through-plane direction in

the presence of electrically oriented clay platelets. Clay platelets were oriented parallel to through-plane direction in a mobile medium of polymer solution during the drying process. After drying, oriented clay clusters with size of $\sim 5 \mu\text{m}$ produced an anisotropic PS/PVME morphology tens of microns in size by pushing away PS domains during the annealing process.

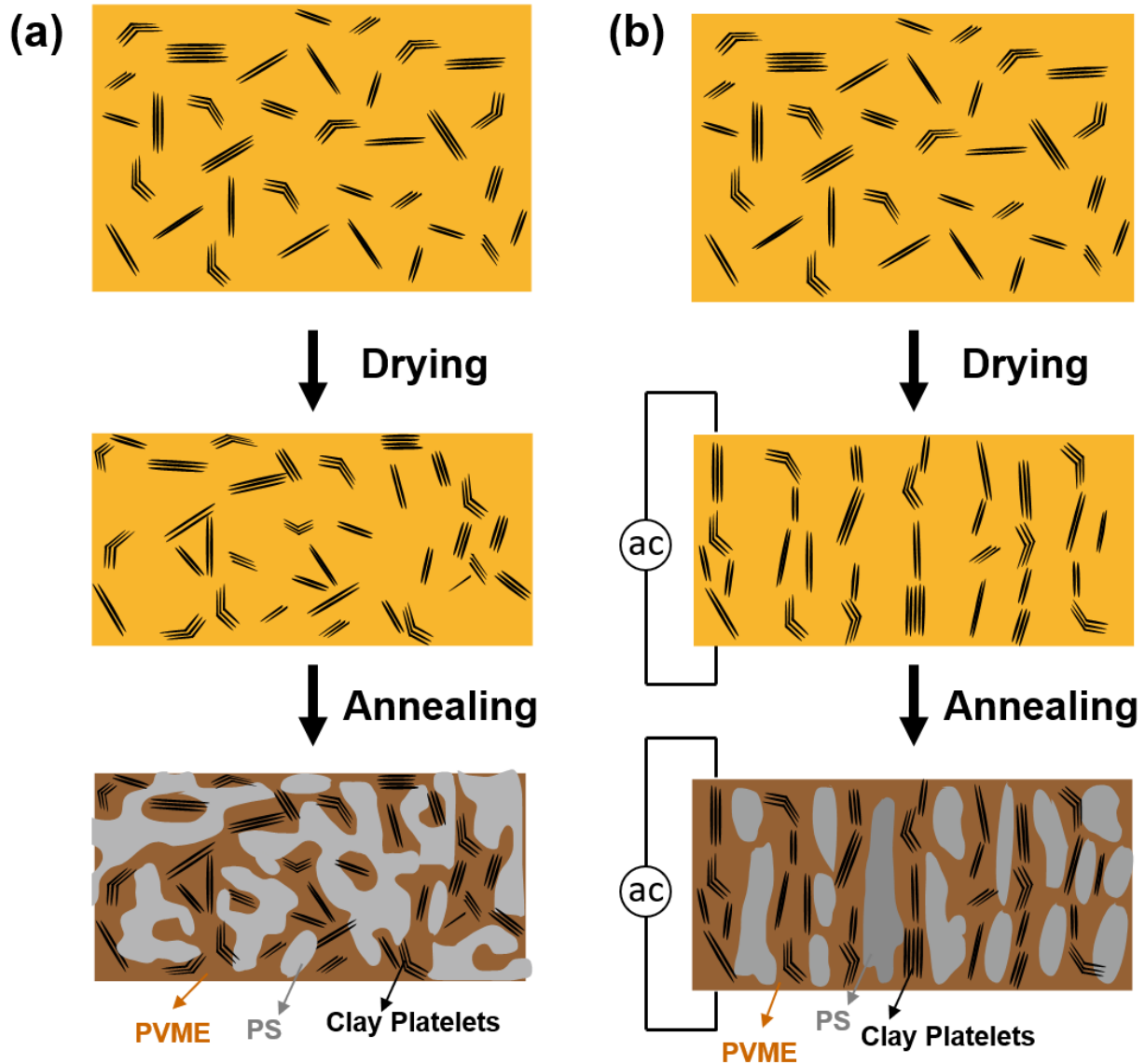


Figure 4-13. Cross-sectional phase-separated morphology of polymer blends with (a) randomly dispersed clay platelets and (b) with oriented clay platelets.

4.3 Conclusion

We demonstrated that the phase-separated morphology of a PS/PVME polymer blend could be controlled by oriented clay platelets in the through-plane direction. The basal plane of the clay platelets was oriented in direction of the film thickness by applying AC field during the drying process. Upon heating above the critical temperature while AC field was continuously applied, elongated PS domains tens of microns in size appeared in the through-plane direction in the presence of oriented clay platelets. Preferential location of clays in PVME probably promoted anisotropic diffusion of PS domains in the through-plane direction in the PVME matrix. Development of an anisotropic morphology by using highly polarizable nanoparticles in AC field provides a general method to produce anisotropic polymer films, which are promising for proton membranes and organic photovoltaic applications.

5. ANISOTROPIC HYDROGELS FORMED BY MAGNETICALLY ORIENTED NANOCCLAY SUSPENSIONS FOR WOUND DRESSINGS

In this chapter, anisotropic hydrogels are produced by magnetic alignment of magnetically sensitized nontronite (natural clay minerals) followed by polymerization of the hydrogel to freeze the developed oriented structure in place. The anisotropy in these hydrogels is quantitatively investigated using birefringence and 2D small-angle X-ray scattering (SAXS) techniques. The oriented natural nontronite, being intrinsically birefringent, provides optical anisotropy to the hydrogel, and this orientation increases with an increasing applied magnetic field strength. Moreover, 2D SAXS patterns also confirm that the nanoclays are oriented parallel to the permanent magnetic field in the hydrogel with an orientation order parameter of up to 0.67. The field-induced birefringence and 2D SAXS orientation results exhibit a linear correlation over the range of 0 to 9 tesla (T). The anisotropic hydrogels exhibit anisotropic optical transparency and compressive mechanical properties parallel to nanoclay orientation direction. Furthermore, the anisotropic hydrogels exhibit substantial swelling anisotropy, making them suitable for wound dressings where the out-of-plane swelling is substantially higher than in-plane swelling to minimize in-plane stress damage to the wounds during healing. This chapter contains content reproduced from Ref. 209 with permission from The Royal Society of Chemistry.

5.1 Introduction

Nanocomposite hydrogels are materials that possess nanoparticles within hydrogel networks. By adding nanoparticles into a hydrogel network, additional functionalities such as mechanical strength,^{210,211} transparency,¹³⁷ swelling kinetics,^{141,212} and conductivities²¹³ can be introduced. Since nanoparticles are randomly dispersed within the three-dimensional (3D) cross-linked network of hydrogels, the structure of nanocomposite hydrogels is usually isotropic. However, control of the nanostructure in hydrogels is often required, for example, to mimic anisotropic mechanical features in natural organisms²¹⁴⁻²¹⁶ or to fully exploit directional mechanical, optical, or electrical properties.^{115,158,159}

Anisotropic swelling is particularly sought after for wound dressing, where the vertical wicking of the exudates is preferred because the lateral movement of the fluid to periwound skin may cause maceration through continued exposure to moisture.²¹⁷ Vertical wicking also increases

the rate of wound healing by locking the fluid in the core wound.²¹⁸ It was reported that the vertical alignment of superabsorbent nanoparticles in polyurethane reduced the lateral swelling of polyurethane by 33%.²¹⁹ It was also shown that the copolymeric gel film exhibited a 40% increase of swelling in vertical direction when the side chain of crystal structures were vertically oriented.²²⁰ These reports show that the direction of swelling can be influenced by the oriented nanostructures in hydrogels.

The most common approach for fabricating anisotropic nanocomposite hydrogels is to orient colloidal nanoparticles in monomer precursors and arrest the aligned nanoparticles in a cross-linked structure by hydrogelation.¹⁵⁴ To orient nanomaterials in a low-viscosity medium before polymerization reaction, the utilization of external shear,^{156,221,222} electric,^{47,111,157} or magnetic^{115,121,158} fields has been proposed. External electric field is used to orient nanomaterials by taking advantage of permanent or induced dipoles in nanomaterials. Although the precise control and assembly of nanoparticles can be achieved by this method,^{223,224} the electrical breakdown in high-strength fields and/or electrophoretic migration of nanoparticles are challenging. In contrast, magnetic fields may have an advantage over other external fields, as they can be uniformly subjected to materials by non-contact and non-destructive ways without any geometrical constraints.

To orient diamagnetic colloidal nanomaterials by using magnetic force, the energy reduction by the orientation of nanomaterials in the magnetic fields should overcome the thermal energy (kBT) that can disorder them.^{136,225,226} For the significant free-energy reduction in the presence of magnetic fields, the anisotropy of diamagnetic susceptibility in nanomaterials should exist. Although anisotropic 1D or 2D nanoparticles often exhibit anisotropy in the magnetic susceptibility originating from their shape, its value is much too small for aligning them under magnetic field strengths obtained from ordinary electromagnets. Nevertheless, the alignment of diamagnetic nanoparticles or block copolymers containing aromatic molecules at the field strengths of a few tesla has been reported.^{115,136} This has been accomplished by taking advantage of the high anisotropy in diamagnetic susceptibility of rigid aromatic molecules, originating from the strong diamagnetic aromatic ring current effect.^{116,227} On the other hand, the ferromagnetic nanoparticles (iron, nickel, cobalt) can be aligned in relatively moderate magnetic fields (< 1 tesla) because they have fairly high magnetic susceptibilities.²²⁸

Swelling clay minerals are natural anisotropic materials composed of metallic oxides that form layered structures. They can form stable colloidal suspensions in water with negative charge on the surface and exchangeable cations between the interlayers. For this reason, the clay aqueous suspensions can easily be incorporated into hydrogels.^{137,229} Among various types of clay minerals, nontronite is a unique clay mineral which has high levels of ferric ions (Fe^{3+}). It has a similar structure to the montmorillonite clays, except that most aluminum ions in the octahedral sheet are replaced by ferric ions. Due to the high ferric (III) ion content in nontronite clays, they are fairly sensitive to magnetic fields. There have been several reports regarding the magnetic orientation of aqueous nontronite minerals^{124,230,231} by using moderate magnetic field strength. However, all subsequent studies were limited to liquid-crystalline behavior of nontronite clay aqueous suspensions. To gain a better understanding of the structure of anisotropic hydrogels, which becomes important for practical applications, further quantitative characterization of these materials synthesized under different magnetic field strengths is necessary.

In this work, we demonstrated anisotropic nanoclay hydrogels by arresting magnetically oriented nontronite nanoclays through the synthesis of hydrogels. The internal anisotropic nanostructure of nanoclay hydrogels was characterized by the measurement of the field-induced birefringence and 2D SAXS. The various anisotropic nanoclay hydrogels were synthesized by controlling the permanent magnetic field strength and nanoclay concentrations. The swelling anisotropy of the resultant hydrogels was also demonstrated.

5.2 Experimental section

5.2.1 Materials

The natural clay mineral (NAu-2) was purchased from Clay Minerals Society at Purdue University. Acrylamide, N,N'-Methylenebis (acrylamide) (MBAA), ammonium persulfate (APS), and N,N,N',N'-Tetramethylethylenediamine (TEMED) were purchased from Sigma-Aldrich and used as received.

5.2.2 Sample preparation

Nanoclay preparation: 0.2 g of raw clay minerals (Nau-2) was ground and dispersed in 20 ml of deionized (DI) water by ultrasonication. For the size fractioning, the clay mineral suspension

was centrifuged at $15,000 \times g$ for 30 minutes. After large clay particles were precipitated, the supernatant of the solution was collected. The collected supernatant was dried in a vacuum oven overnight, and then a powder of nanoclays was obtained. By fractionating the size of clay particles, most of impurities in N Au-2 can be removed.⁵² The nanoclay aqueous suspensions with different concentrations (0.05 wt%, 0.1 wt%, 0.2 wt%, and 0.4 wt%) were prepared by dispersing nanoclays in DI water with ultrasonication. The resultant nanoclay colloidal suspensions were stable over a couple of weeks without any precipitation.

Synthesis of nanoclay hydrogels: Acrylamide (0.15 g) and cross-linker MBAA (0.0075 g) were dissolved in the nanoclay aqueous suspension (4.5 g). After complete mixing, the mixture was degassed by bubbling with dry nitrogen gas for 10 min. Then, the initiator (20 mg/ml aqueous solution of APS, 5 μ L) and catalyst (TEMED, 5 μ L) were added to the mixture. The mixture was loaded in a 1 ml cylindrical vial or a 4.5 ml glass cuvette. The samples were placed in the chamber equipped with a superconducting magnet at 27 °C for 90 min. After 90 min, the mixture turned into an anisotropic nanoclay hydrogel. By keeping the concentration of the monomer, cross-linker, initiator, and catalyst constant, hydrogels were synthesized by the same procedure with different nanoclay concentrations and magnetic field strengths. The magnetic fields were applied to the mixture by using the physical property measurement system (PPMS, Quantum Design). In PPMS, the magnetic field was generated by a superconducting solenoid around the chamber. The solenoid can generate a vertical magnetic field in the chamber up to 9 tesla.

5.2.3 Sample characterization

Powder X-ray diffraction: Nanoclay samples after fractioning size were ground with mortar and pestle and packed in an X-ray sample holder. Powder X-ray diffraction data were collected on a Bragg–Brentano diffractometer (Panalytical Empyrean) with a Cu K α radiation (1.541 Å). X-ray data were collected between 5° and 90° using the Panalytical Data Collector software.

Birefringence measurements: The birefringence was measured by a custom-built machine utilizing an automated birefringence system. The details about the design and capabilities of this machine can be found elsewhere.²⁰⁵ Briefly, this machine can measure various properties of materials including optical retardation (birefringence) and transmission. The in-plane retardation

was obtained by subtracting initial retardation of isotropic hydrogel sample from the retardation of the anisotropic hydrogel samples. Then the birefringence was simply calculated by dividing the in-plane retardation with respect to sample thickness as shown by

$$\Delta n_{12} = \frac{\text{Retardation}}{\text{Thickness}} \quad (1)$$

2D SAXS measurements: The anisotropic nanoclay hydrogels were prepared in the glass capillary with closed ends (1.5 mm diameter, 0.01 mm wall thickness) to carry out the 2D SAXS experiments. SAXS experiments were performed by an Anton Paar SAXSpoint 2.0. X-ray beam with monochromatized Cu K α radiation (1.541 Å) was used for the experiments. The sample-to-detector distance was 1.075 m and the X-ray exposure time was 30 minutes for each sample. The azimuthal plots were constructed by integrating the intensity of the scattering patterns from $q = 0.07 \text{ nm}^{-1}$ to $q = 0.45 \text{ nm}^{-1}$ for every 1° by using SAXS analysis software offered by Anton Paar.

Rheological measurements: The viscosity of hydrogel precursor solution was measured by using a rheometer (Bohlin Gemini HR Nano 200) at room temperature during the polymerization reaction. The viscosity of solution was observed with time at constant shear rate (10 s^{-1}).

Transmission Electron Microscopy (TEM): The 0.01 wt% nanoclay aqueous suspension was prepared by ultrasonication. One drop of the solution was dropped on the TEM copper grid and the sample was dried. Nanoclays were observed by using a Tecnai T20 TEM at 200 kV.

Compression Tests: The non-oriented and oriented cylindrical hydrogels with 9 mm diameter and 5 mm height were prepared with a series of clay concentrations (0.05 wt%, 0.2 wt%, 0.4 wt%). The stress–strain curve of each sample was obtained under uniaxial compression by using DMA 850 (TA Instruments). The constant displacement rate (1 mm/min) was applied for the measurement.

Water swelling tests: For swelling measurements of nanoclay hydrogels, seven different cylindrical samples with 9 mm diameter and 5 mm height were prepared with 0.4 wt% hydrogels with oriented (9 T) and non-oriented (0 T) nanoclays. The diameter, height, and weight of the samples before and after the room-temperature water swelling were measured for various swelling time intervals. The changes in dimensions and weight before and after swelling were measured

with calipers (0.01 mm resolution) and a balance (0.1 mg resolution), respectively. The percentage increase of the diameter and height were calculated along with weight-percent increase.

5.3 Results and discussion

The shape and size of nontronite nanoclays were determined by TEM observation. Most of the nontronite nanoclays appeared as anisotropic lath structures of nanosheets in the TEM images, probably due to the perpendicular orientation of clay nanosheets to the electron beam direction (Figure 5-1). Nanoclays having lengths ranging from 50 nm to 600 nm and widths ranging from 20 nm to 200 nm were observed. The average length and width of nanosheets were 209 nm and 77 nm, respectively.

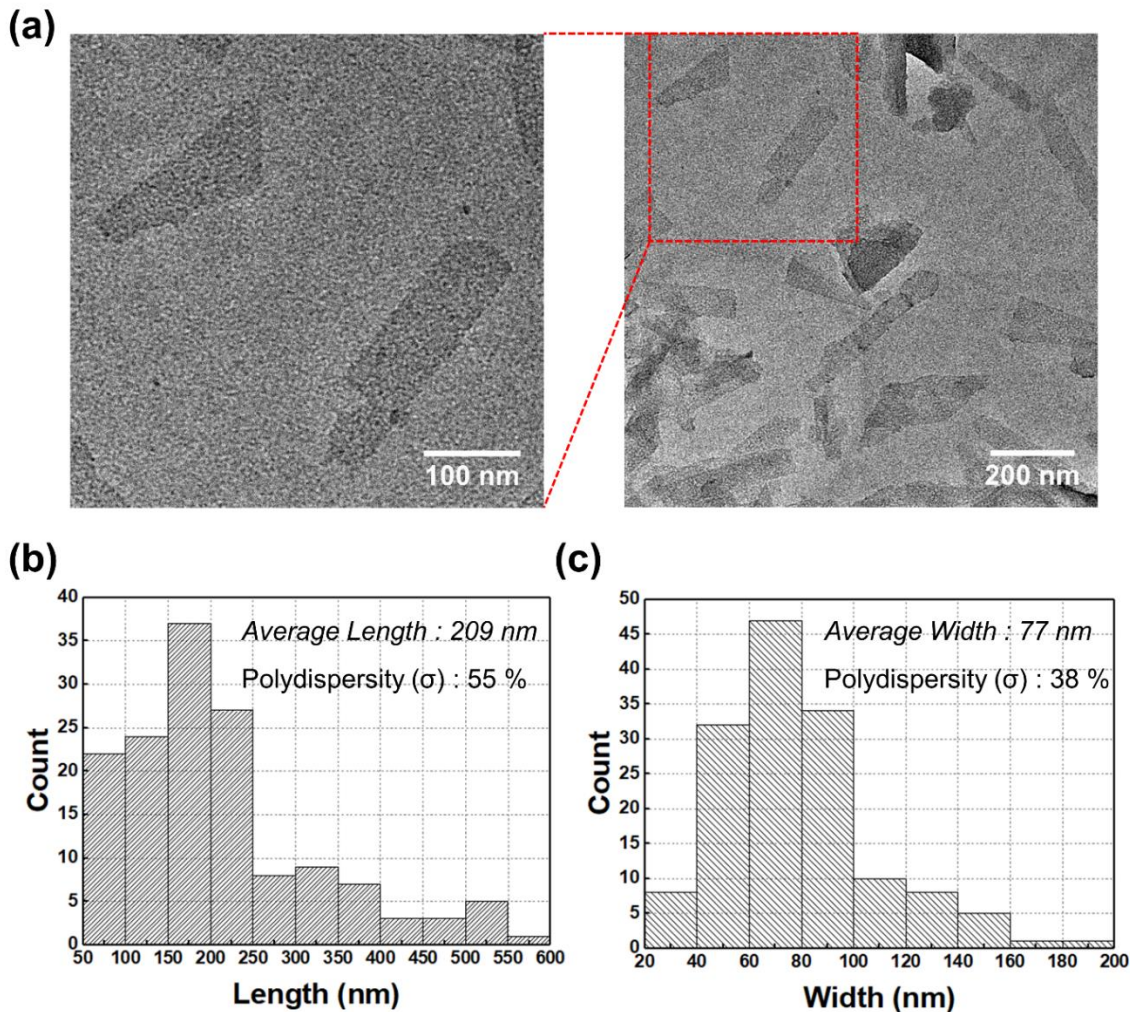


Figure 5-1 (a) TEM images of nontronite nanoclays. (b) Average length and (c) average width of nanoclays with polydispersity.

Nontronite clays (NAu-2) are dioctahedral minerals containing ferric ions (Fe^{3+}) in octahedral sheet as shown in Figure 5-2a. It was reported that the iron oxide (Fe_2O_3) content in NAu-2 is around 38%.⁵² The crystal structure of NAu-2 was investigated by powder X-ray diffraction. Normally, the nontronite clay shows two major peaks at $2\theta = 6^\circ$ and $2\theta = 28^\circ$ from the (001) and (003) plane reflection, respectively.^{232,233} Figure 5-2b clearly shows these two reflections. There are also two distinct peaks at $2\theta = 19.5^\circ$ and 35° indicating (20,11) and (20,13) peaks, which were attributed to dioctahedral 2:1 layer stacking faults of nontronite clays.^{53,234} Figure 5-2c shows the overall sample preparation steps of an anisotropic clay hydrogel by using a permanent superconducting magnet. Briefly, the nontronite aqueous suspension with hydrogel precursor

(monomer, crosslinker, initiator, and catalyst) was prepared in a container. The nanoclays in the mixture were aligned by placing the solution in a superconducting magnet. The following hydrogelation in the presence of the magnetic field immobilized the oriented nanoclays within the hydrogel.

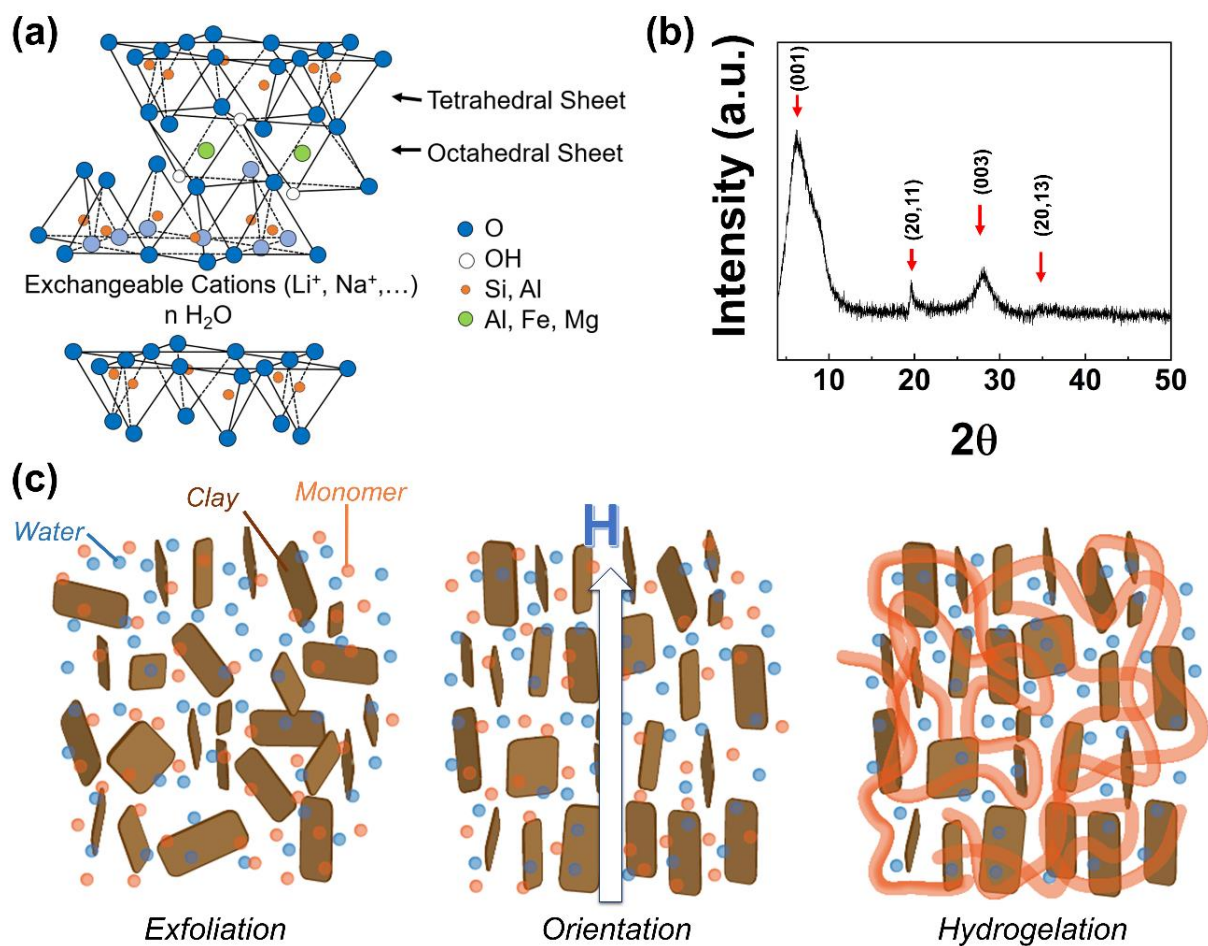


Figure 5-2 (a) The atomic structure of nontronite clay (NAu-2). (b) X-ray diffraction patterns of nontronite nanoclays. (c) Schematic illustration of preparation process of an anisotropic clay hydrogel sample.

To find out the optimal exposure time of the low-viscosity liquid medium to the magnetic field before a polymerization, the viscosity of hydrogel precursor solution was measured as a function of time at room temperature during polymerization. Figure 5-3 shows the increase of viscosity in the hydrogel precursor as the gelation occurs. It means that the reaction time of gelation

can be controlled by adjusting the concentration of initiator and catalyst. By adding 5 μL of initiator and catalyst to 4.5 g of water, we tuned the onset of viscosity rise to 40 min. This result indicated that the nanoclay suspensions were exposed to magnetic fields in the liquid medium approximately for 40 min before the polymerization took place to freeze the developed morphology in place within the structure. Although the real-time nanoclay alignment and monomer gelation kinetics could not be studied due to geometrical restriction, the nanoclay alignment would probably be relatively fast in a liquid state considering the water-like viscosity of the medium. The exposure to the permanent magnetic field for 40 min in the liquid state should be enough for nanoclays to be oriented at the corresponding magnetic field strengths used.

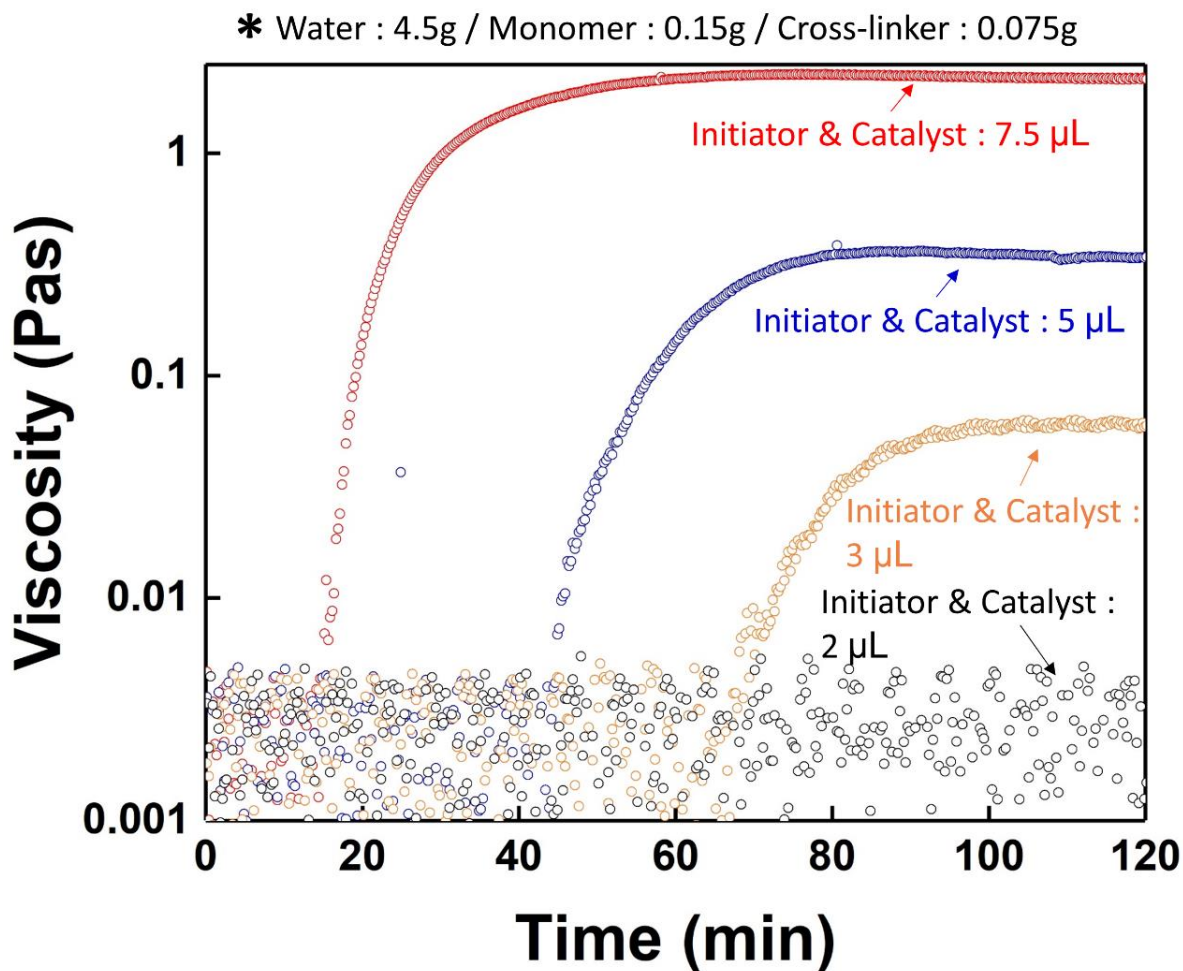


Figure 5-3 The viscosity of hydrogel precursors with different concentration of initiator and catalysis as a function of time.

Figure 5-4a shows cylindrical anisotropic hydrogels with different clay concentrations prepared under the 9 T magnetic field. The resultant nanoclay hydrogels exhibited uniform color from light yellow to dark brown as the concentrations of nanoclays increased from 0.05 wt% to 0.4 wt%. In this study, we report nanoclay hydrogels with relatively low nanoclay concentrations to solely consider the orientation of nanoclay in an isotropic aqueous suspension. One of the important features of nontronite clay minerals is that they can exhibit yield stress in the aqueous state.^{235,236} Because of this characteristic, nontronite nanoclay suspensions can undergo an isotropic/nematic and a sol/gel transition as the overall clay concentration increases. For nontronite clays (Nau-2) aqueous suspensions, isotropic/nematic and sol/gel transitions occur at 0.6 vol% and 0.83 vol%, respectively.¹²⁴ Therefore, the results presented in this study deal with isotropic liquid region to exclude a gelation caused by high clay loading. This means that the hydrogelation of clay suspensions in this report only occurred by a polymerization of acrylamide monomers. For examining the magnetic-field induced nanoclay alignment in hydrogels, the birefringence of the materials was characterized. This technique is suitable for tracking preferential orientation of optically anisotropic particles and other materials.⁵⁵ Nontronite nanoclays are inherently birefringent, as their refractive indices in the basal plane direction and normal to the basal plane directions are substantially different. Thus, the hydrogel nanocomposite can be optically birefringent when nanoclays are preferentially oriented. For this measurement, the anisotropic hydrogel samples were placed between crossed polarizers, and the optical anisotropy was characterized by observing the light intensity at every 45° rotation, as shown in Figure 5-4b. For the nanoclay hydrogel exposed to a relatively low magnetic field of 1 T, the light-transmission intensity change at every 45° rotation was low (Figure 5-4c-1). This increased for the sample prepared at a 3 T magnetic field strength (Figure 5-4c-2). Notably, the strong dark and bright contrast was observed for the sample prepared at the magnetic strength of 9 T as the clays became oriented. (Figure 5-4c-3). The orientation direction of nanoclays with respect to the direction of the magnetic fields was revealed by inserting a first-order lambda plate (red wave plate) between cross polarizers with its slow axis oriented at 45° to the polarizer and analyzer. With a red wave plate, the sample exhibited the contrast interference colors (red → yellow → red → blue) at every 45° rotation (Figure 5-4c-4). Blue interference color appeared at 135° rotation when applied magnetic field direction was parallel to the slow axis direction of the lambda plate, whereas yellow color appeared at 45° rotation as shown in Figure 5-4d (slow axis direction of the red wave plate

is indicated by red double arrow in these figures). The results indicate that (001) basal planes, which have a high refractive index in nanoclay minerals, oriented along the applied magnetic field direction. Thus, the blue color (a high refractive index in Michel-Levy birefringence chart) is exhibited when the (001) basal planes are oriented parallel the slow axis (being the highest refractive index direction) of the first-order (red wave) lambda plate.

To verify that optical anisotropy was only from field-induced orientation of nanoclays and not from polymer chains of hydrogel network, the optical anisotropy of pure hydrogels prepared in 9 T was examined (Figure 5-5). Completely dark polarized optical microscopy (POM) images at every 45° rotation indicated that a hydrogel is optically isotropic.

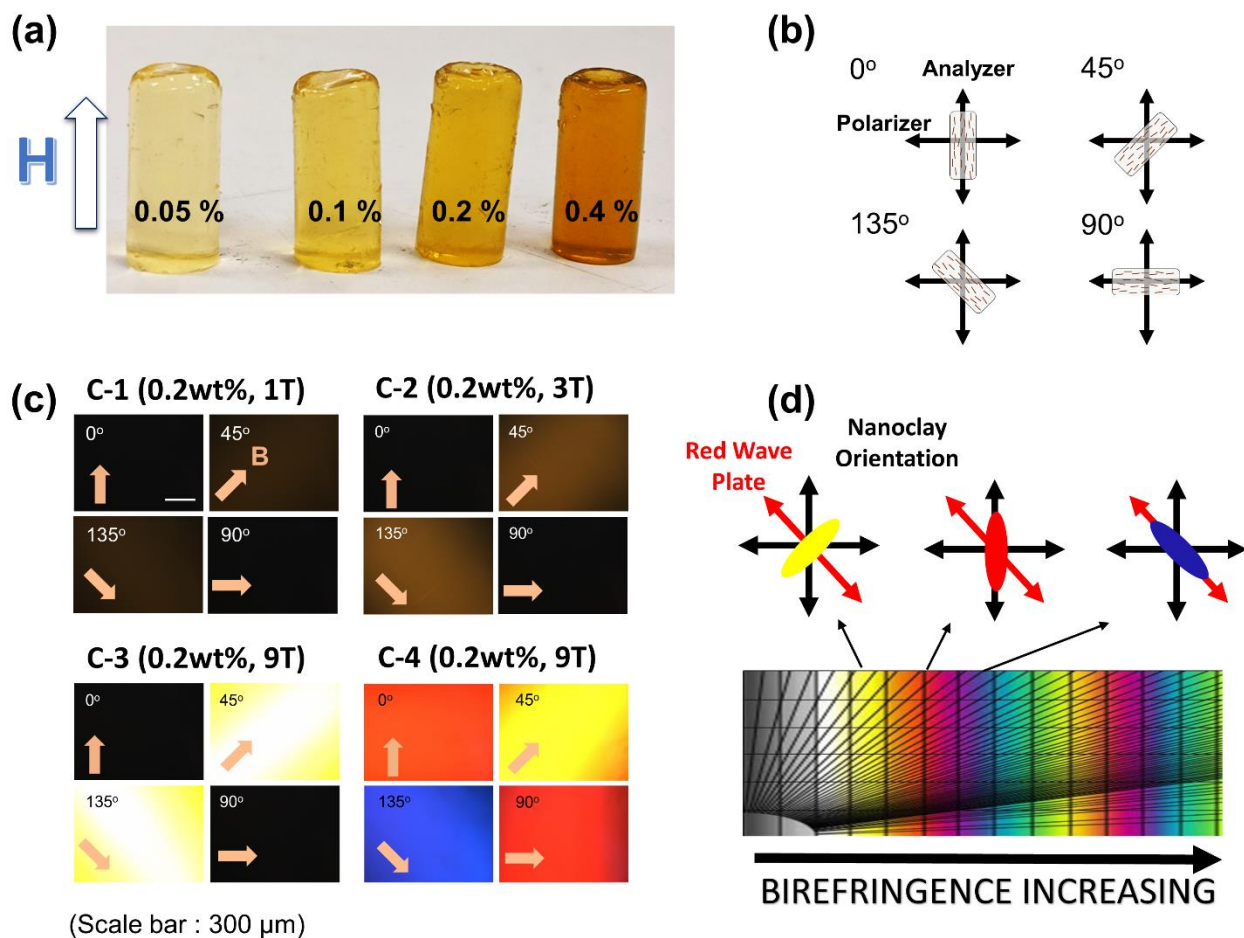


Figure 5-4 (a) Anisotropic hydrogels with different concentrations of nanoclay (0.05 wt%, 0.1 wt%, 0.2 wt%, and 0.4 wt%) prepared under 9 T magnetic field. (b) The direction of the sample rotation between cross polarizers. (c) The optical microscope image of 0.2 wt% anisotropic hydrogels prepared at (c-1) 1 T, (c-2) 3 T, and (c-3) 9 T of magnetic field strength under cross polarizers. (c-4) Identical POM image of (c-3) with a first-order lambda plate (red wave plate) (sale bar: 300 μm). (d) Nanoclay orientation under crossed polarizers with a red wave plate and a corresponding interference color chart.

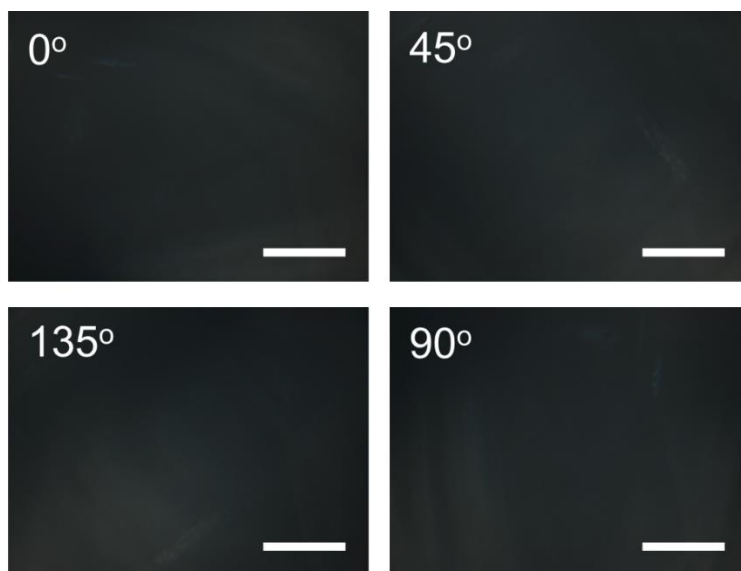


Figure 5-5 The optical microscope image of a pure hydrogel prepared in 9 T under crossed polarizers at every 45° degree rotation. (Scale bar: 300 nm)

For a more detailed examination of the magnetic-field induced birefringence, nanoclay hydrogel samples were prepared in a 4.5 ml glass cuvette with different magnetic field strengths and concentrations. Nanoclay hydrogels optically look similar to each other at the same clay concentrations without crossed polarizers (Figure 5-6a). However, the samples gradually became bright between crossed polarizers as the magnetic field strength increased because of preferential orientation of nanoclays (Figure 5-6b). The gradual enhancement of birefringence intensity was observed for the concentration from 0.05 wt% to 0.2 wt%, while the effect was not significant for 0.4 wt% nanoclay hydrogel samples.

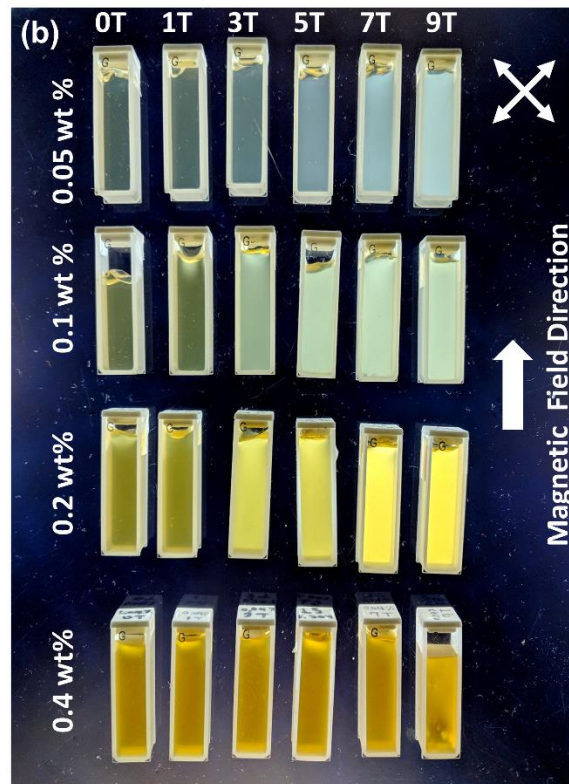
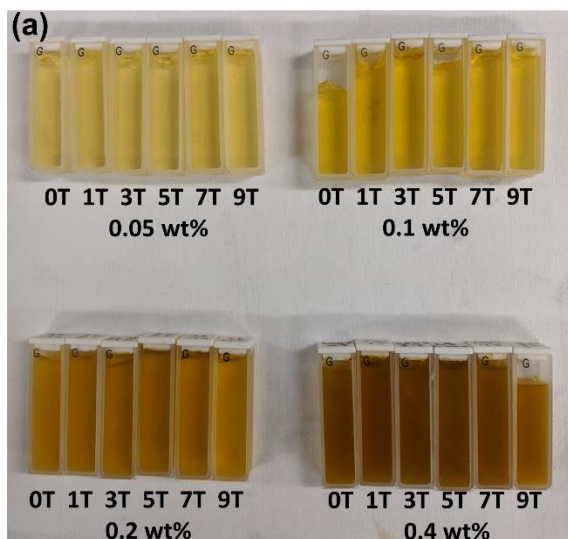


Figure 5-6 Anisotropic hydrogel samples (0.05 wt%, 0.1 wt%, 0.2 wt%, 0.4 wt% of nontronite clays) prepared with various magnetic field strength (0, 1, 3, 5, 7, 9 tesla) (a) without crossed polarizers and (b) with crossed polarizers.

To evaluate the birefringence intensity quantitatively, the in-plane retardation of the samples was measured by using a custom-built apparatus. Birefringence of the sample along the in-plane direction can be simply calculated by $\Delta n_{12} = \text{retardation} / \text{thickness}$. Because the thickness of the sample in glass cuvettes is 10 mm, the birefringence of the sample was calculated by dividing their in-plane retardation values by 10×10^6 nm. The scheme of the experimental set-up and relevant in-plane retardation values are shown in Figure 5-7.

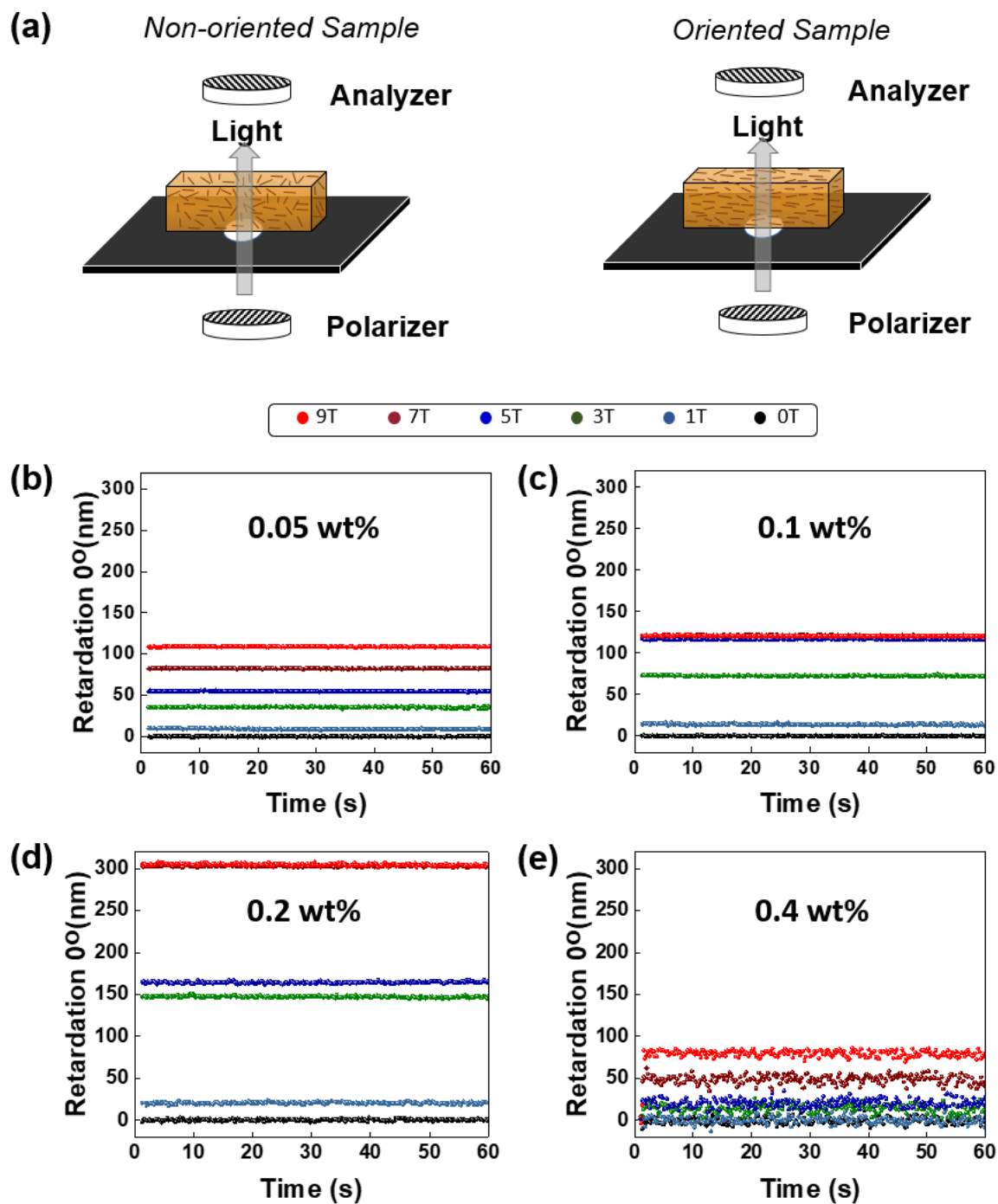


Figure 5-7 The retardation value of nanoclays hydrogel samples with different clay concentration and magnetic field strength. (a) Schematic illustration of retardation measurement of isotropic and anisotropic hydrogel samples. In-plane retardation values of nanoclays hydrogels prepared at various magnetic field strengths with (b) 0.05 wt%, (c) 0.1 wt%, (d) 0.2 wt%, and (e) 0.4 wt% nanoclay concentrations.

Figure 5-8 presents the magnetic-field induced birefringence of nanoclay hydrogels as a function of magnetic field strength. As expected, the field-induced birefringence of nanoclay hydrogels increased with magnetic field strength in all nanoclay concentrations. Interestingly, the birefringence increased with nanoclay concentration from 0.05 wt% to 0.2 wt%, then it dropped when concentration increased to 0.4 wt% at the same magnetic field strength. For dilute colloidal system, the field-induced birefringence is linearly proportional to particle concentrations as expressed by

$$\Delta n = \Delta n_{\text{sat}} \cdot C_v \cdot S \quad (2)$$

where C_v is a volume concentration of particles, S is an orientation order parameter, and Δn_{sat} is a maximum birefringence when $C_v = 1$ and $S = 1$.^{105,123} The field-induced birefringence is dependent on the orientation order parameter (S), with constant C_v and Δn_{sat} . Thus, birefringence is proportional to magnetic field strength at a constant nanoclay concentration as orientation order parameter (S) is increased. Similarly, the field-induced birefringence was increased with nanoclay concentration from 0.05 wt% to 0.2 wt% at the constant external field strength. However, this equation is only applicable for the dilute nanoclay suspensions, where individual nanoclays can independently contribute to the field-induced birefringence by orientating in the field direction without geometric hindrance. For the sample with high nanoclay loading like 0.4 wt% in this study, the nanoclay particles do not act individually anymore as they interfere with the motion of neighboring particles and, hence, restrict their free realignment. Therefore, the overall orientation of the particles decreases slightly because of this spatial restriction effect at higher concentrations.

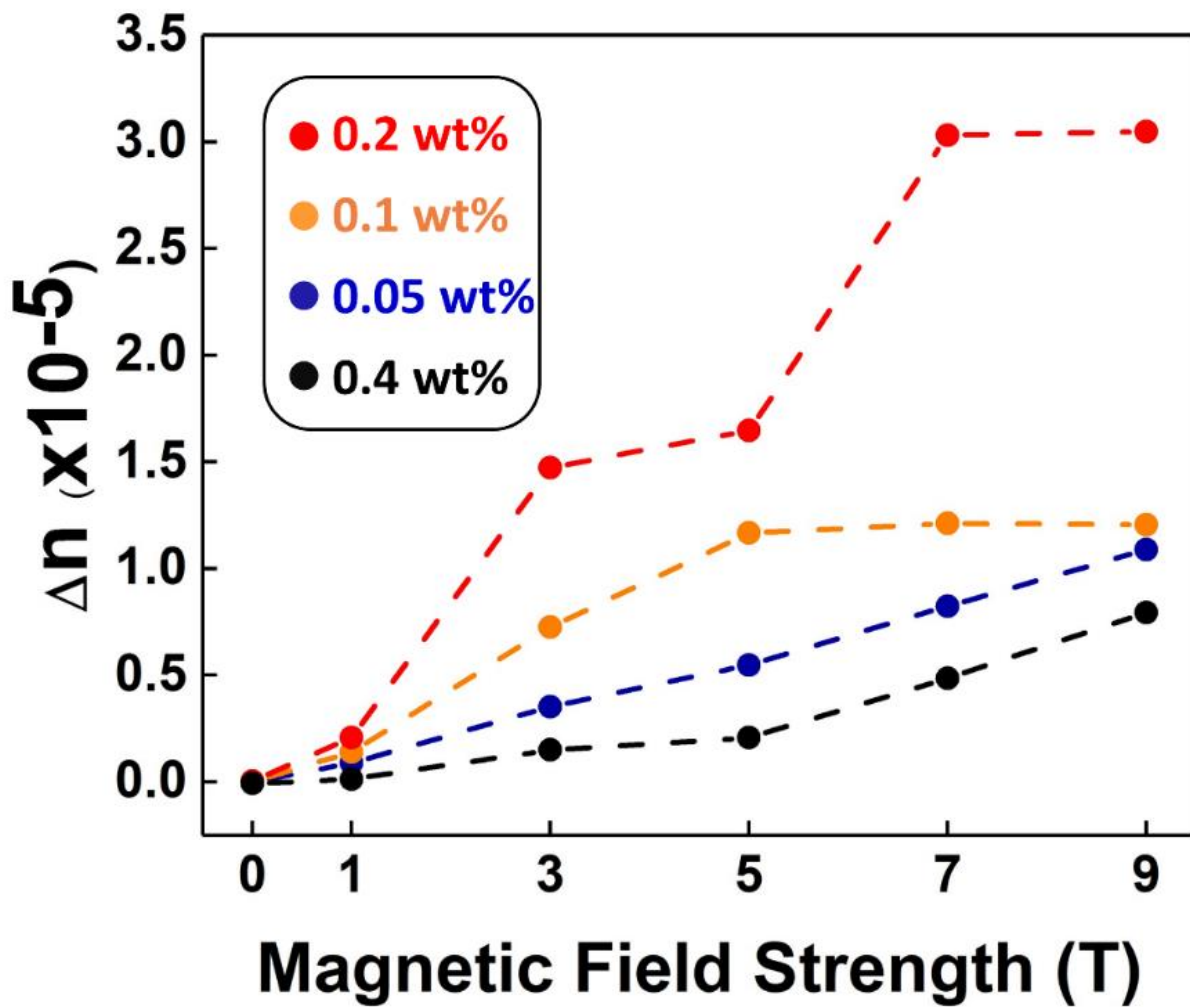


Figure 5-8 Magnetic-field induced birefringence of anisotropic nanoclay hydrogels.

The anisotropic structure of nanoclay hydrogels was also examined by 2D SAXS analysis. To carry out the X-ray scattering experiment, nanoclay hydrogels were prepared in glass capillaries. The X-ray beam was directed at the sample in glass capillaries perpendicular to the applied magnetic field direction as shown in Figure 5-9a. Figure 5-9b shows that 2D SAXS patterns of nanoclay hydrogels (0.1 wt%, nanoclay) prepared with different magnetic field strength. As applied magnetic field increased from 0 T to 9 T, the shape of the X-ray scattering pattern changed from a circular to elliptical shape. The major axis of the elliptical pattern was perpendicular to the direction of applied magnetic fields, indicating that the basal planes of nanoclays were oriented parallel to the direction of applied magnetic fields. This result is also in agreement with the POM image with the lambda (red wave) plate (Figure 5-4c-4). Furthermore, the elliptical diffusive 2D SAXS patterns were observed in all samples prepared at the 9 T magnetic field strength (Figure 5-9c). To verify that the X-ray scattering is from nanoclay structure, the X-ray scattering pattern of the pure hydrogel was examined. The negligible scattering intensity of the pure hydrogel indicates that the X-ray scattering patterns are from nanoclays, not from the hydrogel matrix.

To clarify the degree of the alignment, the azimuthal plot of 2D SAXS patterns of 0.1 wt% nanoclay hydrogels was constructed (Figure 5-10a). The plot of the sample with 0 T showed a single plateau along the azimuthal angles. As the applied magnetic fields increased, two distinct peaks at 90° and 270° azimuthal angles became pronounced. The results clearly indicate the nanoclay hydrogels increasingly become anisotropic as magnetic field strength increased. The constructed azimuthal plot of 2D SAXS patterns of four different samples prepared at 9T exhibited strong intensity at 90° and 270° azimuthal angle in all cases, indicating high alignment of nanoclays in all concentrations (Figure 5-10b).

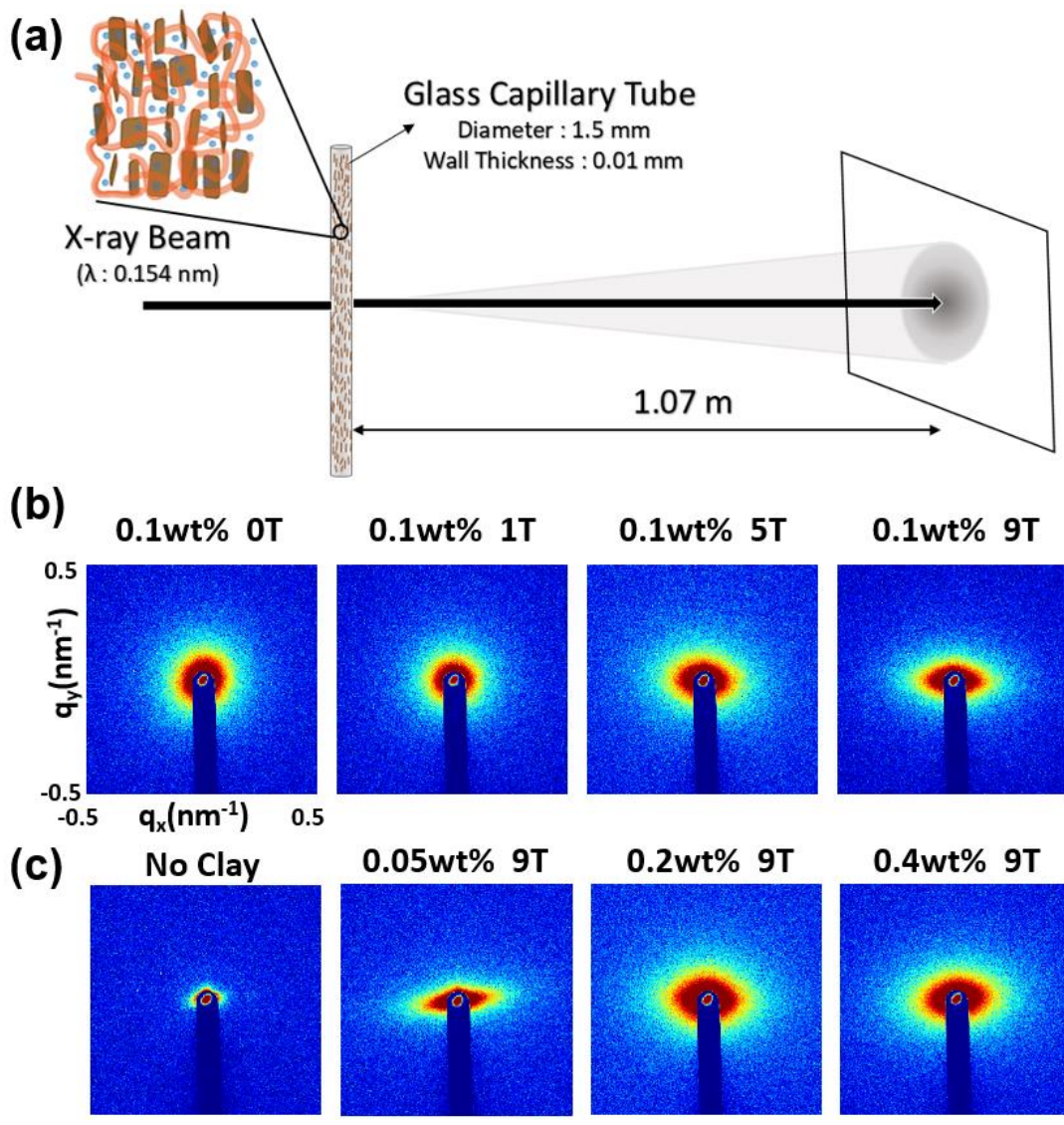


Figure 5-9 (a) Schematic layout of a 2D SAXS experimental setup. (b) 2D SAXS patterns of hydrogels (0.1 wt%) in different magnetic field strength. (c) 2D SAXS patterns of various concentrations of nanoclays prepared at 9 T.

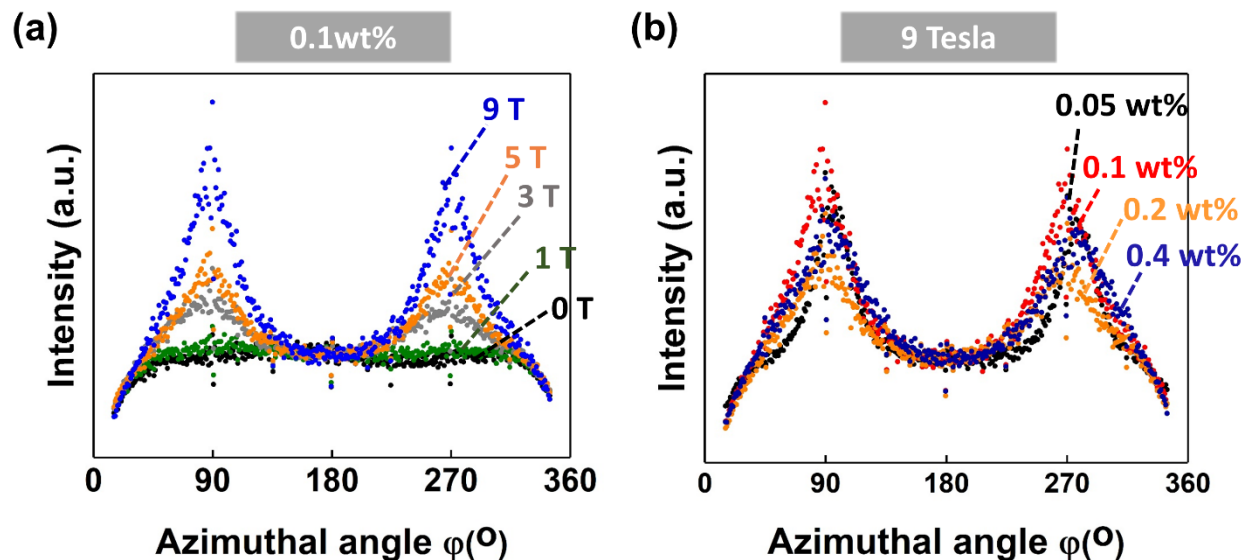


Figure 5-10 (a) Azimuthal angle plots for hydrogels (0.1 wt%) in different magnetic fields. (b) Azimuthal angle plots for anisotropic hydrogels in different concentrations prepared in 9 T magnetic fields.

To quantitatively analyze the nanoclay orientation, the orientation order parameters (S) were calculated by fitting the azimuthal angle plots to the Maier–Saupe distribution function with a baseline and the positions of maximum intensity (90° and 270° in this study). By fitting the plot to this function, we can obtain a parameter (α) that determines the width between two peaks. This width parameter (α) was used to calculate the orientation order parameter. Theoretically, the value of S ranges from 1 (perfect orientation) to 0 (completely random orientation). The detailed calculation method is described elsewhere.^{187,188} The orientation order parameters of the nanoclay hydrogel (0.1 wt%) was increased gradually by increasing the magnetic field strength (Figure 5-11a). The orientation parameter increased along with the magnetic field strength up to 5 T (from 0 to 0.6). This increase slowed down with further increase of magnetic field to 9 T (from 0.6 to 0.68). Figure 5-11b shows the orientation order parameter of nanoclay hydrogels prepared at 9 T with different clay concentrations. For the low-concentration samples (0.05 wt% and 0.1 wt%), the orientation order parameter takes high values ~ 0.68 . It slightly decreased to 0.6 as the concentration of nanoclays increased to 0.2 wt%. However, a further increase in the concentration significantly reduced the orientation order parameter down to 0.43 (0.4 wt%). The results agreed with the decrease in the field-induced birefringence for the sample with high clay loading (0.4 wt%). The plot in Figure 5-11c shows expected linear correlation between the field-induced

birefringence and the orientation order parameter obtained from 2D SAXS over the range of magnetic field strength, ranging from 0 T to 9 T.

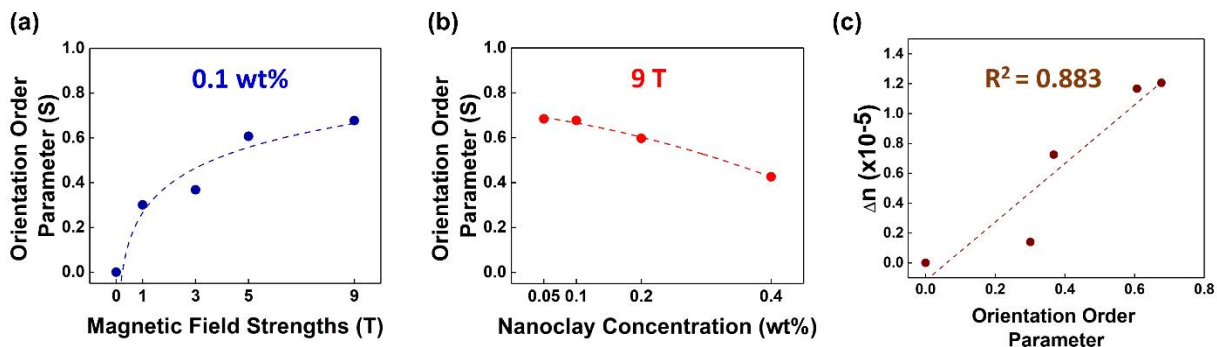


Figure 5-11 (a) The orientation order parameter of 0.1 wt% nanoclay hydrogels as a function of the magnetic field strength. (b) The orientation order parameter of nanoclay hydrogels as a function of nanoclay concentration. (c) The correlation between birefringence and orientation order parameter (0.1 wt% nanoclay hydrogels).

In addition to small-angle scattering data, 2D wide-angle X-ray scattering (WAXS) was also used to detect the information of individual nanoclays in a hydrogel. WAXS can characterize the crystalline structure of nontronite clay minerals. As discussed earlier, nontronite clay powders exhibit X-ray diffraction peaks at $2\theta = 6^\circ$, 19.5° , 28° , and 35° from the (001) and (003) planes and also from dioctahedral 2:1 layer stacking faults (Figure 5-2b). Figure 5-12a showed the 2D WAXS patterns of nanoclay powders, pure hydrogels, and nanoclay hydrogels ranging from 10° to 40° . Three peaks were observed at $2\theta = 19.5^\circ$, 28° and 35° from clay powders as well as a broad peak ranging from 20° to 35° from a pure hydrogel (Figure 5-12b). Interestingly, nanoclay hydrogels did not exhibit crystalline structure peaks of clay powders in different concentrations and field strengths, while they all exhibited a broad hydrogel peak at $20^\circ < 2\theta < 35^\circ$. The results indicate that most of nanoclays were exfoliated in an aqueous medium yielding the near complete elimination of three-dimensional lattice structure and locked in the gel state. The small portion of clay tactoids in the cross-linked hydrogel could not provide enough diffraction patterns.

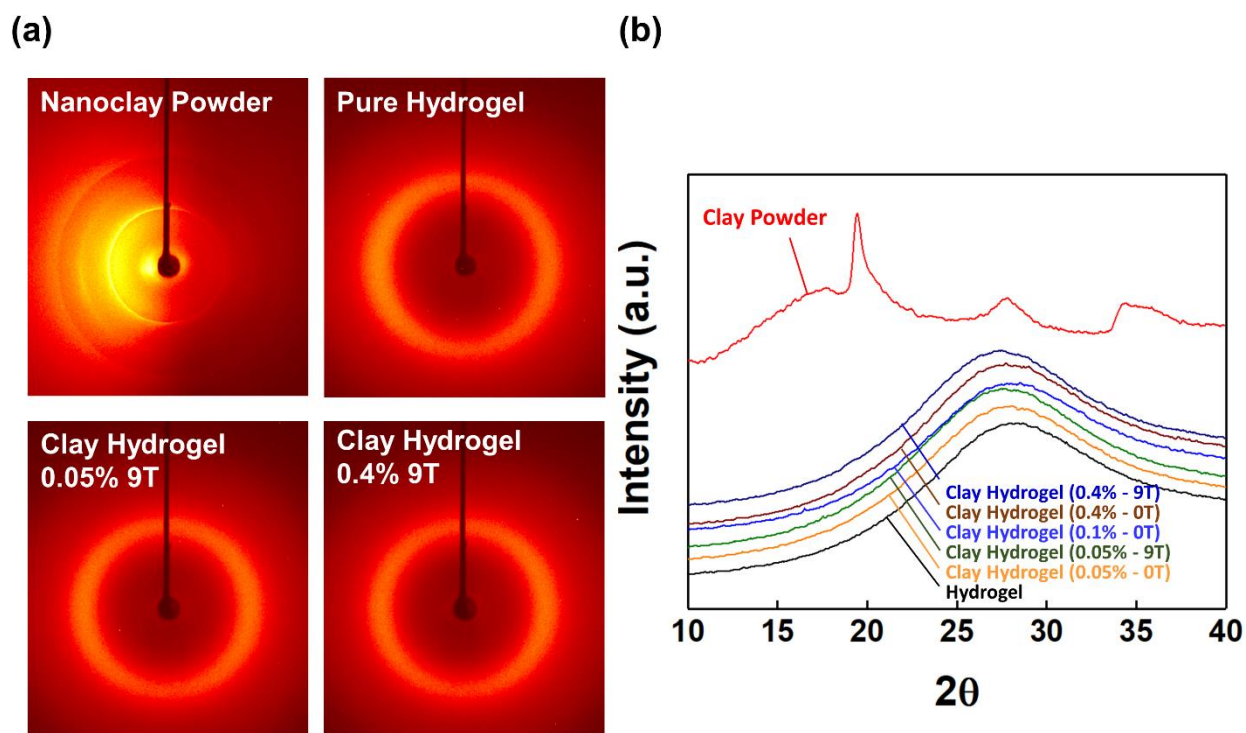


Figure 5-12 (a) 2D WAXS patterns of nanoclay powder, pure hydrogel, and nanoclay hydrogels (0.05% and 0.4%). (b) X-ray diffraction patterns of nanoclay powder, pure hydrogel, and nanoclay hydrogels.

The mechanical properties of nanoclay hydrogels were also investigated along the clay orientation direction at different concentrations. The nanoclay hydrogels showed the typical stress–strain curve of hydrogel materials under compression test (Figure 5-13a). In general, modulus increased with nanoclay concentration even though the clay concentrations we used were quite small. Moreover, anisotropic hydrogels showed slight enhancement in mechanical properties in the clay orientation direction at 50% strain (testing was carried out in normal direction). At all concentrations, the tangent elastic modulus of anisotropic hydrogels was higher than that of isotropic hydrogels at 50% strain (Figure 5-13b). For the 0.4 wt% hydrogels, tangent elastic modulus increased from 15.4 kPa to 18.1 kPa, which corresponded to an 18% increase in mechanical properties. The tangent elastic modulus also increased as the concentration of nanoclay concentration increased for both non-oriented and oriented samples.

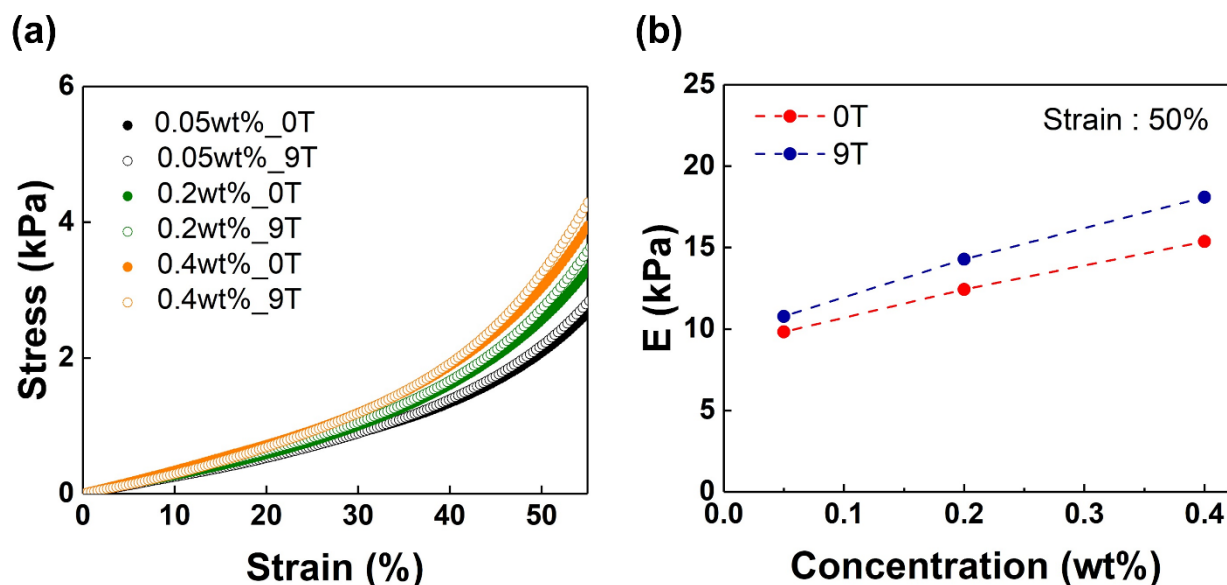


Figure 5-13 Mechanical properties of hydrogels prepared in 0 T and 9 T magnetic field strength with different clay concentrations in uniaxial compression test. (a) Stress–strain curves of completely random (0 T) and highly oriented (9 T) hydrogels with different clay concentrations. (Compression direction is parallel to nanoclay orientation direction for 9 T samples.) (b) Tangent elastic modulus at 50% strain of hydrogels.

The light transmission of nanoclays hydrogels with respect to the applied magnetic fields was also studied. The completely random (0 T) and highly oriented (9 T) samples were prepared at different concentrations as shown in Figure 5-14a. The exhibited color of the samples changed from light yellow to dark brown by increasing the concentration of nanoclays. Figure 5-14b shows the schematic illustration of nanoclay dispersion within a hydrogel, along with the direction of optical transmission measurement and applied magnetic fields. Figure 5-14c represents an optical light transmission of isotropic and anisotropic hydrogel samples as a function of nanoclay concentrations. The light transmission significantly dropped from 84% to 14% as nanoclay concentration increased from 0.05 wt% to 0.4 wt%. In addition to concentration effects on optical transmission, the orientation of nanoclays also influenced the optical transmission of the samples. The optical transmission increased for the anisotropic hydrogels because the clay nanosheets were oriented to the magnetic field direction with all edges pointing to the magnetic field direction. Compared to the sample with randomly dispersed nanoclays, the sample with oriented clays scattered or absorbed less light at the 546 nm wavelength. For 0.1 wt% and 0.2 wt% nanoclay

hydrogel samples, the optical transmission was increase by 7% and 8%, respectively. However, the difference in optical transmission was negligible at the 0.05 wt% and 0.4 wt% nanoclay concentrations. Insignificant increase of light transmission at low clay concentration (0.05 wt%) may be attributed to very small clay loading. At high clay concentration (0.4 wt%), the light transmission was probably more influenced by the high nanoclay concentration than their alignment.

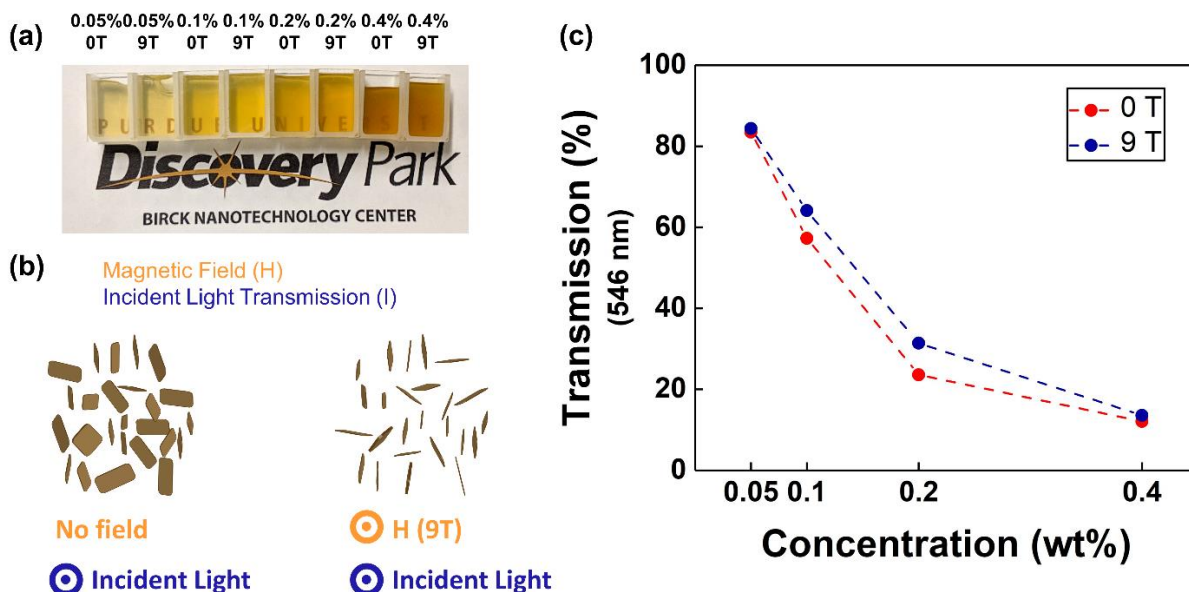


Figure 5-14 (a) The nanoclay hydrogels with different concentrations prepared at 0 T and 9 T. (b) Schematic illustration of nanoclay orientation with respect to magnetic fields and incident light. (c) Optical light transmission of nanoclay hydrogels with different concentrations prepared at 0 T and 9 T.

Lastly, we examined the swelling behavior of the hydrogels with 0.4 wt% nanoclays with the oriented and non-oriented samples. The initial and final dimensions of the sample were measured at different swelling times as shown in Figure 5-15a. We observed that anisotropic hydrogels exhibited high swelling in the direction of orientation of nanoclays. Figure 5-15b shows that the percentage increase of diameter and height along with weight-percent change over the swelling time. At equilibrium swelling state of hydrogel where 60% increase in weight of the hydrogel after 120 h swelling was observed, the thickness and diameter increased 30% and 21%,

respectively. However, the swelling percentage change in the radius and thickness direction was almost identical over time for the sample without the clay orientation (Figure 5-15c). The results indicated that the oriented nanoclay in a hydrogel network facilitated the anisotropic water swelling over time. Anisotropic swelling ratio ($Y\% / X\%$) was plotted over time for the oriented and non-oriented samples in Figure 5-15d. The results show that the hydrogels with oriented nanoclays maintained anisotropic swelling (~ 1.5) after 6h, whereas the hydrogels with non-oriented nanoclays exhibited no anisotropy swelling for all swelling times.

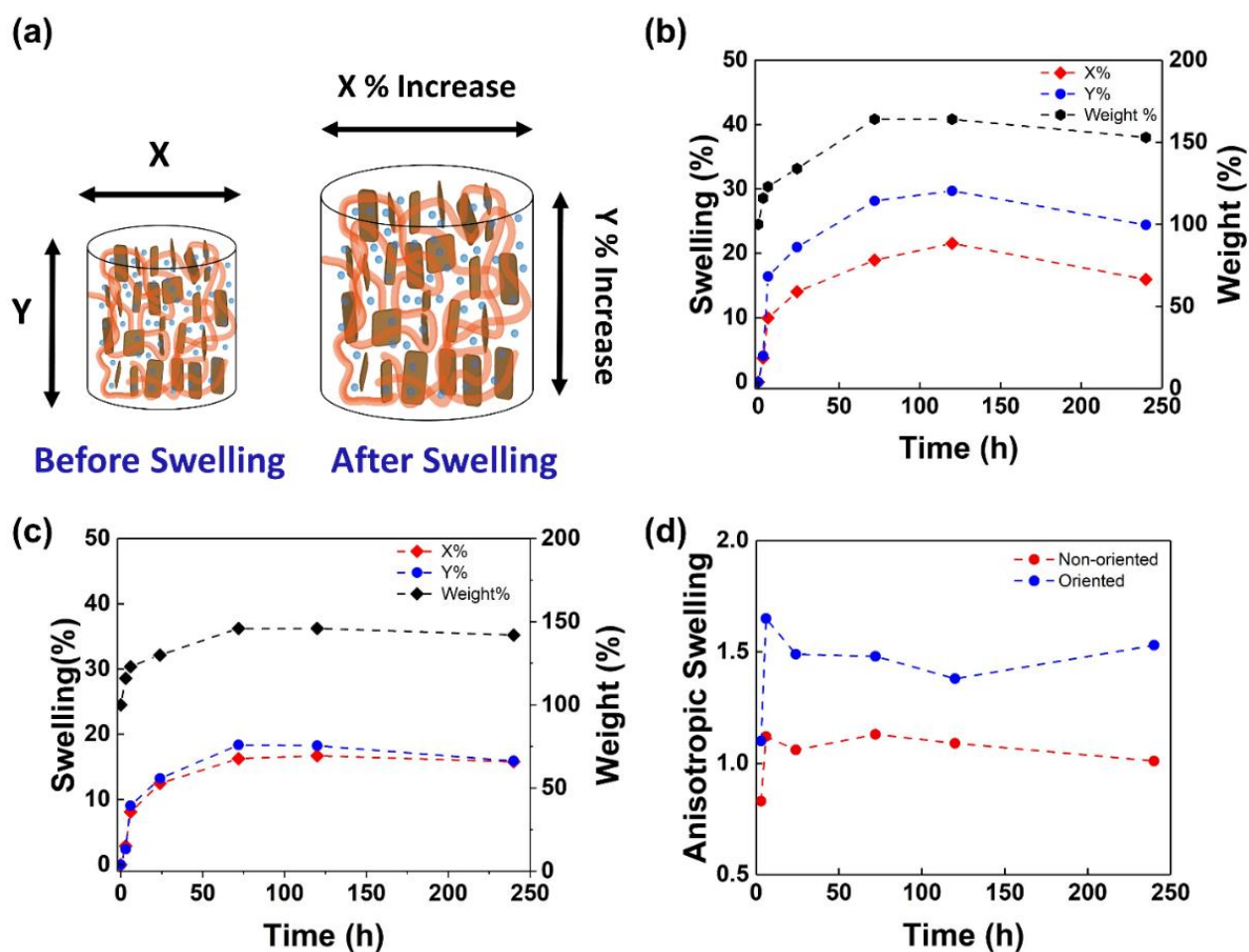


Figure 5-15 Swelling behavior of a 0.4 wt% clay hydrogels prepared in 0 T and 9 T magnetic field. (a) Schematic illustration of a hydrogel before and after swelling and directions of measurement. Time dependence of the swelling to the radius (X) and thickness (Y) direction along with the weight-percent increase of (b) the oriented sample and (c) the non-oriented sample. (d) Anisotropic swelling ratio ($Y\% / X\%$) of the oriented and non-oriented samples over the swelling time.

Table 5-1 shows the swelling anisotropy of polymeric gels in ethanol or water in previous studies. Based on previous findings, the anisotropic swelling exhibited was no higher than 1.4 in ethanol and 1.3 in water with polymeric gels containing anisotropic nanostructure. Here, we report the swelling anisotropy (~1.5) in water, which is the highest among the published literature.

Table 5-1. Anisotropic swelling of polymeric gels.

Materials (Gel)	Swelling Solvent	Anisotropic Swelling
Copolymer of Stearyl acrylate and acrylic acid ²²⁰	Ethanol	1.4
Polyurethane ²¹⁹	Water	1.25
Poly(N-isopropylacrylamide) ¹⁵⁶	Water	1.3
Polyacrylamide*	Water	1.5

5.4 Conclusion

We produced a new type of anisotropic nanocomposite hydrogel by using a magnetic alignment of iron-containing magnetically sensitized clays in the field direction that is potentially useful for wound dressings that exhibit substantial out-of-plane wicking behavior. The anisotropic nanostructure of the nanoclay hydrogels was investigated by measuring birefringence and performing SAXS. The field-induced birefringence and 2D SAXS results revealed that nanoclay suspensions within a hydrogel were oriented parallel to the magnetic field direction and the degree of orientation of the nanoclays increased with applied magnetic field strength. Interestingly, the nanoclays were less responsive to external fields beyond a certain clay loading, where a strong steric hindrance was observed between clay particles forming frustrated structures. In these structures, improved compressive mechanical properties as well as increases in swelling behavior were found in the direction of nanoclay orientation facilitated by the magnetic field.

6. CONCLUSION

Tuning the morphology of clay/polymer and clay/hydrogel nanocomposites by using external forces was comprehensively discussed in this dissertation. As abundant, inexpensive, and environmentally friendly filler materials, clay minerals have been widely incorporated into polymer or gel mediums. By applying external electric or magnetic fields to clay/polymer and clay/hydrogel nanocomposites, field-sensitive clay minerals were directionally organized in the matrix.

In this dissertation, two main studies are reported. The first study addresses the morphology of phase-separated polymer blends containing electrically pre-oriented clay nanoparticles. The second study discusses the development of hydrogels containing magnetically oriented clay minerals for improving anisotropic swelling properties of hydrogels.

In Chapter 3, the temporal morphological change of a polymer mixture undergoing phase separation in the presence of electrically pre-oriented clay fillers was studied. The initial co-continuous phase-separated morphology coarsened and oriented parallel to AC field direction (basal plane direction of clay minerals) in the presence of electrically pre-oriented clay fillers. It was surprising that oriented clay minerals with sizes ranging from 100 nm to a few microns significantly influenced the morphology of the blends as phase separation proceeded by a temperature jump from one phase to two phase above the critical temperature. Orientation of polymer phases may be hard to achieve just by an external electric field strength of $\sim 1000\text{V/mm}$ if the polymers do not have a high contrast in electrical properties. Here, we developed anisotropically oriented polymer phases by taking advantage of electrically pre-oriented clay minerals. This method may be advantageous compared to other techniques, in that this technique can be applied to any types of polymer pairs. Although we used a partially miscible polymer pair (PS and PVEM) with LCST behavior, anisotropic phase separated morphology can be developed in any polymer blends if they have different affinities to montmorillonite (Cloisite 15A).

In Chapter 4, anisotropic phase-separated morphology was created in the through-thickness direction by electrically orienting clay particles along the thickness direction. In the presence of electrically pre-oriented clay particles in through thickness direction, phase separation occurred in the through-thickness direction when a single-phase mixture underwent phase separation. The directionally ordered morphology along the thickness direction is the ideal structure in energy

conversion and storage devices. For industrial applications, such as fuel cell membranes and photovoltaic cells, the properties along the through-thickness direction should be enhanced. For example, the phase-separated morphology of donor and acceptor phases in the active layer of organic photovoltaic cells is critical for determining the efficiency of the devices. Considering that electron-hole dissociation occurs at the interface of donor and acceptor phases with a diffusion length of the dissociation of around 5–10 nm, the nanostructures of oriented donor and acceptor phases normal to the electrodes with sizes that are close to the diffusion length scale may be the optimal morphology for high efficiency. In this study, we demonstrated the directionally oriented phase-separated polymer phases in the through-thickness direction induced by pre-oriented clay particles. Although the results are conceptually satisfactory, there are some limitations. One of the limitations is that the residual clay fillers may influence the performance of the device, in that the clay additives in the blend may not be advantageous for the device. The other limitation is that the size of the anisotropic phase-separated morphology demonstrated here was close to $\sim 10 \mu\text{m}$, which may be not satisfactory for device applications. Nevertheless, a conceptual demonstration of anisotropic phase-separated polymer phases is still meaningful for future studies.

In Chapter 5, the magnetic-field assisted orientation of natural nontronite minerals in a hydrogel medium was demonstrated for wound-dressing applications. Alignment of magnetic-field sensitive natural nontronite clay minerals dispersed in a hydrogel precursor solution was demonstrated under magnetic field, and a following hydrogelation of the medium formed anisotropic hydrogel nanocomposites. The degree of orientation of nontronite minerals in a cross-linked gel was quantitatively analyzed by birefringence measurements and small-angle X-ray scattering. Two key scientific findings of this study are as follows: First, the dispersed clay nanoparticles in hydrogels were irreversibly arrested after the gelation. The result indicates that clay nanoparticles with a size of $\sim 200 \text{ nm}$ were perfectly locked in a cross-linked gel medium. Second, the degree of orientation of clay minerals under magnetic field dropped off when clay minerals reached beyond a certain concentration in the aqueous medium. This result indicates that intermolecular interactions between polar nontronite suspensions impeded the external field orientation of clay suspensions, as the frustrated structure where interference between neighboring particles become significant. The resultant hydrogels with oriented clay particles showed enhanced mechanical, optical, and swelling properties parallel to clay orientation in thickness direction. Anisotropic thickness-direction water swelling behavior is a long-sought property for wound

dressing materials. This enhanced directional swelling along the thickness direction in the wound dressing will reduce in-plane stress damage around the wounded area. Also, vertical wicking of fluid into the wound dressing will minimize periwound maceration damage.

In this dissertation, the development of anisotropic microstructures in clay containing polymeric nanocomposites by means of external fields was comprehensively discussed. In the first part, anisotropic phase-separated morphology of polymer blends in presence of electrically pre-oriented clay particles was described. The result indicates that the morphology of polymer blends can be controlled by taking advantage of external field-sensitive clay particles, even if polymer blends are not sensitive to external fields. This way of controlling blend morphology can be applied to various polymer pairings that are widely used in industrial applications. In the second part, alignment of magnetic-field sensitive clay particles in a hydrogel medium was demonstrated by using external magnetic fields. Hydrogels containing uniaxially oriented clay particles exhibited anisotropic swelling properties that may be applied for wound dressing materials where vertical wicking is preferred.

REFERENCES

- (1) Kumar, S. K.; Benicewicz, B. C.; Vaia, R. A.; Winey, K. I. 50th Anniversary Perspective: Are Polymer Nanocomposites Practical for Applications? *Macromolecules* **2017**, *50*, 714–731.
- (2) Tam, L. H.; Wu, C. Molecular Mechanics of the Moisture Effect on Epoxy/Carbon Nanotube Nanocomposites. *Nanomaterials* **2017**, *7*, 1–20.
- (3) Aziz, S. B. Morphological and Optical Characteristics of Chitosan(1-x):Cuox ($4 \leq x \leq 12$) Based Polymer Nano-Composites: Optical Dielectric Loss as an Alternative Method for Tauc's Model. *Nanomaterials* **2017**, *7*, 1–15.
- (4) Njuguna, J.; Pielichowski, K. Polymer Nanocomposites for Aerospace Applications: Properties. *Adv. Eng. Mater.* **2003**, *5*, 769–778.
- (5) Dul, S.; Fambri, L.; Pegoretti, A. Filaments Production and Fused Deposition Modelling of ABS/Carbon Nanotubes Composites. *Nanomaterials* **2018**, *8*, 1–25.
- (6) Zope, I. S.; Dasari, A.; Camino, G. Elucidating the Catalytic Effect of Metal Ions in Montmorillonite on Thermal Degradation of Organic Modifier. *Mater. Chem. Phys.* **2015**, *157*, 69–79.
- (7) Wu, H. C.; Chang, X.; Liu, L.; Zhao, F.; Zhao, Y. Chemistry of Carbon Nanotubes in Biomedical Applications. *J. Mater. Chem.* **2010**, *20*, 1036–1052.
- (8) Meister, J. J. Introduction to Polymer Modification. In *Polymer modification : principles, techniques, and applications.*; 2000; pp 3–19.
- (9) Manson, J. A.; Sperling, L. H. Reinforcement of Elastomers. In *Polymer Blends and Composites*; 1976; pp 299–333.
- (10) Kojima, Y.; Usuki, A.; Kawasumi, M.; Okada, A.; Fukushima, Y.; Kurauchi, T.; Kamigaito, O. Mechanical Properties of Nylon 6-Clay Hybrid. *J. Mater. Res.* **1993**, *8*, 1185–1189.
- (11) Kato, M.; Usuki, A. Polyamide/Clay Nanocomposites. In *Polymer Nanocomposites*; 2006; pp 3–28.
- (12) Shah, K. S.; Jain, R. C.; Shrinet, V.; Singh, A. K.; Bharambe, D. P. High Density Polyethylene (HDPE) Clay Nanocomposite for Dielectric Applications. *IEEE Trans. Dielectr. Electr. Insul.* **2009**, *16*, 853–861.

- (13) Bhattacharya, S.; Gupta, R. K.; Jollands, M.; Bhattacharya, S. N. Foaming Behavior of High-Melt Strength Polypropylene/Clay Nanocomposites. *Polym. Eng. Sci. Sci.* **2009**, *49*, 2070–2084.
- (14) Hashemifard, S. A.; Ismail, A. F.; Matsuura, T. Effects of Montmorillonite Nano-Clay Fillers on PEI Mixed Matrix Membrane for CO₂ Removal. *Chem. Eng. J.* **2011**, *170*, 316–325.
- (15) Gilman, J. W. Flammability and Thermal Stability Studies of Polymer Layered-Silicate (Clay) Nanocomposites. *Appl. Clay Sci.* **1999**, *15*, 31–49.
- (16) Choudalakis, G.; Gotsis, A. D. Permeability of Polymer/Clay Nanocomposites: A Review. *Eur. Polym. J.* **2009**, *45*, 967–984.
- (17) Zhu, J.; Start, P.; Mauritz, K. A.; Wilkie, C. A. Thermal Stability and Flame Retardancy of Poly(Methyl Methacrylate)-Clay Nanocomposites. *Polym. Degrad. Stab.* **2002**, *77*, 253–258.
- (18) Yang, Z.; Peng, H.; Wang, W.; Liu, T. Crystallization Behavior of Poly(ϵ -Caprolactone)/Layered Double Hydroxide Nanocomposites. *J. Appl. Polym. Sci.* **2010**, *116*, 2658–2667.
- (19) Chua, Y. C.; Lu, X. Polymorphism Behavior of Poly(Ethylene Naphthalate)/Clay Nanocomposites: Role of Clay Surface Modification. *Langmuir* **2007**, *23*, 1701–1710.
- (20) Zhao, C.; Qin, H.; Gong, F.; Feng, M.; Zhang, S.; Yang, M. Mechanical, Thermal and Flammability Properties of Polyethylene/Clay Nanocomposites. *Polym. Degrad. Stab.* **2005**, *87*, 183–189.
- (21) Sharma, S. K.; Nayak, S. K. Surface Modified Clay/Polypropylene (PP) Nanocomposites: Effect on Physico-Mechanical, Thermal and Morphological Properties. *Polym. Degrad. Stab.* **2009**, *94*, 132–138.
- (22) Arunvisut, S.; Phummanee, S.; Somwangthanaroj, A. Effect of Clay on Mechanical and Gas Barrier Properties of Blown Film LDPE/Clay Nanocomposites. *J. Appl. Polym. Sci.* **2007**, *106*, 2210–2217.
- (23) Chua, Y. C.; Wu, S.; Lu, X. Poly(Ethylene Naphthalate)/Clay Nanocomposites Based on Thermally Stable Trialkylimidazolium-Treated Montmorillonite: Thermal and Dynamic Mechanical Properties. *J. Nanosci. Nanotechnol.* **2006**, *6*, 3985–3988.

- (24) Wang, Y.; Gao, J.; Ma, Y.; Agarwal, U. S. Study on Mechanical Properties, Thermal Stability and Crystallization Behavior of PET/MMT Nanocomposites. *Compos. Part B Eng.* **2006**, *37*, 399–407.
- (25) Deka, B. K.; Maji, T. K.; Mandal, M. Study on Properties of Nanocomposites Based on HDPE, LDPE, PP, PVC, Wood and Clay. *Polym. Bull.* **2011**, *67*, 1875–1892.
- (26) Fitaroni, L. B.; De Lima, J. A.; Cruz, S. A.; Waldman, W. R. Thermal Stability of Polypropylene-Montmorillonite Clay Nanocomposites: Limitation of the Thermogravimetric Analysis. *Polym. Degrad. Stab.* **2015**, *111*, 102–108.
- (27) Durmuş, A.; Woo, M.; Kaşgöz, A.; Macosko, C. W.; Tsapatsis, M. Intercalated Linear Low Density Polyethylene (LLDPE)/Clay Nanocomposites Prepared with Oxidized Polyethylene as a New Type Compatibilizer: Structural, Mechanical and Barrier Properties. *Eur. Polym. J.* **2007**, *43*, 3737–3749.
- (28) Mittal, V. Gas Permeation and Mechanical Properties of Polypropylene Nanocomposites with Thermally-Stable Imidazolium Modified Clay. *Eur. Polym. J.* **2007**, *43*, 3727–3736.
- (29) Ke, Z.; Yongping, B. Improve the Gas Barrier Property of PET Film with Montmorillonite by in Situ Interlayer Polymerization. *Mater. Lett.* **2005**, *59*, 3348–3351.
- (30) Grim, R. E.; Kulbicki, G. Montmorillonite: High Temperature Reactions and Classification. *Am. Mineral.* **1967**, *46*, 1329–1369.
- (31) Emmerich, K.; Wolters, F.; Kahr, G.; Lagaly, G. Clay Profiling: The Classification of Montmorillonites. *Clays Clay Miner.* **2009**, *57*, 104–114.
- (32) Bérend, I.; Cases, J. M.; François, M.; Uriot, J. P.; Michot, L.; Masion, A.; Thomas, F. Mechanism of Adsorption and Desorption of Water Vapor by Homoionic Montmorillonites: 2. The Li⁺, Na⁺, K⁺, Rb⁺, and Cs⁺-Exchanged Forms. *Clays Clay Miner.* **1995**, *43*, 324–336.
- (33) Lawrence, M. A. M.; Kukkadapu, R. K.; Boyd, S. A. Adsorption of Phenol and Chlorinated Phenols from Aqueous Solution by Tetramethylammonium- and Tetramethylphosphonium-Exchanged Montmorillonite. *Appl. Clay Sci.* **1998**, *13*, 13–20.
- (34) Haraguchi, K. Synthesis and Properties of Soft Nanocomposite Materials with Novel Organic/Inorganic Network Structures. *Polym. J.* **2011**, *43*, 223–241.
- (35) Liu, P. Polymer Modified Clay Minerals: A Review. *Appl. Clay Sci.* **2007**, *38*, 64–76.

- (36) Le Pluart, L.; Duchet, J.; Sautereau, H.; Gérard, J. F. Surface Modifications of Montmorillonite for Tailored Interfaces in Nanocomposites. *J. Adhes.* **2002**, *78*, 645–662.
- (37) Heinz, H.; Vaia, R. A.; Krishnamoorti, R.; Farmer, B. L. Self-Assembly of Alkylammonium Chains on Montmorillonite: Effect of Chain Length, Head Group Structure, and Cation Exchange Capacity. *Chem. Mater.* **2007**, *19*, 59–68.
- (38) Wang, Z. M.; Nakajima, H.; Manias, E.; Chung, T. C. Exfoliated PP/Clay Nanocomposites Using Ammonium-Terminated PP as the Organic Modification for Montmorillonite. *Macromolecules* **2003**, *36*, 8919–8922.
- (39) Taguet, A.; Cassagnau, P.; Lopez-Cuesta, J. M. Structuration, Selective Dispersion and Compatibilizing Effect of (Nano)Fillers in Polymer Blends. *Prog. Polym. Sci.* **2014**, *39*, 1526–1563.
- (40) Chen, G.; Qi, Z. Shear-Induced Ordered Structure in Polystyrene/Clay Nanocomposite. *J. Mater. Res.* **2000**, *15*, 351–356.
- (41) Dykes, L. M. C.; Torkelson, J. M.; Burghardt, W. R.; Krishnamoorti, R. Shear-Induced Orientation in Polymer/Clay Dispersions via in Situ X-Ray Scattering. *Polymer* **2010**, *51*, 4916–4927.
- (42) Koo, C. M.; Kim, J. H.; Wang, K. I. H.; Chung, I. N. J. Melt-Extensional Properties and Orientation Behaviors of Polypropylene-Layered Silicate Nanocomposites. *J. Polym. Sci. Part B Polym. Phys.* **2005**, *43*, 158–167.
- (43) Park, J. U.; Choi, Y. S.; Cho, K. S.; Kim, D. H.; Ahn, K. H.; Lee, S. J. Time-Electric Field Superposition in Electrically Activated Polypropylene/Layered Silicate Nanocomposites. *Polymer* **2006**, *47*, 5145–5153.
- (44) Kim, D. H.; Cho, K. S.; Mitsumata, T.; Ahn, K. H.; Lee, S. J. Microstructural Evolution of Electrically Activated Polypropylene/Layered Silicate Nanocomposites Investigated by in Situ Synchrotron Wide-Angle X-Ray Scattering and Dielectric Relaxation Analysis. *Polymer* **2006**, *47*, 5938–5945.
- (45) Kim, D. H.; Park, J. U.; Ahn, K. H.; Lee, S. J. Electrically Activated Polypropylene/Clay Nanocomposites. *Macromol. Rapid Commun.* **2003**, *24*, 388–391.
- (46) Koerner, H.; Jacobs, J. D.; Tomlin, D. W.; Busbee, J. D.; Vaia, R. a. Tuning Polymer Nanocomposite Morphology: AC Electric Field Manipulation of Epoxy–Montmorillonite (Clay) Suspensions. *Adv. Mater.* **2004**, *16*, 297–302.

- (47) Batra, S.; Unsal, E.; Cakmak, M. Directed Electric Field Z-Alignment Kinetics of Anisotropic Nanoparticles for Enhanced Ionic Conductivity. *Adv. Funct. Mater.* **2014**, *24*, 7698–7708.
- (48) Paineau, E.; Dozov, I.; Bihannic, I.; Baravian, C.; Krapf, M. E. M.; Philippe, A. M.; Rouzière, S.; Michot, L. J.; Davidson, P. Tailoring Highly Oriented and Micropatterned Clay/Polymer Nanocomposites by Applying an a.c. Electric Field. *ACS Appl. Mater. Interfaces* **2012**, *4*, 4296–4301.
- (49) Paineau, E.; Dozov, I.; Philippe, A. M.; Bihannic, I.; Meneau, F.; Baravian, C.; Michot, L. J.; Davidson, P. In-Situ SAXS Study of Aqueous Clay Suspensions Submitted to Alternating Current Electric Fields. *J. Phys. Chem. B* **2012**, *116*, 13516–13524.
- (50) Guz, L.; Curutchet, G.; Torres Sánchez, R. M.; Candal, R. Adsorption of Crystal Violet on Montmorillonite (or Iron Modified Montmorillonite) Followed by Degradation through Fenton or Photo-Fenton Type Reactions. *J. Environ. Chem. Eng.* **2014**, *2*, 2344–2351.
- (51) Wei, X.; Wu, H.; He, G.; Guan, Y. Efficient Degradation of Phenol Using Iron-Montmorillonite as a Fenton Catalyst: Importance of Visible Light Irradiation and Intermediates. *J. Hazard. Mater.* **2017**, *321*, 408–416.
- (52) Keeling, J. L.; Raven, M. D.; Gates, W. P. Geology and Characterization of Two Hydrothermal Nontronites from Weathered Metamorphic Rocks at the Uley Graphite Mine, South Australia. *Clays Clay Miner.* **2000**, *48*, 537–548.
- (53) Gates, W. P.; Slade, P. G.; Manceau, A.; Lanson, B. Site Occupancies by Iron in Nontronites. *Clays Clay Miner.* **2002**, *50*, 223–239.
- (54) Koerner, H.; Hampton, E.; Dean, D.; Turgut, Z.; Drummy, L.; Mirau, P.; Vaia, R. Generating Triaxial Reinforced Epoxy/Montmorillonite Nanocomposites with Uniaxial Magnetic Fields. *Chem. Mater.* **2005**, *17*, 1990–1996.
- (55) Jennings, B. R.; Wilson, S. R.; Ridler, P. J. Magnetic Birefringence of Minerals. *J. Colloid Interface Sci.* **2005**, *281*, 368–376.
- (56) Bates, F. S. Polymer-Polymer Phase Behavior. *Science* **1991**, *251*, 898–905.
- (57) Swann, J. M. G.; Topham, P. D. Design and Application of Nanoscale Actuators Using Block-Copolymers. *Polymers* **2010**, *2*, 454–469.
- (58) Sinha Ray, S. An Overview of Pure and Organically Modified Clays. In *Clay-Containing Polymer Nanocomposites*; 2013; pp 1–24.

- (59) Ournassat, C. H. T.; Eaman, A. L. N.; Illi eras, F. R. V; Osbach, D. I. R. K. B.; Harlet, L. A. C. Nanomorphology of Montmorillonite Particles : Estimation of the Clay Edge Sorption Site Density by Low-Pressure Gas Adsorption and AFM Observations. *Am. Miner.* **2003**, *88*, 1989–1995.
- (60) Yalcin, B.; Cakmak, M. The Role of Plasticizer on the Exfoliation and Dispersion and Fracture Behavior of Clay Particles in PVC Matrix: A Comprehensive Morphological Study. *Polymer* **2004**, *45*, 6623–6638.
- (61) Hu, H.; Pan, M.; Li, X.; Shi, X.; Zhang, L. Preparation and Characterization of Poly(Vinyl Chloride)/Organoclay Nanocomposites by in Situ Intercalation. *Polym. Int.* **2004**, *53*, 225–231.
- (62) Alexandre, M.; Dubois, P. Polymer-Layered Silicate Nanocomposites: Preparation, Properties and Uses of a New Class of Materials. *Mater. Sci. Eng. R Reports* **2000**, *28*, 1–63.
- (63) Unalan, I. U.; Cerri, G.; Marcuzzo, E.; Cozzolino, C. A.; Farris, S. Nanocomposite Films and Coatings Using Inorganic Nanobuilding Blocks (NBB): Current Applications and Future Opportunities in the Food Packaging Sector. *RSC Adv.* **2014**, *4*, 29393–29428.
- (64) Paul, D. R.; Robeson, L. M. Polymer Nanotechnology: Nanocomposites. *Polymer* **2008**, *49*, 3187–3204.
- (65) Kim, S. H.; Kim, S. C. Crystallization Behavior of Poly(ϵ -Caprolactone)/Layered Double Hydroxide Nanocomposites. *J. Appl. Polym. Sci.* **2007**, *103*, 1262–1271.
- (66) Choi, W. J.; Kim, H. J.; Yoon, K. H.; Kwon, O. H.; Hwang, C. I. Preparation and Barrier Property of Poly(Ethylene Terephthalate)/Clay Nanocomposite Using Clay-Supported Catalyst. *J. Appl. Polym. Sci.* **2006**, *100*, 4875–4879.
- (67) Zou, H.; Wu, S.; Shen, J. Polymer / Silica Nanocomposites : Preparation , Polymer / Silica Nanocomposites : Preparation , Characterization , Properties , And. *Chem. Rev.* **2008**, 3893–3957.
- (68) Feng, Y.; Yuan, H. L.; Zhang, M. Fabrication and Properties of Silver-Matrix Composites Reinforced by Carbon Nanotubes. *Mater. Charact.* **2005**, *55*, 211–218.
- (69) Liu, Y.; Gao, L. A Study of the Electrical Properties of Carbon Nanotube-NiFe 2O4 Composites: Effect of the Surface Treatment of the Carbon Nanotubes. *Carbon* **2005**, *43*, 47–52.

- (70) Kim, H.; Abdala, A. A.; MacOsco, C. W. Graphene/Polymer Nanocomposites. *Macromolecules* **2010**, *43*, 6515–6530.
- (71) Li, H.; Cheng, F.; Duft, A. M.; Adronov, A. Functionalization of Single-Walled Carbon Nanotubes with Well-Defined Polystyrene by “Click” Coupling. *J. Am. Chem. Soc.* **2005**, *127*, 14518–14524.
- (72) Ezzeddine, A.; Chen, Z.; Schanze, K. S.; Khashab, N. M. Surface Modification of Multiwalled Carbon Nanotubes with Cationic Conjugated Polyelectrolytes: Fundamental Interactions and Intercalation into Conductive Poly(Methyl Methacrylate) Composites. *ACS Appl. Mater. Interfaces* **2015**, *7*, 12903–12913.
- (73) Kim, H.; Macosko, C. W. Morphology and Properties of Polyester/Exfoliated Graphite Nanocomposites. *Macromolecules* **2008**, *41*, 3317–3327.
- (74) Rafiee, M. A.; Rafiee, J.; Wang, Z.; Song, H.; Yu, Z. Z.; Koratkar, N. Enhanced Mechanical Properties of Nanocomposites at Low Graphene Content. *ACS Nano* **2009**, *3*, 3884–3890.
- (75) Ramanathan, T.; Abdala, A. A.; Stankovich, S.; Dikin, D. A.; Herrera-Alonso, M.; Piner, R. D.; Adamson, D. H.; Schniepp, H. C.; Chen, X.; Ruoff, R. S.; Nguyen, S. T.; Aksay, I. A.; Prud’Homme, R. K.; Brinson, L. C. Functionalized Graphene Sheets for Polymer Nanocomposites. *Nat. Nanotechnol.* **2008**, *3*, 327–331.
- (76) Stankovich, S.; Dikin, D. A.; Dommett, G. H. B.; Kohlhaas, K. M.; Zimney, E. J.; Stach, E. A.; Piner, R. D.; Nguyen, S. B. T.; Ruoff, R. S. Graphene-Based Composite Materials. *Nature* **2006**, *442*, 282–286.
- (77) Grossiord, N.; Loos, J.; Van Laake, L.; Maugey, M.; Zakri, C.; Koning, C. E.; John Hart, A. High-Conductivity Polymer Nanocomposites Obtained by Tailoring the Characteristics of Carbon Nanotube Fillers. *Adv. Funct. Mater.* **2008**, *18*, 3226–3234.
- (78) Kuilla, T.; Bhadra, S.; Yao, D.; Kim, N. H.; Bose, S.; Lee, J. H. Recent Advances in Graphene Based Polymer Composites. *Prog. Polym. Sci.* **2010**, *35*, 1350–1375.
- (79) Veca, L. M.; Meziani, M. J.; Wang, W.; Wang, X.; Lu, F.; Zhang, P.; Lin, Y.; Fee, R.; Connell, J. W.; Sun, Y. P. Carbon Nanosheets for Polymeric Nanocomposites with High Thermal Conductivity. *Adv. Mater.* **2009**, *21*, 2088–2092.
- (80) Tanaka, H.; Lovinger, A. J.; Davis, D. D. Pattern Evolution Caused by Dynamic Coupling between Wetting and Phase Separation in Binary Liquid Mixture Containing Glass Particles. *Phys. Rev. Lett.* **1994**, *72*, 2581–2584.

- (81) Balazs, A. C.; Ginzburg, V. V.; Qiu, F.; Peng, G.; Jasnow, D. Multi-Scale Model for Binary Mixtures Containing Nanoscopic Particles. *J. Phys. Chem. B* **2000**, *104*, 3411–3422.
- (82) Li, Y.; Shimizu, H. Novel Morphologies of Poly(Phenylene Oxide) (PPO)/Polyamide 6 (PA6) Blend Nanocomposites. *Polymer* **2004**, *45*, 7381–7388.
- (83) Si, M.; Araki, T.; Ader, H.; Kilcoyne, A. L. D.; Fisher, R.; Sokolov, J. C.; Rafailovich, M. H. Compatibilizing Bulk Polymer Blends by Using Organoclays. *Macromolecules* **2006**, *39*, 4793–4801.
- (84) Trifkovic, M.; Hedegaard, A. T.; Sheikhzadeh, M.; Huang, S.; Macosko, C. W. Stabilization of PE/PEO Cocontinuous Blends by Interfacial Nanoclays. *Macromolecules* **2015**, *48*, 4631–4644.
- (85) Filippone, G.; Dintcheva, N. T.; Acierno, D.; La Mantia, F. P. The Role of Organoclay in Promoting Co-Continuous Morphology in High-Density Poly(Ethylene)/Poly(Amide) 6 Blends. *Polymer* **2008**, *49*, 1312–1322.
- (86) Filippone, G.; Dintcheva, N. T.; Mantia, F. P. La; Acierno, D. Using Organoclay to Promote Morphology Re Fi Nement and Co-Continuity in High-Density Polyethylene / Polyamide 6 Blends-Effect of Filler Content and Polymer Matrix Composition. *Polymer* **2010**, *51*, 3956–3965.
- (87) Altobelli, R.; Salzano de Luna, M.; Filippone, G. Interfacial Crowding of Nanoplatelets in Co-Continuous Polymer Blends: Assembly, Elasticity and Structure of the Interfacial Nanoparticle Network. *Soft Matter* **2017**, *13*, 6465–6473.
- (88) De Luna, M. S.; Causa, A.; Filippone, G. Interfacially-Located Nanoparticles Anticipate the Onset of Co-Continuity in Immiscible Polymer Blends. *Polymers* **2017**, *9*, 1–11.
- (89) Stratford, K.; Adhikari, R.; Pagonabarraga, I.; Desplat, J.-C.; Cates, M. E. Colloidal Jamming at Interfaces: A Route to Fluid-Bicontinuous Gels. *Science* **2005**, *309*, 2198–2201.
- (90) Chung, H. J.; Ohno, K.; Fukuda, T.; Composto, R. J. Self-Regulated Structures in Nanocomposites by Directed Nanoparticle Assembly. *Nano Lett.* **2005**, *5*, 1878–1882.
- (91) Herzig, E. M.; White, K. A.; Schofield, A. B.; Poon, W. C. K.; Clegg, P. S. Bicontinuous Emulsions Stabilized Solely by Colloidal Particles. *Nat. Mater.* **2007**, *6*, 966–971.
- (92) Witt, J. A.; Mumm, D. R.; Mohraz, A. Bijel Reinforcement by Droplet Bridging: A Route to Bicontinuous Materials with Large Domains. *Soft Matter* **2013**, *9*, 6773–6780.

- (93) Cai, D.; Clegg, P. S. Stabilizing Bijels Using a Mixture of Fumed Silica Nanoparticles. *Chem. Commun. Chem. Commun* **2015**, *51*, 16984–16987.
- (94) Bai, L.; Fruehwirth, J. W.; Cheng, X.; Macosko, C. W. Dynamics and Rheology of Nonpolar Bijels. *Soft Matter* **2015**, *11*, 5282–5293.
- (95) Li, L.; Miesch, C.; Sudeep, P. K.; Balazs, A. C.; Emrick, T.; Russell, T. P.; Hayward, R. C. Kinetically Trapped Co-Continuous Polymer Morphologies through Intraphase Gelation of Nanoparticles. *Nano Lett.* **2011**, *11*, 1997–2003.
- (96) Yeganeh, J. K.; Goharpey, F.; Moghimi, E.; Petekidis, G.; Foudazi, R. Controlling the Kinetics of Viscoelastic Phase Separation through Self-Assembly of Spherical Nanoparticles or Block Copolymers. *Soft Matter* **2014**, *10*, 9270–9280.
- (97) Huang, S.; Bai, L.; Trifkovic, M.; Cheng, X.; Macosko, C. W. Controlling the Morphology of Immiscible Cocontinuous Polymer Blends via Silica Nanoparticles Jammed at the Interface. *Macromolecules* **2016**, *49*, 3911–3918.
- (98) Liu, X.; Li, R.; Bao, R.; Jiang, W.; Yang, W.; Xie, B.; Yang, M. Suppression of Phase Coarsening in Immiscible, Co-Continuous Polymer Blends under High Temperature Quiescent Annealing. *Soft Matter* **2014**, *10*, 3587–3596.
- (99) Gubbels, F.; Jérôme, R.; Teyssié, P.; Vanlathem, E.; Deltour, R.; Calderone, A.; Parenté, V.; Brédas, J. L. Selective Localization of Carbon Black in Immiscible Polymer Blends: A Useful Tool To Design Electrical Conductive Composites. *Macromolecules* **1994**, *27*, 1972–1974.
- (100) Gubbels, F.; Blacher, S.; Vanlathem, E.; Jérôme, R.; Deltour, R.; Brouers, F.; Teyssié, P. Design of Electrical Conductive Composites: Key Role of the Morphology on the Electrical Properties of Carbon Black Filled Polymer Blends. *Macromolecules* **1995**, *28*, 1559–1566.
- (101) Sumita, M.; Sakata, K.; Asai, S.; Miyasaka, K.; Nakagawa, H. Dispersion of Fillers and the Electrical Conductivity of Polymer Blends Filled with Carbon Black. *Polym. Bull.* **1991**, *25*, 265–271.
- (102) Chung, H. J.; Kim, J.; Ohno, K.; Composto, R. J. Controlling the Location of Nanoparticles in Polymer Blends by Tuning the Length and End Group of Polymer Brushes. *ACS Macro Lett.* **2012**, *1*, 252–256.
- (103) Elias, L.; Fenouillot, F.; Majeste, J. C.; Cassagnau, P. Morphology and Rheology of Immiscible Polymer Blends Filled with Silica Nanoparticles. *Polymer* **2007**, *48*, 6029–6040.

- (104) Goater, A. D.; Pethig, R. Electrorotation and Dielectrophoresis. *Parasitology* **1999**, *117*, 177–189.
- (105) Dozov, I.; Paineau, E.; Davidson, P.; Antonova, K.; Baravian, C.; Bihannic, I.; Michot, L. J. Electric-Field-Induced Perfect Anti-Nematic Order in Isotropic Aqueous Suspensions of a Natural Beidellite Clay. *J. Phys. Chem. B* **2011**, *115*, 7751–7765.
- (106) Batra, S.; Cakmak, M. Ultra-Capacitor Flexible Films with Tailored Dielectric Constant Using Electric Field Assisted Assembly of Nanoparticles. *Nanoscale* **2015**, *7*, 20571–20583.
- (107) Yan, J.; Jeong, Y. G. High Performance Flexible Piezoelectric Nanogenerators Based on BaTiO₃ Nanofibers in Different Alignment Modes. *ACS Appl. Mater. Interfaces* **2016**, *8*, 15700–15709.
- (108) Masud, A. Al; Ounaies, Z. Dielectric Properties of Dielectrophoretically Aligned ZnO-PDMS Composites. *Proc. ASME 2016 Conf. Smart Mater.* **2017**, 1–8.
- (109) Yildirim, A.; Rahimi, R.; Shams Es-haghi, S.; Vadlamani, A.; Peng, F.; Osci, M.; Cakmak, M. Roll-to-Roll (R2R) Production of Ultrasensitive, Flexible, and Transparent Pressure Sensors Based on Vertically Aligned Lead Zirconate Titanate and Graphene Nanoplatelets. *Adv. Mater. Technol.* **2019**, *4*, 1–10.
- (110) Prasse, T.; Cavallé, J. Y.; Bauhofer, W. Electric Anisotropy of Carbon Nanofibre/Epoxy Resin Composites Due to Electric Field Induced Alignment. *Compos. Sci. Technol.* **2003**, *63*, 1835–1841.
- (111) Guo, Y.; Chen, Y.; Wang, E.; Cakmak, M. Roll-to-Roll Continuous Manufacturing Multifunctional Nanocomposites by Electric-Field-Assisted “z” Direction Alignment of Graphite Flakes in Poly(Dimethylsiloxane). *ACS Appl. Mater. Interfaces* **2017**, *9*, 919–929.
- (112) Gaska, K.; Kmita, G.; Rybak, A.; Sekula, R.; Goc, K.; Kapusta, C. Magnetic-Aligned, Magnetite-Filled Epoxy Composites with Enhanced Thermal Conductivity. *J. Mater. Sci.* **2015**, *50*, 2510–2516.
- (113) Chen, Y.; Guo, Y.; Batra, S.; Unsal, E.; Wang, E.; Wang, Y.; Liu, X.; Wang, Y.; Cakmak, M. Large-Scale R2R Fabrication of Piezoresistive Films (Ni/PDMS) with Enhanced through Thickness Electrical and Thermal Properties by Applying a Magnetic Field. *RSC Adv.* **2015**, *5*, 92071–92079.

- (114) Peng, F.; Chen, K.; Yildirim, A.; Xia, X.; Vogt, B. D.; Cakmak, M. M. Tunable Piezoresistivity from Magnetically Aligned Ni(Core)@Ag(Shell) Particles in an Elastomer Matrix. *ACS Appl. Mater. Interfaces* **2019**, *11*, 20360–20369.
- (115) Wu, L.; Ohtani, M.; Takata, M.; Saeki, A.; Seki, S.; Ishida, Y.; Aida, T. Magnetically Induced Anisotropic Orientation of Graphene Oxide Locked by in Situ Hydrogelation. *ACS Nano* **2014**, *8*, 4640–4649.
- (116) Stamenov, P.; Coey, J. M. D. Magnetic Susceptibility of Carbon - Experiment and Theory. *J. Magn. Magn. Mater.* **2005**, *290–291*, 279–285.
- (117) Choi, E. S.; Brooks, J. S.; Eaton, D. L.; Al-Haik, M. S.; Hussaini, M. Y.; Garmestani, H.; Li, D.; Dahmen, K. Enhancement of Thermal and Electrical Properties of Carbon Nanotube Polymer Composites by Magnetic Field Processing. *J. Appl. Phys.* **2003**, *94*, 6034–6039.
- (118) Kitajima, S.; Matsuda, M.; Yamato, M.; Tominaga, Y. Anisotropic Ionic Conduction in Composite Polymer Electrolytes Filled with Clays Oriented by a Strong Magnetic Field. *Polym. J.* **2013**, *45*, 738–743.
- (119) Kaneko, Y.; Shimada, S.; Fukuda, T.; Kimura, T.; Yokoi, H.; Matsuda, H.; Onodera, T.; Kasai, H.; Okada, S.; Oikawa, H.; Nakanishi, H. A Novel Method for Fixing the Anisotropic Orientation of Dispersed Organic Nanocrystals in a Magnetic Field. *Adv. Mater.* **2005**, *17*, 160–163.
- (120) Kaneko, Y.; Fukuda, T.; Onodera, T.; Kasai, H.; Okada, S.; Oikawa, H.; Nakanishi, H.; Matsuda, H. Orientation of Suspended Polar Organic Nanocrystals in Magnetic Fields: Effect of Magnetic Field Configuration. *Jpn. J. Appl. Phys.* **2003**, *42*, L1343–L1345.
- (121) Kim, J. E.; Han, T. H.; Lee, S. H.; Kim, J. Y.; Ahn, C. W.; Yun, J. M.; Kim, S. O. Graphene Oxide Liquid Crystals. *Angew. Chemie - Int. Ed.* **2011**, *50*, 3043–3047.
- (122) Dan, B.; Behabtu, N.; Martinez, A.; Evans, J. S.; Kosynkin, D. V.; Tour, J. M.; Pasquali, M.; Smalyukh, I. I. Liquid Crystals of Aqueous, Giant Graphene Oxide Flakes. *Soft Matter* **2011**, *7*, 11154–11159.
- (123) Shen, T.-Z.; Hong, S.-H.; Song, J.-K. Electro-Optical Switching of Graphene Oxide Liquid Crystals with an Extremely Large Kerr Coefficient. *Nat. Mater.* **2014**, *13*, 394–399.
- (124) Michot, L. J.; Bihannic, I.; Maddi, S.; Funari, S. S.; Baravian, C.; Levitz, P.; Davidson, P. Liquid-Crystalline Aqueous Clay Suspensions. *Proc. Natl. Acad. Sci.* **2006**, *103*, 16101–16104.

- (125) Hori, H.; Urakawa, O.; Yano, O.; Tran-Cong-Miyata, Q. Phase Separation of Binary Polymer Mixtures under an Electric Field. *Macromolecules* **2007**, *40*, 389–394.
- (126) Venugopal, G.; Krause, S. Development of Phase Morphologies of Poly(Methyl Methacrylate)-Polystyrene-Toluene Mixtures in Electric Fields. *Macromolecules* **1992**, *25*, 4626–4634.
- (127) Böker, A.; Knoll, A.; Elbs, H.; Abetz, V.; Müller, A. H. E.; Krausch, G. Large Scale Domain Alignment of a Block Copolymer from Solution Using Electric Fields. *Macromolecules* **2002**, *35*, 1319–1325.
- (128) Olszowka, V.; Hund, M.; Kuntermann, V.; Scherdel, S.; Tsarkova, L.; Böker, A.; Krausch, G. Large Scale Alignment of a Lamellar Block Copolymer Thin Film via Electric Fields: A Time-Resolved SFM Study. *Soft Matter* **2006**, *2*, 1089–1094.
- (129) Olszowka, V.; Hund, M.; Kuntermann, V.; Scherdel, S.; Tsarkova, L.; Böker, A. Electric Field Alignment of a Block Copolymer Nanopattern: Direct Observation of the Microscopic Mechanism. *ACS Nano* **2009**, *3*, 1091–1096.
- (130) Halsey, T. C. Electrorheological Fluids. *Science* **1992**, *258*, 761–766.
- (131) Ha, J. W.; Yang, S. M. Deformation and Breakup of Newtonian and Non-Newtonian Conducting Drops in an Electric Field. *J. Fluid Mech.* **2000**, *405*, 131–156.
- (132) Gasa, J. V.; Weiss, R. A.; Shaw, M. T. Structured Polymer Electrolyte Blends Based on Sulfonated Polyetherketoneketone (SPEKK) and a Poly (Ether Imide) (PEI). *J. of Membrane Sci. J.* **2008**, *320*, 215–223.
- (133) Morkved, A. T. L.; Lu, M.; Urbas, A. M.; Ehrichs, E. E.; Jaeger, H. M.; Mansky, P. Local Control of Microdomain Orientation in Diblock Copolymer Thin Films with Electric Fields. *Science* **1996**, *273*, 931–933.
- (134) Böker, A.; Schmidt, K.; Knoll, A.; Zettl, H.; Hänsel, H.; Urban, V.; Abetz, V.; Krausch, G. The Influence of Incompatibility and Dielectric Contrast on the Electric Field-Induced Orientation of Lamellar Block Copolymers. *Polymer* **2006**, *47*, 849–857.
- (135) Osuji, C.; Ferreira, P. J.; Mao, G.; Ober, C. K.; Sande, J. B. V.; Thomas, E. L. Alignment of Self-Assembled Hierarchical Microstructure in Liquid Crystalline Diblock Copolymers Using High Magnetic Fields. *Macromolecules* **2004**, *37*, 9903–9908.
- (136) Gopinadhan, M.; Majewski, P. W.; Beach, E. S.; Osuji, C. O. Magnetic Field Alignment of a Diblock Copolymer Using a Supramolecular Route. *ACS Macro Lett.* **2012**, *1*, 184–189.

- (137) Haraguchi, K.; Takehisa, T.; Fan, S. Effects of Clay Content on the Properties of Nanocomposite Hydrogels Composed of Poly(N-Isopropylacrylamide) and Clay. *Macromolecules* **2002**, *35*, 10162–10171.
- (138) Pozzo, D. C.; Walker, L. M. Reversible Shear Gelation of Polymer-Clay Dispersions. *Colloids Surfaces A Physicochem. Eng. Asp.* **2004**, *240*, 187–198.
- (139) Can, V.; Okay, O. Shake Gels Based on Laponite-PEO Mixtures: Effect of Polymer Molecular Weight. *Des. Monomers Polym.* **2005**, *8*, 453–462.
- (140) Baghdadi, H. A.; Sardinha, H.; Bhatia, S. R. Rheology and Gelation Kinetics in Laponite Dispersions Containing Poly(Ethylene Oxide). *J. Polym. Sci. Part B Polym. Phys.* **2005**, *43*, 233–240.
- (141) Zhang, J.; Wang, A. Study on Superabsorbent Composites. IX: Synthesis, Characterization and Swelling Behaviors of Polyacrylamide/Clay Composites Based on Various Clays. *React. Funct. Polym.* **2007**, *67*, 737–745.
- (142) Shipway, A. N.; Willner, I. Nanoparticles as Structural and Functional Units in Surface-Confining Architectures. *Chem. Commun. Chem. Commun* **2001**, 2035–2045.
- (143) You, J.; Auguste, D. T. Conductive, Physiologically Responsive Hydrogels. *Langmuir* **2010**, *26*, 4607–4612.
- (144) Skirtach, A. G.; Dejugnat, C.; Braun, D.; Susha, A. S.; Rogach, A. L.; Parak, W. J.; Möhwald, H.; Sukhorukov, G. B. The Role of Metal Nanoparticles in Remote Release of Encapsulated Materials. *Nano Lett.* **2005**, *5*, 1371–1377.
- (145) Ramanujan, R. V; Lao, L. L. The Mechanical Behavior of Smart Magnet–Hydrogel Composites. *Smart Mater. Struct.* **2006**, *15*, 952–956.
- (146) Liu, R.; Liang, S.; Tang, X.-Z.; Yan, D.; Li, X.; Yu, Z.-Z. Tough and Highly Stretchable Graphene Oxide/Polyacrylamide Nanocomposite Hydrogels. *J. Mater. Chem.* **2012**, *22*, 14160.
- (147) Hu, K.; Xie, X.; Szkopek, T.; Cerruti, M. Understanding Hydrothermally Reduced Graphene Oxide Hydrogels: From Reaction Products to Hydrogel Properties. *Chem. Mater.* **2016**, No. 28, 1756–1768.
- (148) Wasalathilake, K. C.; Galpaya, D. G. D.; Ayoko, G. A.; Yan, C. Understanding the Structure-Property Relationships in Hydrothermally Reduced Graphene Oxide Hydrogels. *Carbon* **2018**, *137*, 282–290.

- (149) Xu, Y.; Sheng, K.; Li, C.; Shi, G. Self-Assembled Graphene Hydrogel via a One-Step Hydrothermal Process. *ACS Nano* **2010**, *4*, 4324–4330.
- (150) Wu, J.; Tao, K.; Guo, Y.; Li, Z.; Wang, X.; Luo, Z.; Feng, S.; Du, C.; Chen, D.; Miao, J.; Norford, L. K. A 3D Chemically Modified Graphene Hydrogel for Fast, Highly Sensitive, and Selective Gas Sensor. *Adv. Sci.* **2017**, *4*, 1600319.
- (151) Liu, M.; Ishida, Y.; Ebina, Y.; Sasaki, T.; Aida, T. Photolatently Modulable Hydrogels Using Unilamellar Titania Nanosheets as Photocatalytic Crosslinkers. *Nat. Commun.* **2013**, *4*, 1–7.
- (152) Sun, J.; Schmidt, B. V. K. J.; Wang, X.; Shalom, M. Self-Standing Carbon Nitride-Based Hydrogels with High Photocatalytic Activity. *ACS Appl. Mater. Interfaces* **2017**, *9*, 2029–2034.
- (153) Hu, X.; Liu, J.; He, Q.; Meng, Y.; Cao, L.; Sun, Y.; Chen, J.; Lu, F. Aqueous Compatible Boron Nitride Nanosheets for High-Performance Hydrogels. *Nanoscale* **2016**, *8*, 4260–4266.
- (154) Sano, K.; Ishida, Y.; Aida, T. Synthesis of Anisotropic Hydrogels and Their Applications Minireviews. *Angew. Chemie - Int. Ed.* **2018**, *57*, 2532–2543.
- (155) Le, X.; Lu, W.; Zhang, J.; Chen, T. Recent Progress in Biomimetic Anisotropic Hydrogel Actuators. *Adv. Sci.* **2019**, *6*, 1801584.
- (156) Miyamoto, N.; Shintate, M.; Ikeda, S.; Hoshida, Y.; Yamauchi, Y.; Motokawa, R.; Annaka, M. Liquid Crystalline Inorganic Nanosheets for Facile Synthesis of Polymer Hydrogels with Anisotropies in Structure, Optical Property, Swelling/Deswelling, and Ion Transport/Fixation. *Chem. Commun.* **2013**, *49*, 1082–1084.
- (157) Inadomi, T.; Ikeda, S.; Okumura, Y.; Kikuchi, H.; Miyamoto, N. Photo-Induced Anomalous Deformation of Poly(N-Isopropylacrylamide) Gel Hybridized with an Inorganic Nanosheet Liquid Crystal Aligned by Electric Field. *Macromol. Rapid Commun.* **2014**, *35*, 1741–1746.
- (158) Liu, M.; Ishida, Y.; Ebina, Y.; Sasaki, T.; Hikima, T.; Takata, M.; Aida, T. An Anisotropic Hydrogel with Electrostatic Repulsion between Cofacially Aligned Nanosheets. *Nature* **2015**, *517*, 68–72.
- (159) Kim, Y. S.; Liu, M.; Ishida, Y.; Ebina, Y.; Osada, M.; Sasaki, T.; Hikima, T.; Takata, M.; Aida, T. Thermoresponsive Actuation Enabled by Permittivity Switching in an Electrostatically Anisotropic Hydrogel. *Nat. Mater.* **2015**, *14*, 1002–1007.

- (160) Sano, K.; Ishida, Y.; Aida, T. Synthesis of Anisotropic Hydrogels and Their Applications. *Angew. Chemie - Int. Ed.* **2018**, *57*, 2532–2543.
- (161) Yook, S.; Isik, T.; Ortalan, V.; Cakmak, M. Anisotropic Phase-Separated Morphology of Polymer Blends Directed by Electrically Pre-Oriented Clay Platelets. *Soft Matter* **2020**, *16*, 2104–2113.
- (162) Arns, C. H.; Knackstedt, M. A.; Roberts, A. P.; Pinczewski, V. W. Morphology, Cocontinuity, and Conductive Properties of Anisotropic Polymer Blends. *Macromolecules* **1999**, *32*, 5964–5966.
- (163) Ray, B.; Alam, M. A. Solar Energy Materials & Solar Cells Random vs Regularized OPV : Limits of Performance Gain of Organic Bulk Heterojunction Solar Cells by Morphology Engineering. *Sol. Energy Mater. Sol. Cells* **2012**, *99*, 204–212.
- (164) Han, C. C.; Yao, Y.; Zhang, R.; Hobbie, E. K. Effect of Shear Flow on Multi-Component Polymer Mixtures. *Polymer* **2006**, *47*, 3271–3286.
- (165) Kielhorn, L.; Colby, R. H.; Han, C. C. Relaxation Behavior of Polymer Blends after the Cessation of Shear. *Macromolecules* **2000**, *33*, 2486–2496.
- (166) Venugopal, G.; Krause, S.; Wnek, G. E. Morphological Variations in Polymer Blends Made in Electric Fields. *Chem. Mater.* **1992**, *4*, 1334–1343.
- (167) Serpico, J. M.; Wnek, G. E.; Krause, S.; Smith, T. W.; Luca, D. J.; Van Laeken, A. Effect of Block Copolymer on the Electric Field Induced Morphology of Polymer Blends. *Macromolecules* **1991**, *24*, 6879–6881.
- (168) Dommersnes, P.; Rozynek, Z.; Mikkelsen, A.; Castberg, R.; Kjerstad, K.; Hersvik, K.; Otto Fossum, J. Active Structuring of Colloidal Armour on Liquid Drops. *Nat. Commun.* **2013**, *4*, 2066.
- (169) Taylor, G. Studies in Electrohydrodynamics. I. The Circulation Produced in a Drop by Electrical Field. *Proc. R. Soc. A Math. Phys. Eng. Sci.* **1966**, *291*, 159–166.
- (170) Hopkinson, I.; Myatt, M. Phase Separation in Ternary Polymer Solutions Induced by Solvent Loss. *Macromolecules* **2002**, *35*, 5153–5160.
- (171) Li, L.; Shen, X.; Hong, S. W.; Hayward, R. C.; Russell, T. P. Fabrication of Co-Continuous Nanostructured and Porous Polymer Membranes: Spinodal Decomposition of Homopolymer and Random Copolymer Blends. *Angew. Chemie Int. Ed.* **2012**, *51*, 4089–4094.

- (172) Kwon, T.; Kim, T.; Ali, F. B.; Kang, D. J.; Yoo, M.; Bang, J.; Lee, W.; Kim, B. J. Size-Controlled Polymer-Coated Nanoparticles as Efficient Compatibilizers for Polymer Blends. *Macromolecules* **2011**, *44*, 9852–9862.
- (173) Huang, C.; Gao, J.; Yu, W.; Zhou, C. Phase Separation of Poly (Methyl Methacrylate)/ Poly (Styrene- Co - Acrylonitrile) Blends with Controlled Distribution of Silica Nanoparticles. *Macromolecules* **2012**, *45*, 8420–8429.
- (174) Gam, S.; Corlu, A.; Chung, H.-J.; Ohno, K.; Hore, M. J. A.; Composto, R. J. A Jamming Morphology Map of Polymer Blend Nanocomposite Films. *Soft Matter* **2011**, *7*, 7262–7268.
- (175) Hillmyer, M. A.; Maurer, W. W.; Lodge, T. P.; Bates, F. S.; Almdal, K. Model Bicontinuous Microemulsions in Ternary Homopolymer/Block Copolymer Blends. *J. Phys. Chem. B* **1999**, *103*, 4814–4824.
- (176) Galloway, J. A.; Jeon, H. K.; Bell, J. R.; Macosko, C. W. Block Copolymer Compatibilization of Cocontinuous Polymer Blends. *Polymer* **2005**, *46*, 183–191.
- (177) Lyu, S. P.; Jones, T. D.; Bates, F. S.; Macosko, C. W. Role of Block Copolymers on Suppression of Droplet Coalescence. *Macromolecules* **2002**, *35*, 7845–7855.
- (178) Wang, Y.; Zhang, Q.; Fu, Q. Compatibilization of Immiscible Poly (Propylene)/Polystyrene Blends Using Clay. *Macromol. Rapid Commun.* **2003**, *24*, 231–235.
- (179) Khatua, B. B.; Lee, D. J.; Kim, H. Y.; Kim, J. K. Effect of Organoclay Platelets on Morphology of Nylon-6 and Poly(Ethylene- Ran -Propylene) Rubber Blends. *Macromolecules* **2004**, *37*, 2454–2459.
- (180) Yurekli, K.; Karim, A.; Amis, E. J.; Krishnamoorti, R. Influence of Layered Silicates on the Phase-Separated Morphology of PS-PVME Blends. *Macromolecules* **2003**, *36*, 7256–7267.
- (181) Kriisa, A.; Roth, C. B. Jumping In and Out of the Phase Diagram Using Electric Fields: Time Scale for Remixing of Polystyrene/Poly(Vinyl Methyl Ether) Blends. *ACS Macro Lett.* **2019**, *8*, 188–192.
- (182) Kriisa, A.; Roth, C. B. Electric Fields Enhance Miscibility of Polystyrene / Poly (Vinyl Methyl Ether) Blends. *J. Chem. Phys.* **2014**, *8*, 134908.
- (183) Cabral, J. T.; Higgins, J. S.; McLeish, T. C. B.; Strausser, S.; Magonov, S. N. Bulk Spinodal Decomposition Studied by Atomic Force Microscopy and Light Scattering. *Macromolecules* **2001**, *34*, 3748–3756.

- (184) Liang, G. D.; Tjong, S. C. Electrical Properties of Percolative Polystyrene/Carbon Nanofiber Composites. *IEEE Trans. Dielectr. Electr. Insul.* **2008**, *15*, 214–220.
- (185) Pathmanathan, K.; Johari, G. P. A Dielectric Study of Chain Motions in Poly(Vinyl Methyl Ether). *J. Polym. Sci. Part B Polym. Phys.* **1987**, *25*, 379–386.
- (186) Zhang, S.; Runt, J. Segmental Dynamics and Ionic Conduction in Poly(Vinyl Methyl Ether)–Lithium Perchlorate Complexes. *J. Phys. Chem. B* **2004**, *108*, 6295–6302.
- (187) Feng, S.; Xiong, X.; Zhang, G.; Xia, N.; Chen, Y.; Wang, W. Hierarchical Structure in Oriented Fibers of a Dendronized Polymer. *Macromolecules* **2009**, *42*, 281–287.
- (188) Nie, Y.; Huang, G.; Qu, L.; Wang, X.; Weng, G.; Wu, J. New Insights into Thermodynamic Description of Strain-Induced Crystallization of Peroxide Cross-Linked Natural Rubber Filled with Clay by Tube Model. *Polymer* **2011**, *52*, 3234–3242.
- (189) Xia, T.; Huang, Y.; Jiang, X.; Lv, Y.; Yang, Q.; Li, G. The Molecular Mechanism of the Morphology Change in PS / PVME / Silica Blends Based on Rheology. *Macromolecules* **2013**, *46*, 8323–8333.
- (190) Xia, T.; Qin, Y.; Huang, Y.; Huang, T.; Xu, J.; Li, Y. Sequence Control of Phase Separation and Dewetting in PS/PVME Blend Thin Films by Changing Molecular Weight of PS. *J. Chem. Phys.* **2016**, *145*, 204903.
- (191) Martin, C. A.; Sandler, J. K. W.; Windle, A. H.; Schwarz, M.; Bauhofer, W. Electric Field-Induced Aligned Multi-Wall Carbon Nanotube Networks in Epoxy Composites. *Polymer* **2005**, *46*, 877–886.
- (192) Chen, G.; Wang, H.; Zhao, W. Fabrication of Highly Ordered Polymer/Graphite Flake Composite with Eminent Anisotropic Electrical Property. *Polym. Adv. Technol.* **2008**, *19*, 1113–1117.
- (193) Cabral, J. T.; Higgins, J. S.; Yerina, N. A.; Magonov, S. N. Topography of Phase-Separated Critical and off-Critical Polymer Mixtures. *Macromolecules* **2002**, *35*, 1941–1950.
- (194) Chem, P.; Chen, J.; Hsu, C. Polymer Chemistry Conjugated Polymer Nanostructures for Organic Solar Cell Applications. *Polym. Chem.* **2011**, *2*, 2707–2722.
- (195) Scharber, M. C.; Sariciftci, N. S. Progress in Polymer Science Efficiency of Bulk-Heterojunction Organic Solar Cells. *Prog. Polym. Sci.* **2013**, *38*, 1929–1940.

- (196) Watkins, P. K.; Walker, A. B.; Verschoor, G. L. B. Dynamical Monte Carlo Modelling of Organic Solar Cells: The Dependence of Internal Quantum Efficiency on Morphology. *Nano Lett.* **2005**, *5*, 1814–1818.
- (197) Hao, T. Electrorheological Fluids. *Adv. Mater.* **2001**, *13*, 1847.
- (198) Ha, J. W.; Yang, S. M. Effects of Surfactant on the Deformation and Stability of a Drop in a Viscous Fluid in an Electric Field. *J. Colloid Interface Sci.* **1995**, *175*, 369–385.
- (199) Xi, K.; Krause, S. Droplet Deformation and Structure Formation in Two-Phase Polymer / Polymer / Toluene Mixtures in an Electric Field. *Macromolecules* **1998**, *31*, 3974–3984.
- (200) Liu, W.; Wang, C.; Ding, H.; Shao, J.; Ding, Y. Applied Surface Science AC Electric Field Induced Dielectrophoretic Assembly Behavior of Gold Nanoparticles in a Wide Frequency Range. *Appl. Surf. Sci.* **2016**, *370*, 184–192.
- (201) Velev, O. D.; Bhatt, K. H. On-Chip Micromanipulation and Assembly of Colloidal Particles by Electric Fields. *Soft Matter* **2006**, *2*, 738–750.
- (202) Mahmoodi, S. R.; Raissi, B.; Marzbanrad, E.; Shojayi, N.; Aghaei, A.; Zamani, C. Procedia Chemistry Dielectrophoretic Assembly of ZnO Nanorods for Gas Sensing. *Procedia Chem.* **2009**, *1*, 947–950.
- (203) Guo, Y.; Batra, S.; Chen, Y.; Wang, E.; Cakmak, M. Roll to Roll Electric Field “z” Alignment of Nanoparticles from Polymer Solutions for Manufacturing Multifunctional Capacitor Films. *ACS Appl. Mater. Interfaces* **2016**, *8*, 18471–18480.
- (204) Cakmak, M.; Guo, Y.; Batra, S. Electric Field “z” Direction Alignment of Nanoparticles in Polymer Solutions. U.S. Patent 0355155A1, December 14, 2017.
- (205) Unsal, E.; Drum, J.; Yucel, O.; Nugay, I. I.; Yalcin, B.; Cakmak, M. Real-Time Measurement System for Tracking Birefringence, Weight, Thickness, and Surface Temperature during Drying of Solution Cast Coatings and Films. *Rev. Sci. Instrum.* **2012**, *83*, 025114.
- (206) Ras, R. H. A.; Umemura, Y.; Johnston, C. T.; Schoonheydt, R. A. Ultrathin Hybrid Films of Clay Minerals. *Phys. Chem. Chem. Phys.* **2007**, *9*, 918–932.
- (207) Earley, J. W.; Osthaus, B. B.; Milne, I. H. Purification and Properties of Montmorillonite. *Am. Mineral.* **1952**, *38*, 707–724.

- (208) Fenouillot, F.; Cassagnau, P.; Majesté, J. C. Uneven Distribution of Nanoparticles in Immiscible Fluids: Morphology Development in Polymer Blends. *Polymer* **2009**, *50*, 1333–1350.
- (209) Yook, S.; Shams Es-Haghi, S.; Yildirim, A.; Mutlu, Z.; Cakmak, M. Anisotropic Hydrogels Formed by Magnetically-Oriented Nanoclay Suspensions for Wound Dressings. *Soft Matter* **2019**, *15*, 9733–9741.
- (210) Wang, Q.; Mynar, J. L.; Yoshida, M.; Lee, E.; Lee, M.; Okuro, K.; Kinbara, K.; Aida, T. High-Water-Content Mouldable Hydrogels by Mixing Clay and a Dendritic Molecular Binder. *Nature* **2010**, *463*, 339–343.
- (211) Haraguchi, K.; Li, H. J. Mechanical Properties and Structure of Polymer-Clay Nanocomposite Gels with High Clay Content. *Macromolecules* **2006**, *39*, 1898–1905.
- (212) Mu, J.; Zheng, S. Poly(N-Isopropylacrylamide) Nanocrosslinked by Polyhedral Oligomeric Silsesquioxane: Temperature-Responsive Behavior of Hydrogels. *J. Colloid Interface Sci.* **2007**, *307*, 377–385.
- (213) Zhao, X.; Ding, X.; Deng, Z.; Zheng, Z.; Peng, Y.; Long, X. Thermoswitchable Electronic Properties of a Gold Nanoparticle/Hydrogel Composite. *Macromol. Rapid Commun.* **2005**, *26*, 1784–1787.
- (214) Thomsen, D. L.; Keller, P.; Naciri, J.; Pink, R.; Jeon, H.; Shenoy, D.; Ratna, B. R. Liquid Crystal Elastomers with Mechanical Properties of a Muscle. *Macromolecules* **2001**, *34*, 5868–5875.
- (215) Mow, V. C.; Guo, X. E. Mechano-Electrochemical Properties Of Articular Cartilage: Their Inhomogeneities and Anisotropies. *Annu. Rev. Biomed. Eng.* **2002**, *4*, 175–209.
- (216) Ní Annaidh, A.; Bruyère, K.; Destrade, M.; Gilchrist, M. D.; Otténio, M. Characterization of the Anisotropic Mechanical Properties of Excised Human Skin. *J. Mech. Behav. Biomed. Mater.* **2012**, *5*, 139–148.
- (217) Woo, K. Y.; Beeckman, D.; Chakravarthy, D. Management of Moisture-Associated Skin Damage : A Scoping Review. *Adv. Skin Wound Care* **2017**, *30*, 494–501.
- (218) Okan, D.; Woo, K.; Ayello, E. A.; Sibbald, R. G. The Role of Moisture Balance in Wound Healing. *Adv. Skin Wound Care* **2007**, *20*, 39–53.

- (219) Guo, Y.; Pan, S.; Jiang, F.; Wang, E.; Miinea, L.; Marchant, N.; Cakmak, M. Anisotropic Swelling Wound Dressings with Vertically Aligned Water Absorptive Particles. *RSC Adv.* **2018**, *8*, 8173–8180.
- (220) He, X.; Takahara, A.; Kajiyama, T. Anisotropic Swelling Behavior of Copolymeric Gel Film with Crystalline Oriented Side Chains. *Polym. Gels Networks* **1997**, *5*, 429–438.
- (221) Lin, X. Y.; Wang, Z. J.; Pan, P.; Wu, Z. L.; Zheng, Q. Monodomain Hydrogels Prepared by Shear-Induced Orientation and Subsequent Gelation. *RSC Adv.* **2016**, *6*, 95239–95245.
- (222) Zhu, Z.; Li, Y.; Xu, H.; Peng, X.; Chen, Y. N.; Shang, C.; Zhang, Q.; Liu, J.; Wang, H. Tough and Thermosensitive Poly(N-Isopropylacrylamide)/Graphene Oxide Hydrogels with Macroscopically Oriented Liquid Crystalline Structures. *ACS Appl. Mater. Interfaces* **2016**, *8*, 15637–15644.
- (223) Hu, Z.; Fischbein, M. D.; Querner, C.; Drndić, M. Electric-Field-Driven Accumulation and Alignment of CdSe and CdTe Nanorods in Nanoscale Devices. *Nano Lett.* **2006**, *6*, 2585–2591.
- (224) Ryan, K. M.; Mastroianni, A.; Stancil, K. A.; Liu, H.; Alivisatos, A. P. Electric-Field-Assisted Assembly of Perpendicularly Oriented Nanorod Superlattices. *Nano Lett.* **2006**, *6*, 1479–1482.
- (225) Kimura, T.; Uemura, T.; Kimura, T.; Takagi, S.; Inoue, H. Magnetic Alignment of Rhodamine B Intercalated in Synthetic Mica. *Macromol. Symp.* **2006**, *242*, 120–125.
- (226) Eguchi, M.; Angelone, M. S.; Yennawar, H. P.; Mallouk, T. E. Anisotropic Alignment of Lamellar Potassium Hexaniobate Microcrystals and Nanoscrolls in a Static Magnetic Field. *J. Phys. Chem. C* **2008**, *112*, 11280–11285.
- (227) Charbonneau, G. P.; Rivet, P. Diamagnetism and Thermal Motion in Rigid-Body Molecules. Application to Biphenyl. *Acta Crystallogr. Sect. A* **1980**, *36*, 51–53.
- (228) Chen, Y.; Guo, Y.; Batra, S.; Wang, E.; Wang, Y.; Liu, X.; Wang, Y.; Cakmak, M. Transparent and through Thickness Conductive Polystyrene Films Using External Magnetic Fields for “z” Alignment of Nickel Nanoparticles. *Nanoscale* **2015**, *7*, 14636–14642.
- (229) Okay, O.; Oppermann, W. Polyacrylamide-Clay Nanocomposite Hydrogels: Rheological and Light Scattering Characterization. *Macromolecules* **2007**, *40*, 3378–3387.

- (230) Abrahamsson, C.; Nordstierna, L.; Nordin, M.; Dvinskikh, S. V.; Nydén, M. Magnetic Orientation of Nontronite Clay in Aqueous Dispersions and Its Effect on Water Diffusion. *J. Colloid Interface Sci.* **2015**, *437*, 205–210.
- (231) MacGregor-Ramiassa, M.; Abrahamsson, C.; Röding, M.; Nydén, M. Magnetic Alignment of Nontronite Dispersions. *Appl. Clay Sci.* **2015**, *116–117*, 167–174.
- (232) Li, Y. L.; Vali, H.; Sears, S. K.; Yang, J.; Deng, B.; Zhang, C. L. Iron Reduction and Alteration of Nontronite N_{Au}-2 by a Sulfate-Reducing Bacterium. *Geochim. Cosmochim. Acta* **2004**, *68*, 3251–3260.
- (233) Liu, D.; Dong, H.; Bishop, M. E.; Zhang, J.; Wang, H.; Xie, S.; Wang, S.; Huang, L. Microbial Reduction of Structural Iron in Interstratified Illite-Smectite Minerals by a Sulfate-Reducing Bacterium. *Geobiology* **2012**, *10*, 150–162.
- (234) Tchoubar, C. Use of Diffraction and MGssbauer Methods for the Structural and Crystallochemical Characterization of Nontronites. *J. Appl. Crystallogr.* **1983**, *16*, 374–383.
- (235) Coussot, P.; Nguyen, Q. D.; Huynh, H. T.; Bonn, D. Avalanche Behavior in Yield Stress Fluids. *Phys. Rev. Lett.* **2002**, *88*, 1755011–1755014.
- (236) Abou, B.; Bonn, D.; Meunier, J.; Meunier, J. Nonlinear Rheology of Laponite Suspensions under an External Drive. *J. Rheol.* **2003**, *47*, 979.